Advances in Experimental Medicine and Biology 1035

Ruslan I. Dmitriev *Editor*

Multi-Parametric Live Cell Microscopy of 3D Tissue Models

Springer

Advances in Experimental Medicine and Biology

More information about this series at http://www.springer.com/series/5584

Ruslan I. Dmitriev
Editor

Multi-Parametric Live Cell Microscopy of 3D Tissue Models

Springer

Editor
Ruslan I. Dmitriev
Metabolic Imaging Group
School of Biochemistry and Cell Biology
University College Cork
Cork, Ireland

ISSN 0065-2598 ISSN 2214-8019 (electronic)
Advances in Experimental Medicine and Biology
ISBN 978-3-319-67357-8 ISBN 978-3-319-67358-5 (eBook)
DOI 10.1007/978-3-319-67358-5

Library of Congress Control Number: 2017956200

Printed on acid-free paper

This Springer imprint is published by Springer Nature
The registered company is Springer International Publishing AG
The registered company address is: Gewerbestrasse 11, 6330 Cham, Switzerland

Preface

Stem cells, 3D tissue models, bioprinting, artificial organs and regenerative medicine are becoming widely accepted as new venues in pursuit of human knowledge. The growing need and substantial progress experienced by these biomedical science and engineering areas over the recent years lead mankind to the coming 'age of biomaterials'.

The multidisciplinary territory of 3D tissue models formed by the successful fusion of developmental and cell biology, physics, chemistry, mathematics and engineering holds great promise for translational applications such as cancer biology, regenerative medicine, 'clinical trial on chip' and personalized medicine-aided 'healthy ageing'. However, newcomers and even experts working with 3D tissue models should not be mistaken by apparent ease of growing artificial tissues—with some exceptions, a great number of technical challenges exist, which must be faced and solved. Thus, the microheterogeneity and the single-cell level analysis of metabolism, hypoxia, cell proliferation status and other biomarkers have to be measured, quantitatively and with *live tissue* material. Indeed, majority of research groups try to avoid these issues and still rely on the use of fixed or artificially treated, optically cleared tissue samples or end-point assays inherited from the twentieth century, without realizing that the 'future' is already here.

Live cell imaging uses novel microscopy techniques and extensively developing probe chemistries to help in facing and solving this problem.

For example, imaging depth can be significantly improved using multiphoton and light-sheet microscopy approaches; on the other hand, the coevolution of fluorescence and phosphorescence lifetime imaging microscopies and data analysis algorithms combined with nanoparticles and new probe chemistries allows to significantly extend the number of measured parameters, creating truly multi-parametric quantitative imaging approach. The area is still very young and immature and needs strong commitment from the users to become widespread and start bringing up its results. To this end, the aim of our book is to bring together some of the leaders and pioneers in the area, to share their experience and provide easy to adapt and modify protocols, methods and techniques.

The book first introduces the reader into the *state of the art* of 3D tissue models, their general compatibility with live cell imaging and advanced imaging options (FLIM and PLIM microscopies) and highlights the available probes and sensors, which are ready to use for multi-parametric imaging in 3D (Chaps. 1, 2, 3, and 4). To extend the scope of the book, Chap. 5 provides a

brief methodological overview in the manufacturing process of 3D scaffold materials, highly useful in creating, maintaining and optimizing the 3D tissue models. The following chapters comprehensively cover most of the available applications of multi-parametric imaging and provide experimental protocols, full of technical details, necessary to guide the beginner in this area: sequential FLIM-PLIM imaging of O_2 and cell cycle in intestinal organoids is described in Chap. 6, intracellular pH imaging in tumour models is described in Chap. 7, technical tips on setting up FLIM microscope and analysis of autofluorescence are described in Chap. 8, high-resolution imaging of Ca^{2+} in live brain is described in Chap. 8 and example of viscosity imaging is described in Chap. 9. Some advanced applications, which can be potentially compatible with FLIM and PLIM, conclude the book: light-sheet microscopy for in situ monitoring of cancer cell invasion (Chap. 10) and Raman microscopy (Chap. 11). Overall, the applications are selected in order to (i) cover the majority of available and successfully used measurement options (including endogenous cofactors, exogenous dyes, nanoparticles and genetically encoded biosensors) and (ii) provide an overview of the practical use of available imaging platforms—from inexpensive laser-scanning systems to two-photon FLIM and light-sheet microscopes. Most of the 'missing' applications are discussed in introductory Chaps. 1, 2, 3, and 4.

I wish to thank all the contributors for joining me in this venture, and I believe that altogether the final book represents a comprehensive starting reference guide for the multi-parametric analysis of 3D tissue models, will serve its main function to invite and engage the new people in the area and will remain highly useful for generations of scientists.

Cork, Ireland Ruslan I. Dmitriev

Contents

Contributors

Kamlesh Awasthi Department of Applied Chemistry and Institute of Molecular Science, National Chiao Tung University, Hsinchu, Taiwan

Katie Bardsley Institute for Science and Technology in Medicine, Keele University, Stoke-on-Trent, UK

Wolfgang Becker Becker & Hickl GmbH, Berlin, Germany

Anthony J. Deegan Institute for Science and Technology in Medicine, Keele University, Stoke-on-Trent, UK

Ruslan I. Dmitriev Metabolic Imaging Group, School of Biochemistry and Cell Biology, University College Cork, Cork, Ireland

Neil O'Donnell Metabolic Imaging Group, School of Biochemistry and Cell Biology, University College Cork, Cork, Ireland

Irina N. Druzhkova Institute of Biomedical Technologies, Nizhny Novgorod State Medical Academy, Nizhny Novgorod, Russia

Varvara V. Dudenkova Institute of Biomedical Technologies, Nizhny Novgorod State Medical Academy, Nizhny Novgorod, Russia

Tara Foley Department of Anatomy and Neuroscience, University College Cork, Cork, Ireland

Alicia El Haj Institute for Science and Technology in Medicine, Keele University, Stoke-on-Trent, UK

Nadezhda I. Ignatova Institute of Biomedical Technologies, Nizhny Novgorod State Medical Academy, Nizhny Novgorod, Russia

Shinji Kajimoto Graduate School of Pharmaceutical Sciences, Tohoku University, Sendai, Japan

Anastasia Koroleva Laser Zentrum Hannover e.V., Hannover, Germany

Marina K. Kuimova Department of Chemistry, Imperial College London, London, UK

Daria Kuznetsova Institute of Biomedical Technologies, Nizhny Novgorod State Medical Academy, Nizhny Novgorod, Russia

Maria M. Lukina Institute of Biology and Biomedicine, Nizhny Novgorod State University, Nizhny Novgorod, Russia

Marco Marcello Department of Biochemistry and Centre for Cell Imaging, Institute of Integrative Biology, University of Liverpool, Liverpool, UK

Alix Le Marois Department of Physics, King's College London, London, UK

David Mason Department of Biochemistry and Centre for Cell Imaging, Institute of Integrative Biology, University of Liverpool, Liverpool, UK

Natalia M. Mishina Shemyakin–Ovchinnikov Institute of Bioorganic Chemistry RAS, Moscow, Russia

Takakazu Nakabayashi Graduate School of Pharmaceutical Sciences, Tohoku University, Sendai, Japan

Raluca A. Niesner Deutsches Rheuma-Forschungszentrum, a Leibniz Institute, Berlin, Germany

German Rheumatism Research Center, Berlin, Germany

Nobuhiro Ohta Department of Applied Chemistry and Institute of Molecular Science, National Chiao Tung University, Hsinchu, Taiwan

Irina A. Okkelman Laboratory of Biophysics and Bioanalysis, School of Biochemistry and Cell Biology, University College Cork, Cork, Ireland

Dmitri B. Papkovsky Laboratory of Biophysics and Bioanalysis, School of Biochemistry and Cell Biology, University College Cork, Cork, Ireland

Helena Radbruch Neuropathology, Charité–Universitätsmedizin, Berlin, Germany

Asylkhan Rakymzhan Deutsches Rheuma-Forschungszentrum, a Leibniz Institute, Berlin, Germany

Rosalie Richards Department of Biochemistry and Centre for Cell Imaging, Institute of Integrative Biology, University of Liverpool, Liverpool, UK

Angelika Rück Becker & Hickl GmbH, Berlin, Germany

Violaine Sée Department of Biochemistry and Centre for Cell Imaging, Institute of Integrative Biology, University of Liverpool, Liverpool, UK

Lubov' E. Shimolina Institute of Biology and Biomedicine, Nizhny Novgorod State University, Nizhny Novgorod, Russia

Institute of Biomedical Technologies, Nizhny Novgorod State Medical Academy, Minin and Pozharsky Square, Nizhny Novgorod, Russia

Marina V. Shirmanova Institute of Biomedical Technologies, Nizhny Novgorod State Medical Academy, Nizhny Novgorod, Russia

Vladislav Shcheslavskiy Becker & Hickl GmbH, Berlin, Germany

Anastasia Shpichka Institute for Regenerative Medicine, Sechenov First Moscow State Medical University, Moscow, Russia

Klaus Suhling Department of Physics, King's College London, London, UK

Mizuki Takeuchi Graduate School of Pharmaceutical Sciences, Tohoku University, Sendai, Japan

Peter Timashev Institute for Regenerative Medicine, Sechenov First Moscow State Medical University, Moscow, Russia

Ying Yang Institute for Science and Technology in Medicine, Keele University, Stoke-on-Trent, UK

Elena V. Zagaynova Institute of Biomedical Technologies, Nizhny Novgorod State Medical Academy, Nizhny Novgorod, Russia

Part I

Introduction: 3D Tissue Models, Methodology and Toolkit

Current *State-of-the-Art* 3D Tissue Models and Their Compatibility with Live Cell Imaging

1

Katie Bardsley, Anthony J. Deegan, Alicia El Haj, and Ying Yang

Abstract

Mammalian cells grow within a complex three-dimensional (3D) microenvironment where multiple cells are organized and surrounded by extracellular matrix (ECM). The quantity and types of ECM components, alongside cell-to-cell and cell-to-matrix interactions dictate cellular differentiation, proliferation and function in vivo. To mimic natural cellular activities, various 3D tissue culture models have been established to replace conventional two dimensional (2D) culture environments. Allowing for both characterization and visualization of cellular activities within possibly bulky 3D tissue models presents considerable challenges due to the increased thickness and subsequent light scattering features of such 3D models. In this chapter, *state-of-the-art* methodologies used to establish 3D tissue models are discussed, first with a focus on both scaffold-free and scaffold-based 3D tissue model formation. Following on, multiple 3D live cell imaging systems, mainly optical imaging modalities, are introduced. Their advantages and disadvantages are discussed, with the aim of stimulating more research in this highly demanding research area.

Keywords

3D tissue model • 3D live imaging • Confocal microscopy • FLIM • PLIM • OCT • microCT

1.1 Introduction

In in vitro research, both basic and clinical, and the pharmaceutical industry, two-dimensional (2D) cellular monolayer culturing is a well-established and indispensable protocol that has been in use since the 1900s. The adhesion dependent cells, either freshly isolated or immortalized or culture expanded, are seeded and spread on

K. Bardsley • A.J. Deegan • A. El Haj • Y. Yang (✉)
Institute for Science and Technology in Medicine, Keele University, Stoke-on-Trent ST4 7QB, UK
e-mail: y.yang@keele.ac.uk

R.I. Dmitriev (ed.), *Multi-Parametric Live Cell Microscopy of 3D Tissue Models*,
Advances in Experimental Medicine and Biology 1035, DOI 10.1007/978-3-319-67358-5_1

polystyrene plastic coated with various molecules via focal adhesions. Their responses to chemical, biological and physical stimulations can be easily recorded at cellular, protein and gene levels through live and fixed cell samples. The 2D cell culture system has multiple advantages: easier environmental control for the investigation of individual factors; low cost for multiple sample tests (up to 384 samples in a single well plate); convenient and rapid live cell observation by multiple optical imaging modalities; and a rich body of literature accumulated over decades for comparative study. Whilst it is widely accepted that cells adapt to different culture systems and respond to local signalling cues, the culturing of cells on 2D surfaces simply does not mimic the physiological environment required for truly replicative tissue models [1]. Such monolayer culturing results in changes in cell morphology, such as cell flattening, which can subsequently alter phenotype, gene expression and protein synthesis patterns [2, 3].

With regards to cells of native tissues, it is easy to understand that they will behave differently, both structurally and functionally, when removed and seeded on 2D surface-coated substrates. Mammalian cells grow within a complex three-dimensional (3D) microenvironment where multiple cells are organized within extracellular matrix (ECM) enabling the incorporation of the vascular and immune systems. The high degree of structural complexity and multicellular 3D morphology ensures the tissues' homeostasis and healthy metabolism.

In recent years, the creation of 3D tissue models has become an intensive research area. Thanks largely to the development of Tissue Engineering and Regenerative Medicine, complex 3D models have been established for numerous tissues, such as bone, cartilage, skin, lung, liver, and cornea. Tissue engineering combines material science with stem cell technology and biomimetic culture environments to create highly tuneable, functional 3D tissues [4]. Shifting from 2D to 3D culture systems can affect numerous, if not all, cell functions, including proliferation and differentiation, allowing for greater cell-to-cell contact and intracellular signalling, and the organisation of more tissue-like structures [5]. With that, technological developments have been moving toward the use of 3D cultures, which have been shown to promote the natural morphology of cells and allow for the production of more physiologically relevant environments [6].

Whilst biologists, biomaterial scientists and biotechnologists have been working tirelessly to establish more biomimetically accurate 3D tissue models for the replication of their natural counterparts, the characterisation of such models presents considerable challenges. The convenient optical imaging systems, such as brightfield, phase microscopy, and epifluorescent microscopy, that rely on light being transmitted through thin samples, such as 2D cell cultures, do not translate to 3D tissue models due to the opaqueness and often thick sample dimensions. In this chapter, current *state-of-the-art* 3D tissue models and the live cell imaging modalities adapted to study them are reviewed.

1.2 Types of 3D Tissue Models

3D tissue models typically, but not exclusively, involve the combination of cells with 3D matrices and molecular signals intended to replicate tissue-specific cells and ECM. 3D environments, therefore, provide a microenvironment for the optimal growth, differentiation and functionality of cells, allowing for the production of tissue-like constructs and models in vitro. These 3D environments can be achieved either through scaffold-free cultures, such as cellular aggregates, or scaffold-cell constructs.

1.2.1 Scaffold-Free Cultures

Scaffold-free cultures, commonly referred to as micromass or aggregate cultures, rely on the hypothesis that cellular aggregation can greatly enhance in vitro tissue development by mimicking in vivo pathways. A prime example of this sees bone cells being aggregated in vitro to replicate the in vivo formation of an ossification centre, which is an essential step in bone

development or regeneration via the intramembranous ossification pathway.

There are a number of methods one can use to culture cells in a scaffold-free 3D environment. Wang et al. for example, used photolithography and micropatterning techniques to fabricate moulds, which were then used to aggregate mesenchymal stem cells (MSC) for the study of differentiation efficiency [7]. Deegan et al. altered the surface chemistry of a biomaterial to create a suspension culture environment that actively encouraged cells to self-organise into 3D structures allowing for the study of cellular aggregate mineralisation [8]. Hildebrandt et al. used a number of different 3D culturing techniques to study the differentiation of MSCs, and concluded that 3D culturing provided cells with an environment corresponding to that of in vivo biological conditions [9]. 3D culturing in this way not only offers the opportunity to replicate the intricacies of naturally formed tissues for the development of 3D tissue models, but may also offer an insight into the regulatory signalling cascades induced by particular bioactive elements and factors [10].

If scaffold-free culturing is to be the link between conventional 2D or monolayer culturing and the development of whole organs, the co-culturing of multiple cell types should be considered [7]. A significant hurdle in the development of large tissue-engineered models is the maintenance of core cell viability. In the case of large bone grafts for example, cellular necrosis and graft failure often result from an inadequate supply of oxygen and nutrients [11, 12]. A viable solution for such a hindrance is the development of pre-vascular structures within 3D tissue models via the co-culturing of multiple cell types. For example, numerous attempts have been made to culture endothelial cells (EC) with various other cell types within scaffold constructs in the hope of developing vascularised tissues [13–16]. However, to truly replicate the in vivo formation of vascularised tissues, one should consider the co-culturing of cells within a scaffold-free model. Scaffold-free culture environments allow cohabiting cell types to self-organise and form inner-construct structures more replicative of in vivo vascularised tissues [17]. Saleh and colleagues did just that by co-culturing ECs with MSCs using a 3D in vitro model (50:50 ratio) and successfully observed cellular self-assembly and cell-type partitioning [17]. A study carried out by Deegan et al. also co-cultured ECs with MSCs using 3D cellular aggregates, and also observed cellular self-assembly. This study did so, however, using a cell-to-cell ratio more replicative of in vivo tissues (5% ECs), two different aggregation techniques with differing self-assembly characteristics, and a dynamic culture environment previously shown to replicate the shear stresses experienced by bone cells in vivo, i.e. hydrostatic loading. It was shown that by tailoring specific parameters, the growth of 3D tissue models can be refined to more accurately replicate those of in vivo tissues. What this and other studies have shown is that by having the correct physical and chemical cues, one can affect the ability of the cells to spatially arrange, grow, proliferate, differentiate and mature [4].

Morimoto and colleagues too showed the benefits of co-culturing multiple cell types for generating highly organised structures with the development of a 3D skeletal muscle model with motor neurons [18]. The model was successful in having produced highly aligned muscle fibres and functioning neuromuscular junctions, which could potentially be used to study pharmacokinetic assays related to neuromuscular junction disease therapies. A recent study carried out by Giacomelli and colleagues produced a 3D cardiac tissue model comprised of cardiomyocytes and ECs [19]. Whilst the model lacks the cellular alignment seen with other cardiac models, simultaneously co-differentiating both cell types to produce the model holds great scope for further refinement [20].

1.2.2 Scaffold-Cell Constructs

The use of scaffolds allows for the production of larger tissue models and supports cells in vitro while they create an ECM, which will provide a foundation for the formation of a new tissue model [21]. 3D scaffolds can be manufactured from a range of natural or synthetic materials;

however, it is essential that these materials are biocompatible, biodegradable and allow for cell adhesion.

Natural scaffolds are composed of ECM proteins such as collagen [22], fibrin [23] and hyaluronic acid [24]. The advantages to using ECM proteins are that they have many cell adhesion sites and are naturally occurring within tissues. The disadvantages, however, are that there is batch-to-batch variation in the quality of biomaterials and some of them are animal derived, which makes it difficult to use these ECM proteins for clinical applications. Synthetic scaffolds have the advantages of having a defined chemical structure, which means there is little batch-to-batch variation, and the mechanical and degradation properties can be tuned [25]. These scaffolds are formed as polymers, such as poly(lactic-co-glycolic) acid, ceramics, such as hydroxyapatite, and self-assembling peptides.

Acting as mechanical support and a structural template, scaffolds in 3D tissue models are usually either in porous, fibrous or hydrogel form, enabling large spaces for cells seeding and neo-ECM formation [26, 27]. The pore size, shape and interconnectivity within the scaffolds provide a microenvironment for cells and affect cells' viability, metabolism and phenotype, with the degradation feature of the scaffold material changing such parameters dynamically. Dimensionally, scaffold-cell constructs are far larger than scaffold-free cultured 3D tissue models (2–100 times). Although scaffold-cell constructs are a more transferrable tissue model for clinical applications, monitoring live cells within them is highly challenging. Considerable efforts have been undertaken to select the appropriate scaffolds for specific cell types and tissues to be grown and evaluated.

1.3 Imaging Modalities for Live Cells

3D tissue models provide important tools to study cellular metabolism and response to external stimuli, individually or in combination, as occurring in the native environment. Hence, real-time, non-destructive and non-invasive imaging modalities will play crucial roles in displaying information enabling the tracking of cell location, proliferation, differentiation and some functions of these cells in a temporal and spatial manner. For scaffold-cell constructs, the degradation of scaffolds interacts with the cells and dictates the cells' metabolism, which adds an extra living element to the live cell-imaging task.

3D tissue models represent a number of challenges for live cell imaging that require different approaches to those of 2D models. A few imaging modalities conventionally used in the medical field for 3D objects, such as MRI, ultrasound and computer tomography, are not applicable for live cell imaging within 3D tissue models because of a number of practical barriers. First is resolution. None of the modalities mentioned have the capacity to visualise cell dimensions at a non-toxic dose of imaging energy source. Second is the cost of the associated instruments; they are not affordable for daily laboratory applications. The bulk instrument setting is another shortcoming of these modalities. Optical imaging techniques that rely on the detection of fluorescence, phosphorescence as well as backscattered light from samples are the more suitable and widely used modalities in 3D tissue model studies. Incorporating the confocal and interferometric contrast enhancement mechanisms, a few tomographic modalities, including confocal laser scanning microscopy, fluorescence and phosphorescence lifetime microscopies, and optical coherence tomography (OCT), have made great contributions to 3D tissue model studies and tracking cellular activities. Micro computerised tomography (microCT) with high resolution has also been utilised for 3D tissue model studies.

When imaging live cells in scaffold-cell constructs, the scaffold's properties will have a great impact, which can help or hinder the imaging of cells within them. These properties include optical opacity, density and auto-fluorescence. Solid scaffolds, such as hydroxyapatite, are optically opaque which can make some imaging modalities difficult to use. Microscopy techniques for example, will be hindered due to low light penetration into the scaffold, and whilst this can be overcome by

increasing the porosity of the scaffolds, this will also change the material properties. Balancing these changes is crucial for the creation of a 3D tissue model. Other scaffolds such as collagen gels will be contracted by the cells during the development of the 3D model, which increases the density of the tissue required to be imaged. Once again, this can be overcome by seeding collagen on filter paper to reduce the amount of contraction. Collagen is also extremely auto-fluorescent at lower wavelengths; therefore, there are limitations to the wavelengths, which can be used during fluorescent imaging of collagen gels.

1.3.1 Confocal Laser Scanning Microscopy and Epifluorescence Microscopy

Fluorescence microscopy, in brief, works by irradiating a sample with a wavelength of light, typically from visible through ultraviolet, which excites a fluorescent species, and then separates the weaker emitted fluorescence from the excitation light to reveal fluorescent structures. Through the use of filters, specific wavelengths of illuminating light can be chosen, which allows for the visual localization of specific target molecules [28]. Epifluorescence microscopes are the most common form of fluorescence microscope used in life sciences that simply illuminate a specimen from above. Confocal laser scanning microscopes are inherently more complex and work on the premise of collecting light from a single focus plane within a sample or 3D tissue model. Confocal microscopy is carried out with the use of a low powered, near infrared (IR) laser that focuses light on a specific area within a 3D tissue sample. Light reflected or scattered from this point is collected through a pin-sized aperture by a detector. The light source, illuminated point and detector are all optically conjugated to a specific optical focal plane, which therefore, allows for the collection of data from a specific point within a 3D tissue model. This allows for the better resolution of light signals when compared to normal epifluorescence or brightfield microscopy. Due to the complexity of the equipment required to obtain the high-resolution images, however, the equipment required can be expensive when compared to other microscopic imaging techniques.

The pros of confocal microscopy are that it allows for the collection of high-resolution images from within opaque tissues; however, the depth of penetration can be limited by the tissue or sample type. An additional challenge when imaging cells within 3D scaffold-supported constructs is the production of auto fluorescence by the scaffold material. As mentioned, collagen is well known to exhibit bright auto-fluorescence making it difficult to visualise live cells within these constructs. Scaffold-free, aggregate cultures also have their own difficulties when it comes to imaging. Due to their dense nature, it is often difficult for the light source to penetrate the aggregate, rendering full 3D imaging difficult. This characteristic will also affect opaque solid scaffolds, such as calcium phosphates.

Both techniques often, but not always, require the use of immunohistochemical staining prior to imaging. Immunohistochemistry fundamentally identifies the presence of antigens or proteins in tissues by means of specific antibodies. Antigen—antibody interactions can be seen by a coloured histochemical reaction with the use of confocal or epifluorescence microscopes [29]. Such staining has been used to visualise the presence of specific markers, such as osteogenic markers (i.e. bone-specific alkaline phosphatase (ALP), collagen type 1 (Col1), and osteocalcin (OCN)), or the location of specific cells within 3D structures, such as ECs via EC surface markers (i.e. CD31) [30]. Such a technique can also be used to distinguish living cells from dead cells, which is particularly important for monitoring cellular health within 3D tissues [31]. As mentioned, for both scaffold-free and scaffold-supported constructs, the density of the model can be an impeding factor for imaging, but also for immunohistochemistry. The dense nature of such constructs often impedes the penetration of antibodies, making it difficult to acquire complete 3D images. Given that the majority of scaffold-supported constructs require the free movement of cells throughout, however, limited antibody

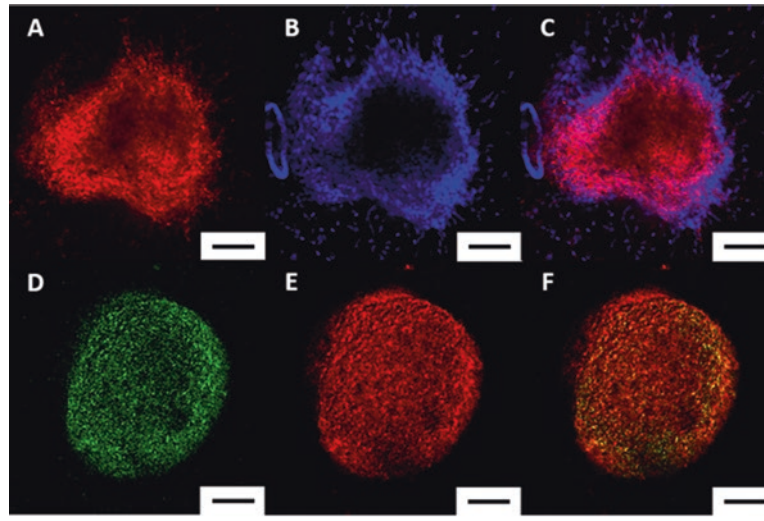

Fig. 1.1 Confocal laser scanning of two different techniques used for cell tracking within scaffold-free, 3D co-cultured cellular aggregates. (**a**) ECs stained with a common membrane marker, CD-31, within an EC/MSC co-cultured cellular aggregate, post-formation. (**b**) All cells stained with a common nuclei marker, DAPI, within the same cellular aggregate, post-formation. (**c**) a and b merged. (**d**) ECs fluorescently-tagged with a common membrane dye conjugated with a FITC fluorophore, within an EC/MSC co-cultured cellular aggregate, pre-formation. (**e**) MSCs fluorescently-tagged with a common membrane dye conjugated with a TRITC fluorophore, within the same cellular aggregate, pre-formation. (**f**) d and e merged. Scale bar represents 200 μm

penetration is often more of an issue with scaffold-free cellular aggregates.

Novel non-antibody protocols are currently being developed to be used alongside confocal microscopy techniques. With regards to identifying the spatial distribution of cells throughout a 3D model, recent advances in cell biology have led to the development of live cell tracker dyes that can be non-specifically adhered to the cellular membrane prior to seeding within a 3D construct. Over a given period of time, this technique will allow for the spatial and temporal tracking of cells within the 3D environment. Figure 1.1 below shows two cellular aggregates, one stained post aggregation with a specific antibody and the second being tagged prior to aggregation with a non-specific membrane dye. Note how the aggregate on the top row (A – C) has a void in its centre where imaging could not detect the presence of any fluorophores. This is due to the density of the aggregate restricting the penetration of the antibody to its centre. The aggregate on the bottom row, however (D – F), does not display the same void, despite both aggregates being of a similar size and density. This is because the cells of the aggregate on the bottom row were tagged prior to seeding; thus, the cells in its centre were not affected by a lack of antibody penetration and could be imaged more thoroughly.

Confocal microscopy can also be used in reflectance mode, which doesn't require the use of fluorescence staining for live cell imaging. Reflectance confocal microscopy detects backscattered light from illuminated tissue, displaying an image with high resolution and contrast, without the requirement of fluorescent probes. This technique is often used in combination with fluorescent labelling.

1.3.2 Fluorescence Lifetime Imaging (FLIM) and Phosphorescence Lifetime Imaging (PLIM)

In addition to using fluorescence intensity for image contrasting, fluorescence decay time contains rich information, which can be used to build

unique imaging modalities. Two of such imaging techniques are Fluorescence Lifetime Imaging (FLIM) and Phosphorescence Lifetime Imaging (PLIM). The fluorescence excited-state lifetime (decay time) is a unique, intrinsic property of a fluorophore, which is independent of the fluorophore concentration or light path length but dependent upon excited-state reactions, such as fluorescence resonance energy transfer (FRET), with the FRET being very sensitive towards changes in physiological parameters in living cells. Quantification of FRET is the main application of FLIM, whilst application of PLIM is predominately based on phosphorescence quenching since quenching of phosphorescence by a physiological parameter affects phosphorescence lifetime. In recent years, both FLIM and PLIM techniques have been actively explored for live cell measurements in 3D tissue models, enabling the gathering of information on the formation/consumption of metabolites or respiratory gaseous gradients, spatially and temporally.

FLIM measurements have been used to measure intramolecular distances [32], and to observe dynamic conformational changes in proteins in 2D cell culture [33]. Extending the technique, Chennell et al. successfully incorporated a modified Adenosine Monophosphate (AMP) Activated Protein Kinase (AMPK) FRET probe in to 3D tumour spheroids [34]. The comparison of FLIM images between the 2D and 3D models revealed that the cells in the 3D model had a similar response to 2D culture towards the stimulation of AMPK activator, 991, suggesting that 991 was able to diffuse through the spheroids and uniformly activate the probe. Thus, the FLIM technique enables one to evaluate the efficacy of therapeutic treatments of diseases within 3D tissue models.

The capacity to measure the partial oxygen concentration makes PLIM a powerful tool to quantify the hypoxic environment in 3D tissue models for diverse tissues and tumours. Oxygenation is a critical physiological parameter which influences the proliferation, differentiation, metabolism, gene expression and response to drug treatments. Live cell imaging with cell-penetrating phosphorescent O_2-sensitive probes allows quantification and high-resolution mapping of O_2 distribution in 3D tissue models. The Dmitriev group developed a number of novel Pt-porphyrin-based nanoparticle oxygen-sensitive probes. The probes are designed to incorporate multiple functions into conjugated polymer matrices including light harvesting antenna, reference and O_2 sensing indicator dyes [35]. The charged groups in the probes enhance the penetration of the probes into cells and tissues, and also their stability in aqueous solutions. These nanoparticles allow for the ratio metric intensity measurement, quantifying the oxygen distribution within 3D tissue models in real-time. Figure 1.2 demonstrates the O_2-sensitive probe, SI-0.1^{+}/0.1^{-}, intracellularly incorporated in to spheroids comprised of HCT116 cells. The spheroid was co-stained with Cholera toxin, subunit B-Alexa Fluor 488 conjugate. 3D reconstruction of O_2 distribution by PLIM for the spheroid by one-photon confocal microscopy delineated clearly the heterogeneous oxygenation feature. With a similar setting and probe, PLIM has been used in the quantification of oxygen supply and consumption in pseudoislets formed under different substrates leading to different cell-cell contact arrangements [36].

The PLIM images reflected the oxygenation pattern in different pseudoislets, and correlated well with cell viability and insulin production when using glucose to stimulate the pseudoislets.

1.3.3 Optical Coherence Tomography

Optical coherence tomography (OCT) is a relatively new optical imaging modality based on the scattering of light from a 3D object with penetration depths of up to several millimetres. The modality uses interferometric techniques to enhance the contrast and measure the time-of-flight of scattered photons. OCT images result from the different back-scattering/back-reflection properties of different structures within transparent or opaque subjects.

The ability to visualise opaque subjects with relatively high depth (a few millimetres), high resolution (a few micrometres) and fast image

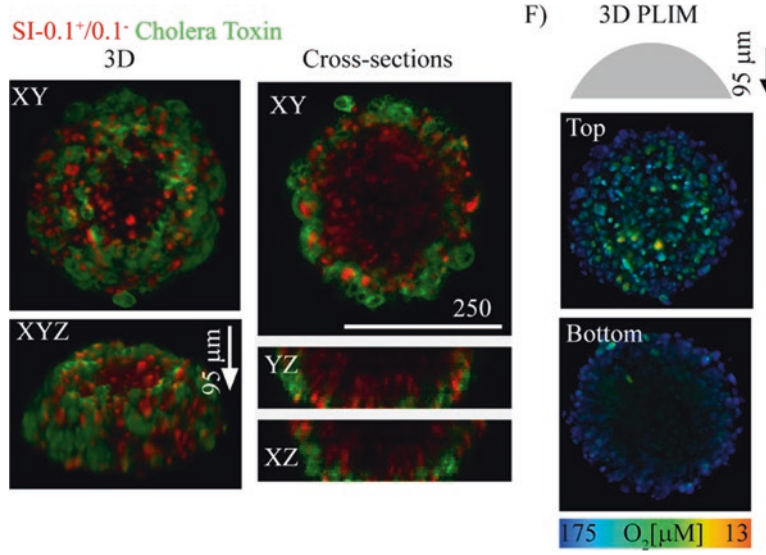

Fig. 1.2 Staining of 3D tissue model (tumor spheroids from HCT116 cells) with SI-0.1^{+}/0.1^{-} nanoparticle probe. Sample was co-stained with Cholera toxin, subunit B-Alexa Fluor 488 conjugate. 3D reconstruction of HCT116 spheroids revealed by one-photon confocal microscopy. 3D reconstruction of O_2 distribution by PLIM for the same spheroid. Scale bar is in micrometers. Taken with permission from [35]

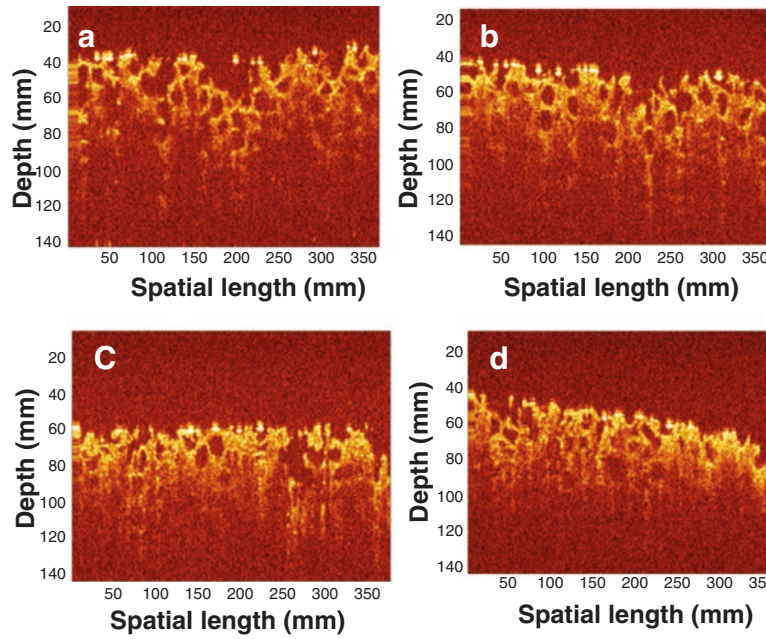

Fig. 1.3 Optical coherence tomography images of scaffold-cell constructs cultured for 4 weeks with MG63 cells. (**a**) A blank PLA scaffold. (**b**) A statically-cultured construct. (**c**) A perfusion-cultured construct. (**d**) A perfusion and compression-cultured construct [37]

acquisition rate makes OCT unique in monitoring 3D scaffold-cell tissue models. Scaffolds in 3D scaffold-cell tissue models are usually porous and degradable structures. The parameters of the scaffolds, such as pore size, porosity and pore interconnectivity, affect cell activity, cell distribution, proliferation and differentiation within the scaffolds. Since OCT can image the porous structure of scaffolds clearly, continuously and non-destructively without sample preparation, and with pore size and porosity of the scaffolds being dynamic parameters in the culture period that closely correlate with cell growth profiles and tissue turnover, it is hypothesised that quantifying porosity changes over culture time and conditions through OCT imaging can reveal cell growth profiles. Figure 1.3 illustrates the OCT images of statically- and dynamically-cultured

PLLA scaffolds seeded with MG63 bone cells for 4 weeks. A blank scaffold image is included.

A striking pore structure change in response to different culture conditions can be observed. It is noted that the light penetration depth of the construct was reduced after the four weeks culture period in comparison to the blank scaffold. Furthermore, the pore size and porosity had decreased significantly, i.e. the darker area in the images was reduced. From the cell seeding procedure and the expected cell growth profile, the increased brighter areas in the scaffolds were ascribed to the cells and the ECM generated by the cells, which increased the optical scattering properties of the constructs, leading to an increased back-scattering of OCT signal. Based on the pore architecture changes, a local porosity analysis of scaffolds from OCT images has been proposed to quantify the porosity change, which has been used to semi-quantify the tissue turnover rate [37, 38].

Viewing tissues at cellular level is difficult with conventional OCT if it uses super luminescent diodes as a light source. The highest longitudinal resolution OCT achieved to date has been obtained by using a femtosecond Ti: sapphire laser, with which sub-cellular imaging with a longitudinal resolution of approximately 1 μm has been demonstrated using this source. Optical coherence microscopy (OCM) is a variation of OCT. It utilizes a high NA objective to achieve a higher imaging depth through rejecting scattered and out-of-focus light [39]. Thus, it can obtain cellular images in 3D tissue model with a similar transverse spatial resolution as confocal microscopy, but without the required labelling [40].

1.3.4 Micro-Computerised Tomography

Micro computerised tomography (microCT) is a non-destructive technique that provides a 3D image of the internal structure of a sample. MicroCT exploits variations in X-ray absorption, refraction and scattering to form an image based on alterations in contrast, highlighting the spatial distribution of material densities within a sample [41, 42]. In brief, microCT works by producing an X-ray beam via an X-ray generator, which is then passed through a sample and onto a detector to produce a radiograph. The sample is then rotated by a fraction of a degree and another image is taken. These images are then processed and reconstructed using computer software to produce a 3D image of the sample.

As microCT shows excellent contrast between soft and hard tissues, the evolution of this technique has largely been driven by research centred on bone. To the field of regenerative medicine, microCT is an invaluable tool that is used to evaluate the skeletal system, both in vivo and ex vivo [43]. The resolution of conventional microCT does not allow illustration of cell morphology, however, the monitoring of cellular activities is indirectly related to matrix production, especially mineralized matrix. With that, recent advances have seen microCT become a frequently used tool for in vivo studies focused on the temporal analysis of bone formation [44–46]. MicroCT has proven itself a valuable tool for measuring mineralized matrix formation [47]. Figure 1.4a, b shows examples of an MSC cellular aggregate imaged over two culture time points (96 and 168 h).

The aggregate was cultured in such a way as to encourage the deposition of minerals in vitro in a way similar to that of maturing bone in vivo. Note how the aggregates imaged at the later time point appeared to have more material; thus, microCT was able to visualise and monitor over time the development of mineralized structures.

An interesting study by the Guldeberg group [48, 49] demonstrated the development of special rigs which allow for the monitoring of mineralization within scaffold-cell constructs over a prolonged culture period (up to 5–8 weeks). The samples have repeated scanning to view the mineralization along culture time or to assess sample size effect and spatial distribution of minerals in response to perfusion conditions within a bioreactor (Fig. 1.4c).

With regards to the spatial and temporal analysis of 3D tissue models, however, one of the main limitations of microCT is that it involves relatively low X-ray absorption-based contrasting;

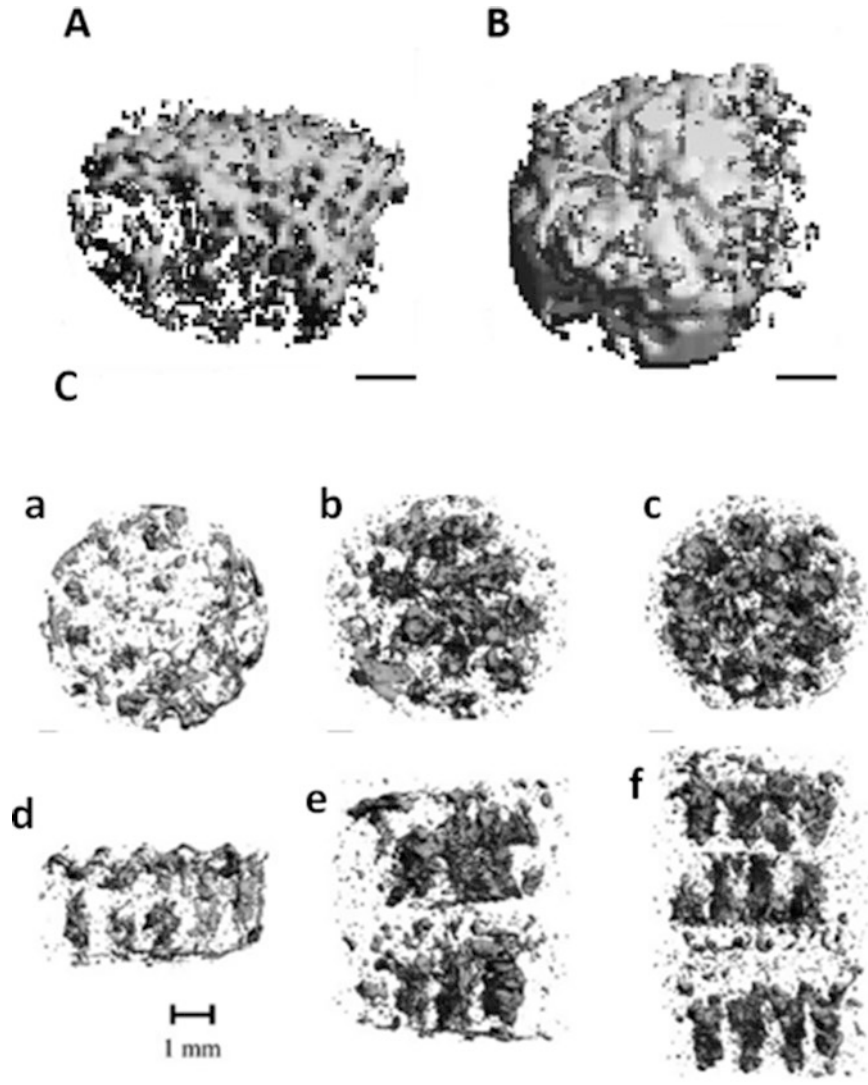

Fig. 1.4 Micro-computerised tomography images of scaffold-free cellular aggregates. (**a**) An MSC aggregate after 96 h in osteogenic-supplemented medium. (**b**) The same MSC aggregate as A, after 168 h in osteogenic-supplemented medium. Scale bar represents 100 μm. (**c**) Mineral deposits within stacked PCL + Collagen scaffolds seeded with rat MSCs after 5 weeks of perfusion culture at 0.2 ml/min. (*a–c*) The top view; (*d–f*) side view. (*a*, *d*): 3 mm; (*b*, *e*): 6 mm; (*c*, *f*): 9 mm scaffold. The 6 and 9 mm constructs (**e**, **f**) show mineral localized within each individual 3 mm thick scaffold, but few mineral deposits at the interfaces between each scaffold. Taken with permission from [48]

meaning it can be difficult to distinguish soft tissues from soft biomaterials, such as hydrogels, and/or hard tissues from hard biomaterials or scaffolds, such as ceramic-based matrices. In an effort to overcome these limitations, contrast agents have been developed for the visualization of soft tissues. Microfil and barium sulphate, for example, have been utilized for the study of tissue model vascularization [50], and collagen has been stained with heavy metal contrast agents to display the 3D structure of engineered tissues. Continued development is required, however, if such agents are to be used for the continued or online monitoring of tissues and models given that they can be toxic and are, therefore, only utilized for endpoint analyses.

1.3.5 Indirect Live Cell Imaging

1.3.5.1 Monitoring Scaffold Degradation

Cells in 3D tissue models can also be imaged indirectly by investigating changes in the supporting scaffolds, which are typically utilized for the creation of larger tissue models. Scaffold degradation has been characterized using a wide range of techniques including weight loss [51], high performance liquid chromatography (HPLC) [52] and gel permeation chromatography [53]. These techniques, however, require the destruction of the 3D tissue model and, therefore, do not allow for real-time, live imaging of the constructs and associated scaffold degradation. A novel online monitoring technique has utilized scaffold chemistry in order to tag biomaterials with fluorescent molecules and subsequently assess degradation through changes in fluorescence overtime [54, 55]. These fluorescent tagging approaches have been utilized on several biomaterials to date, including chitosan, PEG-dextran, collagen, fibrin and PLGA, both in vitro and in vivo (Fig. 1.5I) [54–57].

Monitoring scaffold degradation is an essential technique as degradation has been shown to have a significant effect on cells within tissues. Figure 1.5II shows that MG63 cells maintained a high proliferation rate and a homogenous distribution around a slowly degrading porous PLGA scaffold, whilst the same cell type exhibited an aggregated morphology in a faster degrading PLGA scaffold with high differentiation activities. To quantify the effect of scaffold degradation on cellular activities, Bardsley et al. defined a turnover index for the correlation of biomaterial degradation and cell-based ECM synthesis using fluorescent tagging techniques [58]. The work showed that the degradation of a range of biomaterials can influence cell behaviour including proliferation and gene and protein expression. Slower degrading biomaterials were shown to increase cell proliferation when compared to

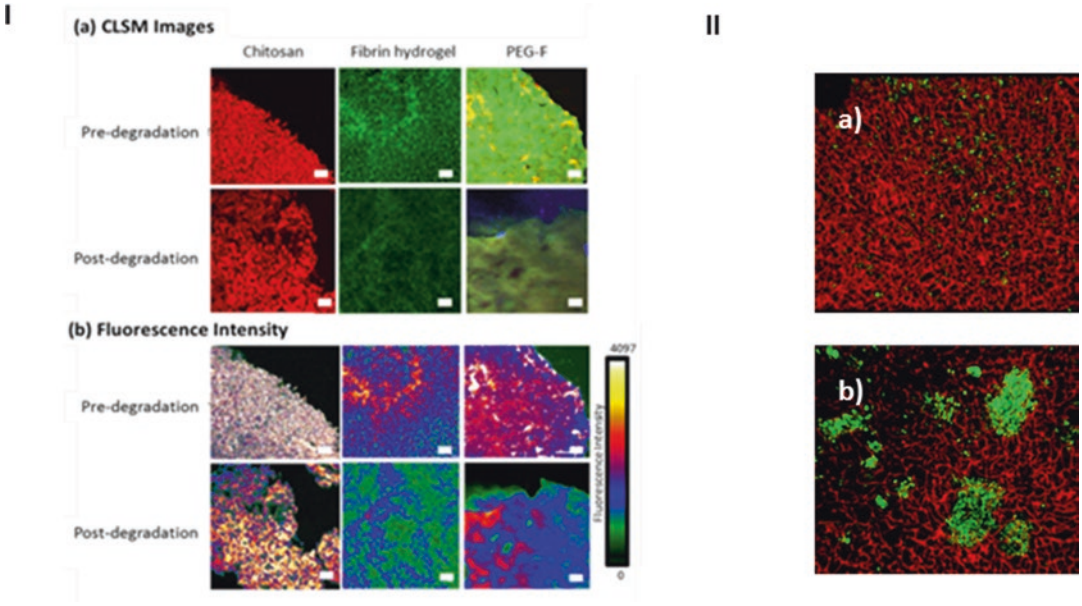

Fig. 1.5 (I) Fluorescence (**a**) and intensity (**b**) images of tagged scaffolds cultured for 10 days, obtained using confocal laser scanning microscopy. The confocal laser scanning microscopy intensity images (**b**) correspond to the fluorescence in the x/y plane of the biomaterials showing distribution throughout the depth of the scaffold (z plane) (n = 3). The fluorescence was shown to be decreased after the 10 day degradation period in the degrading fibrin; however, no change in intensity was observed in the non-degrading chitosan. Scale bar represents 500 μm [55]. (II) The variation of cellular morphology (MG63 cells) in scaffolds (PLGA) with slow (**a**) and fast (**b**) degradation rate

Table 1.1 Relative turnover indices which were calculated relative to the non-degrading chitosan, with values greater than 1 indicating that the cell-based parameter was increased on the test biomaterial when compared to the non-degrading chitosan, while values less than 1 indicated a decrease (n = 3) [58]

	Chitosan	Aprotinin fibrin	Lipase chitosan	Fibrin
(a) *MG63 relative TI*				
Cell proliferation	**1**	0.8	0.5	0.2
Cell metabolism	**1**	0.8	0.4	0.2
Osteocalcin expression	1	2.7	9.5	**16.9**
Alkaline phosphatase expression	1	3.2	4.5	**5.4**
Osteopontin expression	1	3.0	3.2	**6.1**
Collagen deposition	1	0.4	1.0	**4.9**
(b) *hMSC relative TI*				
Cell proliferation	**1**	0.8	0.70	0.4
Cell metabolism	**1**	0.5	0.2	0.1
Osteocalcin expression	1	1.2	1.6	**2.6**
Alkaline phosphatase expression	1	3.2	11.2	**16.4**
Osteopontin expression	1	1.2	1.7	**2.4**
Collagen deposition	1	1.5	2.1	**2.6**

faster degrading biomaterials, whereas faster degrading biomaterials were shown to increase osteogenic protein deposition (Table 1.1).

It is generally believed that biomaterial degradation should be at equilibrium with ECM deposition by the cells within the tissues, allowing for unimpeded tissue formation while retaining mechanical stability. It is consequently essential that the degradation profile of biomaterials utilized within 3D tissue models is well defined and does not hinder tissue development.

1.3.5.2 Monitoring Extracellular Matrix Deposition by Live Cells

As well as monitoring live cells, the monitoring of ECM deposition by those cells in a non-destructive, real-time manner would also be advantageous. The monitoring of ECM would enable the tissue development and cell metabolism within the 3D model to be observed and could also provide information on scaffold remodelling, where natural ECM scaffolds have been utilized. The ECM is known to be a complex network of proteins, which are essential for providing biological cues as well as mechanical and structural support to the cells within the tissue models [59]. ECM molecules are extremely bioactive and play an important role in fundamental cellular processes, such as adhesion, proliferation, differentiation, migration and apoptosis [59, 60]. The production of ECM by the cells within the tissue model is essential for providing integrity and ensuring a defined biological function [61].

The majority of methods used to evaluate ECM deposition within 3D tissue models is performed after culturing and are destructive, endpoint techniques. This makes it difficult to understand what is occurring within the tissue models as they develop. Collagen, as one of the main proteins within the ECM, has often been used as a measure of tissue quality and it has previously been shown that it can be tagged through the addition of modified prolines to the cell culture medium. More recently, this technique has been utilized to fluorescently-tag collagen molecules within the cell-produced ECM, allowing for tissue quality, morphology and ECM turnover to be monitored online in a non-destructive manner. This smart method involves the addition of modified azide-L-proline to the cell culture medium allowing for the neo-formed col-

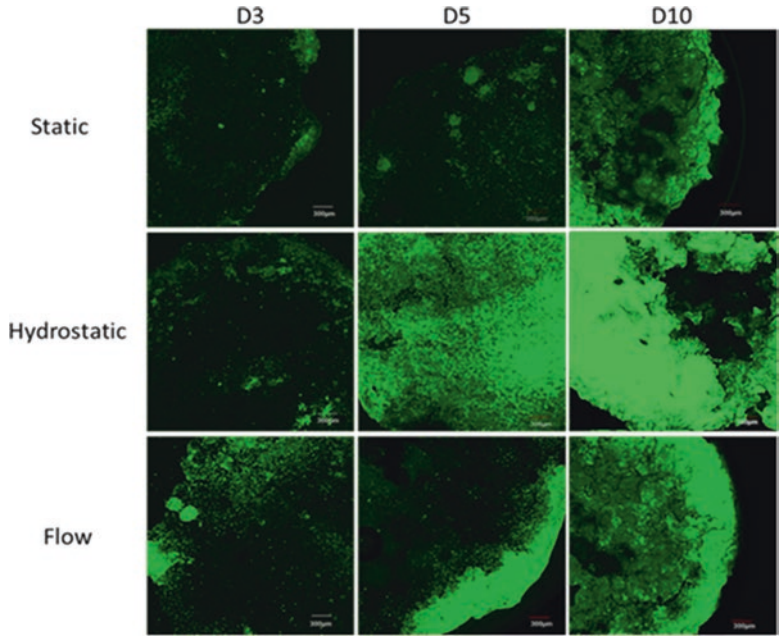

Fig. 1.6 The real-time monitoring of cell-produced collagen deposition on 3D PLGA scaffolds under static, cyclic hydrostatic pressure and flow conditions, using confocal laser scanning microscopy. Cells were cultured with an azide-modified proline, which was incorporated into the cell-produced collagen and detected through a secondary staining step using Click-IT Alex Fluor 488 DIBO Alkyne. The deposition of cell-produced collagen was continuously monitored within the PLGA scaffolds with images being shown at days 3, 5, and 10 under differing culture conditions. (n = 5; scale bars = 300 μm) [62]

lagen to be tagged by azide. This azide-labelled collagen can then be detected by a reaction with 10 mM of Click-IT Alexa Fluor 488 DIBO Alkyne [62]. Figure 1.6 shows the effect of mechanical stimulation on the spatial deposition of collagen ECM by cells cultured on porous, salt-leached poly(lactic-co-glycolic) acid scaffolds, as imaged using confocal laser scanning microscopy.

The use of perpendicular flow, as provided by the Quasi-Vivo bioreactor (Kirkstall Ltd., UK), led to the formation of a collagen shell surrounding the outer edge of the scaffolds, whereas the application of hydrostatic pressure and static culturing allowed for a more even deposition of collagen throughout the scaffolds. The ability to define (a) the quantity and (b) the spatial deposition of collagen within 3D tissue models is essential as not only does it allow for an assessment of tissue quality, but it can also highlight issues, such as the formation of a collagen shell, which may lead to decreased nutrient exchange with in the construct and a subsequent necrotic core.

1.4 Advantages and Challenges of Live Cell Imaging

The use of live cell imaging has transformed the way both 2D and 3D cellular models have been utilized to investigate cell biology. 3D live cell imaging has allowed for biologists and tissue engineers to study cell morphology, ECM deposition, gene expression (through the use of Smartflares) and tissue formation in real-time and over time. Understanding tissue formation and cell processes can be essential for the study of these tissue models and to improve their development. Live cell imaging allows for continued monitoring and the study of dynamic changes

within 3D tissues in vitro. This allows for a decrease in the reliance on end-point snap shots, allowing for a single sample to be monitored through to completion, which reduces the number of samples required. Live cell imaging is also less prone to experimental errors when compared to fixed sample imaging, which maybe reliant on antibodies or special dye staining steps. With that, it usually provides a more reliable picture of the 3D tissue models.

However, live cell imaging can be challenging. As with all live cell imaging experiments, one of the main challenges is to keep cells alive and healthy over a period of time while they are exposed to the chosen imaging modality. It is vital that cells are maintained in a stable temperature and pH environment. Microscopic imaging modalities usually achieve this by using an environmental chamber attached to the microscopy stage, or larger chambers which surround the entire microscope itself. During relatively long term experiments, it is essential that gaseous and nutrient requirements of the live cells are also taken into account. The imaging of live cells under both physiological and non-physiological conditions can be very useful in live cell imaging. Some of the imaging modalities may also cause cellular stress, such as the laser and X-ray exposure required for confocal microscopy and microCT, respectively. Therefore, exposure to these sources should be limited either through imaging at lower resolutions or imaging less frequently. Labelling with fluorescent probes needs to be optimized for the particular assay readout, spectral compatibility and signal-to-noise level, and live cell imaging of dynamic processes requires active observation over time.

1.5 Prospect and Summary

The imaging of 3D constructs is vital when monitoring cell proliferation, differentiation and the production of relevant tissue models and in vitro grafts. The ability to image 3D tissues in a non-invasive, non-destructive manner has, until recently, required destructive end point techniques, using either histological methods or destructive assays, which provide valuable information but result in only being able to obtain a snapshot of the tissue development at one particular time point. The development of the 3D imaging techniques described in this chapter has been vital for the development of the field of tissue engineering and basic biological research.

All of the imaging techniques described in this chapter have varying advantages and pitfalls when it comes to imaging 3D tissues and will, therefore, require optimization for each individual sample with some imaging techniques being more suitable for certain tissues than for others. However, due to the importance of 3D imaging these techniques are constantly evolving to overcome these pitfalls to allow for higher biocompatibility and higher resolution imaging.

References

1. Baker BM, Chen CS (2012) Deconstructing the third dimension: how 3D culture microenvironments alter cellular cues. J Cell Sci 125(Pt 13):3015–3024
2. Thomas CH, Collier JH, Sfeir CS, Healy KE (2002) Engineering gene expression and protein synthesis by modulation of nuclear shape. Proc Natl Acad Sci 99(4):1972–1977
3. Vergani L, Grattarola M, Nicolini C (2004) Modifications of chromatin structure and gene expression following induced alterations of cellular shape. Int J Biochem Cell Biol 36(8):1447–1461
4. Nam KH, Smith AS, Lone S, Kwon S, Kim DH (2015) Biomimetic 3D tissue models for advanced high-throughput drug screening. J Lab Autom 20(3):201–215
5. Cukierman E, Pankov R, Yamada KM (2002) Cell interactions with three-dimensional matrices. Curr Opin Cell Biol 14(5):633–639
6. Knight E, Przyborski S (2015) Advances in 3D cell culture technologies enabling tissue-like structures to be created in vitro. J Anat 227(6):746–756
7. Wang W, Itaka K, Ohba S, Nishiyama N, Chung U-I, Yamasaki Y et al (2009) 3D spheroid culture system on micropatterned substrates for improved differentiation efficiency of multipotent mesenchymal stem cells. Biomaterials 30(14):2705–2715
8. Deegan AJ, Aydin HM, Hu B, Konduru S, Kuiper JH, Yang Y (2014) A facile in vitro model to study rapid mineralization in bone tissues. Biomed Eng Online 13(1):136
9. Hildebrandt C, Büth H, Thielecke H (2011) A scaffold-free in vitro model for osteogenesis of human mesenchymal stem cells. Tissue Cell 43:91–100
10. Berrier AL, Yamada KM (2007) Cell–matrix adhesion. J Cell Physiol 213(3):565–573

11. Kanczler JA, Ginty PJ, Barry JJA, Clarke NMP, Howdle SM, Shakesheff KM et al (2008) The effect of mesenchymal populations and vascular endothelial growth factor delivered from biodegradable polymer scaffolds on bone formation. Biomaterials 29(12):1892–1900
12. Rouwkema J, Rivron NC, van Blitterswijk CA (2008) Vascularization in tissue engineering. Trends Biotechnol 26:434–441
13. Fuchs S, Hofmann A, Kirkpatrick C (2007) Microvessel-like structures from outgrowth endothelial cells from human peripheral blood in 2-dimensional and 3-dimensional co-cultures with osteoblastic lineage cells. Tissue Eng 13(10):2577–2588
14. Melero-Martin JM, De Obaldia ME, Kang SY, Khan ZA, Yuan L, Oettgen P et al (2008) Engineering robust and functional vascular networks in vivo with human adult and cord blood-derived progenitor cells. Circ Res 103(2):194–202
15. Fuchs S, Ghanaati S, Orth C, Barbeck M, Kolbe M, Hofmann A et al (2009) Contribution of outgrowth endothelial cells from human peripheral blood on in vivo vascularization of bone tissue engineered constructs based on starch polycaprolactone scaffolds. Biomaterials 30(4):526–534
16. Tsigkou O, Pomerantseva I, Spencer JA, Redondo PA, Hart AR, O'Doherty E et al (2010) Engineered vascularized bone grafts. Proc Natl Acad Sci 107(8):3311–3316
17. Saleh FA, Whyte M, Genever PG (2011) Effects of endothelial cells on human mesenchymal stem cell activity in a three-dimensional in vitro model. Eur Cell Mater 22:242–257. discussion 57
18. Morimoto Y, Kato-Negishi M, Onoe H, Takeuchi S (2013) Three-dimensional neuron–muscle constructs with neuromuscular junctions. Biomaterials 34(37):9413–9419
19. Giacomelli E, Bellin M, Sala L, van Meer BJ, Tertoolen LG, Orlova VV et al (2017) Three-dimensional cardiac microtissues composed of cardiomyocytes and endothelial cells co-differentiated from human pluripotent stem cells. Development 144(6):1008–1017
20. Mannhardt I, Breckwoldt K, Letuffe-Brenière D, Schaaf S, Schulz H, Neuber C et al (2016) Human engineered heart tissue: analysis of contractile force. Stem Cell Rep 7(1):29–42
21. Howard D, Buttery LD, Shakesheff KM, Roberts SJ (2008) Tissue engineering: strategies, stem cells and scaffolds. J Anat 213(1):66–72
22. Baharvand H, Hashemi SM, Kazemi Ashtiani S, Farrokhi A (2006) Differentiation of human embryonic stem cells into hepatocytes in 2D and 3D culture systems in vitro. Int J Dev Biol 50(7):645–652
23. Willerth SM, Arendas KJ, Gottlieb DI, Sakiyama-Elbert SE (2006) Optimization of fibrin scaffolds for differentiation of murine embryonic stem cells into neural lineage cells. Biomaterials 27(36):5990–6003
24. Gerecht S, Burdick JA, Ferreira LS, Townsend SA, Langer R, Vunjak-Novakovic G (2007) Hyaluronic acid hydrogel for controlled self-renewal and differentiation of human embryonic stem cells. Proc Natl Acad Sci U S A 104(27):11298–11303
25. O'Brien FJ (2011) Biomaterials & amp; scaffolds for tissue engineering. Mater Today 14(3):88–95
26. Yang Y, El Haj AJ (2006) Biodegradable scaffolds--delivery systems for cell therapies. Expert Opin Biol Ther 6(5):485–498
27. Jafari M, Paknejad Z, Rad MR, Motamedian SR, Eghbal MJ, Nadjmi N et al (2017) Polymeric scaffolds in tissue engineering: a literature review. J Biomed Mater Res B Appl Biomater 105(2):431–459
28. Dabbs DJ (2013) Diagnostic immunohistochemistry e-book. Elsevier Health Sciences, Amsterdam
29. Ramos-Vara JA (2005) Technical aspects of immunohistochemistry. Vet Pathol 42(4):405–426
30. Pusztaszeri MP, Seelentag W, Bosman FT (2006) Immunohistochemical expression of endothelial markers CD31, CD34, von Willebrand factor, and Fli-1 in normal human tissues. J Histochem Cytochem 54(4):385–395
31. Gantenbein-Ritter B, Sprecher CM, Chan S, Illien-Junger S, Grad S (2011) Confocal imaging protocols for live/dead staining in three-dimensional carriers. Methods Mol Biol 740:127–140
32. Clegg RM, Murchie AI, Lilley DM (1993) The four-way DNA junction: a fluorescence resonance energy transfer study. Braz J Med Biol Res 26(4):405–416
33. Deniz AA, Laurence TA, Beligere GS, Dahan M, Martin AB, Chemla DS et al (2000) Single-molecule protein folding: diffusion fluorescence resonance energy transfer studies of the denaturation of chymotrypsin inhibitor 2. Proc Natl Acad Sci U S A 97(10):5179–5184
34. Chennell G, Willows RJW, Warren SC, Carling D, French PMW, Dunsby C et al (2016) Imaging of metabolic status in 3D cultures with an improved AMPK FRET biosensor for FLIM. Sensors 16(8):1312
35. Dmitriev RI, Borisov SM, Dussmann H, Sun S, Muller BJ, Prehn J et al (2015) Versatile conjugated polymer nanoparticles for high-resolution O2 imaging in cells and 3D tissue models. ACS Nano 9(5):5275–5288
36. Elttayef A, Dmitriev R, Kelly C, Yang Y (2017) Fabrication and characterisation of pseudoislets with different size and cell-cell contact. Abstract booklet of TCES annual conference, Manchester, UK
37. Yang Y, Bagnaninchi PO, Wood MA, El Haj AJ, Guyot E, Dubois A et al (2005) Monitoring cell profile in tissue engineering by optical coherence tomography. Proc SPIE 5695:51–57
38. Yang Y, Dubois A, Qin XP, Li J, El Haj A, Wang RK (2006) Investigation of optical coherence tomography as an imaging modality in tissue engineering. Phys Med Biol 51(7):1649–1659
39. Izatt JA, Swanson EA, Fujimoto JG, Hee MR, Owen GM (1994) Optical coherence microscopy in scattering media. Opt Lett 19(8):590–592
40. Tan W, Vinegoni C, Norman JJ, Desai TA, Boppart SA (2007) Imaging cellular responses to mechanical

stimuli within three-dimensional tissue constructs. Microsc Res Tech 70(4):361–371
41. Appel AA, Anastasio MA, Larson JC, Brey EM (2013) Imaging challenges in biomaterials and tissue engineering. Biomaterials 34(28):6615–6630
42. Martín-Badosa E, Amblard D, Nuzzo S, Elmoutaouakkil A, Vico L, Peyrin F (2003) Excised bone structures in mice: imaging at three-dimensional synchrotron radiation micro CT. Radiology 229(3):921–928
43. Kallai I, Mizrahi O, Tawackoli W, Gazit Z, Pelled G, Gazit D (2011) Microcomputed tomography-based structural analysis of various bone tissue regeneration models. Nat Protoc 6(1):105–110
44. Taiani JT, Buie HR, Campbell GM, Manske SL, Krawetz RJ, Rancourt DE et al (2014) Embryonic stem cell therapy improves bone quality in a model of impaired fracture healing in the mouse; tracked temporally using in vivo micro-CT. Bone 64:263–272
45. Lienemann PS, Metzger S, Kivelio AS, Blanc A, Papageorgiou P, Astolfo A et al (2015) Longitudinal in vivo evaluation of bone regeneration by combined measurement of multi-pinhole SPECT and micro-CT for tissue engineering. Sci Rep 5:10238
46. Tower RJ, Campbell GM, Muller M, Gluer CC, Tiwari S (2015) Utilizing time-lapse micro-CT-correlated bisphosphonate binding kinetics and soft tissue-derived input functions to differentiate site-specific changes in bone metabolism in vivo. Bone 74:171–181
47. Jones AC, Milthorpe B, Averdunk H, Limaye A, Senden TJ, Sakellariou A et al (2004) Analysis of 3D bone ingrowth into polymer scaffolds via micro-computed tomography imaging. Biomaterials 25(20):4947–4954
48. Porter BD, Lin AS, Peister A, Hutmacher D, Guldberg RE (2007) Noninvasive image analysis of 3D construct mineralization in a perfusion bioreactor. Biomaterials 28(15):2525–2533
49. Cartmell S, Huynh K, Lin A, Nagaraja S, Guldberg R (2004) Quantitative microcomputed tomography analysis of mineralization within three-dimensional scaffolds in vitro. J Biomed Mater Res A 69A(1):97–104
50. Young S, Kretlow JD, Nguyen C, Bashoura AG, Baggett LS, Jansen JA et al (2008) Microcomputed tomography characterization of neovascularization in bone tissue engineering applications. Tissue Eng B Rev 14(3):295–306
51. Nagata M, Oi A, Sakai W, Tsutsumi N (2012) Synthesis and properties of biodegradable network poly(ether-urethane)s from L-lysine triisocyanate and poly(alkylene glycol)s. J Appl Polym Sci 126(S2):E358–EE64
52. Giunchedi P, Conti B, Scalia S, Conte U (1998) In vitro degradation study of polyester microspheres by a new HPLC method for monomer release determination. J Control Release 56(1–3):53–62
53. Proikakis CS, Mamouzelos NJ, Tarantili PA, Andreopoulos AG (2006) Swelling and hydrolytic degradation of poly(D,L-lactic acid) in aqueous solutions. Polym Degrad Stab 91(3):614–619
54. Artzi N, Oliva N, Puron C, Shitreet S, Artzi S, Bon Ramos A et al (2011) In vivo and in vitro tracking of erosion in biodegradable materials using non-invasive fluorescence imaging. Nat Mater 10(9):704–709
55. Bardsley K, Wimpenny I, Yang Y, El Haj AJ (2016) Fluorescent, online monitoring of PLGA degradation for regenerative medicine applications. RSC Adv 6(50):44364–44370
56. Cunha-Reis C, El Haj AJ, Yang X, Yang Y (2013) Fluorescent labeling of chitosan for use in non-invasive monitoring of degradation in tissue engineering. J Tissue Eng Regen Med 7(1):39–50
57. Wolbank S, Pichler V, Ferguson JC, Meinl A, van Griensven M, Goppelt A et al (2015) Non-invasive in vivo tracking of fibrin degradation by fluorescence imaging. J Tissue Eng Regen Med 9(8):973–976
58. Bardsley K, Wimpenny I, Wechsler R, Shachaf Y, Yang Y, El Haj AJ (2016) Defining a turnover index for the correlation of biomaterial degradation and cell based extracellular matrix synthesis using fluorescent tagging techniques. Acta Biomater 45:133–142
59. Muiznieks LD, Keeley FW (2013) Molecular assembly and mechanical properties of the extracellular matrix: a fibrous protein perspective. Biochim Biophys Acta 1832(7):866–875
60. Kim S-H, Turnbull J, Guimond S (2011) Extracellular matrix and cell signalling: the dynamic cooperation of integrin, proteoglycan and growth factor receptor. J Endocrinol 209(2):139–151
61. Kozel BA, Rongish BJ, Czirok A, Zach J, Little CD, Davis EC et al (2006) Elastic fiber formation: a dynamic view of extracellular matrix assembly using timer reporters. J Cell Physiol 207(1):87–96
62. Bardsley K, Yang Y, El Haj AJ (2017) Fluorescent labeling of collagen production by cells for noninvasive imaging of extracellular matrix deposition. Tissue Eng Part C Method 23(4):228–236

2 Simultaneous Phosphorescence and Fluorescence Lifetime Imaging by Multi-Dimensional TCSPC and Multi-Pulse Excitation

Wolfgang Becker, Vladislav Shcheslavskiy, and Angelika Rück

Abstract

TCSPC FLIM/PLIM is based on a multi-dimensional time-correlated single-photon counting process. The sample is scanned by a high-frequency-pulsed laser beam which is additionally modulated on/off synchronously with the pixels of the scan. FLIM is obtained by building up the distribution of the photons over the scanning coordinates and the times of the photons in the excitation pulse sequence, PLIM is obtained by building up the photon distribution over the scanning coordinates and the photon times in the modulation period. FLIM and PLIM data are thus obtained simultaneously within the same imaging process. Since the technique uses not only one but many excitation pulses for every phosphorescence signal period the sensitivity is much higher than for techniques that excite with a single pulse only. TCSPC FLIM/PLIM works both with one-photon and two-photon excitation, does not require a reduction of the laser pulse repetition rate by a pulse picker, and eliminates the need of high pulse energy for phosphorescence excitation.

Keywords

Fluorescence • Phosphorescence • FLIM • PLIM • TCSPC • Metabolic imaging • pO_2 imaging

2.1 Motivation of Using Phosphorescence Lifetime Imaging

Phosphorescence occurs when an excited molecule transits from the first excited singlet state, S1, into the first triplet state, T1, and returns

W. Becker (✉) • V. Shcheslavskiy • A. Rück
Becker & Hickl GmbH, Berlin, Germany
e-mail: becker@becker-hickl.de

R.I. Dmitriev (ed.), *Multi-Parametric Live Cell Microscopy of 3D Tissue Models*,
Advances in Experimental Medicine and Biology 1035, DOI 10.1007/978-3-319-67358-5_2

from there to the ground state by emitting a photon [1]. Both the S1-T1 transition and the T1-S0 transition are 'forbidden' processes. The transition rates are therefore much smaller than for the S1-S0 transition. That means that phosphorescence is a slow process, with lifetimes on the order of microseconds or even milliseconds. Phosphorescence of organic dyes or endogenous fluorophores is extremely weak or even not detectable at room temperature. However, strong phosphorescence with lifetimes from the microsecond up to the millisecond range is obtained for lanthanide complexes [2] and organic complexes of ruthenium [1, 3], platinum [1, 4–6], terbium, and palladium [5]. Of special interest for live-cell imaging is that the phosphorescence of these complexes is strongly quenched by oxygen. The dyes are therefore excellent oxygen sensors [1, 5–10]. Applications are aiming at the measurement of oxygen partial pressure (pO_2) in biological objects, and its effect on the metabolism of the cells. To reach this target it is desirable that PLIM and FLIM measurements are performed simultaneously. The oxygen concentration is then derived from the PLIM data, the metabolic information from the FLIM data, preferably from the NAD(P)H and the FAD fluorescence [11].

Metabolic imaging requires that the FLIM process resolves the bound and the unbound decay components of NAD(P)H and FAD, which requires an instrument response function shorter than 200 ps and a time-channel width of about 50 ps. The recording process must provide an optimum photon efficiency, i.e. a maximum signal-to-noise ratio of the recorded fluorescence and phosphorescence lifetimes for a given number of photons. Moreover, it is important that the imaging process delivers data from a defined plane inside cells or tissues, that it suppresses lateral and longitudinal scattering, and that it does so without compromising the photon efficiency. A strict requirement is compatibility with deep tissue imaging by multiphoton excitation and non-descanned detection. The only technique that meets these requirements is the combination of multi-dimensional TCSPC and laser scanning [12–15].

TCSPC FLIM has taken a impressive development in the last decade. Images as large as 2048 x 2048 pixels can be recorded without compromising the time resolution, and additional parameters can be included in the recording process [13, 16, 17]. As a result, TCSPC FLIM not only records conventional FLIM images at high resolution but also z stacks, lateral mosaics, multi-wavelength images, images at several excitation wavelengths, and images of fast dynamic effects induced in the sample. Moreover, TCSPC FLIM has been extended to record PLIM simultaneously with FLIM [13, 18]. Challenges, solutions, and typical applications of combined FLIM/PLIM will be described in this chapter.

2.2 Technical Challenges

2.2.1 Excitation Pulse Period and Laser Power

The obvious problem of PLIM is that the excitation pulse period must be a few times longer than the phosphorescence decay time. For ruthenium dyes with phosphorescence lifetimes below 1 µs the reduction in laser repetition rate may still be feasible, see Hosny et al. [3]. However, the lifetimes for platinum and palladium-based dyes are on the order of 50–100 µs, and the lifetimes of europium and terbium dyes can be in the millisecond range. PLIM with these dyes would require a laser repetition rate of less than 10 kHz. Reducing the repetition rate—if possible at all—results in a substantial decrease in the average excitation power, and, consequently, decrease in phosphorescence intensity, see Fig. 2.1a. Attempts to compensate for the decrease in average power by higher peak power are limited by the capabilities of the laser, by saturation and other nonlinear effects in the sample, or, in multiphoton systems, unwanted excitation of higher energy levels or even ionisation. In other words, the effect of reducing the excitation pulse rate is poor sensitivity. Low sensitivity can partially be compensated by high concentration of the phosphorescence marker.

However, the commonly used phosphorescence dyes are potentially toxic, and using them in high concentration is not desirable.

2.2.2 Pile-Up Effect

Simply reducing the laser repetition rate causes a significant problem for recording FLIM simultaneously with PLIM. In principle, it would be possible to derive FLIM and PLIM data from a one and the same decay curve that is excited by low-repetition rate laser pulses and simultaneously recorded at two different time scales. One channel would record a photon distribution over the FLIM time scale, the other over the PLIM time scale. However, this would unavoidably create a pile-up problem for the FLIM channel. The lifetimes of the decay components are in the range from a few 100 ps to a few nanoseconds. Neither the detector nor the TCSPC electronics of the FLIM channel are able to detect several photons within this time and determine their arrival times at picosecond accuracy. Detection of several photons per excitation pulse must therefore be avoided. That means the detection rate must be kept at a level no higher than 10% of the excitation rate [12–14]. This is not a problem for FLIM with laser repetition rates in the 50–80 MHz range. However, for excitation rates on the order of 100 kHz (for Ruthenium) and 10 kHz (for Platinum and Palladium) the available detection rates would become extremely low, and, consequently, the acquisition times unacceptably long.

2.2.3 Detector Overload

Another problem is that any sample that emits phosphorescence necessarily also emits fluorescence. The fluorescence both comes from endogenous fluorophores of the sample, and from singlet emission of the phosphorescence probe. At high laser peak power the peak power of fluorescence becomes extremely high, see Fig. 2.1b. This causes transient overload and extreme afterpulsing in the detectors. It is then impossible to detect a correct phosphorescence decay in the first few microseconds after the laser pulse. In principle, the overload problem can be solved by using laser pulses with a duration in the microsecond range. However, apart from the fact this is not simply feasible with most lasers it would make simultaneous FLIM impossible. Moreover, microsecond pulse duration is not an option for multiphoton excitation.

2.2.4 Interference with Scanning

PLIM in scanning systems has also another problem. The time the scanner stays within the excited sample volume must be longer than the phosphorescence lifetime. If the scanner runs off the excited volume within the phosphorescence decay time photons in the tail of the decay function are lost, and the recorded decay profile gets distorted, see Fig. 2.1c. Reasonable recording, even of pure intensity images, can thus be obtained only by sufficiently slow scanning. Moreover, the pixel time and the excitation pulse period are on the same order of magnitude. The number of excitation pulses in the individual pixels can thus vary systematically and induce Moiré effects in the images, see Fig. 2.1d. The problem can be solved by synchronising the laser pulses with the pixel frequency, but there is usually no provision for this in normal laser scanning microscopes. Without synchronisation, the pixel time had to be at least 100 times longer than the laser period. This leads to extremely long scan times, and to a further increase of the acquisition time (Fig. 2.1).

2.3 FLIM—PLIM by Multipulse Excitation

The problems described above are avoided by a FLIM/PLIM technique developed by bh in 2010 [18]. The technique is based on the idea that, if a single short laser pulse is not efficient in exciting phosphorescence, a burst of multiple laser pulses will perform much better. As long as the burst duration is shorter than the phosphorescence lifetime the excitation efficiency will increase in proportion to the number of pulses within the burst.

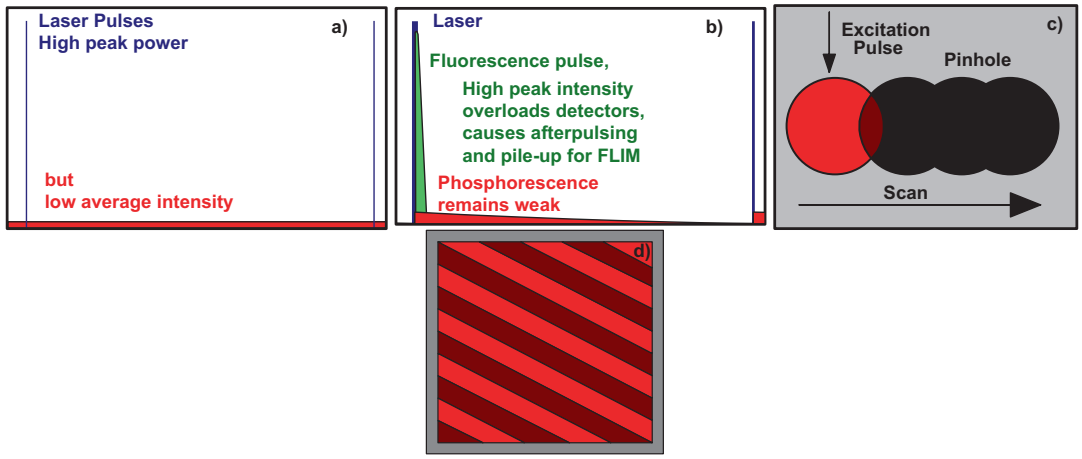

Fig. 2.1 Challenges of PLIM. (**a**) Low laser repetition rate results in low average excitation intensity. (**b**) High peak-to-average power ratio causes high peak intensity of fluorescence, detector overload and afterpulsing, and pile-up in parallel FLIM recording. The phosphorescence intensity remains low due to low average excitation power. (**c**) Scanning must be slow enough to stay in the excited pixel over the time of the phosphorescence decay. (**d**) Low scan rate interferes with low laser pulse repetition rate. This induces Moiré effects in the images

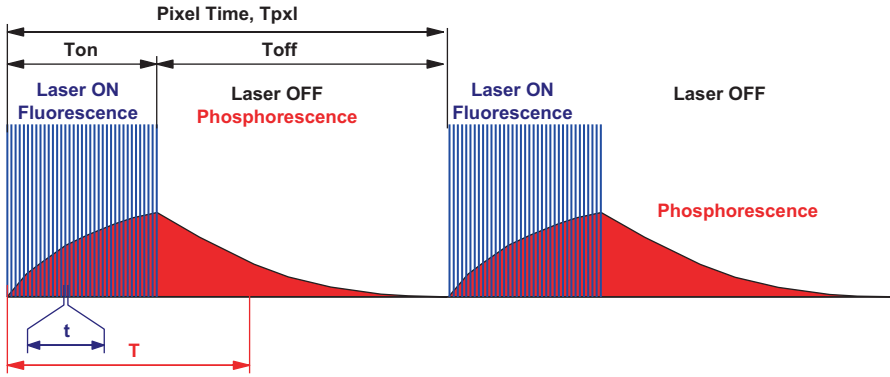

Fig. 2.2 Principle of Microsecond FLIM. A high-frequency pulsed laser is on-off modulated synchronously with the pixels. FLIM is recorded in the Laser ON phases, PLIM in the Laser OFF phases

Multi-pulse excitation has been used for multi-photon phosphorescence imaging earlier [6] but bh were first to apply it to TCSPC PLIM.

The principle is shown in Fig. 2.2. The sample is excited by a pulsed laser running at a repetition rate in the 50–80 MHz range, i.e. at a repetition rate as it is typically used for TCSPC FLIM. However, the laser does not run continuously. Instead, it is turned on only for a given period of time, T_{on}, at the beginning of each pixel. Within the on-time, T_{on}, the laser pulses excite fluorescence, and, pulse by pulse, build up phosphorescence. The phosphorescence intensity at the end of the laser-on time is far higher than for a single laser pulse.

For the rest of the pixel time the laser is turned off. After the last laser pulse, the fluorescence decays quickly, and for the rest of the pixel dwell time, T_{off}, pure phosphorescence is detected.

The build-up of TCSPC FLIM and PLIM images with this excitation sequence is straightforward. For each photon, the TCSPC module

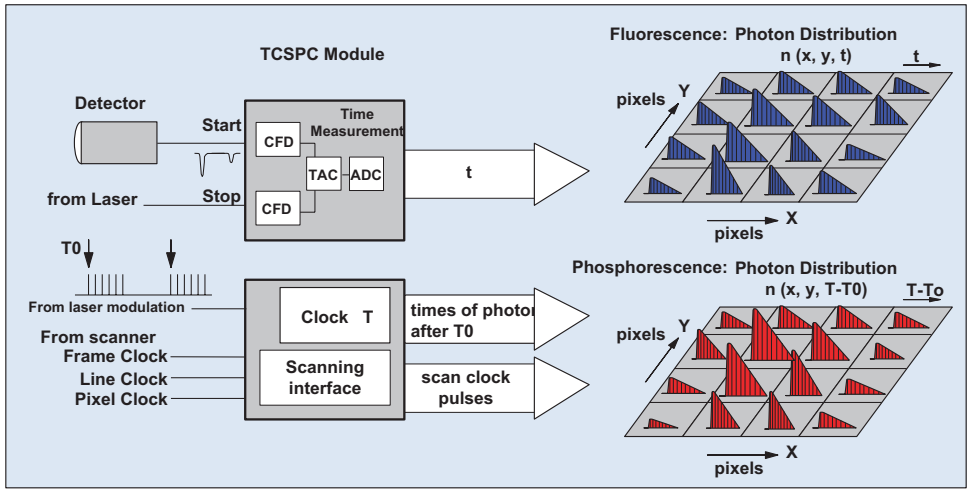

Fig. 2.3 Simultaneous fluorescence and phosphorescence lifetime imaging

determines the time, t, within the laser pulse period, and the time, T, after the start of the modulation pulse. The TCSPC process builds up photon distributions over these times and the scan coordinates [14, 16, 18–20].

The TCSPC principle is shown in Fig. 2.3. A fluorescence lifetime image is obtained by building up a photon distribution over the times, t, of the photons in the laser pulse period, and the scanner position, x, y, during the T_{on} periods. The phosphorescence lifetime image is obtained by building up a similar distribution over the times, T, within the laser modulation period and the beam position, x, y. Thus, fluorescence and phosphorescence lifetime images are obtained simultaneously, in the same scan, and from photons excited by the same laser pulses.

The procedure can be further refined by using the laser on/off information as a routing signal to better separate the fluorescence in laser-on phases from the phosphorescence in the laser-off phases, please see [13, 21, 22] for details.

The principle solves all the problems discussed in the previous section. The excitation pulse rate of FLIM gets de-coupled from the excitation rate of PLIM: The FLIM excitation rate is the laser pulse period, the PLIM excitation period is the period of the on/off modulation. The average excitation intensity drops only by the duty cycle of the laser modulation, and the effective FLIM excitation rate remains high. High phosphorescence intensity is obtained, and there is no problem with pile-up. The peak intensity of the laser pulses need not be higher than for a normal TCSPC FLIM measurement. The principle thus remains compatible with multiphoton excitation. Moreover, there is no excessively high fluorescence peak intensity, and no detector overload problem. Also the Moiré problem is solved: The laser modulation is automatically synchronised with the pixels of the scan. Every pixel thus gets the same number of excitation pulses.

2.4 Implementation in Laser Scanning Systems

The implementation of combined FLIM/PLIM in a laser scanning microscope requires that the microscope has or can be upgraded with a pulsed excitation laser, and that this laser can be on/off modulated by a signal from the scanner or from the FLIM/PLIM electronics. Picosecond diode lasers can be modulated electronically, supercontinuum Lasers can be modulated via the AOTF (acousto-optical filter) that is normally used to select the desired wavelength. In multiphoton microscopes the Ti:Sapphire lasers can normally be modulated via the AOM or EOM that is used to control the intensity.

Moreover, it must be possible to select a sufficiently slow scan speed that avoids that the scanner is running off the excited pixel during the phosphorescence decay time. The required pixel times up to about 100 µs are available in almost any laser scanning microscope.

2.4.1 DCS-120 Confocal Scanning FLIM System

Laser on/off modulation in the bh DCS-120 laser scanning system [21] is integrated in the scan controller hardware. The modulation is achieved via the laser multiplexing function of the scan controller module. The DCS system normally has two lasers which can be multiplexed within one pixel. PLIM operation for one laser is obtained by enabling the pixel multiplexing function, and turning the second laser off. The laser then turns on at the beginning of each pixel, runs for a fraction of the pixel time, and then turns off. The multiplexing function also routes photons from the 'Laser ON' and 'Laser OFF' phases into different memory blocks, and thus provides separate images for the FLIM and PLIM signal, and the total luminescence. The laser on/off function is the same for systems with diode lasers, with a supercontinuum laser, and for multiphoton systems with a Ti:Sapphire laser. Different than other laser scanning systems, the DCS-120 scanner has an has an option to run along the lines in steps of the individual pixels. This avoids that the scanner runs off the excited spot during the pixel time.

2.4.2 Zeiss LSM 710, 780, 880 Systems

For the FLIM systems for the Zeiss LSM 710 /780/880 microscope family [21] a bh DDG-210 pulse generator card is added to the FLIM system. The DDG card triggers on the pixel clock of the LSM, and sends a 'Laser On' signal to the laser controller of the microscope. The principle is shown in Fig. 2.4. The pixel clock is split off from the scan synchronisation cable and connected into the trigger input of the DDG card. The 'Laser On' signal is connected into the laser control module of the Zeiss LSM via a 'PLIM' input. This input is optional; it has to be ordered from Zeiss via an 'INDIMO' (individual modification) request. PLIM Laser control via the DDG-210 card is integrated in the bh SPCM software. The card also generates a 'routing' signal that directs the photons from the 'Laser ON' phases and the 'Laser OFF' phases into different memory blocks of the TCSPC system. This way, separate images for the FLIM signal, the PLIM signal, and the total luminescence signal can be provided and displayed during the measurement. Please see [21] for further details.

2.4.3 Leica SP Multiphoton Systems

As for the Zeiss LSMs, the laser on-off function is controlled by a bh DDG-210 pulse generator module that is added to the FLIM system. The card is triggered by the pixel clock of the microscope. The on-off signal from the DDG is fed

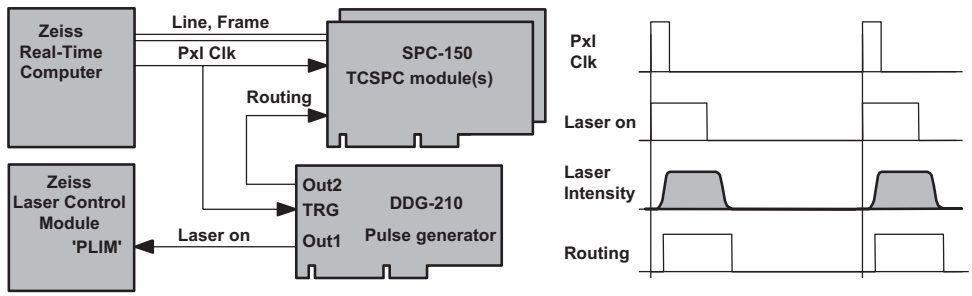

Fig. 2.4 *Left*: Principle of laser on/off control for the Zeiss LSMs

into the beam blanking control of the microscope via a logic gate.

Laser power control in the Leica multiphoton systems is performed by an EOM (electro-optical modulator). The EOM is fast enough for PLIM on-off modulation. However, we often found that it does not turn the laser entirely off, especially when the EOM control parameters are not accurately adjusted. This is no problem in standard imaging applications but it can be a problem for PLIM. Spurious excitation during the 'laser-off' phases causes a large background in the phosphorescence decay or even makes it impossible to record phosphorescence at all. The solution is an ND filter in the excitation beam path. FLIM/PLIM is performed at no more than 5% of the available laser power. A filter that transmits about 20% shifts the power range from 0–5% to 0–25%, and reduces the laser power in the off phases sufficiently to avoid spurious excitation. A reflective filter should be used (an absorptive filter may crack).

The Leica systems use a sinusoidal scan in x direction. The nonlinearity of the scan is compensated by a non-uniform pixel time. This is not a problem for the bh FLIM systems: The bh systems use the pixel clock from the Leica scanner and thus avoid distortion of the images [15]. For PLIM, however, the variable pixel time results in a variable laser on/off period along the lines and a variable effective PLIM excitation rate. Also this is not normally a problem. However, the scan rate should be selected slow enough to let the phosphorescence completely decay within the pixel time. Normally, incomplete decay can be taken into account by a suitable model in the SPCImage data analysis [13]. However, this requires that the excitation period is constant over the entire image. This is not the case for PLIM with the Leica microscopes.

2.4.4 Sutter Instrument MOM Microscopes

The Sutter Instrument MOM (movable objective) microscope [22] is a modular platform for imaging deep within live samples. It uses multi-photon excitation by a titanium-sapphire laser in combination with non-descanned detection. Typical applications of the MOM system are autofluorescence imaging of cells, and autofluorescence imaging in tissue and whole organisms. These benefit considerably from the combination with FLIM/PLIM. The general principle is the same as for the Zeiss and Leica multiphoton microscopes. The difference is that there is no direct input for a laser on/off signal. Instead, the intensity-control signal of the Sutter system is coupled out via an existing connector and multiplied with the laser ON/OFF modulation signal from a DDG-210 card. The combined signal is fed back into the intensity-control signal path of the MOM system.

2.5 Applications

2.5.1 Oxygen Sensing

Oxygen sensing by PLIM has become a hot topic in biomedical microscopy, see [5–10]. Until recently, phosphorescence imaging has mainly been performed by gated camera techniques. The disadvantage of the camera is that does not suppress out-of-focus light and lateral and longitudinal scatterin. A camera is therefore not a good solution for deep-tissue imaging. PLIM by the technique described here solves these problems by confocal and two-photon laser scanning microscopy, and, additionally, yields FLIM and PLIM simultaneously. An increasing number of publications therefore aims at the use of PLIM for oxygen sensing in cells and tissue. Toncelly et al. used the technique to characterize the sensor dyes [23]. The penetration into cells and the behaviour of the dyes in the biological environment was investigated by Dmitriev et al. [24]. The response of the cells and cell clusters to variation in the oxygen concentration under physiological conditions has been investigated by [9, 25–28]. Lukina et al. used single-point fluorescence/phosphorescence decay measurements to measure the metabolic activity and the oxygen concentration in tumors in live mice via a fibre-optical system [29]. An overview on the FLIM/

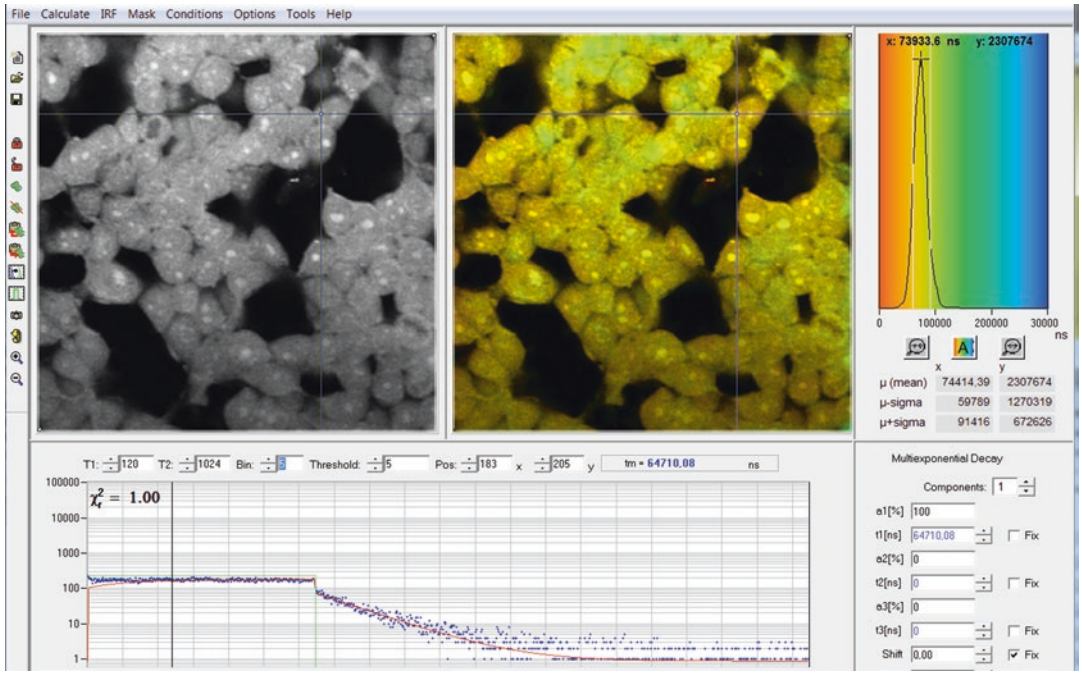

Fig. 2.5 HEK cells incubated with a palladium dye under atmospheric oxygen partial pressure. Recorded by bh DCS-120 confocal scanning system, data analysis by bh SPCImage. Lifetime scale 0 (*red*) to 300 μs (*blue*). Phosphorescence lifetime at the Cursor-Position 65 μs. The maximum of the lifetime distribution over the pixels is at 75 μs

PLIM technique and an introduction into the use of an oxygen-sensitive solid matrix for cells has been given by Jenkins et al. [30].

Examples are shown in the figures below. Figures 2.5 and 2.6 show cultured human embryonic kidney cells incubated with a palladium-based phosphorescence dye. Figure 2.5 was recorded under atmospheric oxygen partial pressure. The maximum of the lifetime distribution over the pixels is at 75 μs. Figure 2.6 was recorded under decreased oxygen partial pressure. As expected, the maximum of the lifetime distribution has shifted to longer decay times, in this case 144 μs.

2.5.2 Simultaneous Recording of pO_2 and NAD(P)H Images

Simultaneously recorded fluorescence and phosphorescence lifetime images of live cultured human squamous carcinoma (SCC-4) cells stained with tris (2,2′-bipyridyl) dichlororuthenium (II) hexahydrate are shown in Fig. 2.7, left and right. The data were acquired by a Zeiss LSM 780 NLO multiphoton microscope with a bh Simple-Tau 152 TCSPC system. The excitation wavelength was 750 nm. The image on the left was recorded in a wavelength interval from 440 to 480 nm. It contains mainly fluorescence of NAD(P)H. The data were analysed with a double-exponential decay model. The image shows the ratio of the amplitudes, a1 and a2, of the decay components. The a1/a2 ratio directly represents the ratio of unbound (a1) and bound (a2) NAD(P)H. The image on the right is the PLIM image. It shows the phosphorescence lifetime of the Ruthenium dye. The lifetime is reciprocally related to the oxygen concentration.

Although the results obtained so far look promising caution appears indicated when PLIM data are interpreted in terms of absolute O_2 concentration measurement. As can be seen from Fig. 2.7 the ruthenium dye binds to the constituents of the cells. The phosphorescence

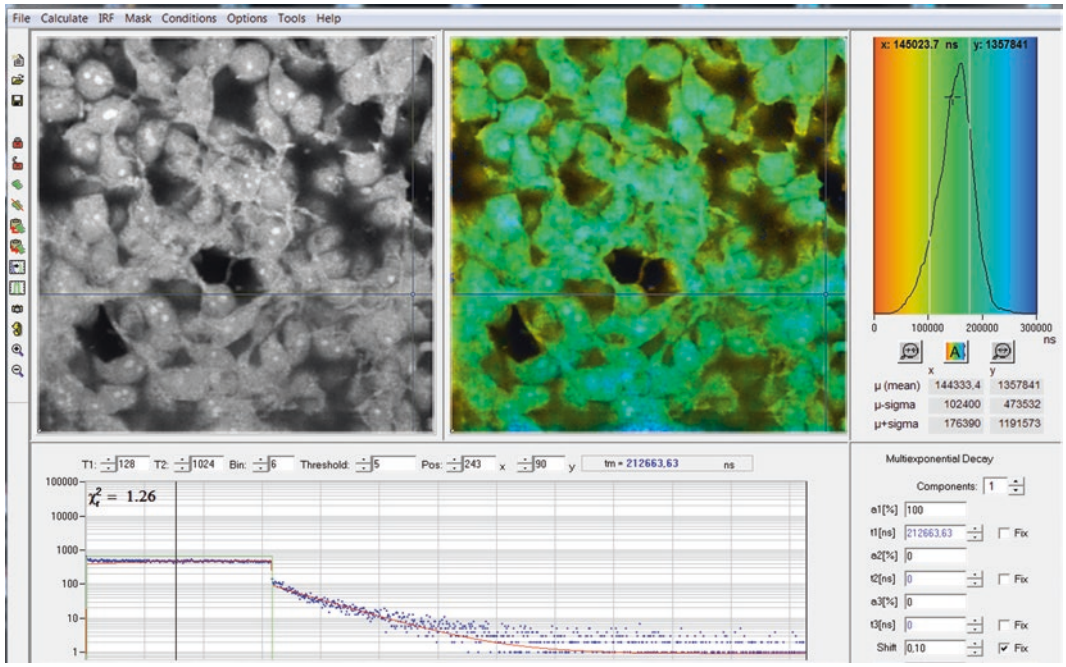

Fig. 2.6 HEK cells incubated with a palladium dye under reduced oxygen partial pressure. Recorded by bh DCS-120 confocal scanning system, data analysis by bh SPCImage. Lifetime scale 0 (*red*) to 300 μs (*blue*). Phosphorescence lifetime at the Cursor-Position 212 μs. The maximum of the lifetime distribution over the pixels is at 144 μs

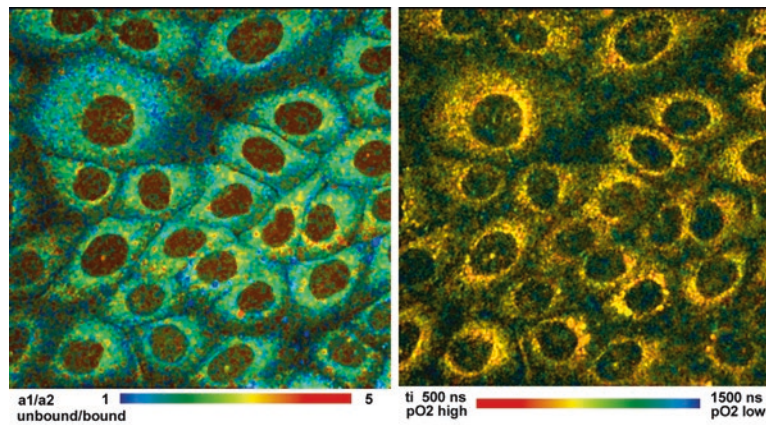

Fig. 2.7 FLIM and PLIM images of SCC-4 cells stained with (2,2′-bipyridyl) dichlororuthenium (II) hexahydrate. FLIM shown *left*, PLIM shown *right*. Zeiss LSM 780 NLO with PLIM option, bh Simple-Tau 152 FLIM/PLIM system, 2-photon excitation at 750 nm

lifetime of bound and unbound dye can be different. Moreover, quenching phenomena are at least in part diffusion-controlled. The quenching rate - and thus the sensitivity to oxygen - more or less depends on the oxygen diffusion constant. The diffusion constant may be different inside the cells and outside, and in different compartments of the cells. pO_2 results derived from PLIM decay times may therefore not necessarily be comparable for different sub-structures of the cells.

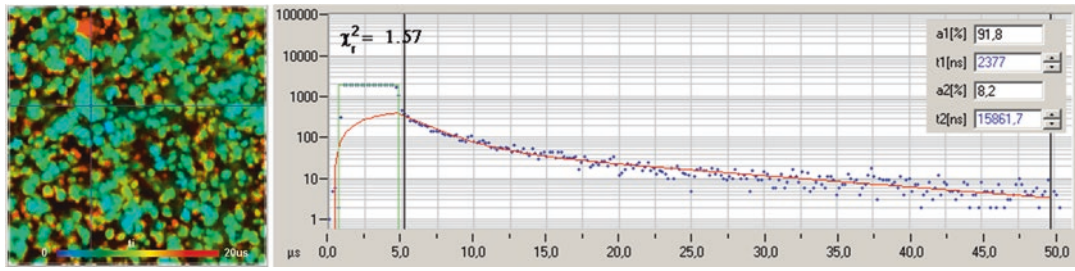

Fig. 2.8 PLIM of zinc oxide nanoparticles. *Left*: Lifetime image, intensity weighted lifetime of double-exponential fit. *Right*: Decay curve at cursor position. Zeiss LSM 710, two-photon excitation at 750 nm, non-descanned detection

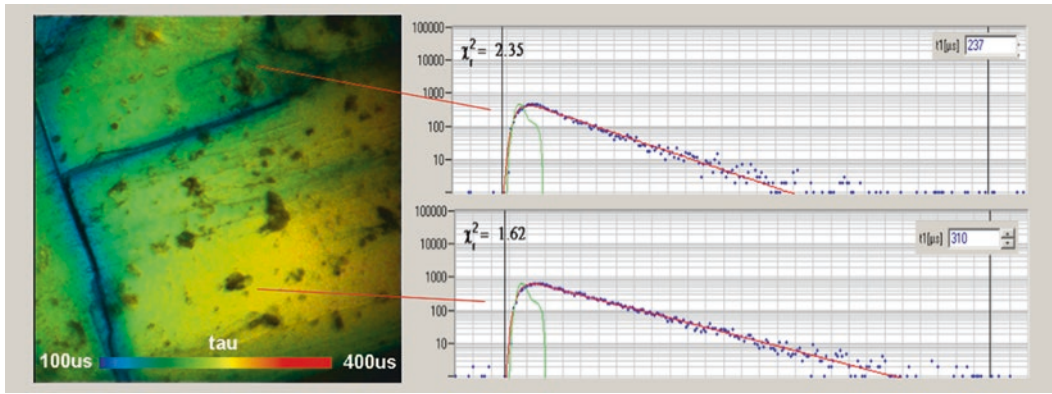

Fig. 2.9 PLIM image of a uranium mineral. Decay curves if two arbitrary selected spots are shown on the right. 256 × 256 pixels, 256 time channels, pixel time 3.6 ms, excitation 405 nm, emission filter long pass 435 nm

2.5.3 Detection of Zinc Oxide Nanoparticles

Nanoparticles often emit luminescence with decay times in the microsecond range. This makes them distinguishable from biological tissue which normally does not emit any detectable amount of phosphorescence. PLIM signals can thus be used to identify nanoparticles in biological tissue, and follow their migration or possible dissolution. The principle has been used to track ZnO nanoparticles from sunscreens or cosmetical products in human skin, and investigate possible influence on the viability by simultaneously recording the fluorescence of NAD(P)H [31]. Figure 2.8 shows zinc oxide particles detected by PLIM. The decay function is multi-exponential, with average (intensity-weighted) lifetimes up to 20 µs.

2.5.4 PLIM of Inorganic Materials

Figure 2.9 was obtained from an Autumit crystal (a uranium mineral). The phosphorescence lifetimes vary from about 100–400 µs. The lifetime image is shown on the left, decay curves of two selected spots on the right. The pixel time was 3.6 ms, the laser-on time 200 µs. The excitation wavelength was 405 nm, a 435 nm long pass filter was used in the emission path.

2.6 Suppression of Autofluorescence

Other applications are using PLIM for the suppression of autofluorescence. The sample is stained with a phosphorescent dye, and the long lifetime is used as a discrimination param-

eter [32, 33]. The SPCM software of the bh FLIM/PLIM systems offers this option online, without the need of special data analysis, see [13, 21].

2.7 Summary

Compared with PLIM techniques that use a single excitation pulse for every phosphorescence decay cycle the techniques described here has a number of significant advantages. The first one is that excitation with multiple pulses obtains a significantly higher triplet population than excitation with a single pulse. The sensitivity is therefore much higher. The technique can thus be used at correspondingly lower concentration of the phosphorescence probe, which, in turn, helps reduce possible toxicity. The second advantage is that it is compatible with multiphoton excitation. Due to the excitation with multiple laser pulses it does not require higher laser power or laser pulse energy than normal confocal or multiphoton FLIM. A third advantage is related to the TCSPC technique itself. TCSPC FLIM can record no more than one photon per laser pulse. The photon rate thus has to be limited to no more than 10% of the excitation pulse rate. This is no problem for the 80 MHz or 50 MHz pulse rates of Ti:Sapphire or picosecond diode lasers but it would be a problem if the pulse repetition rate was reduced to the kHz range. The technique described avoids this limitation because it works at the full laser repetition rate. The acquisition times is therefore on the order of 10–100 s, depending on the expectations to the signal-to-noise ratio of the lifetimes [12, 13]. The only remaining limitation is in the scan rate. The pixel time must not be shorter than about five times the phosphorescence decay time. This leads to minimum frame times in the range of 1 s for ruthenium dyes and about 10 s for platinum dyes. This no longer than the acquisition time required to obtain the desired signal-to-noise ratio. It thus has no influence on the total acquisition time of the FLIM/PLIM process.

References

1. Lakowicz JR (2006) Principles of fluorescence spectroscopy, 3rd edn. Springer, Heidelberg
2. Charbonniere LJ, Hildebrandt N (2008) Lanthanide complexes and quantum dots: a bright wedding for resonance energy transfer. Eur J Inorg Chem 2008:3241–3251
3. Hosny NA, Lee DA, Knight MM (2012) Single photon counting fluorescence lifetime detection of pericellular oxygen concentrations. J Biomed Opt 17(1):016007-1–016007-12
4. Fercher A, Borisov SM, Zhdanov AV et al (2011) Intracellular O_2 sensing probe based on cell-penetrating phosphorescent nanoparticles. ACS Nano 5:5499–5508
5. Lebedev AY, Cheprakov AV, Sakadzic S et al (2009) Dendritic phosphorescent probes for oxygen imaging in biological systems. Appl Mater Interfaces 1:1292–1304
6. Sakadžic S, Roussakis E, Yaseen MA et al (2010) Two-photon high-resolution measurement of partial pressure of oxygen in cerebral vasculature and tissue. Nat Methods 7:755–759
7. Gerritsen HC, Sanders R, Draaijer A et al (1997) Fluorescence lifetime imaging of oxygen in cells. J Fluoresc 7:11–16
8. Papkovsky D, Zhdanov AV, Fercher A et al (2012) Phosphorescent oxygen-sensitive probes. Springer
9. Papkovsky DB, Dmitriev RI (2013) Biological detection by optical oxygen sensing. Chem Soc Rev 42:8700–8732
10. Shibata M, Ichioka S, Ando J, Kamiya A (2001) Microvascular and interstitial PO2 measurement in rat skeletal muscle by phosphorescence quenching. J Appl Physiol 91:321–327
11. Skala MC, Riching KM, Bird DK et al (2007) In vivo multiphoton fluorescence lifetime imaging of protein-bound and free nicotinamide adenine dinucleotide in normal and precancerous epithelia. J Biomed Opt 12:02401-1–02401-10
12. Becker W (2005) Advanced time-correlated single-photon counting techniques. Springer, Berlin, Heidelberg, New York
13. Becker W (2015) The bh TCSPC handbook, 6th edn. Becker & Hickl GmbH, Berlin. Available from: www.becker-hickl.com
14. Becker W (2015) Introduction to multi-dimensional TCSPC. In: Becker W (ed) Advanced time-correlated single photon counting applications. Springer, Berlin, Heidelberg, New York, pp 1–63
15. Becker W, Shcheslavskiy V, Studier H (2015) TCSPC FLIM with different optical scanning techniques. In: Becker W (ed) Advanced time-correlated single photon counting applications. Springer, Berlin, Heidelberg, New York, pp 65–117
16. Becker W (2015) Fluorescence lifetime imaging by multi-dimensional time correlated single photon counting. Med Photon 27:41–61

17. Studier H, Becker W (2014) Megapixel FLIM. Proc SPIE 8948:89481K
18. Becker W, Su B, Bergmann A et al (2011) Simultaneous fluorescence and phosphorescence lifetime imaging. Proc SPIE 7903:790320
19. Becker W (2015) Fluorescence lifetime imaging techniques: time-correlated single-photon counting. In: Marcu L, French PMW, Elson DS (eds) Fluorecence lifetime spectroscopy and imaging. Principles and applications in biomedical diagnostics. CRC Press, Taylor & Francis Group, Boca Raton, London, New York, pp 203–232
20. Shcheslavskiy VI, Neubauer A, Bukowiecki R et al (2016) Combined fluorescence and phosphorescence lifetime imaging. Appl Phys Lett 108:091111-1–091111-5
21. Becker & Hickl GmbH (2015) DCS-120 confocal scanning FLIM systems. In: User handbook, 6th edn. Available from: www.becker-hickl.com
22. Sutter instrument, Movable objective microscope. www.sutter.com/microscopes
23. Toncelli C, Arzhakova OV, Dolgova A et al (2014) Oxygen-sensitive phosphorescent nanomaterials produced from high density polyethylene films by local solvent-crazing. Anal Chem 86(3):1917–1923
24. Dmitriev RI, Kondrashina AV, Koren K et al (2014) Small molecule phosphorescent probes for O2 imaging in 3D tissue models. Biomater Sci 2:853–866
25. Dmitriev RI, Zhdanov AV, Nolan YM, Papkovsky DB (2013) Imaging of neurosphere oxygenation with phosphorescent probes. Biomaterials 34:9307–9317
26. Kalinina S, Shcheslavskiy V, Becker W et al (2016) Correlative NAD(P)H-FLIM and oxygen sensing-PLIM for metabolic mapping. J Biophotonics 9(8):800–811
27. Kurokawa H, Ito H, Inoue M et al (2015) High resolution imaging of intracellular oxygen concentration by phosphorescence lifetime. Sci Rep 5:1–13
28. Zhdanov AV, Golubeva AV, Okkelman IA et al (2015) Imaging of oxygen gradients in giant umbrella cells: an ex vivo PLIM study. Am J Phys Cell Phys 309:C501–C509
29. Lukina M, Orlova A, Shirmanova M et al (2017) Interrogation of metabolic and oxygen states of tumors with fiber-based luminescence lifetime spectroscopy. Opt Lett 42(4):731–734
30. Jenkins J, Dmitriev RI, Papkovsky DB (2015) Imaging cell and tissue O_2 by TCSPC-PLIM. In: Becker W (ed) Advanced time-correlated single photon counting applications. Springer, Berlin, Heidelberg, New York, pp 225–247
31. Sanchez WY, Pastore M, Haridass I et al (2015) Fluorescence lifetime imaging of the skin. In: Becker W (ed) Advanced time-correlated single photon counting applications. Springer, Berlin, Heidelberg, New York, pp 457–508
32. Baggaley E, Botchway SW, Haycock JW et al (2014) Long-lived metal complexes open up microsecond lifetime imaging microscopy under multiphoton excitation: from FLIM to PLIM and beyond. Chem Sci 5:879–886
33. Baggaley E, Gill MR, Green NH et al (2014) Dinuclear ruthenium(II) complexes as two-photon, time-resolved emission microscopy probes for cellular DNA. Angew Chem Int Ed Eng 53:3367–3371

Quantitative Live Cell FLIM Imaging in Three Dimensions

3

Alix Le Marois and Klaus Suhling

Abstract

In this chapter, the concept of fluorescence lifetime and its utility in quantitative live cell imaging will be introduced, along with methods to record and analyze FLIM data. Relevant applications in 3D tissue and live cell imaging, including multiplexed FLIM detection, will also be detailed.

Keywords

FLIM techniques • Time-correlated single photon counting (TCSPC) • Multi-channel FLIM • Multi-modal FLIM • Optical sectioning • FLIM data analysis

3.1 Introduction

Fluorescence is a photophysical process which is used to generate contrast in optical microscopy. Its omnipresence in biological imaging is explained by its many advantages, the most important of which is its compatibility with live cell imaging, allowing the observation of dynamics and function, rather than simply morphology and structure. Fluorescence is also tunable, and boasts a wide spectral observation window, so several distinct features of interest can be studied at once and in relation with each other. Its sensitivity goes down to the single molecule level, which has allowed particle tracking and the development of fluorescence super-resolution microscopy methods. Moreover, fluorescence measurements can be quantitative and multiparametric: fluorescence emission is characterized by its intensity, wavelength, lifetime and polarization. The fluorescence lifetime describes the characteristic time that a fluorophore stays in the excited state before emission of the fluorescence photon, and it is considered an intrinsic property of the molecule. For this reason, fluorescence lifetime measurements are especially attractive since they do not depend on local fluorophore concentration or fluorescence intensity [1]. Therefore, lifetime-based imaging allows acquisition of quantitative information in cases where the fluorophore concentration cannot be

A. Le Marois • K. Suhling (✉)
Department of Physics, King's College London, Strand, London WC2R 2LS, UK
e-mail: klaus.suhling@kcl.ac.uk

R.I. Dmitriev (ed.), *Multi-Parametric Live Cell Microscopy of 3D Tissue Models*,
Advances in Experimental Medicine and Biology 1035, DOI 10.1007/978-3-319-67358-5_3

accurately controlled or determined, which is usually the case in biological experiments. Fluorescence lifetime imaging (FLIM) relies on the design and selection of fluorophores for the sensitivity of their lifetime to the local environment, e.g., viscosity, calcium concentration, refractive index [2], or of its chemical state (i.e. protonation, redox state). Endogenous fluorophores such as NADH, FAD and melanin can also be identified using their characteristic fluorescence lifetime [3], which is specifically interesting for tissue imaging applications where homogeneous, non-invasive and reliable labelling is not always straightforward. In particular, FLIM of NADH can reveal orientation towards glycolytic or oxidative pathways, since the lifetime of this cofactor increases from <400 ps in free form to ~2 ns upon binding to its coenzyme, which is promoted during oxidative phosphorylation [4]. FLIM is also the most sensitive method to detect protein-protein interactions via Förster Resonance Energy Transfer (FRET) [2].

One of the main challenges in tissue and 3D live cell imaging remains the scattering and absorption of light through the layers of the sample. The spatial resolution is decreased and contrast reduced, and the identification of features is limited at depths exceeding tens of microns. This currently prevents the use of fluorescence-based methods—and optical methods generally speaking—for thick samples [5]. However, precisely because fluorescence lifetime is largely insensitive to intensity artefacts which may appear in scattering media, FLIM is indeed a method of choice for the generation of contrast in tissue imaging [6]. Furthermore, the development of confocal and multiphoton excitation, light-sheet microscopy and spatial light modulation have allowed innovation and progress in tissue imaging with FLIM.

FLIM has been implemented in many different imaging modalities such as laser-scanning confocal and multi-photon excitation microscopy, wide-field imaging, super-resolved imaging, and is now used for a broad range of applications in the biomedical sciences. Forays into other fields such as materials science have also been reported. This chapter, rather than attempting a comprehensive review of technical achievements in FLIM and its variety of applications already available elsewhere [2], focuses on the possibilities and requirements of FLIM for quantitative 3D tissue and live cell imaging. Different methods to achieve lifetime contrast in microscopy are described and illustrated with selected examples of applications; their advantages and limitations when it comes to optical sectioning will also be mentioned.

3.2 Implementations of Fluorescence Lifetime Imaging

Several technical possibilities exist to implement fluorescence lifetime imaging in optical microscopy contexts. A distinction can be made between time-domain techniques, which aim at measuring the time between a pulsed excitation and the detection of fluorescence photons, and frequency domain techniques, which measure the intensity demodulation and phase shift created by fluorescence absorption and emission upon modulated excitation intensity. Both present advantages and limitations, as discussed elsewhere [7–9], and the methods employed to analyze the data produced also differ.

3.2.1 Time-Domain FLIM Systems

3.2.1.1 Time-Correlated Single Photon Counting (TCSPC)

TCSPC is a time-domain technique, which detects single fluorescence photons after short, repeated excitation pulses. Excitation sources are typically pulsed lasers. From the single photon arrival times, histograms describing the fluorescence decay after excitation can be reconstructed (Fig. 3.1a).

The fluorescence lifetime parameters can then be determined by direct fitting of the intensity decays. In TCSPC, detectors include Single-Photon Avalanche Photodiodes (SPADs), time-resolved photomultiplier tubes (PMTs), or their hybrid alternatives; several detectors can be used

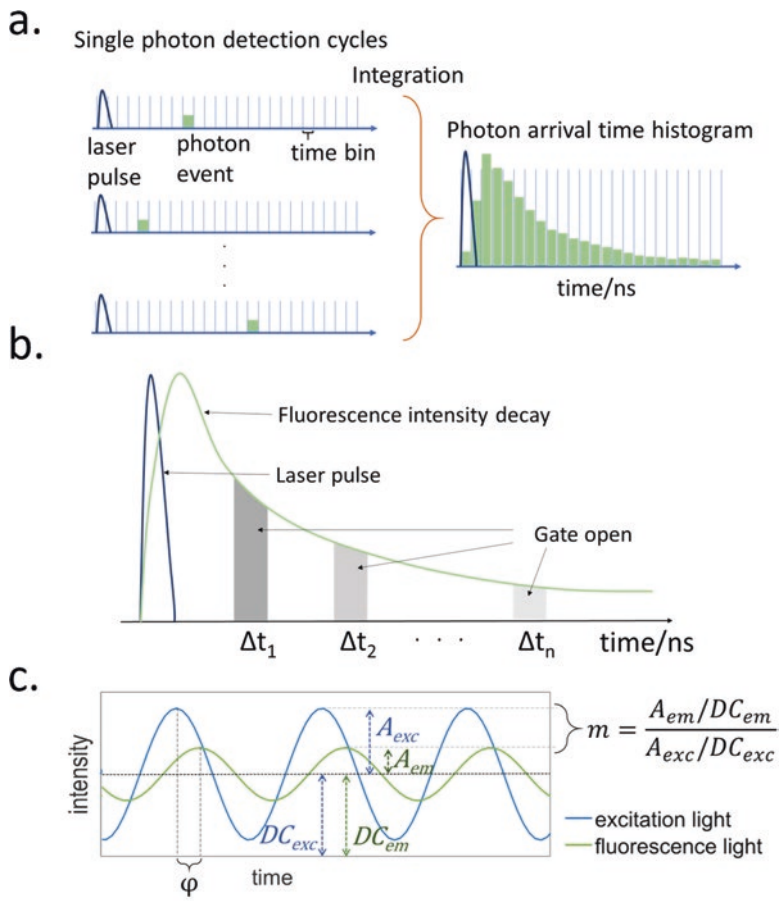

Fig. 3.1 FLIM recording implementations. (**a**) The TCSPC method: single photon pulses are detected after a laser pulse and timed with picosecond resolution for each cycle; integration over all cycles constitutes the photon arrival time histogram. Note that in practice, photons are not detected in each cycle (detection rate is usually kept at around 1% of the excitation rate, i.e. one photon for each 100 cycles). Inspired by refs [1, 10]. (**b**) The time-gated method: the fluorescence decay is sampled at increasing delays after a pulsed excitation by a gated optical intensifier (GOI). Inspired by refs [1, 58]. (**c**) Frequency domain FLIM: the excitation intensity is modulated, and the lifetime information is extracted from the phase difference between the excitation and the emission (φ) and the demodulation of the emission with respect to the excitation (m). Note that here the offset values DC_{exc} and DC_{em} are identical, but may differ in practice. Adapted from refs [1, 36]

for multiplexed experiments [10, 11]. These detectors are single-point (i.e., they have no spatial resolution), and are therefore usually coupled with scanning imaging techniques such as Laser-Scanning Confocal Microscopy (LSCM).

Confocal TCSPC-FLIM

Confocal microscopy is a widespread technique to achieve optical sectioning into the depth of a fluorescent sample. A pinhole is placed in front of the detector, on an optical plane conjugated to the sample plane. This aperture ensures that the light reaching the detector originates only from this specific plane, while the signal emanating from the planes above and below is excluded. Confocal microscopy has allowed drastic improvement in the axial resolution of scanning microscopes, and can be used to image successive z-planes into the sample [12]. For confocal FLIM, excitation sources include picosecond-pulsed diode lasers or pulsed supercontinuum lasers, for example.

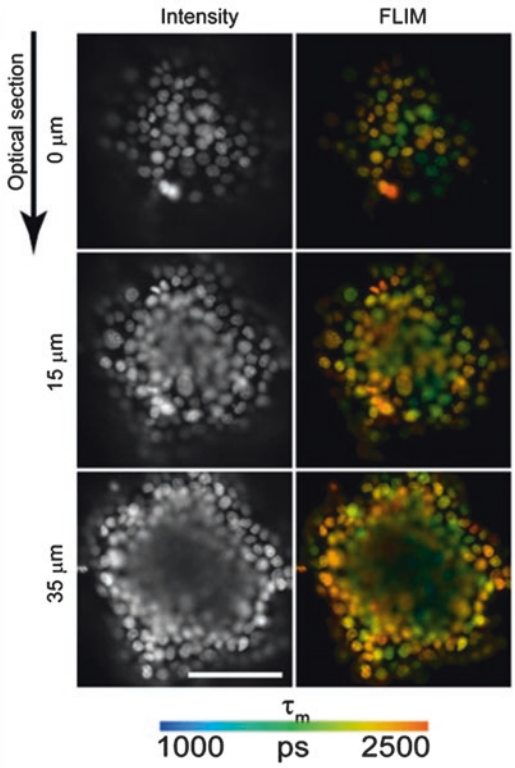

Fig. 3.2 FLIM imaging of tumor spheroids loaded with Hoechst and BrdU. The panels show images at different depths as indicated. In the cells displaying shorter lifetimes (*green*), Hoechst quenching by BrdU is enhanced, which indicates uptake of BrdU in dsDNA during the S phase. Reprinted from ref. [13] with permission under Creative Commons license. Scale bar is 100 µm

Okkelman et al. [13] have used confocal TCSPC-FLIM to detect cell proliferation in live tissue models such as tumor spheroids and organoids with thicknesses of up to 200 µm. They implemented a cell cycle assay by using a uridine compound, BrdU, to quench the fluorescence of well-known DNA-binding Hoechst dyes. BrdU is only incorporated in double-strand DNA upon DNA synthesis, so the quenching occurs selectively in cells entering in the S phase. FLIM offered remarkably enhanced contrast and unambiguous results compared to intensity-based measurements, by detecting lower lifetimes in the quenched nuclei of cells undergoing DNA synthesis throughout the 3-dimensional samples (Fig. 3.2).

While confocal microscopy provides improved axial resolution, the limitations linked to light scattering and absorption in the tissue are still present. Moreover, the process of confocal detection can be seen as inefficient, since much of the fluorescence light is blocked by the pinhole and therefore not collected.

Multi-Photon TCSPC-FLIM

Since longer wavelengths are less prone to scattering due to weaker interactions with the small features of the sample, using excitation sources in the long wavelength range can improve penetration into the sample. To this effect, multi-photon microscopy is an attractive option for 3D live cell and tissue imaging [14]. A fluorescent molecule can be promoted to the excited state by absorbing one photon of wavelength λ (single photon absorption), or two simultaneous (less energetic) photons of wavelengths λ_1 and λ_2, such that $\lambda_1^{-1} + \lambda_2^{-1} = \lambda^{-1}$ [14, 15] (two-photon absorption). Usually, the two photons are of the same wavelength $\lambda/2$ and are produced by a single laser source, though the wavelengths are permitted to be different, and two-color, two photon excitation has been reported [16], allowing the effective excitation of tryptophan. The fluorescence photon is then emitted following the same process in both cases (Kasha's rule states that the fluorescent molecule retains no memory of its excitation process [17]). In practice, two-photon excitation is achieved by focusing the light of very short (femtosecond) laser pulses through a microscope objective. Since the likelihood of two simultaneous photons being absorbed is non-zero only at the focal point, there is no longer need for confocal detection, since fluorescence in the sample originates only from the focal spot. Thanks to this remarkable phenomenon theorized by Maria Göppert-Mayer in the early twentieth century [18], excitation light with near-IR wavelengths (>700 nm), which travel deeper into the sample and cause less photodamage can be used. Because multiphoton microscopy requires pulsed laser sources, it is also ideally combined with TCSPC-FLIM. Two-photon excitation FLIM is now a widespread microscopy technique to image samples in three dimensions. FLIM of autofluorescence is

often carried out with multiphoton excitation, since endogenous fluorophores such as NADH usually have UV excitation bands and lifetimes below 3–4 ns, compatible with the fixed high repetition rate of the Titanium:Sapphire (around 80 MHz) used for multiphoton FLIM.

Recently, Lakner et al. [19] have used two-photon TCSPC-FLIM of autofluorescent compound NADH to image metabolic changes in live colorectal adenocarcinoma (Caco-2) cells upon treatment with metabolically active compounds. The cells were cultured in 3D matrices to constitute an in vitro tissue model. Other applications of multiphoton-FLIM to study proliferation of various cancerous cells in a 3D configuration can be found in refs [4, 20, 21].

Metabolism in other types of physiological processes, such as germ cell differentiation, was mapped in mice seminiferous tubes by Stringari et al. [3] using fluorescence signals from several endogenous fluorophores (free and bound NADH, FAD, retinoic acid, retinol and collagen) as well as GFP fused to Oct4, a transcription factor expressed in undifferentiated cells.

Blacker et al. [22] have used an elegant mathematical approach based on lifetime analysis of NADH/NADPH autofluorescence to map the relative importance of the distinct biochemical pathways associated with these two cofactors. NADPH synthesis and binding levels were genetically and chemically modified in HEK293 cells so as to establish the relationship between the [NADPH]/[NADH] cellular ratios and the lifetime parameters in the sample. This method was further applied to live cochlear tissue, and revealed different metabolic signatures and sensitivity to NADPH binding inhibition in different cell types within the tissue.

Whilst they offer good optical sectioning and depth penetration, the relatively long time required to scan over the whole field of view constitutes the main drawback of scanning systems. For these reasons, it is also interesting to consider wide-field approaches to FLIM. Wide-field TCSPC is currently being developed in our group [23], with successful imaging of live cells in a TIRF-TCSPC-FLIM configuration [24, 25] and ongoing efforts to produce a light-sheet TCSPC-FLIM system. Alternatively, state of the art wide-field FLIM systems relying on timing instrumentations different from TCSPC are extensively used in live cell imaging, and are described in the following sections.

3.2.1.2 Time-Gated systems

In time-gated systems, series of fluorescence images are collected at increasing delays after a short excitation pulse, using Gated Optical Intensifiers (GOI) in front of a camera [26, 27]. In other words, the fluorescence decay is sampled at increasing times, in all pixels simultaneously (Fig. 3.1b). The lifetime information is obtained by direct analysis of the intensity decays [28], or from the intensity ratios between these time gates [26].

One advantage of Time-Gated FLIM compared to TCSPC is its compatibility with wide-field detection [7, 14]. In wide-field microscopy, light from the entire field of view is collected simultaneously using camera-based detection. This acquisition method allows much faster frame rates than achievable with scanning microscopes, and limits photodamage since the sample is illuminated with a homogeneous field of light (such as achieved by Koehler illumination) rather than a focused beam. However, for the same reason, wide-field illumination does not confer optical sectioning and axial resolutions comparable to scanning methods. To overcome this limitation, optical sectioning techniques such as structured illumination [28–30], multi-focal scanning [31], spinning disk [32] and line-scanning microscopes [33] have been developed and combined with FLIM in order to improve the resolution problem.

In ref. [28], Cole et al. developed a time-gated microscope which incorporates a grating in the excitation path, to provide a 3D FLIM capability through structured illumination. Rat ear samples with a thickness of 10 μm were imaged, the lifetime contrast based on presence of endogenous fluorophores readily evidenced distinctive features in the sample such as blood vessels and cartilage. Time-gated FLIM can also be combined with laser-scanning systems in alternative detector architectures such as the one developed by Popleteeva et al. [34], allowing spectrally-resolved FLIM (see section 3.1).

3.2.2 Frequency Domain systems

In frequency domain fluorescence lifetime imaging, excitation intensity is modulated to typically produce a sinusoidal wave. The phase shift between the excitation and the fluorescence light is then detected, and reports on the lifetime of the excited state [1, 35]. Additionally, the demodulation of the fluorescence signal due to some fluorophores emitting when the excitation intensity is at a minimum can also be used to extract lifetime information (Fig. 3.1c). Usually, both the phase and intensity demodulation signals are measured for varying excitation modulation frequencies, and used together to extract the fluorescence lifetime.

Frequency-domain FLIM is ideally coupled with wide-field microscopy [36], and hence will benefit from fast acquisition times, but suffer from the same type of limitations as time-gated FLIM concerning depth penetration. One other possible method of providing optical sectioning to wide-field imaging is light-sheet microscopy (LSM, also known as Single Plane Illumination Microscopy, or SPIM). With this technique, the sample is illuminated by a thin sheet of light, corresponding to the object plane of the detection optics. The sheet is then scanned across the sample to reconstruct a three-dimensional image [37]. An additional advantage of SPIM is the low photodamage linked to a low field intensity of the excitation light at each point of the sample [20]. This makes it an attractive and promising technique for live-cell and 3D imaging, as proven by the many recent developments of LSM in combination with other microscopy techniques [37–39].

Frequency-Domain FLIM was combined with SPIM by Greger et al. [40]: Madine-Darby Canine Kidney (MDCK) cysts expressing EGFP fused to E-Cadherin were embedded in an agarose gel matrix for SPIM imaging, and images were acquired on 100 planes at 500 nm spacing, hence providing optically-sectioned lifetime images in a sample of 50 μm thickness, with cellular resolution (Fig. 3.3). Our colleagues at King's College London have also recently implemented a light-sheet FLIM system to study GFP-labelled zebrafish, allowing the rapid collection of volumetric FLIM data [41].

3.3 Multi-Channel FLIM

3.3.1 Multi-Color and Spectrally-Resolved FLIM

As stated in the introduction, fluorescence offers a wide spectral observation window, which can be used to image several features of interest at once by tagging them with fluorophores or quantum dots of distinct emission wavelengths. Spectrally-resolved FLIM can also be used to study the lifetime of a single fluorophore as a function of its emission wavelength.

Spectral resolution in microscopy is achieved by splitting the emission light according to its spectrum, using dichromatic mirrors, beam splitters, diffraction gratings or prisms. The spectrally-separated fluorescence is then projected onto an array of single-point detectors [10, 34, 42, 43] or distinct areas of a wide-field detector [33, 44–46]. Alternatively, each spectral window can be imaged sequentially using different emission filters [47, 48]. Combined with time-resolved fluorescence instrumentation as detailed in the previous sections, FLIM images can hence be acquired in multiple spectral regions using TCSPC [43, 49], time-gated [33, 44, 47, 48] or frequency domain approaches [50]. Note that it may be then necessary to use more than one excitation source, if the fluorophores used cannot be excited at the same wavelength. Two-photon absorption facilitates spectral multiplexing, since the two-photon absorption spectra of fluorophores tend to be broader [51, 52].

Time-Gated spectrally-resolved FLIM architectures include a line-scanning microscope developed by the group of P. French at Imperial College London [33, 44]. Here, lines of the sample are scanned sequentially, while the second dimension of the detector is used to spread the fluorescence emission according to wavelength. Applied to samples of unstained tissue such as rat tail and atherosclerotic human arteries, this method clearly discriminates different functional zones such as lipid-rich and fibrous domains. Another time-gated architecture was developed by Popleteeva et al. [34], where a two-photon

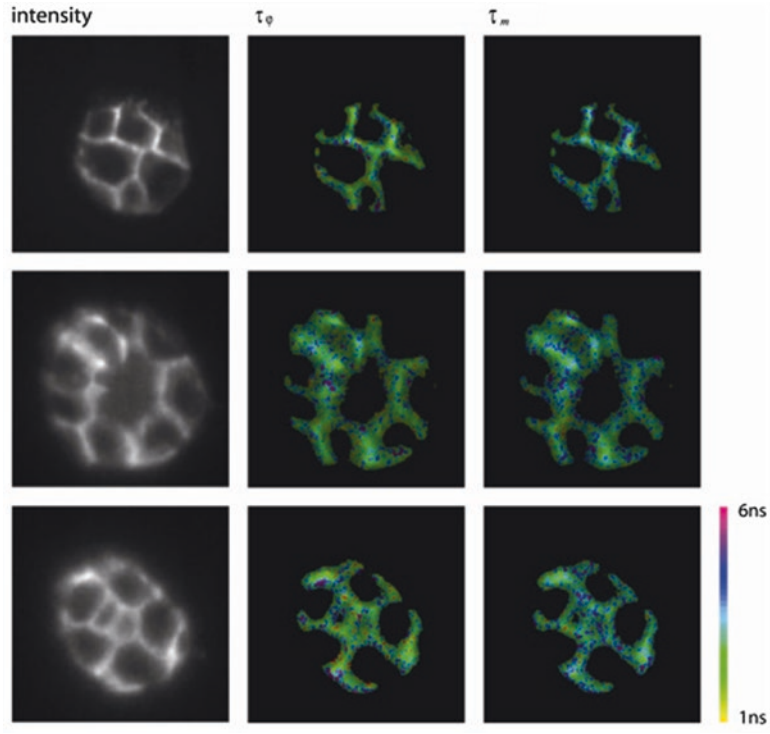

Fig. 3.3 Light-sheet FLIM sections of MDCK cysts acquired using a frequency domain system; images are shown at 3 depths within a 50 μm sample. Note that the lifetime contrast was computed using the phase (*central panel*) and demodulation (*right-hand panel*) information, independently. Reprinted from Ref. [40] with permission from OSA publishing

scanning microscope was combined with a 64 × 4 SPAD array detector. The fluorescence is spectrally separated onto the width of the detector, offering 64 spectral bins, while the timing is provided by using the four SPADs in each spectral bin as successive time gates. Using this system, label-free spectral FLIM imaging of liver tissue from a tumorogenic mouse model was performed, identifying distinct cellular layers in the wall of a blood vessel.

In ref. [50], Zhao et al. combined frequency-domain FLIM with several excitation and detection channels and scanning microscopy to image two FRET pairs in live zebrafish embryos simultaneously, namely a CFP-Venus pair reporting on Calcium ion concentration, and GFP-RFP, reporting on cAMP levels. The microscopy method used allowed up to 1 mm depth penetration with a cellular resolution (25 μm). 3D volumes were acquired by rotating the sample after each imaging step. However, the simultaneous use of these two FRET pairs may create ambiguous results, since GFP and Venus fluorescent proteins have poor spectral separation.

Indeed, when multiple fluorophores are imaged, spectral crosstalk between them can become an issue. The development of new probes facilitating spectral imaging, such as dyes with narrow emission bands, quantum dots, near-infrared dyes, or dark acceptors for FRET, is therefore an area of active research. Laviv et al. [49] have recently designed a blue-excitable, red-emitting FRET donor fluorescent protein (FP), mCyRFP1. The large Stokes shift of this FP enables simultaneous excitation with GFP, while its acceptor, Maroon, emits in the far red and is hence spectrally separated from GFP. GFP was then associated in a FRET pair with a dark acceptor, dimVenus (Fig. 3.4a).

This combination allowed dual color FLIM-FRET imaging, which was used to monitor the activation dynamics of two distinct proteins, namely kinase CaMKIIα and GTPase RhoA, in single dendritic spines of hippocampal brain

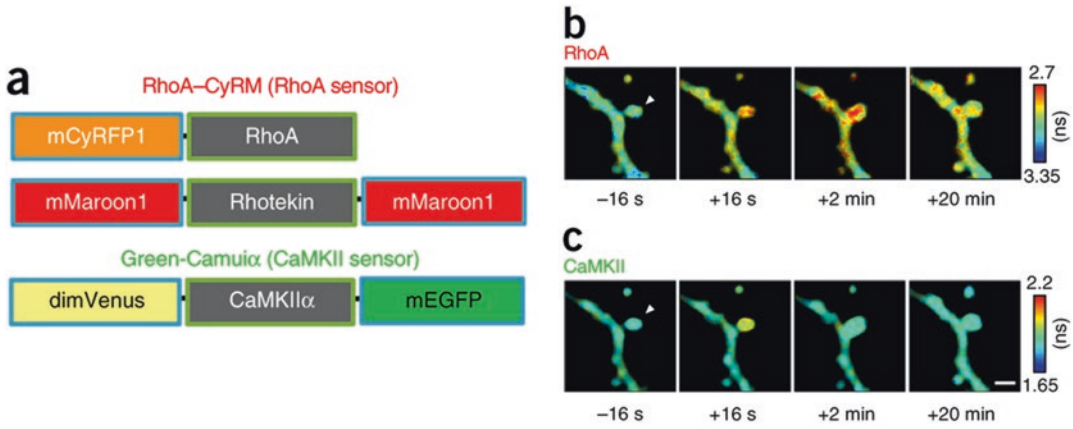

Fig. 3.4 Activation of RhoA and CaMKII monitored in time upon dendritic stimulation in hippocampal tissue slices by dual-color TCSPC FLIM-FRET. (**a**): Architecture of the two FRET sensors. RhoA binds to Rhotekin upon activation, and this binding is monitored by donor lifetime of mCyRFP1-mMaroon at 590–650 nm. In the same time, upon activation, CaMKII undergoes an intramolecular rearrangement, which is monitored by donor lifetime of GFP-dimVenus at 490–550 nm. (**b**, **c**): Time evolution of the donor fluorophore lifetimes in the two spectral channels: mCyRFP1 lifetime is decreased durably in the spine and adjacent dendrite upon stimulation (**b**—note that the *colour map* is inverted), while mEGFP lifetime is increased transiently and exclusively in the spine, while the lifetime in the dendrite is unchanged. Adapted by permission from Macmillan Publishers Ltd.: Nature Methods [49], copyright (2016)

tissue slices which were stimulated using photo-induced glutamate release (Fig. 3.4b, c). This showed that CaMKII had a transient and localized activation, while RhoA activation was long-lasting and spread throughout the dendrite.

3.3.2 Polarization-Resolved FLIM

The polarization of light is used to describe the orientation of the electric field vector as light propagates through a medium. The probability of a fluorophore being excited depends on the relative orientation of the excitation polarization with the excitation transition dipole moment of the fluorophore. This dipole moment is related to the way the geometry of the electronic cloud of the molecule is modified when transitioning from the ground state to the excited state. Since lasers, which have an inherent linear polarization, are usually used as excitation sources, the molecules in the sample are excited selectively according to their orientation [17, 53]. Once excited, the fluorophore always emits light with a linear polarization corresponding to the orientation of its emission transition dipole moment. Detecting fluorescence in a polarization-resolved manner hence allows resolution of molecular orientation. Depolarizing phenomena which occur within the lifetime of the excited state can also be investigated, and these include Förster Resonance Energy Transfer (FRET), and molecular rotational motion. Polarization-resolved FLIM achieves quantitative resolution of these phenomena since the depolarization can be recorded in time after the excitation pulse [54].

In practice, a polarizing beamsplitter is placed in the emission path to separate and project the fluorescence light in two polarized components, parallel and perpendicular to the excitation light, onto two detectors. A measure of fluorescence depolarization, the fluorescence anisotropy, is then computed as the normalized difference between the polarization-resolved signals [55]. Time-resolved anisotropy imaging can be achieved using time-gated [56–60] setups, TCSPC [54, 55], and in the frequency domain [61, 62].

Vishwasrao et al. [63] have combined time- and polarization-resolved fluorescence microscopy of live hippocampal tissue to study the response of

NADH fluorescence in normoxic and hypoxic conditions, using anisotropy as a signature of the bound or free state of the NADH molecule.

In a recent study, Zheng et al. [64] have mapped and quantified the diffusivity of a small fluorescent molecule, Alexa Fluor 350, in the extracellular environment of hippocampal brain slices. Polarization-resolved FLIM images were acquired sequentially on a two-photon TCSPC-FLIM microscope, at a depth of 100 µm within the samples, to ensure healthy state of the tissue section while imaged. The dynamics of molecular diffusion were investigated in interstitial and intracellular compartments, revealing slower overall motion in the tissue than in free medium, as well as differential diffusion in the cellular soma and in the dendrites. Furthermore, imaging the extracellular area of giant synaptic clefts (4–8 µm) formed onto CA3 pyramidal cells revealed that diffusion within the synaptic area was slower than in non-synaptic extracellular space.

3.4 FLIM in Combination with Other Microscopy Techniques

In the case of tissue and 3D imaging, it is useful to obtain structural and functional information of the sample simultaneously, or to monitor several biophysical parameters. To this effect, multimodal systems combine FLIM with other imaging techniques.

3.4.1 Combined FLIM and PLIM

Phosphorescence occurs when a molecule is excited to the singlet state, and rather than emitting a fluorescence photon, transfers to another energy level, called the triplet state. This transition is in general forbidden and can occur in certain conditions such as in presence of heavy atoms [1]. The molecule returns to the ground state by emitting a photon, similarly to fluorescence, but since the triplet state is much lower in energy than the singlet state, its emission spectrum is red-shifted compared to the fluorescence spectrum, and the lifetime of the triplet state is much longer than that of fluorescence, usually in the range of microseconds to milliseconds. Phosphorescent molecules can be designed to exhibit environmentally-sensitive lifetimes, and so can report on various chemical environments, such as dioxygen levels, since oxygen is a phosphorescence quencher [1, 65]. TCSPC experiments can be designed to simultaneously measure FLIM and PLIM, by using pulsed excitation and assuming a linear superposition of short fluorescence decays and long phosphorescence decays in each pixel [11]. This is a convenient way to investigate two features in the sample simultaneously without the need for additional instrumentation [13, 66], since the excitation and acquisition do not differ from a classic FLIM experiment.

In reference [66], Hille et al. have elegantly combined FLIM of endogenous fluorophore FAD and PLIM of ruthenium-based oxygen sensor Kr341 in live tissue samples of cockroach salivary ducts. Hence, the cellular metabolic state could be correlated to oxygen consumption upon treatment with metabolism-altering compounds such as dopamine.

3.4.2 FLIM and Optical Coherence Tomography (OCT)

The development of fluorescence-based methods (including FLIM) in combination with Optical Coherence Tomography is a dynamic field of instrument and method development [67–70], notably in the group of J. Jo [71–74]. The aim is to provide simultaneous recording of structural and functional information in thick tissue samples.

Park et al. [74] demonstrated the technical implementation of such dual-modality systems (Fig. 3.5). The 3-dimensional topography of cancerous model tissue (hamster cheek pouch epithelium) is resolved with OCT (Fig. 3.5a), while the lifetime contrast of endogenous fluorescence shows the modified metabolic state of cancer cells through their reduced NADH lifetime (Fig. 3.5b, c).

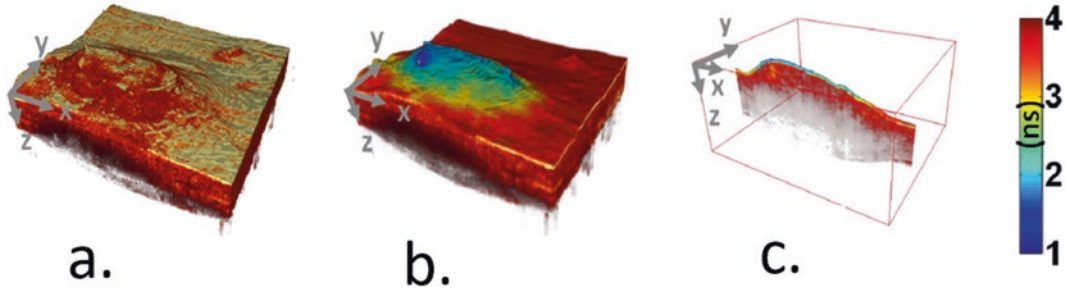

Fig. 3.5 Dual modality imaging of cancerous hamster cheek pouch. The volume dimensions are 2-by-2-by-0.65 mm. (**a**) OCT topology map. (**b**) OCT-FLIM overlay at 390 nm detection band. (**c**) Slice from (**b**). Reprinted from [74] with permission from OSA

3.4.3 FLIM with Nonlinear Microscopy Techniques for Label-Free Imaging of Complex Tissue

Tissue models are often composed of several distinct components, such as different cell types and extracellular matrix. FLIM in combination with non-linear scattering techniques such as Raman spectroscopy and Second-Harmonic Generation (SHG) can be used to map the organization of complex samples. For example, FLIM of autofluorescence can indicate the metabolic state of cells, while collagen can be imaged by detecting its second-harmonic signal. Raman scattering methods can report non-invasively on specific chemical markers within a tissue, such as lipidic material. The scattering response is instantaneous compared to the fluorescence process so does not interfere with the lifetime measurement, and can be spectrally separated from fluorescence.

In ref. [75], Datta et al. have used FLIM of autofluorescence in combination with third-harmonic generation to show the organization of adipose tissue. An intracellular endogenous fluorescent signal was determined to be emitted by oxidized lipid inside lipid droplets, while the third harmonic signal was generated at the interface between lipid droplets and the surrounding medium. The 3D–structure of white adipose tissue was reconstructed with a depth of over 70 µm. Coherent Anti-Stokes Raman Spectroscopy (CARS) was also used to confirm the lipidic nature of the fluorescent species.

3.4.4 FLIM for Clinical Imaging

Clinical imaging also tackles issues related to imaging through thick samples, and its technical implementations draw from expertise in microscope development. Clinical FLIM systems have been developed to image live tissues in patients, such as the Fluorescence Lifetime Imaging Ophtalmoscopy (FLIO) device developed by the group of D. Schweitzer in Jena, which can be used to detect changes in the ocular fundus linked to various pathologies such as Alzheimer's disease [76], macular degeneration [77], diabetic retinopathy [78] or glaucoma [79].

Skin can also be imaged by FLIM in a clinical context; the Derma-Inspect skin imaging device developed by JenLab combines optical coherence tomography and multiphoton fluorescence with a FLIM capability to image skin and intraoperative samples in live patients [80–82]. This approach effectively provides 3-dimensional optical biopsies with information on morphology and metabolism at a subcellular level, and does not require any removal of tissue samples, or any other mechanical or chemical treatment. Recently, Kantelhardt et al. have reported the combined use of multiphoton tomography and FLIM to successfully differentiate healthy from

cancerous tissue during an neurosurgical operation, using the clinical tomograph designed by Jenlab [81]. Apart from early detection of skin diseases, the Derma-Inspect device could also be used to monitor the progression of wound healing and the effect of cosmetics on the skin [83].

Phipps et al. [47, 48] have used sequential imaging in two or three spectral windows combined with time-gated FLIM, to determine clinically relevant features such as presence of elastin, macrophages, collagen and lipid-rich regions, in atherosclerotic human aorta and carotid samples. Their optical setup allows this biochemical mapping through sample thicknesses of 250 µm. Study [47] was based on surgical biopsies and attributed a risk level to each patient using the lifetime parameters of the sample, showing the utility of FLIM-based imaging for clinical diagnostics.

3.4.5 Perspective: Adaptive Optics for Improved Optical Sectioning in High Resolution Microscopy

Adaptive optics was first developed in astronomy to compensate the scattering and distortion observed in telescope images caused by the terrestrial atmosphere. It consists in deliberately introducing aberrated optics such as deformable mirrors, to correct the deformation of the wave-front. Adaptive optics are now used in biomedical imaging contexts to image in scattering media [84]. Recently, this has been applied to STED imaging by M.J. Booth et al. to image through brain tissue of *Drosophila melanogaster* at a depth of 10 microns below the surface [85, 86]. The group of J. Keller has also developed a light-sheet microscope incorporating spatiotemporal wave-front correction based on adaptive optics, accounting for heterogeneity of the aberrating properties in live organisms [87]. While these instances do not provide lifetime contrast, STED is a scanning technique which can be readily combined with TCSPC-FLIM [88, 89].

3.5 Analysis of FLIM Data

3.5.1 Time-Domain Data

3.5.1.1 Pixel-Wise Decay Fitting

TCSPC and time-gated FLIM sample the fluorescence decay at several time points in each pixel. The most obvious and widespread technique to analyze such data is exponential decay fitting (Fig. 3.6a). The model can be single- or multi-exponential; the number of exponential terms is determined by the user according to the assumptions on the number of emitting species or micro-environments in each pixel, and the evaluation of the goodness of fit for a particular model. Pixel-wise exponential decay fitting is attractive since it allows quantitative resolution of all the decay parameters: amplitudes and lifetimes. This type of analysis is available in most commercial software programs developed by TCSPC manufacturers: Becker& Hickl (SPCImage) [10], PicoQuant (SymPhoTime), Horiba (DAS), Edinburgh Instruments (F980, FAST) and microscope manufacturers whose products have an inbuilt FLIM capability.

The goodness of fit parameter is often based on a weighted least-squares estimation (Fig. 3.6a), which assumes Gaussian signal-dependent noise. This is a reasonable assumption for high intensity data and in time-gated FLIM; with TCSPC however, the data is acquired as single photons, which follow a Poisson law to a good approximation. The correct goodness of fit for such data is therefore the Poisson likelihood [90, 91], which has been proved to yield more accurate fits, especially in data with low counts. Bayesian estimation of lifetime parameters has also produced significant improvements in the field [92, 93]. Such routines can be developed in-house, and have been made available as software packages by several groups. The TRI2 software package, developed by P. Barber at King's College London and the University of Oxford, is freely available and gives several options as to the minimization model [94].

In situations where it is expected that the fluorophores in the sample will display a continuous

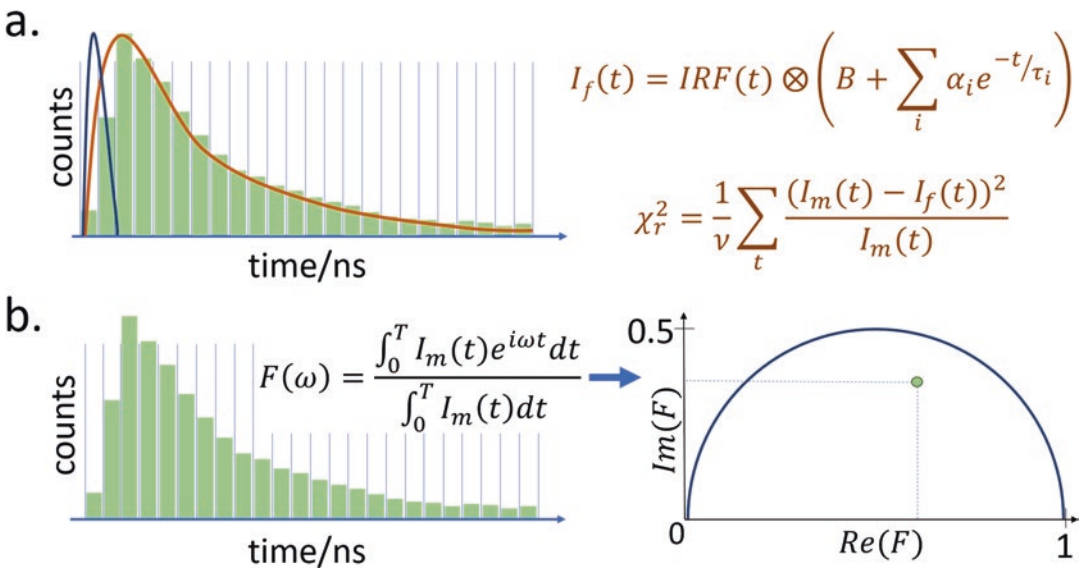

Fig. 3.6 FLIM analysis techniques. (**a**) Curve fitting approach—the decay histogram $I_m(t)$ (displayed in green) is fitted to a multi-exponential decay model $B + \sum_i \alpha_i e^{-t/\tau_i}$ (*orange curve*) convolved to the instrument response function *IRF*(*t*) (mainly comprised of the laser pulse width, shown in *blue*). The procedure yields the fitted intensity decay $I_f(t)$. In the nonlinear least squares minimization, the goodness of fit is assessed by the reduced chi-square: χ_r^2 is the weighted sum of squares, reduced by scaling to the number of degrees of freedom, ν. χ_r^2 values close to unity are considered to report on a good fit. (**b**) Phasor approach—the decay histogram $I_m(t)$ is transformed using the phasor operation $F(\omega)$ at a defined frequency ω (usually chosen to provide widest spread of data in phasor space). Plotting the real part Re(*F*) against the imaginary part Im(*F*) of $F(\omega)$ yields a point on the phasor space (right, in *green*); single exponential decays falling on the universal circle (*blue*), and multi-exponential decays on a line connecting the individual pure single-exponentials of the superposition

distribution of lifetimes rather than discrete values, a stretched-exponential model can be adopted [95, 96]. In this model, a heterogeneity parameter describes the spread of the lifetime distribution.

The main limitation of pixel-wise fitting is the strong dependence of fitting results to signal to noise ratios of the data. Resolving two exponential components with acceptable accuracy avoiding substantial lifetime-intensity parameter correlation [1] requires several tens of thousands of photons in each decay [97], which can be difficult to achieve in live samples where short acquisition times are needed. Pixels can be locally binned to improve the signal-to-noise, but this is at the expense of spatial resolution. Non-fitting parametric techniques such as mean arrival time calculations are coarse since they do not provide information about the success of the procedure or the complexity of the decay within one pixel, but can allow to calculate FRET efficiencies with low intensities, as shown in refs [98–100].

3.5.1.2 Global Fitting Techniques

Analysis methods aimed at extracting exponential parameters in low signal-to-noise data are the object of ongoing research. Global fitting methods relinquish pixel-by pixel independence of the lifetime parameters by using fixed lifetimes [101]. The lifetimes can be determined beforehand using calibration samples, or can be calculated in each image as global parameters. The amplitudes are then resolved with increased accuracy and confidence, improving the quality of multi-exponential fitting, which is especially useful for FRET experiments [102]. A software package implementing global fitting, FLIMfit, was developed by S.C. Warren et al. [103], and is freely available. It also includes anisotropy data analysis.

3.5.2 Frequency Domain Data

Frequency domain FLIM measures the phase shift and demodulation in the fluorescence emission at varying frequencies of modulated excitation. As the frequency of the excitation increases, the phase shift of the emission increases while the modulation decreases due to the fluorescence process, yielding two independent measurements which constitute the frequency response of the sample [1]. The phase shift and demodulation can be predicted analytically at any frequency for any intensity decay, so the frequency response data can be used to extract the lifetime and amplitude parameters using a least-squares minimization process, similarly to time-domain data analysis. Frequency-domain FLIM can also be analyzed using Fourier-domain methods such as the phasor analysis method [36], further described in the next section.

3.5.3 Global Analysis Techniques

When the data at hand does not lend itself to direct fitting, for example because the signal-to-noise ratio is low, the number of distinct emitting species is unknown, or the fluorescence signal is distorted by instrumental artefacts (wide pulse from the laser, high background, incomplete decays), non-fitting based approaches can be employed.

3.5.3.1 Phasor Analysis

Initially developed for frequency domain data, phasor analysis is a projection method where the decay in each pixel is transformed using a Fourier domain operation at the frequency of the excitation modulation [104]. The transform yields a complex number, and the real and imaginary parts (forming the phasor coordinates) can be used to project the data on a 2-D plot (Fig. 3.6b).

Phasor coordinates of a single exponential decay fall on a semi-circle, while multi-exponential decay coordinates lie within or outside of the circle, on a line connecting the pure single exponential components. The position of a point on this line informs on the relative abundance of these two components in the initial decay. This method has since then been extended to time domain data as well, and allows rapid visualization of the abundance distribution of decay components in the image without using exponential fitting. Phasor analysis software was developed by the group of E. Gratton in the Laboratory of Fluorescence Dynamics in Irvine and was made commercially available. Phasor analysis is also included in several of the software packages mentioned above, including SPCImage and TRI2. In Fig. 3.7a, b, FLIM data of a HeLa cell stained with polarity-sensitive dye di-4-ANEPPDHQ and analyzed with phasor analysis is shown; contrast between the more ordered plasma membrane and the more disordered internal membranes is readily observable using this approach. This phasor routine was developed in-house using Matlab.

3.5.3.2 Noise-Corrected Principal Component Analysis

While phasor analysis has opened the possibility of analyzing complex data without the need for decay fitting, it suffers from its high sensitivity to the shape of the decay: incomplete decays, decays with high background or distorted by the shape of the laser pulse will be displaced away from the position dictated by the lifetime information, hence requiring calibration measurements. Moreover, projection onto a 2-dimensional plot complicates the analysis of samples with potentially more than two fluorescent species. One alternative method based on the Laguerre expansion method was developed by J. Jo and co-workers [105, 106]. In our group, we have developed another kind of data projection technique based on Principal Component Analysis (PCA) [107]. This method resolves the variations in the decay profiles between pixels in the image with low intensities, and is not limited to two components. Since the instrumental distortions cited previously affect all the pixels simultaneously, they do not constitute a source of variance between pixels and do not affect the result of the analysis. We have tailored our PCA routine to TCSPC data with a Poisson noise correction and made it freely available as a software package. Figure 3.7b shows data of the di-4-

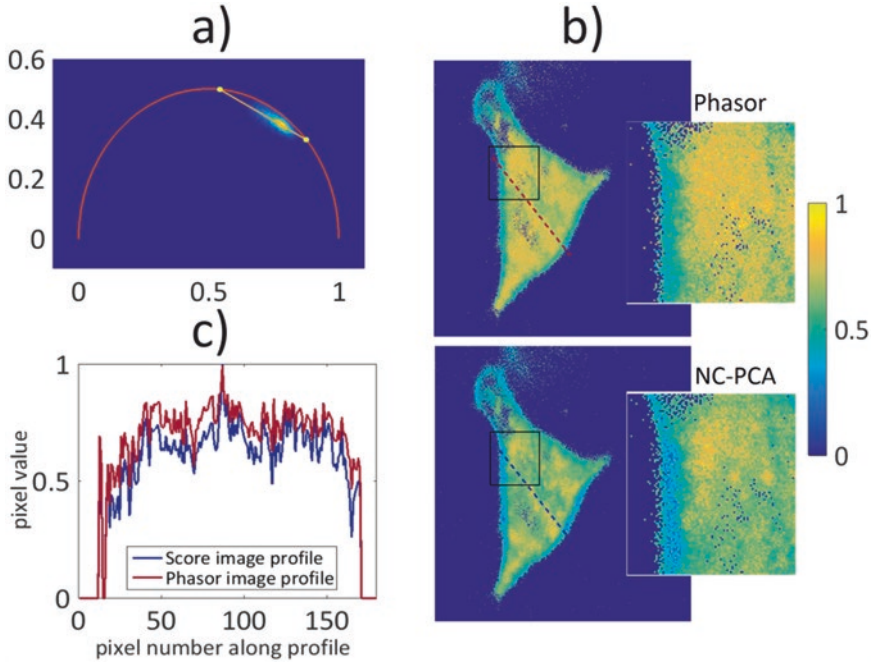

Fig. 3.7 Global analysis of a live HeLa cell stained with order-sensitive membrane dye di-4-ANEPPDHQ. (**a**): Phasor analysis. The phasor cloud is fitted to a straight line (*orange*), and the projection values of each pixel on this line is used as a contrast range for the phasor image. (**b**) Comparison of phasor image (*above*) and score image produced by NC-PCA (*below*). Insets show a zoom of 100-by-100 pixel region indicated by the square in the full image. (**c**) Profiles of the phasor (*red*) and score (*blue*) values, along the hashed line shown on the images in (**b**). Reprinted from ref. [107] with permission

ANEPPDHQ-stained HeLa cell analyzed by NC-PCA. The same type of contrast as with phasor analysis is observed, proving that this method is sensitive to lifetime contrast in low intensity situations and can resolve multiple decay components within the image. This method could be extended easily to other types of data where the noise model is known.

3.6 Conclusion

Fluorescence imaging methods are relevant and vital for the investigation of live cells, organisms and tissue models in vitro and in vivo. Fluorescence lifetime imaging yields high information content on the samples and can be performed in a variety of microscopy contexts to solve many different biological questions, as seen by the applications mentioned in this review. While video-rate FLIM is accessible via time-gated and frequency-domain FLIM, TCSPC remains the most sensitive and photon-efficient technique to measure fluorescence lifetimes. Moreover, scanning approaches offer the best optical sectioning to date in 3D tissue samples. However, this single-point requirement, because of its slow acquisition process, remains a bottleneck concerning the use of TCSPC-FLIM in some cases. Progress in analysis methods such as Bayesian fitting or phasor analysis have improved the resolution of decay information in low intensity situations, hence allowing for shorter acquisition times. Interesting innovations have also been put forward to increase the acquisition speeds of such systems, such as the multi-focal FLIM approach developed in the group of S. Ameer-Beg [108]. Another option is the 16-anode parallelized time-resolved detector developed by LaVision [109], which has for example been used by Rinnenthal et al. [110] to

detect Calcium levels using FRET intravitally in mice, with more than 100 micron depth penetration and with an image acquisition rate of 2 Hz. Further developments of high-speed, high resolution systems offer promising prospects for the investigation of dynamic processes in live biological samples.

References

1. Lakowicz JR (2006) Principles of Fluorescence Spectroscopy. 3rd edition, Springer US, Boston, MA.
2. Suhling K et al (2015) Fluorescence lifetime imaging (FLIM): Basic concepts and some recent developments. Med Photonics 27:3–40
3. Stringari C, Cinquin A, Cinquin O, Digman MA, Donovan PJ, Gratton E (2011) Phasor approach to fluorescence lifetime microscopy distinguishes different metabolic states of germ cells in a live tissue. Proc Natl Acad Sci U S A 108(33):13582–13587
4. Skala MC et al (2007) In vivo multiphoton fluorescence lifetime imaging of protein-bound and free NADH in normal and pre-cancerous epithelia. J Biomed Opt 12(2):024014
5. Appel AA, Anastasio MA, Larson JC, Brey EM (2013) Imaging challenges in biomaterials and tissue engineering. Biomaterials 34(28):6615–6630
6. Elson D et al (2004) Time-domain fluorescence lifetime imaging applied to biological tissue. Off J Eur Photochem Assoc Eur Soc Photobiol 3(8):795–801
7. Gratton E, Breusegem S, Sutin J, Ruan Q, Barry N (2003) Fluorescence lifetime imaging for the two-photon microscope: time-domain and frequency-domain methods. J Biomed Opt 8(3):381–390
8. Hedstrom J, Sedarous S, Prendergast FG (1988) Measurements of fluorescence lifetimes by use of a hybrid time-correlated and multifrequency phase fluorometer. Biochemistry 27(17):6203–6208
9. Valeur B (2005) Pulse and phase fluorometries: an objective comparison. In: Hof PM, Hutterer PR, Fidler PV (eds) Fluorescence spectroscopy in biology. Springer, Berlin Heidelberg, pp 30–48
10. Becker W (2012) The bh TCSPC handbook, 5th edn. Becker and Hickl GmbH, Berlin
11. Becker W (2005) Advanced time-correlated single photon counting techniques, vol 81. Springer, Berlin, Heidelberg
12. Masters, BR (2006) Confocal microscopy and multiphoton excitation microscopy. The genesis of live cell imaging–chapter 7. SPIE Press, Bellingham
13. Okkelman IA, Dmitriev RI, Foley T, Papkovsky DB (2016) Use of fluorescence lifetime imaging microscopy (FLIM) as a timer of cell cycle S phase. PLoS One 11(12):e0167385
14. So PTC, Dong CY, Masters BR, Berland KM (2000) Two-photon excitation fluorescence microscopy. Annu Rev Biomed Eng 2(1):399–429
15. Hoover EE, Squier JA (2013) Advances in multiphoton microscopy technology. Nat Photonics 7(2):93–101
16. Quentmeier S, Denicke S, Gericke K-H (2009) Two-color two-photon fluorescence laser scanning microscopy. J Fluoresc 19(6):1037–1043
17. Valeur B, Berberan-Santos MN (2012) Molecular fluorescence: principles and applications. John Wiley & Sons, Hoboken, NJ
18. Grzybowski A, Pietrzak K (2013) Maria Goeppert-Mayer (1906–1972): two-photon effect on dermatology. Clin Dermatol 31(2):221–225
19. Lakner PH, Monaghan MG, Möller Y, Olayioye MA, Schenke-Layland K (2017) Applying phasor approach analysis of multiphoton FLIM measurements to probe the metabolic activity of three-dimensional in vitro cell culture models. Sci Rep 7:42730
20. König K, Uchugonova A, Gorjup E (2011) Multiphoton fluorescence lifetime imaging of 3D-stem cell spheroids during differentiation. Microsc Res Tech 74(1):9–17
21. Skala MC et al (2005) Multiphoton microscopy of endogenous fluorescence differentiates normal, precancerous, and cancerous squamous epithelial tissues. Cancer Res 65(4):1180–1186
22. Blacker TS et al (2014) Separating NADH and NADPH fluorescence in live cells and tissues using FLIM. Nat Commun 5:3936
23. Hirvonen LM, Suhling K (2017) Wide-field TCSPC: methods and applications. Meas Sci Technol 28(1):012003
24. Suhling K et al (2016) Wide-field TCSPC-based fluorescence lifetime imaging (FLIM) microscopy. SPIE Proc 9858:98580J
25. Hirvonen LM et al (2016) Picosecond wide-field time-correlated single photon counting fluorescence microscopy with a delay line anode detector. Appl Phys Lett 109(7):071101
26. Sytsma J, Vroom JM, De Grauw CJ, Gerritsen HC (1998) Time-gated fluorescence lifetime imaging and microvolume spectroscopy using two-photon excitation. J Microsc 191(1):39–51
27. Soloviev VY et al (2007) Fluorescence lifetime imaging by using time-gated data acquisition. Appl Opt 46(30):7384–7391
28. Cole MJ et al (2001) Time-domain whole-field fluorescence lifetime imaging with optical sectioning. J Microsc 203(3):246–257
29. Hinsdale T, Olsovsky C, Rico-Jimenez JJ, Maitland KC, Jo JA, Malik BH (2017) Optically sectioned wide-field fluorescence lifetime imaging microscopy enabled by structured illumination. Biomed Opt Express 8(3):1455–1465
30. Webb SED et al (2002) A wide-field time-domain fluorescence lifetime imaging microscope with optical sectioning. Rev Sci Instrum 73:1898
31. Grant DM et al (2007) High speed optically sectioned fluorescence lifetime imaging permits study of live cell signaling events. Opt Express 15(24):15656–15673

32. Grant DM, Elson DS, Schimpf D, Dunsby C, Requejo-Isidro J, Auksorius E, Munro I, Neil MAA, French PMW, Nye E, Stamp G, Courtney P, 2005 Optically sectioned fluores-cence lifetime imaging using a Nipkow disk microscope and atunable ultrafast continuum excitation source. Opt Lett 30:3353—3355
33. Beule PD et al (2007) Rapid hyperspectral fluorescence lifetime imaging. Microsc Res Tech 70(5):481–484
34. Popleteeva M et al (2015) Fast and simple spectral FLIM for biochemical and medical imaging. Opt Express 23(18):23511–23525
35. Esposito A, Gerritsen HC, Wouters FS (2007) Optimizing frequency-domain fluorescence lifetime sensing for high-throughput applications: photon economy and acquisition speed. J Opt Soc Am A 24(10):3261–3273
36. Verveer PJ, Hanley QS (2009) Frequency domain FLIM theory, instrumentation, and data analysis. Lab Tech Biochem Mol Biol 33:59–94
37. Santi PA (2011) Light sheet fluorescence microscopy: a review. J Histochem Cytochem 59(2):129–138
38. Stelzer EHK (2015) Light-sheet fluorescence microscopy for quantitative biology. Nat Methods 12(1):23–26
39. Rieckher M (2017) Light sheet microscopy to measure protein dynamics. J Cell Physiol 232(1):27–35
40. Greger K, Neetz MJ, Reynaud EG, Stelzer EHK (2011) Three-dimensional fluorescence lifetime imaging with a single plane illumination microscope provides an improved signal to noise ratio. Opt Express 19(21):20743–20750
41. Mitchell CA et al (2017) Functional in vivo imaging using fluorescence lifetime light-sheet microscopy. Opt Lett 42(7):1269–1272
42. Krstajić N, Levitt J, Poland S, Ameer-Beg S, Henderson R (2015) 256 × 2 SPAD line sensor for time resolved fluorescence spectroscopy. Opt Express 23(5):5653–5669
43. Niehörster T et al (2016) Multi-target spectrally resolved fluorescence lifetime imaging microscopy. Nat Methods 13(3):257–262
44. Owen DM et al (2007) Excitation-resolved hyperspectral fluorescence lifetime imaging using a UV-extended supercontinuum source. Opt Lett 32(23):3408–3410
45. Hanley QS, Arndt-Jovin DJ, Jovin TM (2002) Spectrallyresolved fluorescence lifetime imaging microscopy. Appl. Spectrosc 56:155–166.
46. Vitali M et al (2011) Wide-field multi-parameter FLIM: long-term minimal invasive observation of proteins in living cells. PLoS One 6(2):e15820
47. Phipps JE, Sun Y, Fishbein MC, Marcu L (2012) A fluorescence lifetime imaging classification method to investigate the collagen to lipid ratio in fibrous caps of atherosclerotic plaque. Lasers Surg Med 44(7):564–571
48. Phipps J, Sun Y, Saroufeem R, Hatami N, Fishbein MC, Marcu L (2011) Fluorescence lifetime imaging for the characterization of the biochemical composition of atherosclerotic plaques. J Biomed Opt 16(9):096018
49. Laviv T, Kim BB, Chu J, Lam AJ, Lin MZ, Yasuda R (2016) Simultaneous dual-color fluorescence lifetime imaging with novel red-shifted fluorescent proteins. Nat Methods 13(12):989–992
50. Zhao M, Wan X, Li Y, Zhou W, Peng L (2015) Multiplexed 3D FRET imaging in deep tissue of live embryos. Sci Rep 5:13991
51. Xu C, Zipfel W, Shear JB, Williams RM, Webb WW (1996) Multiphoton fluorescence excitation: new spectral windows for biological nonlinear microscopy. Proc Natl Acad Sci U S A 93(20):10763–10768
52. Bestvater F et al (2002) Two-photon fluorescence absorption and emission spectra of dyes relevant for cell imaging. J Microsc 208(Pt 2):108–115
53. Periasamy A, Clegg RM (2009) FLIM microscopy in biology and medicine. CRC Press, Boca Raton, FL
54. Levitt JA et al (2015) Simultaneous FRAP, FLIM and FAIM for measurements of protein mobility and interaction in living cells. Biomed Opt Express 6(10):3842–3854
55. Suhling K, Levitt J, Chung P-H (2014) Time-resolved fluorescence anisotropy imaging. In: Engelborghs Y, Visser AJWG (eds) Fluorescence spectroscopy and microscopy, vol 1076. Humana Press, Totowa, NJ, pp 503–519
56. Siegel J et al (2003) Wide-field time-resolved fluorescence anisotropy imaging (TR-FAIM): imaging the rotational mobility of a fluorophore. Rev Sci Instrum 74(1):182–192
57. Suhling K et al (2004) Time-resolved fluorescence anisotropy imaging applied to live cells. Opt Lett 29(6):584
58. Devauges V et al (2012) Homodimerization of amyloid precursor protein at the plasma membrane: a homoFRET study by time-resolved fluorescence anisotropy imaging. PLoS One 7(9):e44434
59. Bader AN, Hofman EG, Voortman J, en Henegouwen PM, Gerritsen HC (2009) Homo-FRET imaging enables quantification of protein cluster sizes with subcellular resolution. Biophys J 97(9):2613–2622
60. Bader AN, Hofman EG, en Henegouwen PM, Gerritsen HC (2007) Imaging of protein cluster sizes by means of confocal time-gated fluorescence anisotropy microscopy. Opt Express 15(11):6934–6945
61. Clayton AHA, Hanley QS, Arndt-Jovin DJ, Subramaniam V, Jovin TM (2002) Dynamic fluorescence anisotropy imaging microscopy inthe frequency domain (rFLIM). Biophys J 83(3):1631–1649
62. Lidke DS et al (2003) Imaging molecular interactions in cells by dynamic and static fluorescence anisotropy (rFLIM and emFRET). Biochem Soc Trans 31(Pt 5):1020–1027

63. Vishwasrao HD, Heikal AA, Kasischke KA, Webb WW (2005) Conformational dependence of intracellular NADH on metabolic state revealed by associated fluorescence anisotropy. J Biol Chem 280(26):25119–25126
64. Zheng K, Jensen TP, Savtchenko LP, Levitt JA, Suhling K, Rusakov DA (2017) Nanoscale diffusion in the synaptic cleft and beyond measured with time-resolved fluorescence anisotropy imaging. Sci Rep 7:42022
65. Dmitriev RI et al (2014) Small molecule phosphorescent probes for O2 imaging in 3D tissue models. Biomater Sci 2(6):853–866
66. Jahn K, Buschmann V, Hille C (2015) Simultaneous fluorescence and phosphorescence lifetime imaging microscopy in living cells. Sci Rep 5:14334
67. Pahlevaninezhad H et al (2014) A high-efficiency fiber-based imaging system for co-registered autofluorescence and optical coherence tomography. Biomed Opt Express 5(9):2978–2987
68. Jiang M, Liu T, Liu X, Jiao S (2014) Simultaneous optical coherence tomography and lipofuscin autofluorescence imaging of the retina with a single broadband light source at 480nm. Biomed Opt Express 5(12):4242–4248
69. Khan KM, Kumar R, Krishna H, Rao KD, Majumder SK (2016) A dual-modal optical system combining depth-sensitive laser induced fluorescence (LIF) spectroscopy and optical coherence tomography (OCT) for analyzing layered biological tissue. Biomed Spectrosc Imaging 5(3):313–324
70. Dai C, Liu X, Jiao S (2012) Simultaneous optical coherence tomography and autofluorescence microscopy with a single light source. J Biomed Opt 17(8):0805021–0805023
71. Pande P et al (2016) Automated analysis of multimodal fluorescence lifetime imaging and optical coherence tomography data for the diagnosis of oral cancer in the hamster cheek pouch model. Biomed Opt Express 7(5):2000–2015
72. Shrestha S et al (2016) Multimodal optical coherence tomography and fluorescence lifetime imaging with interleaved excitation sources for simultaneous endogenous and exogenous fluorescence. Biomed Opt Express 7(9):3184–3197
73. Jo JA et al (2010) In vivo simultaneous morphological and biochemical optical imaging of oral epithelial cancer. IEEE Trans Biomed Eng 57(10):2596–2599
74. Park J, Jo JA, Shrestha S, Pande P, Wan Q, Applegate BE (2010) A dual-modality optical coherence tomography and fluorescence lifetime imaging microscopy system for simultaneous morphological and biochemical tissue characterization. Biomed Opt Express 1(1):186–200
75. Datta R, Alfonso-García A, Cinco R, Gratton E (2015) Fluorescence lifetime imaging of endogenous biomarker of oxidative stress. Sci Rep 5:9848
76. Jentsch S et al (2015) Retinal fluorescence lifetime imaging ophthalmoscopy measures depend on the severity of Alzheimer's disease. Acta Ophthalmol 93(4):e241–e247
77. Klemm M, Schweitzer D, Peters S, Sauer L, Hammer M, Haueisen J (2015) FLIMX: a software package to determine and analyze the fluorescence lifetime in time-resolved fluorescence data from the human eye. PLoS One 10(7):e0131640
78. Schmidt J et al (2017) Fundus autofluorescence lifetimes are increased in non-proliferative diabetic retinopathy. Acta Ophthalmol 95(1):33–40
79. Ramm L, Jentsch S, Augsten R, Hammer M (2014) Fluorescence lifetime imaging ophthalmoscopy in glaucoma. Albrecht Von Graefes Arch Klin Exp Ophthalmol 252(12):2025–2026
80. Koenig K, Riemann I (2003) High-resolution multiphoton tomography of human skin with subcellular spatial resolution and picosecond time resolution. J Biomed Opt 8(3):432
81. Kantelhardt SR et al (2016) In vivo multiphoton tomography and fluorescence lifetime imaging of human brain tumor tissue. J Neuro-Oncol 127(3):473–482
82. König K (2008) Clinical multiphoton tomography. J Biophotonics 1(1):13–23
83. Lin LL et al (2011) Time-correlated single photon counting for simultaneous monitoring of zinc oxide nanoparticles and NAD(P)H in intact and barrier-disrupted volunteer skin. Pharm Res 28(11):2920
84. Marsh PN, Burns D, Girkin JM (2003) Practical implementation of adaptive optics in multiphoton microscopy. Opt Express 11(10):1123–1130
85. Patton BR, Burke D, Owald D, Gould TJ, Bewersdorf J, Booth MJ (2016) Three-dimensional STED microscopy of aberrating tissue using dual adaptive optics. Opt Express 24(8):8862–8876
86. Gould TJ, Burke D, Bewersdorf J, Booth MJ (2012) Adaptive optics enables 3D STED microscopy in aberrating specimens. Opt Express 20(19):20998–21009
87. Royer LA et al (2016) Adaptive light-sheet microscopy for long-term, high-resolution imaging in living organisms. Nat Biotechnol 34(12):1267–1278
88. Auksorius E et al (2008) Stimulated emission depletion microscopy with a supercontinuum source and fluorescence lifetime imaging. Opt Lett 33(2):113
89. Lesoine MD, Bose S, Petrich JW, Smith EA (Jul. 2012) Supercontinuum stimulated emission depletion fluorescence lifetime imaging. J Phys Chem B 116(27):7821–7826
90. Hauschild T, Jentschel M (2001) Comparison of maximum likelihood estimation and chi-square statistics applied to counting experiments. Nucl Instrum Methods Phys Res Sect Accel Spectrometers Detect Assoc Equip 457(1–2):384–401
91. Kim J, Seok J (2013) Statistical properties of amplitude and decay parameter estimators for fluorescence lifetime imaging. Opt Express 21(5):6061–6075
92. Rowley MI, Coolen ACC, Vojnovic B, Barber PR (2016) Robust Bayesian fluorescence lifetime estimation, decay model selection and instrument

response determination for low-intensity FLIM imaging. PLoS One 11(6):e0158404
93. Rowley MI, Barber PR, Coolen ACC, Vojnovic B (2011) Bayesian analysis of fluorescence lifetime imaging data. Proc SPIE 7903:790325
94. Barber PR et al (2009) Multiphoton time-domain fluorescence lifetime imaging microscopy: practical application to protein–protein interactions using global analysis. J R Soc Interface 6(Suppl 1):S93–S105
95. Lee KCB et al (2001) Application of the stretched exponential function to fluorescence lifetime imaging. Biophys J 81(3):1265–1274
96. Włodarczyk J, Kierdaszuk B (2003) Interpretation of fluorescence decays using a power-like model. Biophys J 85(1):589–598
97. Köllner M, Wolfrum J (1992) How many photons are necessary for fluorescence-lifetime measurements? Chem Phys Lett 200(1–2):199–204
98. Lee S-JR, Escobedo-Lozoya Y, Szatmari EM, Yasuda R (2009) Activation of CaMKII in single dendritic spines during long-term potentiation. Nature 458(7236):299–304
99. Padilla-Parra S, Audugé N, Coppey-Moisan M, Tramier M (2008) Quantitative FRET analysis by fast acquisition time domain FLIM at high spatial resolution in living cells. Biophys J 95(6):2976–2988
100. Leray A, Padilla-Parra S, Roul J, Héliot L, Tramier M (2013) Spatio-temporal quantification of FRET in living cells by fast time-domain FLIM: a comparative study of non-fitting methods. PLoS One 8(7):e69335
101. Knutson JR, Beechem JM, Brand L (1983) Simultaneous analysis of multiple fluorescence decay curves: a global approach. Chem Phys Lett 102(6):501–507
102. Verveer PJ, Squire A, Bastiaens PIH (2000) Global analysis of fluorescence lifetime imaging microscopy data. Biophys J 78(4):2127–2137
103. Warren SC et al (2013) Rapid global fitting of large fluorescence lifetime imaging microscopy datasets. PLoS One 8(8):e70687
104. Digman MA, Caiolfa VR, Zamai M, Gratton E (2008) The phasor approach to fluorescence lifetime imaging analysis. Biophys J 94(2):L14–L16
105. Jo JA, Fang Q, Marcu L (2005) Ultrafast method for the analysis of fluorescence lifetime imaging microscopy data based on the Laguerre expansion technique. IEEE J Quantum Electron 11(4):835–845
106. Jo JA, Fang Q, Papaioannou T, Marcu L (2004) Fast model-free deconvolution of fluorescence decay for analysis of biological systems. J Biomed Opt 9(4):743–752
107. Le Marois A, Labouesse S, Suhling K, Heintzmann R (2016) Noise-corrected principal component analysis of fluorescence lifetime imaging data. J Biophotonics. https://doi.org/10.1002/jbio.201600160
108. Poland SP et al (2015) A high speed multifocal multiphoton fluorescence lifetime imaging microscope for live-cell FRET imaging. Biomed Opt Express 6(2):277–296
109. Schroeer U TriM scope II FLIM device. LaVision BioTec GmbH. [Online]. Available from: http://lavisionbiotec.com/trim-scope-ii-flim-device.html. (Accessed 28 Mar 2017)
110. Rinnenthal JL et al (2013) Parallelized TCSPC for dynamic intravital fluorescence lifetime imaging: quantifying neuronal dysfunction in neuroinflammation. PLoS One 8(4):e60100

4 Three-Dimensional Tissue Models and Available Probes for Multi-Parametric Live Cell Microscopy: A Brief Overview

Neil O'Donnell and Ruslan I. Dmitriev

Abstract

In recent years, the advances in tissue engineering and regenerative medicine have resulted in introduction of novel 3D tissue models, materials and methods to the regular practice of cell biologists, material scientists and specialists from related areas. 3D tissue models allow mimicking in vivo cell and tissue organization. However, the efficient work in three dimensions has significant challenges, such as compatibility with conventional cell biology methods, live cell imaging and quantification readouts. Here, we briefly discuss the applicability of 3D tissue models to different live cell microscopy modalities and the available range of fluo- and phosphorescent probes and sensors allowing for multi-parametric imaging.

Keywords

3D tissue model • FLIM • Live cell microscopy • Metabolism • PLIM

4.1 Three-dimensional tissue models

A number of cell-cell and cell-extracellular matrix (ECM) interactions establish a communication network that maintains physiological characteristics of a living tissue. These include (but not are limited to) structural tensile strength, cellular polarity, adhesion, differentiation, migration and proliferation [1]. In vitro cell cultures that establish these physiological interactions can mimic real in vivo tissues much more closely than two-dimensional (2D) cultures. Cell flattening occurring in conventional 2D culture results in abnormal (significantly different from those in 3D) alterations in cytoskeleton, gene expression, nuclear shape, cellular proliferation and differentiation, susceptibility to drug therapies [2]. Currently, 3D tissue models are used in stem cell therapies as a support matrix for the growth and transplantation and in vitro systems mimicking closely in vivo mor-

N. O'Donnell • R.I. Dmitriev (✉)
Metabolic Imaging Group, School of Biochemistry and Cell Biology, University College Cork, Cork, Ireland
e-mail: r.dmitriev@ucc.ie

R.I. Dmitriev (ed.), *Multi-Parametric Live Cell Microscopy of 3D Tissue Models*, Advances in Experimental Medicine and Biology 1035, DOI 10.1007/978-3-319-67358-5_4

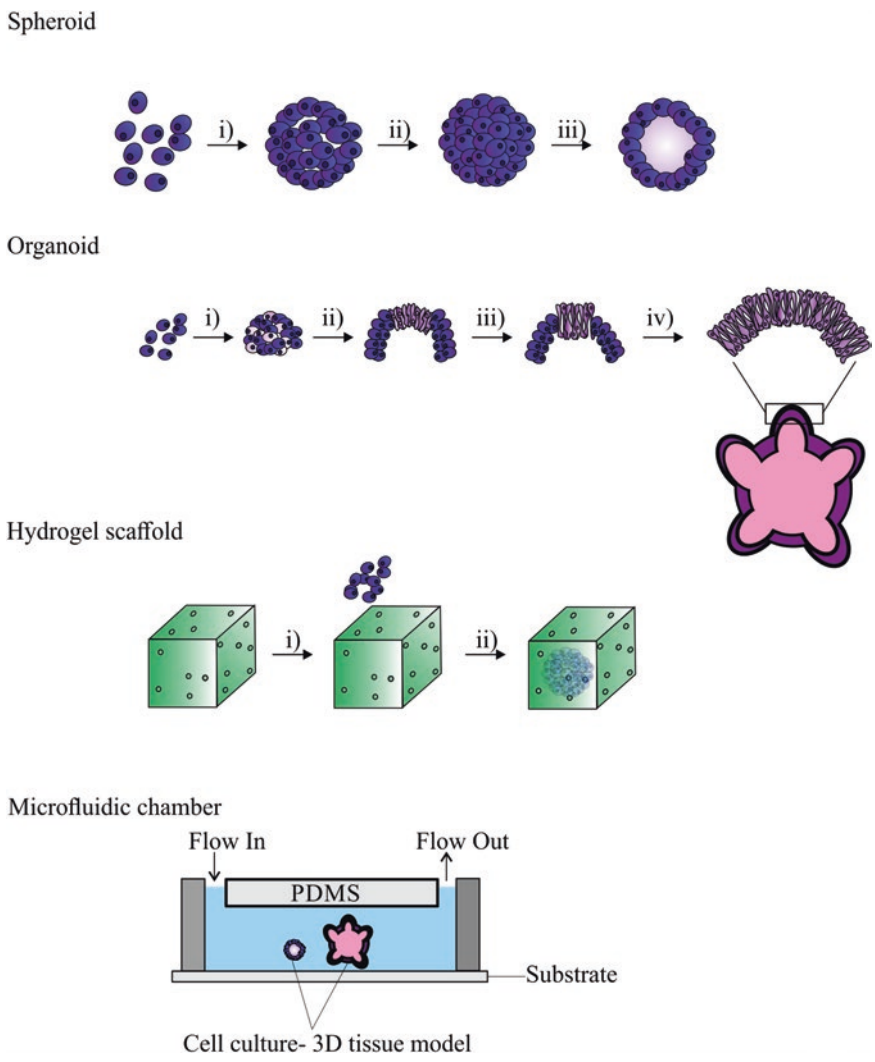

Fig. 4.1 Examples of 3D tissue models. Cells can aggregate together forming spheroids (i), then polarize (ii), and differentiate (iii). In organoid system, stem cells differentiate (i) and self-organize by processes of cell sorting (ii) and lineage commitment (iii) into fully developed structures possessing many features of real tissue (iv). Hydrogel and related scaffold structures provide structured and rigid 3D environment for cells and aggregates growing within. Microfluidic chamber allows culturing the 3D tissue model under the controlled flow

phology, for cell physiology and drug therapy studies. Apart from stem cell-based therapies, regenerative and personalized medicine applications, 3D tissue models are useful for studying cancer, modeling its growth and developing therapies against it (see Chap. 1). 3D tissue models can be categorized into two main groups, which will be discussed below: scaffold-based and scaffold-free systems (Fig. 4.1).

4.1.1 Scaffold-Free 3D Tissue Models

Scaffold-free models utilize the ability of cells to synthesize their own ECM or naturally produce it within live tissue. They include spheroids [3], organoids [4], tissue explants [5, 6], artificial tissue [7] and xenografts [8]. The most common scaffold-free model is *spheroids*, which are

produced via assembly of mono- or multi-cell type-consisting spherical shape aggregates, typically of 50–500 μm size [3]. Spheroids can be produced in several ways such as liquid overlay technique [9], hanging drop technique [10], microwell arrays via micropatterned wells [11] or by bioprinting. Cells within the spheroid can re-establish mutual contacts and re-create specific microenvironments (e.g. O_2, pH and metabolite diffusion gradients), therefore reproducing cellular morphology in vivo. For cancer cell spheroids, often referred as multi-cellular tumor spheroids (MCTS), four phenotype classifications have been proposed: round, mass, grape-like, and stellate phenotype [12–14]. The round-type spheroid is characterized by strong cell–cell adhesion, with regularly organized nuclei, and lumen forming the center. The mass-type spheroids are also spherical in shape but are much larger and possessing disorganized nuclei. The grape-like type spheroids form loose clusters with weak cell-cell interactions. The stellate-type spheroids are invasive, possessing stellate projections that migrate chains of cells migrating into the ECM. The phenotype of tumor spheroids is dependent on gene and protein expression profiles of the cell lines [12] and signals from tumor microenvironment [13]. Due to heterogeneity of conditions and gradients of metabolites, nutrients, metabolic waste and soluble factors (growth factors, chemokines, cytokines) spheroids are often comprised of cells in various stages of the cell cycle [15]. Radial structure of MCTS results in radial differences in gene and protein expression, cell regulation and drug metabolism. These gradients and cellular heterogeneity within the spheroid culture closely resemble *in vivo* tumors [16]. MCTS used to study cell metabolism have shown similar increased glycolysis and lactate production, Warburg effect of metabolic switching seen as in tumors in vivo [17, 18]. Culturing MCTS with stromal and immune cells allows for the study of host-tumor and microenvironment interactions that play key roles in cellular regulation, angiogenesis, and invasiveness of tumors [19–21]. Therefore, MCTS are useful tools in studying tumor biology and drug treatment. Spheroids can be imaged via number of modalities including light sheet microscopy [22], confocal fluorescence and phosphorescence microscopy [23, 24] and two-photon microscopy [25].

Organoids are cultured organ-specific 3D cellular clusters produced from primary tissue, embryonic stem cells (ESCs) or induced pluripotent stem cells (iPSCs). In contrast to spheroids, they contain different cell types, are capable of self-renewal, organization via self-sorting, and, to some extent, possess functionality seen in the tissues they are derived from in vivo [26]. Organoids produced to date include intestinal [27], kidney [28], brain [29], retinal [30], stomach [31], lung [32] and liver-like tissues known as liver buds, using progenitor stem cell types or induced pluripotent stem cells [33]. Despite being a more physiological 3D tissue model than spheroids, amenable to established experimental techniques, and disease modeling, organoids still lack proper vascularization and blood supply. However, these issues can be overcome by co-culturing with additional cell types (e.g. stroma and immune cells), by perfusion and microfluidic approaches to generate concentration gradients of growth and signaling factors [34] and mimic blood flow through tissue [35]. Organoids are also compatible with standard confocal and two-photon excited fluorescence microscopies, which were applied to study chromosome segregation by genetically encoded fluorescent proteins [36], analyse proliferating cells by fluorescence lifetime imaging microscopy (FLIM) [37] and responses to drug treatments [38].

4.1.2 Microfluidics in 3D Tissue Models

Microfluidics allows precise control of fluid flow and mass exchange in micrometer-size structures, such as channels and chambers. In 3D tissue models it can provide spatial and temporal control for co-cultures of multiple cell types, fluid flow and sheer stress (e.g. perfusion of circulating vasculature and immune cells) and biomolecule gradients [39]. Microfluidic systems

can be prepared by a multitude of approaches such as 'soft lithography' [40, 41]. Frequently used optically clear and O_2-permeable polydimethylsiloxane (PDMS) is compatible with live cell fluorescence imaging [42], but often shows high autofluorescence.

Organ-on-chip technology combines microfluidics with 3D tissue culture of spheroids or organoids to mimic tissue and organ physiology in vivo [40]. Organ-on-chips have been reported for a range of organs including liver [43, 44], intestine [45, 46], lung [47, 48], heart [49, 50], kidney [51, 52], vasculature [53–55], and blood brain barrier [56]. Organ-on-chip models have been applied in disease modeling [57], drug screening and toxicity testing [58]. However, it is unclear to what degree organ-on-chips can model the real tissue. Cell seeding and growth in microfluidic channels limits the size of produced tissue models and exposes cells to various types of stress such as temporary hypoxia or anoxia [59, 60].

4.1.3 Scaffold-Based Tissue Models

Scaffolds are designed to encourage adhesion, proliferation, differentiation, and migration of cells seeded and grown within. They provide mechanical strength, porosity, and efficient exchange of gases, nutrients, and metabolites. Frequently used hydrogels represent water-rich 3D networks of hydrophilic cross-linked polymers, that mimic closely the ECM with mechanics of soft tissues, supporting transport of metabolites and waste, and cell adhesion [61]. Hydrogels are represented by natural (e.g. cellulose, collagen, chitosan) and synthetic materials (e.g. polyethylene glycol) [62]. Scaffolds can be produced from synthetic polymers such as polycaprolactone [63], polylactide [64], polystyrene [65] or other materials [66].

Collagen is a fibrous protein, it comprises a right-handed bundle of three parallel, left-handed polyproline II-type helices, and provides structural support to body tissues [67]. Collagen hydrogels are primarily comprised of type I collagen, derived from pepsin- or acid-solubilized form, frequently sourced from rat tail tendon. The hydrogel is formed by increasing temperature and pH, inducing collagen fibril assembly in presence of culture media or cells [68].

Matrigel™ is a cocktail of ECM proteins extracted from Englebreth-Holm-Swarm (EHS) epithelial tumors in mice, where they form a basement membrane (BME). The BME is an important ECM in epithelial and endothelial tissues which supports tissue integrity acting as a barrier to cells and molecules, separating different tissue types and maintaining tissue specificity, and acting as transducer for various growth factors and enzymes [69]. Matrigel primarily consists of BME-derived components laminin, collagen IV, entactin, and heparin sulfate proteoglycan. These provide structural and signaling functions seen in the BME. Matrigel forms a hydrogel at 24–37°C and is frequently used 3D scaffold [70]. In 3D tumor cell culture it helps to create microenvironment for cancer 'stem-like' cells, influencing miRNA expression involved in cell regulation, adhesion and migration [71, 72]. Matrigel is also widely applied in morphological and developmental studies of non-malignant cell lines, such as breast and intestinal epithelia, with and without microfluidics [73]. The limitations of Matrigel are its composition (e.g. decreased content of collagen-I and hyaluronan), batch-to-batch variability and dependence on storage conditions. Thus, further research is directed towards hybrid matrices that can replace Matrigel [74].

Cellulose is the primary structural component of the cell wall in plants, algae, fungi, and bacteria. Its backbone consists of glucose units connected by β-glycosidic linkages and arranged into highly organized fibrillar structure. The extensive inter and intra-chain hydrogen bonding restricts flexibility and provides rigidity to the polymer. Cellulose possesses structural and functional similarity with collagen, the major ECM component of animal tissue, and can therefore mimic its features and functions such as hydrophilicity and rigidity. Nanocellulose refers to extracts or processed cellulose materials with nano-size dimensions, which can be divided into three groups according to their morphology and

method of production; cellulose nanocrystals (CNC), nanofibril cellulose (NFC) and bacterial cellulose (BC) [75]. NFCs are comprised of cellulose nanofibers derived from raw cellulose material via enzymatic hydrolysis and mechanical shearing processes [76]. NFC hydrogels have been utilized as 3D tissue culture scaffolds due to their rigid, porous and tunable structure, e.g. in research of human pluripotent stem cells (hPSC) [77] and liver progenitor cells [78]. Conveniently, cellulose-based scaffolds can be further degraded by cellulase treatment.

4.1.4 Future of 3D Tissue Models

Ensuring the reproducibility and physiological relevance of the different 3D models is of paramount importance. How close to the real tissue is the engineered model? How long can it survive in culture? How big can it grow and how fast? How well it can be transplanted or grafted? Different approaches, separately or in combination, can help to tackle these issues: microfluidics, bioprinting, high-resolution live cell imaging and 'smart' scaffold materials. While microfluidics can help model blood flow and shear stress experienced by cells, the bioprinting allows patterning (3D printing) of biological materials including cells, biomolecules and biomaterials to produce tissue-mimicking constructs. The technology has been already used in transplantation [79], printing of 3D heterogeneous hydrogel structures [80] for research in regenerative medicine [81, 82], and drug screening [83, 84]. However, printing requires prior knowledge of what to print. Indeed, the gradients of O_2, pH, metabolites and waste products experienced by cells have to be known or predictable, in order to re-create physiologically relevant tissue. Multi-parametric live cell imaging (two-photon excited, confocal, light-sheet and FLIM-PLIM microscopies) and other minimally invasive techniques have to be used for that. Imaging approaches can be ultimately integrated in the design of scaffolds and tissue models, in order to achieve the desired and controllable functional properties of engineered tissue, such as variability or morphology [65, 85, 86]. In the next part of review we will briefly introduce the reader to the quantitative multi-parametric imaging of 3D tissue models.

4.2 Live Cell Microscopy and Different Imaging Modalities

Traditionally, engineered cell and tissue samples are largely assessed by destructive methods such as histology or immunofluorescence of fixed and sectioned samples, tissue disintegration and flow cytometry, cell lysis and extraction of RNA, DNA, proteins, metabolites with subsequent assays: Western blotting, PCR, sequencing, microarrays, ELISA, immunohistochemistry, in situ hybridization, mass spectrometry and others. These methods usually assess cellular processes as end-point 'snapshots', without dynamic, real-time monitoring. In case of flow cytometry, western blotting, immunoenzyme- and other assays, measured parameters are averaged across large cell populations, thus compromising the relevance and level of detail of the results produced. Apart from global averaging and inability to study individual cells, dynamics and 3D gradients, significant errors and experimental artifacts are brought by the complex sample preparation procedures (e.g. lysis, fixation, optical clearing) [87].

Thankfully, several methods can provide live, real-time dynamic analysis of engineered tissue on a single cell scale: optical imaging, Raman spectroscopy, electron spin resonance, and micro-OCT [88]. Optical live cell imaging is a noninvasive study of cells in their natural environment using fluorescence based probes and sensors. Thus, fluorescent reporter (small molecule, nanoparticle or genetically encoded protein construct) can be targeted to a specific cell type or sub-cellular compartment, to inform on some useful biomarker, cellular function or local environment. Depending on the molecular structure of the chromophore its ancillary interaction with light can produce fluorescence, phosphorescence or inform on other processes [89]. Fig. 4.2 shows

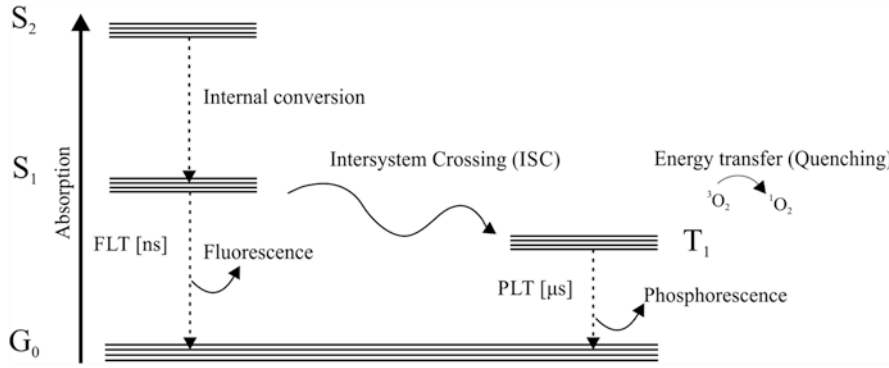

Fig. 4.2 Jablonski diagram. After absorption of a photon of light, luminescent molecule gets excited into high energy levels S_1, S_2. Fluorescent molecules return back to the ground state G_0, emitting light within ps-ns time interval. Some compounds transition to triplet state(s) via the process of intersystem crossing. Emission from T_1 is a forbidden process, which occurs at µs-ms scale. Transfer of energy to donors or quenchers (e.g. paramagnetic O_2 molecule) shortens the emission (phosphorescence lifetime, PLT)

Jablonski diagram of energy transitions in luminescent molecules and the processes of fluo- and phosphorescence.

The fluorescent reporter is illuminated with a quantum of light exciting a chromophore and bringing it to higher (excited) energy level. Chromophore can emit fluorescence (10^{-12}–10^{-9} s) and return to the ground (G_0) state. Due to dissipation of energy, emission occurs at a longer wavelength (Stokes shift). Some structures, phosphors, undergo energy transitions much slower and emit light after 10^{-8}–10^{-3} s (phosphorescence). The average time, which the chromophore spends in excited states before emitting light, is called fluorescence or phosphorescence lifetime. Specific brightness of a chromophore is determined by its molar absorptivity, quantum yield and photostability, which are mainly functions of its chemical structure. Chemical modifications, encapsulation in nanoparticles, protecting chemical or polypeptide structures can be used to improve brightness. Some dyes show sensitivity of their fluorescence or phosphorescence to protonation, interaction with other molecules (e.g. ions), quenchers (O_2), viscosity and temperature [90], which alter their emission intensity and lifetime. This can be used to design various probes and biosensors.

Fluorescence Stokes shift allows efficient separation of the emitted light from high-energy excitation, thus only detecting the fluorescent reporter of interest (intensity-based imaging). Fluorescence imaging can be realized using different instruments, including widefield and laser scanning confocal microscope (LSCM), two-photon excited microscope, macroscopic animal imager, super-resolution and other imaging devices.

4.2.1 Platforms for Intensity-Based Measurements

In *widefield* fluorescence microscope a parallel beam of light produced by single-wavelength light-emitting diodes (LEDs) or mercury lamps, illuminates and excites the selected fluorophore in the sample. The emitted wavelength of fluorescence light is selected with the appropriate optical filters. Widefield fluorescence microscopy can achieve quality resolution, contrast, sensitivity, and fast acquisition speeds. However, this mode is suitable only for relatively thin samples (up to 50 µm thick) and has limited applicability for imaging in 3D.

In *LSCM* a laser beam of excitation light passes through a pinhole aperture in the optical plane focusing the light on a specific region of the sample. The emitted light is channeled to light sensing detectors via pinhole aperture, rejecting the out of focus light and increasing spatial resolution. The excitation light from laser beam and its corre-

sponding detection point are scanned across the sample via dichroic mirrors and the image is constructed. The main limitation of LCSM is the limited light penetration depth across the sample (due to the light scattering and diffraction), achieving practically 100–200 µm. The longwave emitting dyes help improving the light penetration depth. Other approaches complement the LCSM, light-sheet microscopy [91] and two-photon excited laser-scanning microscopy (2PLSM) [92]. *Two photon-excited* fluorescence laser scanning microscopy (2PLSM) is a non-linear optical microscopy process developed for improved light penetration across thick biological samples [92]. The setup of 2PLSM is largely similar to the confocal microscope but in contrast it uses a laser with ultra-short pulse duration (10^{-15} s), and epi-detection pathway, wherein all the light collected by the objective is guided to the detector to capture as much of the scattered photons as possible [92]. 2PLSM utilizes fluorescence excitation by the process of 'two photon' absorption, in which two photons of near-infrared light simultaneously excite a fluorophore to achieve higher energy state, sufficient for fluo- or phosphorescence in visible range (shorter than excitation light) [93]. 2PLSM provides improved resolution with thicker samples (up to ~500 µm or more, depending on the sample), minimizes photobleaching and photodamage as the fluorescence excitation is limited to a narrow area of the sample [94]. 2PLSM does not improve spatial resolution compared to confocal [95] and can cause more substantial photodamage in thin samples [96].

A powerful solution to improve the light penetration depth and minimize the photodamage is to selectively illuminate a single focal plane and optically section the sample. One such modality that utilizes optical sectioning is *light sheet* fluorescence microscopy (LSFM). The principle of LSFM is that an illuminating sheet of light in X-Y plane is passed through the side of the sample, overlapping the focal plane, perpendicular to the excitation light. LSFM is carried out by selective plane illumination microscopy (SPIM) [97]. Due to only a thin plane of sample being exposed to light there is a reduction in scattered out of focus light improving resolution, while the photodamage is confined only to the thin illuminated section, and acquisition speeds are increased compared to single point scanning measurements [91]. A 3D image of the sample can be generated by passing the light sheet through the sample, forming image stacks [98]. LSFM has been used to image 3D cell culture samples, such as human mammary spheroids MCF10A (50–150 µm thick) expressing H2B-PAmCherry [99], microfluidic co-culture of human umbilical vein endothelial cells (HUVECs) with hepatocellular carcinoma cells (HepG2) [100] and others. LSFM reduces phototoxic damage and allows for long-term observations of thick 3D cell culture models with high spatial resolution. SPIM can be bought commercially (e.g. ZEISS Lightsheet Z.1) or can be built by the users themselves (OpenSPIM [101]) allowing them to tailor the setup to their requirements, such as combining it with FLIM and PLIM.

From the resolution point of view, a number of methods were proposed over the last decade to achieve imaging resolution below the diffraction limit; they are often collectively described as '*super-resolution microscopy*'. These methods include SIM, STORM, PALM and others [102]. Structured illumination microscopy (SIM) is based on fluorescence microcopy using conventional fluorophores, however it uses non-uniform illumination of light in form of a sinusoidal grid with images taken at three phase shifts for three different grid orientations. The final image is made up of nine images with resolution increased two fold of that of widefield fluorescence microscopy [103]. SIM can be applied in three dimensions (3D–SIM) to improve resolution by using three beams of interfering light, generating a pattern along the axial (Z) direction and the lateral (X and Y) directions [104]. 3D–SIM is also compatible with live cell imaging.

Stochastic optical reconstruction microscopy (STORM), is another super-resolution technique that produces a fluorescence image from the localization of specially designed organic fluorophores that are switched on and off using light of different colors in a series of imaging cycles. In each cycle only certain fluorophores are switched on allowing for the position of these to be determined with high accuracy, repeating the cycle

and constructing an overall image [105]. STORM was first demonstrated with Cy3-Cy5 pair of cyanine dyes [105] but since then have been optimized for other switchable fluorophores in direct STORM (dSTORM) [106].

Fluorescence Photoactivation Localization Microscopy (FPALM) uses light-inducible fluorophores to control the number of visible fluorophores by separating the optically active. The sample is illuminated with two different wavelengths, one for readout and other for photoactivation. The photoactivated fluorophores become active when illuminated, subsequently localized and inactivated after period via photobleaching. When this cycle is repeated for other photoactivated fluorophores present in sample, the image is constructed [107].

Stimulated emission depletion (STED) microscopy uses selective deactivation of fluorophores to create fluorescence image, thereby minimizing the area of illumination at the focal point, enhancing the resolution. STED utilizes a laser beam to excite the fluorophores. Once excited the fluorescence emission can be suppressed via stimulated emission using a depletion beam (STED beam), which suppresses the fluorophores back into the ground state. The excitation and STED beam are scanned across the sample forming a sub-diffraction image [108].

Traditionally designed for fixed tissue specimens prepared in special way, superresolution microscopy methods are becoming optimized for analysis of live and thick 3D samples, such as 3D tissue models. 2PLSM has been combined with STED to improve image resolution, achieving live imaging of neuronal morphology up to 30-μm deep in living brain tissue [109].

Measuring fluo- or phosphorescence intensity using above-mentioned instruments allows performing labeling, localization, tracking and semi-quantitative measurements in live cells and 3D tissue models. So-called ratiometric detection is based on the use of dyes or biosensors able to be excited or emitting in response to environmental parameter (e.g. O_2, pH, Ca^{2+} etc.) differently [110]. With the help of calibration, the ratiometric response allows performing quantitative measurements. However, reliance on different wavelengths has a negative side: normally ratiometric biosensors display spectrally well separated 'reference' and 'sensing' wavelengths; with thick and heterogeneous samples these will be absorbed and scattered by tissue differently, depending on the measurement depth. This means that ratiometric calibration will not be valid across the whole sample in 3D and questions the overall applicability of the approach. A number of other than intensity-based methods were proposed and measurements fluo- or phosphorescence lifetimes are among of the most advanced ones.

4.2.2 Measurement of Fluo- and Phosphorescence Lifetimes

Although known for decades, only in recent years the methods of fluorescence lifetime imaging microscopy (FLIM) and phosphorescence lifetime imaging microscopy (PLIM) are becoming popular. FLIM and PLIM scanners can be implemented on most of 'traditional' microscopy platforms including LSCM, widefield microscopy, 2PLSM, superresolution and light-sheet microscopy. FLIM and PLIM expand the use of available tracers, which can be distinguished not only by the spectral properties but also by the luminescence lifetime [111] and provide quantitative readouts for pH, ions, O_2 and other parameters.

The key advantage of fluorescence *lifetime* imaging over fluorescence *intensity* imaging is that it is an intrinsic property of a fluorophore, independent upon the method of measurement. Therefore, results are largely independent from fluorophore concentration and imaging is not affected by light scattering, photobleaching, and variations in excitation light [90]. The fluorescence lifetime of the fluorophore depends on its energetically unstable state, making it susceptible to quenching via differences in polarity [112], pH, temperature [24], ion concentration, protein interactions and other factors. The shortening of lifetime via quenching-induced conformational changes provides information on the molecular environment of the fluorophore, and allows quantitative differentiation between populations of quenched and unquenched fluorophores, in

form of simplified calibration relationships [90]. PLIM shows a number of similar applications, largely including measurement of O_2 and temperature [113, 114]. The limitation of PLIM is that it is a slower process than FLIM, however, PLIM provides the possibility of time-gated detection, allowing to effectively filter out the sample background autofluorescence, which is indispensable in analysis of some tissue types, e.g. gastrointestinal tract.

A number of experimental approaches were developed for FLIM and PLIM, including frequency and time domain-based readout, with variations such as time-correlated single photon counting (TCSPC) using fast-gated image intensifiers [115, 116] (Chaps. 2 and 3). In TCSPC the luminescent molecules are excited by a pulsed laser source with a high repetition rate. Photons emitted by the sample are detected and the time with respect to the excitation pulse is measured, constructing a decay curve. This method provides high detection sensitivity, accurate lifetime measurements and, when combined with LSCM and 2PLSM, it allows optical sectioning of the sample. TCSPC is also compatible with PLIM, allowing fast (1 min or shorter) acquisition times. FLIM and PLIM are also highly compatible with live cell imaging: the lasers employed in this approach are not constantly illuminating the sample; instead they do it via combination of very short (typically in 10^{-12} s range) pulses. This ensures much lower degree of sample photodamage than in conventional widefield or laser-scanning microscopies. Systems such as TCSPC also rely on highly efficient photon counting detectors, allowing using lower laser power intensities. These are the main advantages of the methodology, making it highly suitable for analysis of 3D tissue models.

4.3 Probes for Live Cell Multi-Parametric Imaging of 3D Tissue Models

Imaging of 3D cell and tissue cultures requires high depth penetration of light, fast imaging speed, and use of mild (non-destructive) intensity of excitation light. High depth penetration of light is needed to image the thick 3D samples avoiding light scattering reducing the resolution of the image. The depth penetration of light depends on two factors: (1) the ability to image the fluorophore or phosphor (via microscopy techniques and its physical properties such as spectra) and (2) actual presence of the probe distributed within the sample, ideally in homogeneous manner. Fast image acquisition speed and low intensity of excitation light are needed to prevent and limit photobleaching and phototoxicity, leading to loss of luminophore function and toxic effects on live samples. Photobleaching and phototoxicity occur due to energy emitted by excited luminophores not always being in the form of fluorescence or phosphorescence. The dissipated energy can cause the reaction with O_2, producing reactive oxygen species (ROS). The quenching of phosphorescence also produces singlet oxygen – this process is however causes minimal sample damage with modern O_2 probes [114].

The probes and fluorescent tracers needed for multi-parametric imaging of 3D tissue models can be adapted from traditional intensity-based measurements and from advanced FLIM and PLIM applications. Virtually everything is compatible with 3D tissue models, but practical challenge is the ability to efficiently stain the 3D tissue model in reasonably short period of time (few hours or less): the small molecules, nanoparticles can display very poor distribution across the sample or stain only particular cell types; most nanoparticles also poorly stain formed 3D tissue models. The use of genetically encoded biosensors is mainly limited to use of transgenic models and is challenging for transient transfection (lipofection or electroporation). Multi-parametric analysis can be also complemented by classical immunofluorescence (e.g. post-analysis): however, antibodies are bulky molecules demanding either prolonged staining protocols or laborious sectioning of the samples. In addition, the use of intensity-based probes and biosensors should take into account their actual distribution and varied intensity across the sample.

The development of luminescence lifetime probes can be targeted to solve the challenges involved in live cell imaging of 3D tissue models.

Lifetime imaging is independent of fluorophore concentration and is therefore unaffected by light scattering, in relation to sample thickness and phototoxicity [90]. While reader can refer to the reviews covering these areas (e.g. by Blacker and Duchen [117], Lukyanov on fluorescent proteins [118, 119], Achilefu and Berezin on FLIM [90, 120] and Wolfbeis on nanoparticles [121]), below we will highlight the usability of some probes for multi-parametric imaging of 3D tissue models (Table 4.1).

Endogenous fluorophores are fluorescent biomolecules present already within a sample and contributing to the cell and tissue autofluorescence (normally caused by aromatic amino acids, reduced nicotinamide adenine dinucleotide (NADH) and Flavin adenine dinucleotide (FAD)). FLIM of endogenous fluorophores and their expression profiles provides information on the metabolic and functional state of the sample, which can be used to differentiate healthy tissue from diseased. The main advantage of endogenous fluorophores is that no specific labeling is required. However, the fluorescence signals are often weak and non-specific due to limitations in light penetration and low expression of the fluorophores; their interaction with cellular components and proteins is also very complex, resulting in multi-exponential decays and uneasy interpretation of measured fluorescence lifetimes. Due to short excitation wavelengths (near-UV for NADH), normally two-photon excited imaging has to be employed. In comparison to *state-of-the-art* approaches to analyze the balance of cell energy production pathways [148, 149], metabolic imaging with NAD(P)H does not provide direct information on OxPhos, glycolysis and Krebs cycle fluxes and thus can be viewed as supplementary parameter in analysis of cell metabolism.

Exogenous fluorophores and phosphors address such limitations of endogenous fluorophores as signal weakness and low specificity. They have a large diversity in wavelength and lifetime range, and in the way they are produced (proteins, bioconjugates, nanoparticles etc.). The luminescence lifetime of fluorophores is frequently sensitive to changes in their microenvironment, including self-aggregation, interaction with lipids, proteins, their molecular rotation etc. Thus, the responsive FLIM probes can be designed that changes in their luminescent lifetimes will be a function of their environment and allowing measurement of quantitative responses to broad range of analytes. The main directions in design of FLIM and PLIM probes are: (1) optimization of their sensing properties (spectral properties, brightness, photostability, specificity and the maximal response to the measured parameter), to achieve reliable calibration; (2) design of optimal delivery features such as cell permeability, and intracellular or tissue localization. Indeed, the probe should minimally interfere with cell physiology or particular process it is helping to analyze: for example, probe directed for analysis of O_2 should have no effects on oxygen consumption rate (cell mitochondrial function) and energy production pathways. Probes are frequently present in form of simple dyes, small molecule conjugates, fluorescent proteins, supramolecular conjugates or nanoparticles. From this list, nanoparticles often display the best overall sensing features, including reliable calibration. However, their bio-delivery often represents a complicated task. In contrast, small molecule dyes can stain 3D tissue model very easily but their calibration frequently is strongly concentration-dependent, due to often-unpredictable behavior inside the cells and presence of multiple heterogeneous cell layers in 3D tissue model. More complex is the interaction between the probe and the environment, the more complicated the interpretation of FLIM/PLIM data will be.

Similarly to probes, *solid-state sensing materials* can be used for multi-parametric imaging of 3D tissue models: in this case, the sensing dye is used for modification of 3D scaffold in which the cells or tissue are cultured. For example, hybrid phosphorescent O_2-sensing scaffolds were proposed for range of cell-based models, including tumor spheroids and brain slices [65]. In this case, cells and tissue do not need to be stained and their functional status is analyzed indirectly, via analysis of extra- and pericellular O_2 gradients and hypoxia. Similarly, the scaffolds based on other

Table 4.1 Probes and biosensors with useful properties for multi-parametric quantitative imaging of 3D tissue models

Measured parameter	Description of probe(s)	Spectral properties, FLIM/PLIM-compatible (?)	3D tissue models tested. Comments. References
Autofluorescence 'metabolic' imaging	Endogenous NAD(P)H, FAD	340 nm exc. (700–740 nm two-photon)/ 460 nm em. FLIM (1–6 ns) FAD: 450 nm exc./520 nm em	Tumor spheroids and 'organoids' [122–124]
Cytosolic NADH-NAD^+ ratio	Genetically encoded biosensor Peredox	488 nm exc. (800 nm two-photon)/ 525 nm em. FLIM (1.87–2.6 ns)	Needs transfection. More selective and brighter than autofluorescence imaging. Tested on live brain slices (*ex vivo*) [125]
Redox/ROS	Genetically encoded reduction-oxidation-sensitive green fluorescent protein 1 (roGFP1)	488 nm exc. (740–950 nm two-photon)/ 525 nm em. Ratiometric, FLIM (2.46 ns)	Needs transfection. Moderate responses in fluorescence lifetime (but better in ratiometric intensity mode) to changes in redox ratio. Tested on live brain slices (ex vivo) [126]
Molecular oxygen (O_2)	Nanoparticles: PA2, NanO2/MM2, SI/SII	405 nm exc. (740–780 nm two-photon)/ 650–660 nm em. PLIM (20–70 µs) SII-series: 470 and 632 nm exc./770 nm em. PLIM (10–40 µs)	Neurospheres, brain slices, tumor spheroids. Most bright, photostable and reliable calibration but typically need 'continuous staining' procedure [23, 127]
Molecular oxygen (O_2)	Small molecule probes Pt-Glc, Pt-Gal	One-photon excited, 405 nm exc./650 nm em. PLIM (20–57 µs)	Tested in neurospheres, brain slices, tumor spheroids, *ex vivo* colon, bladder and intestinal tissues. Pt-Glc displays some tissue-specificity in calibration. More efficient tissue staining than with nanoparticles [128–134]
Molecular oxygen (O_2)	Porous polymer-based O_2-sensitive scaffolds for 3D culture	405, 540 nm exc./650 nm em. PLIM (20–55 µs)	Tested with tumor spheroids (HCT116, PC12) and live brain slices. Allow monitoring of pericellular O_2 in 3D culture grown within polymer scaffold [65, 135]
Intracellular temperature	Nanoparticles	546 nm exc./585 nm em. FLIM (2.4–2.7 ns)	Tumor spheroids [24]
pH	Genetically encoded fluorescent proteins	pHRed: 440 nm exc. (860 nm two-photon)/ 610 nm em. FLIM (1.7–2.1 ns) ECFP: 440 nm exc./512 nm em.) FLIM (1.8–2.8 ns)	Need transfection. Not tested with 3D tissue models. Some are visible only under two-photon excitation [136, 137]
pH	Nanoparticles	546 nm exc./600 nm em. FLIM (3.7–4.7 ns)	Tested with rat primary neurospheres. Localize in lysosomes [138]
pH	BCECF and other small molecule dyes	Green-red fluorescence. FLIM	Concentration and cell-type dependent responses, low photostability [138]. Tested with cockroach salivary duct tissue [139]
Ca^{2+}	Small molecule probes Oregon Green BAPTA-1 (OGB-1) and others	OGB-1: 488 nm exc./510 nm em. FLIM (0.6–3.9 ns)	Live brain slices [140–142]
Ca^{2+}	Genetically encoded biosensor Cerulean	432 nm exc./530 nm em. FLIM (0.8–2.4 ns)	Needs transfection or transgenic animals. Live brain slices. Preferred use in two-photon excited mode [143, 144]
Lactate/ glycolysis	Genetically encoded ratiometric sensors	430 nm exc./485 and 535 nm em. (ratiometric) Not tested in FLIM	Needs transfection. Live brain slices [145, 146]
Labeling of proliferating cells	Cell-permeable dye (Hoechst 33342) quenched by BrdU	405 nm exc./440 nm em. FLIM (1.3–2.2 ns)	Tumor spheroids and intestinal organoids. Needs comparison between BrdU (+/−) cells in the experimental model. Can be adapted to other dyes staining nuclei [37]
Viscosity	Small molecule probes (BODIPY-based rotors)	488 nm exc. (800 nm two-photon)/515 nm em. FLIM (1–3 ns)	Tumor spheroids. Concentration-dependent calibration complicates data interpretation for 3D tissue models [147]

materials and for analysis of other physiologically important biomolecules (e.g. pH) can be realized.

pH gradients play important roles in cellular processes such as proliferation, senescence, and apoptosis, endo- and exocytosis (secretory pathway), intracellular transport, contraction of muscle cells, and regulation of ion influxes. pH is tightly regulated within mammalian cells and their organelles all requiring different pH for their respective functions. For instance, in the cytosol pH values around seven are needed for the proper function of organelles, acidic pH of 4–5 in lysosomes for degradation of proteins, and alkaline pH of 7.5–8.0 in mitochondria for oxidative phosphorylation. Pathologic conditions can alter significantly intra- and extracellular pH via perturbing effects on ion homeostasis. pH is an important biomarker for disease states, such as cancer and neurological disorders. Changes in intracellular pH can be measured via number of dyes (BCECF), fluorescent proteins and nanoparticles. While FLIM is the preferred readout, there are only a few suitable probes (nanoparticles and fluorescent proteins) with good (few ns) lifetime range over physiological pH (Table 4.1).

A number of genetically encoded fluorescent proteins were described for imaging of metabolism (Peredox for NADH-NAD^+ ratio, pyruvate, lactate, ATP), reactive oxygen species and overall redox potential (HyPer1, HyPer3, TriPer, roGFP1), pH, Ca^{2+} and other parameters. While some of these proteins suffer from low magnitude of response in FLIM or cross-sensitivity with pH and need in transfection (or need in use of transgenic animals), not always compatible with experimental needs, they are often very bright, selective and performing better than autofluorescence imaging and traditional small molecule probes. Some promising candidates are listed in Table 4.1.

While the specific, sensitive and quantitative determination of reactive oxygen species (ROS) is still hardly possible [150], detection of molecular oxygen (O_2) is well-developed area [114]. Last decade of research on intracellular phosphorescent probes and sensors helped to develop comprehensive panel of small molecule (efficient tissue staining), nanoparticle (most reliable calibration, brightness and broad compatibility across detection platforms) and solid-state sensors and probes. The phosphorescent O_2 probes often display mono-exponential decay, large Stokes shift and μs-range of phosphorescence lifetimes, making them compatible with multiplexing with virtually any other biosensors and thus are often superior to FLIM-based probes to other analytes. O_2 probes help in studies of hypoxia-dependent cell responses, direct analysis of mitochondrial function, cell and tissue viability, intra- and pericellular gradients and become more and more popular with 3D tissue models – spheroids, aggregates, *ex vivo* tissues and organoids. A number of tested probes and sensor materials is listed in Table 4.1, some of them were already demonstrated in multi-parametric imaging of O_2 [24, 37, 65, 127, 132, 151, 152]. The example of protocol of use of O_2 probe in multi-parametric imaging of intestinal organoids is presented in Chap. 6.

Cellular and tissue temperatures are tightly regulated via adaptive thermogenesis pathways within a narrow temperature range [153–155]. Temperature affects such important processes as biomolecule diffusion, energy production in mitochondria and enzyme function. Elevated temperatures activate heat shock pathway. Temperature regulation is also important in the imaging and treatments of diseases [156], such as cancer [157], and is therefore can represent a useful biomarker. Similarly, the viscosity of cytoplasm and other intracellular organelles can be an important factor in drug diffusion, especially in 3D. Viscosity can be measured by fluorescent probes called molecular rotors, also sensitive in fluorescence lifetime domain. A number of fluorescent T-sensitive and viscosity probes for intracellular measurements were designed but only few of them were tested with 3D tissue models (Table 4.1).

The introduction of FLIM and PLIM to multiparametric imaging area prompts new applications and probes. Thus, our group discovered that the process of BrdU-dependent fluorescence quenching of nuclear-labeling dye, Hoechst 33342, reveals strong response in fluorescence lifetime and thus can be employed for labeling of proliferating cells in live culture [37]. The degree of quenching can depend on the cell type and staining

conditions (conc. of BrdU and Hoechst, incubation time) and has to be evaluated with every new biological model. Once it is done, it can be applied for study of drug-induced effects on the duration of cell cycle, identification and discrimination of proliferating cells in complex tissue models. Hoechst dye is two-photon excitable and similar type of quenching effects can be observed for other nuclear stains, e.g. SiR-Hoechst [158].

FLIM-FRET with various pairs of fluorescent proteins is another application area, facilitating the analysis of 3D tissue models at new quantitative level, e.g. in studies of signaling pathways (CaMKII and RhoA) on live brain slices [159], activation of apoptosis in tumor spheroids [160] and cancer cell invasion *in vitro* and *in vivo* models [161].

However, the growing toolkit of biosensors and analytical methods allowing quantitative multi-parametric imaging also needs development of advanced cell-specific labeling agents. In order to obtain maximally useful information on e.g. pH or O_2 gradients within the tissue, the cell-specific fluorescent stains allowing identifying morphology and particular 'niche regions' within the sample are needed. This is possible by a number of approaches: (1) novel genome editing methods such as CRISPR-Cas9 [162] allowing easier production of transgenic cell lines, expressing fluorescent proteins tags; (2) a number of live cell dyes displays cell-specific staining (both in intensity or lifetime domains), however this list is rather limited and relatively unstudied; (3) some tissues display characteristic autofluorescence 'signature', e.g. lumen area of small intestinal organoids with unusual long-living red autofluorescence; (4) after the imaging, the sample still can be fixed, immunostained and probed with antibodies. Depending on the approach, a number of issues have to be addressed with the existing cell-specific labeling agents: in general, the use of brighter and photostable dyes and biomolecules is encouraged. Improving the algorithms of data acquisition and analysis on the microscope, when the multi-parametric analysis is being performed is also important area of technical development [163]. This is especially important for fast 3D scanning algorithms and reconstructions of imaging data, as the 3D tissue models rarely represent ideal and immobile flat geometrical shapes.

4.4 Conclusion

The brief overview of existing 3D tissue models, imaging modalities and the biosensor toolkit summarizes the opportunity for performing multi-parametric imaging of live 3D tissue models: a huge number of imaging platforms can and has to be used, in advanced tissue engineering, allowing unprecedented level of cell-cell, biomarker and metabolite heterogeneity to be monitored. Proof-of-concept research works demonstrate how such approach can be used in optimizing the viability, cell-cell heterogeneity, creating stem and cancer cell niche regions, helping to perform actual control of microscopic (in contrast to macroscopic external control of flow rate or conditions in the incubator) changes in cell status within 3D tissue model. This interdisciplinary research approaches its critical mass, which should catalyze the further development of methodology and its widespread use. A great number of improvements over existing problems in all three constituting areas (design of 3D tissue model, imaging instrumentation and biosensors) have to be implemented. The described methodology of multi-parametric imaging opens an exciting opportunity and new horizons in research and application sides of 3D tissue models and we expect significant discoveries in relevant life science areas in the coming years.

Acknowledgments This work was supported by Science Foundation Ireland (SFI) grant 13/SIRG/2144. We thank Prof. D. Papkovsky for useful comments on the manuscript.

References

1. Kleinman HK, Philp D, Hoffman MP (2003) Role of the extracellular matrix in morphogenesis. Curr Opin Biotechnol 14:526–532
2. Neelam S, Hayes PR, Zhang Q, Dickinson RB, Lele TP (2016) Vertical uniformity of cells and nuclei in epithelial monolayers. Sci Rep 6:19689
3. Fennema E, Rivron N, Rouwkema J, van Blitterswijk C, de Boer J (2013) Spheroid culture as a tool for

creating 3D complex tissues. Trends Biotechnol 31:108–115
4. Fatehullah A, Tan SH, Barker N (2016) Organoids as an in vitro model of human development and disease. Nat Cell Biol 18:246–254
5. Yamada KM, Cukierman E (2007) Modeling tissue morphogenesis and cancer in 3D. Cell 130:601–610
6. Lozano E, Segarra M, García-Martínez A, Hernández-Rodríguez J, Cid MC (2008) Imatinib mesylate inhibits in vitro and ex vivo biological responses related to vascular occlusion in giant cell arteritis. Ann Rheum Dis 67:1581–1588
7. Arslan-Yildiz A, El Assal R, Chen P, Guven S, Inci F, Demirci U (2016) Towards artificial tissue models: past, present, and future of 3D bioprinting. Biofabrication 8:1758–5090
8. Marangoni E, Vincent-Salomon A, Auger N, Degeorges A, Assayag F, de Cremoux P et al (2007) A new model of patient tumor-derived breast cancer xenografts for preclinical assays. Clin Cancer Res 13:3989–3998
9. Costa EC, Gaspar VM, Coutinho P, Correia IJ (2014) Optimization of liquid overlay technique to formulate heterogenic 3D co-cultures models. Biotechnol Bioeng 111:1672–1685
10. Foty R (2011) A simple hanging drop cell culture protocol for generation of 3D spheroids. J Vis Exp 51:2720
11. Markovitz-Bishitz Y, Tauber Y, Afrimzon E, Zurgil N, Sobolev M, Shafran Y et al (2010) A polymer microstructure array for the formation, culturing, and high throughput drug screening of breast cancer spheroids. Biomaterials 31:8436–8444
12. Kenny PA, Lee GY, Myers CA, Neve RM, Semeiks JR, Spellman PT et al (2007) The morphologies of breast cancer cell lines in three-dimensional assays correlate with their profiles of gene expression. Mol Oncol 1:84–96
13. Luca AC, Mersch S, Deenen R, Schmidt S, Messner I, Schäfer K-L et al (2013) Impact of the 3D microenvironment on phenotype, gene expression, and EGFR inhibition of colorectal cancer cell lines. PLoS One 8:e59689
14. Härmä V, Virtanen J, Mäkelä R, Happonen A, Mpindi J-P, Knuuttila M et al (2010) A comprehensive panel of three-dimensional models for studies of prostate cancer growth, invasion and drug responses. PLoS One 5:e10431
15. Laurent J, Frongia C, Cazales M, Mondesert O, Ducommun B, Lobjois V (2013) Multicellular tumor spheroid models to explore cell cycle checkpoints in 3D. BMC Cancer 13:73
16. Hirschhaeuser F, Menne H, Dittfeld C, West J, Mueller-Klieser W, Kunz-Schughart LA (2010) Multicellular tumor spheroids: an underestimated tool is catching up again. J Biotechnol 148:3–15
17. Liao J, Qian F, Tchabo N, Mhawech-Fauceglia P, Beck A, Qian Z et al (2014) Ovarian cancer spheroid cells with stem cell-like properties contribute to tumor generation, and chemotherapy resistance through hypoxia-resistant metabolism. PLoS One 9:e84941
18. Longati P, Jia X, Eimer J, Wagman A, Witt M-R, Rehnmark S et al (2013) 3D pancreatic carcinoma spheroids induce a matrix-rich, chemoresistant phenotype offering a better model for drug testing. BMC Cancer 13:95
19. Herrmann D, Conway JRW, Vennin C, Magenau A, Hughes WE, Morton JP et al (2014) Three-dimensional cancer models mimic cell–matrix interactions in the tumour microenvironment. Carcinogenesis 35:1671–1679
20. Dolznig H, Rupp C, Puri C, Haslinger C, Schweifer N, Wieser E et al (2011) Modeling colon adenocarcinomas in vitro a 3D co-culture system induces cancer-relevant pathways upon tumor cell and stromal fibroblast interaction. Am J Pathol 179:487–501
21. Bingle L, Lewis CE, Corke KP, Reed MWR, Brown NJ (2006) Macrophages promote angiogenesis in human breast tumour spheroids in vivo. Br J Cancer 94:101–107
22. Pampaloni F, Ansari N, Stelzer EHK (2013) High-resolution deep imaging of live cellular spheroids with light-sheet-based fluorescence microscopy. Cell Tissue Res 352:161–177
23. Dmitriev RI, Borisov SM, Düssmann H, Sun S, Müller BJ, Prehn J et al (2015) Versatile conjugated polymer nanoparticles for high-resolution O2 imaging in cells and 3D tissue models. ACS Nano 9:5275–5288
24. Jenkins J, Borisov SM, Papkovsky DB, Dmitriev RI (2016) Sulforhodamine nanothermometer for multiparametric fluorescence lifetime imaging microscopy. Anal Chem 88:10566–10572
25. König K, Uchugonova A, Gorjup E (2011) Multiphoton fluorescence lifetime imaging of 3D-stem cell spheroids during differentiation. Microsc Res Tech 74:9–17
26. Lancaster MA, Knoblich JA (2014) Organogenesis in a dish: modeling development and disease using organoid technologies. Science 345:1247125
27. Fujii M, Matano M, Nanki K, Sato T (2015) Efficient genetic engineering of human intestinal organoids using electroporation. Nat Protoc 10:1474–1485
28. Takasato M, Er PX, Chiu HS, Maier B, Baillie GJ, Ferguson C et al (2015) Kidney organoids from human iPS cells contain multiple lineages and model human nephrogenesis. Nature 526:564–568
29. Lancaster MA, Renner M, Martin C-A, Wenzel D, Bicknell LS, Hurles ME et al (2013) Cerebral organoids model human brain development and microcephaly. Nature 501:373–379
30. Völkner M, Zschätzsch M, Rostovskaya M, Overall Rupert W, Busskamp V, Anastassiadis K et al (2016) Retinal organoids from pluripotent stem cells efficiently recapitulate retinogenesis. Stem Cell Rep 6:525–538
31. McCracken KW, Cata EM, Crawford CM, Sinagoga KL, Schumacher M, Rockich BE et al (2014) Modelling human development and disease in

pluripotent stem-cell-derived gastric organoids. Nature 516:400–404
32. Dye BR, Hill DR, Ferguson MAH, Tsai Y-H, Nagy MS, Dyal R et al (2015) In vitro generation of human pluripotent stem cell derived lung organoids. elife 4:e05098
33. Guye P, Ebrahimkhani MR, Kipniss N, Velazquez JJ, Schoenfeld E, Kiani S et al (2016) Genetically engineering self-organization of human pluripotent stem cells into a liver bud-like tissue using Gata6. Nat Commun 7:10243
34. Moreno EL, Hachi S, Hemmer K, Trietsch SJ, Baumuratov AS, Hankemeier T et al (2015) Differentiation of neuroepithelial stem cells into functional dopaminergic neurons in 3D microfluidic cell culture. Lab Chip 15:2419–2428
35. Khademhosseini A, Eng G, Yeh J, Kucharczyk PA, Langer R, Vunjak-Novakovic G et al (2007) Microfluidic patterning for fabrication of contractile cardiac organoids. Biomed Microdevices 9:149–157
36. Drost J, van Jaarsveld RH, Ponsioen B, Zimberlin C, van Boxtel R, Buijs A et al (2015) Sequential cancer mutations in cultured human intestinal stem cells. Nature 521:43–47
37. Okkelman IA, Dmitriev RI, Foley T, Papkovsky DB (2016) Use of fluorescence lifetime imaging microscopy (FLIM) as a timer of cell cycle S phase. PLoS One 11:e0167385
38. Walsh AJ, Cook RS, Sanders ME, Aurisicchio L, Ciliberto G, Arteaga CL et al (2014) Quantitative optical imaging of primary tumor organoid metabolism predicts drug response in breast cancer. Cancer Res 74:5184–5194
39. van Duinen V, Trietsch SJ, Joore J, Vulto P, Hankemeier T (2015) Microfluidic 3D cell culture: from tools to tissue models. Curr Opin Biotechnol 35:118–126
40. Bhatia SN, Ingber DE (2014) Microfluidic organs-on-chips. Nat Biotechnol 32:760–772
41. Anderson JR, Chiu DT, Wu H, Schueller O, Whitesides GM (2000) Fabrication of microfluidic systems in poly (dimethylsiloxane). Electrophoresis 21:27–40
42. Hsiao AY, Y-S T, Tung Y-C, Sud S, Taichman RS, Pienta KJ et al (2009) Microfluidic system for formation of PC-3 prostate cancer co-culture spheroids. Biomaterials 30:3020–3027
43. Bhise NS, Manoharan V, Massa S, Tamayol A, Ghaderi M, Miscuglio M et al (2016) A liver-on-a-chip platform with bioprinted hepatic spheroids. Biofabrication 8:1758–5090
44. Au SH, Chamberlain MD, Mahesh S, Sefton MV, Wheeler AR (2014) Hepatic organoids for microfluidic drug screening. Lab Chip 14:3290–3299
45. Kim HJ, Ingber DE (2013) Gut-on-a-Chip microenvironment induces human intestinal cells to undergo villus differentiation. Integr Biol 5:1130–1140
46. Kim HJ, Huh D, Hamilton G, Ingber DE (2012) Human gut-on-a-chip inhabited by microbial flora that experiences intestinal peristalsis-like motions and flow. Lab Chip 12:2165–2174
47. Benam KH, Villenave R, Lucchesi C, Varone A, Hubeau C, Lee H-H et al (2016) Small airway-on-a-chip enables analysis of human lung inflammation and drug responses in vitro. Nat Methods 13:151–157
48. Huh D, Matthews BD, Mammoto A, Montoya-Zavala M, Hsin HY, Ingber DE (2010) Reconstituting organ-level lung functions on a chip. Science 328:1662–1668
49. Grosberg A, Alford PW, McCain ML, Parker KK (2011) Ensembles of engineered cardiac tissues for physiological and pharmacological study: heart on a chip. Lab Chip 11:4165–4173
50. Agarwal A, Goss JA, Cho A, McCain ML, Parker KK (2013) Microfluidic heart on a chip for higher throughput pharmacological studies. Lab Chip 13:3599–3608
51. Nieskens TT, Wilmer MJ (2016) Kidney-on-a-chip technology for renal proximal tubule tissue reconstruction. Eur J Pharmacol 790:46–56
52. Wilmer MJ, Ng CP, Lanz HL, Vulto P, Suter-Dick L, Masereeuw R (2016) Kidney-on-a-chip technology for drug-induced nephrotoxicity screening. Trends Biotechnol 34:156–170
53. Young EWK, Watson MWL, Srigunapalan S, Wheeler AR, Simmons CA (2010) Technique for real-time measurements of endothelial permeability in a microfluidic membrane chip using laser-induced fluorescence detection. Anal Chem 82:808–816
54. Ryu H, Oh S, Lee HJ, Lee JY, Lee HK, Jeon NL (2015) Engineering a blood vessel network module for body-on-a-chip applications. J Lab Autom 20:296–301
55. Kim S, Lee H, Chung M, Jeon NL (2013) Engineering of functional, perfusable 3D microvascular networks on a chip. Lab Chip 13:1489–1500
56. van der Helm MW, van der Meer AD, Eijkel JCT, van den Berg A, Segerink LI (2016) Microfluidic organ-on-chip technology for blood-brain barrier research. Tissue Barriers 4:e1142493
57. Benam KH, Dauth S, Hassell B, Herland A, Jain A, Jang K-J et al (2015) Engineered in vitro disease models. Annu Rev Pathol 10:195–262
58. Esch EW, Bahinski A, Huh D (2015) Organs-on-chips at the frontiers of drug discovery. Nat Rev Drug Discov 14:248–260
59. Kondrashina AV, Papkovsky DB, Dmitriev RI (2013) Measurement of cell respiration and oxygenation in standard multichannel biochips using phosphorescent O2-sensitive probes. Analyst 138:4915–4921
60. Wikswo JP, Block FE III, Cliffel DE, Goodwin CR, Marasco CC, Markov DA et al (2013) Engineering challenges for instrumenting and controlling integrated organ-on-chip systems. IEEE Trans Biomed Eng 60:682–690
61. Tibbitt MW, Anseth KS (2009) Hydrogels as extracellular matrix mimics for 3D cell culture. Biotechnol Bioeng 103:655–663
62. Gulrez SKH, Al-Assaf S (2011) Hydrogels: methods of preparation, characterisation and applications. Intech, Rijeka

63. Meadhbh ÁB, Audrey R, Anne-laure G, Cyril DA, Steven N, Valerie T et al (2015) 3D cell culture and osteogenic differentiation of human bone marrow stromal cells plated onto jet-sprayed or electrospun micro-fiber scaffolds. Biomed Mater 10:045019
64. Danilevicius P, Georgiadi L, Pateman CJ, Claeyssens F, Chatzinikolaidou M, Farsari M (2015) The effect of porosity on cell ingrowth into accurately defined, laser-made, polylactide-based 3D scaffolds. Appl Surf Sci 336:2–10
65. Jenkins J, Dmitriev RI, Morten K, McDermott KW, Papkovsky DB (2015) Oxygen-sensing scaffolds for 3-dimensional cell and tissue culture. Acta Biomater 16:126–135
66. Place ES, George JH, Williams CK, Stevens MM (2009) Synthetic polymer scaffolds for tissue engineering. Chem Soc Rev 38:1139–1151
67. Shoulders MD, Raines RT (2009) Collagen structure and stability. Annu Rev Biochem 78:929–958
68. Artym VV, Matsumoto K (2010) Imaging cells in three-dimensional collagen matrix. Curr Protocol Cell Biol. Chapter:Unit-10.18:1–20
69. Yurchenco PD (2011) Basement membranes: cell scaffoldings and signaling platforms. Cold Spring Harb Perspect Biol 3. https://doi.org/10.1101/cshperspect.a004911
70. Kleinman HK, Martin GR (2005) Matrigel: basement membrane matrix with biological activity. Semin Cancer Biol 15:378–386
71. Benton G, Kleinman HK, George J, Arnaoutova I (2011) Multiple uses of basement membrane-like matrix (BME/Matrigel) in vitro and in vivo with cancer cells. Int J Cancer 128:1751–1757
72. Price KJ, Tsykin A, Giles KM, Sladic RT, Epis MR, Ganss R et al (2012) Matrigel basement membrane matrix influences expression of microRNAs in cancer cell lines. Biochem Biophys Res Commun 427:343–348
73. Dolega ME, Abeille F, Picollet-D'hahan N, Gidrol X (2015) Controlled 3D culture in Matrigel microbeads to analyze clonal acinar development. Biomaterials 52:347–357
74. Nyga A, Cheema U, Loizidou M (2011) 3D tumour models: novel in vitro approaches to cancer studies. J Cell Commun Signal 5:239
75. Abitbol T, Rivkin A, Cao Y, Nevo Y, Abraham E, Ben-Shalom T et al (2016) Nanocellulose, a tiny fiber with huge applications. Curr Opin Biotechnol 39:76–88
76. Pääkkö M, Ankerfors M, Kosonen H, Nykänen A, Ahola S, Österberg M et al (2007) Enzymatic hydrolysis combined with mechanical shearing and high-pressure homogenization for nanoscale cellulose fibrils and strong gels. Biomacromolecules 8:1934–1941
77. Lou YR, Kanninen L, Kuisma T, Niklander J, Noon LA, Burks D et al (2014) The use of nanofibrillar cellulose hydrogel as a flexible three-dimensional model to culture human pluripotent stem cells. Stem Cells Dev 23:380–392
78. Malinen MM, Kanninen LK, Corlu A, Isoniemi HM, Lou Y-R, Yliperttula ML et al (2014) Differentiation of liver progenitor cell line to functional organotypic cultures in 3D nanofibrillar cellulose and hyaluronan-gelatin hydrogels. Biomaterials 35:5110–5121
79. Murphy SV, Atala A (2014) 3D bioprinting of tissues and organs. Nat Biotechnol 32:773–785
80. Nadernezhad A, Khani N, Skvortsov GA, Toprakhisar B, Bakirci E, Menceloglu Y et al (2016) Multifunctional 3D printing of heterogeneous hydrogel structures. Sci Rep 6
81. Lee VK, Lanzi AM, Haygan N, Yoo S-S, Vincent PA, Dai G (2014) Generation of multi-scale vascular network system within 3D hydrogel using 3D bioprinting technology. Cell Mol Bioeng 7:460–472
82. Jung JW, Lee J-S, Cho D-W (2016) Computer-aided multiple-head 3D printing system for printing of heterogeneous organ/tissue constructs. Sci Rep 6:21685
83. Zhao Y, Yao R, Ouyang L, Ding H, Zhang T, Zhang K et al (2014) Three-dimensional printing of Hela cells for cervical tumor model in vitro. Biofabrication 6:1758–5082
84. Seol YJ, Kang HW, Lee SJ, Atala A, Yoo JJ (2014) Bioprinting technology and its applications. Eur J Cardiothorac Surg 46:342–348
85. Gjorevski N, Sachs N, Manfrin A, Giger S, Bragina ME, Ordóñez-Morán P et al (2016) Designer matrices for intestinal stem cell and organoid culture. Nature 539:560–564
86. Sachs N, Tsukamoto Y, Kujala P, Peters PJ, Clevers H (2017) Intestinal epithelial organoids fuse to form self-organizing tubes in floating collagen gels. Development 144:1107–1112
87. Schnell U, Dijk F, Sjollema KA, Giepmans BNG (2012) Immunolabeling artifacts and the need for live-cell imaging. Nat Methods 9:152–158
88. Jamieson LE, Harrison DJ, Campbell CJ (2015) Chemical analysis of multicellular tumour spheroids. Analyst 140:3910–3920
89. Quaranta M, Borisov SM, Klimant I (2012) Indicators for optical oxygen sensors. Bioanal Rev 4:115–157
90. Berezin MY, Achilefu S (2010) Fluorescence lifetime measurements and biological imaging. Chem Rev 110:2641–2684
91. Swoger J, Pampaloni F, Stelzer EH (2014) Light-sheet-based fluorescence microscopy for three-dimensional imaging of biological samples. Cold Spring Harb Protoc 1:1–8
92. Helmchen F, Denk W (2005) Deep tissue two-photon microscopy. Nat Methods 2:932–940
93. Benninger RKP, Piston DW (2001) Two-photon excitation microscopy for the study of living cells and tissues. Curr Protocols Cell Biol. https://doi.org/10.1002/0471143030.cb0411s59
94. Hopt A, Neher E (2001) Highly nonlinear photodamage in two-photon fluorescence microscopy. Biophys J 80:2029–2036
95. Ustione A, Piston DW (2011) A simple introduction to multiphoton microscopy. J Microsc 243:221–226

96. Patterson GH, Piston DW (2000) Photobleaching in two-photon excitation microscopy. Biophys J 78:2159–2162
97. Huisken J, Swoger J, Del Bene F, Wittbrodt J, Stelzer EHK (2004) Optical sectioning deep inside live embryos by selective plane illumination microscopy. Science 305:1007–1009
98. Santi PA (2011) Light sheet fluorescence microscopy. J Histochem Cytochem 59:129–138
99. Cella Zanacchi F, Lavagnino Z, Perrone Donnorso M, Del Bue A, Furia L, Faretta M et al (2011) Live-cell 3D super-resolution imaging in thick biological samples. Nat Methods 8:1047–1049
100. Patra B, Peng YS, Peng CC, Liao WH, Chen YA, Lin KH et al (2014) Migration and vascular lumen formation of endothelial cells in cancer cell spheroids of various sizes. Biomicrofluidics 8:052109
101. Marx V (2016) Microscopy: openSPIM 2.0. Nat Methods 13:979–982
102. Hell SW (2007) Far-field optical nanoscopy. Science 316:1153–1158
103. Hirvonen LM, Wicker K, Mandula O, Heintzmann R (2009) Structured illumination microscopy of a living cell. Eur Biophys J 38:807–812
104. Gustafsson MGL, Shao L, Carlton PM, Wang CJR, Golubovskaya IN, Cande WZ et al (2008) Three-dimensional resolution doubling in wide-field fluorescence microscopy by structured illumination. Biophys J 94:4957–4970
105. Rust MJ, Bates M, Zhuang X (2006) Sub-diffraction-limit imaging by stochastic optical reconstruction microscopy (STORM). Nat Methods 3:793–796
106. van de Linde S, Loschberger A, Klein T, Heidbreder M, Wolter S, Heilemann M et al (2011) Direct stochastic optical reconstruction microscopy with standard fluorescent probes. Nat Protoc 6:991–1009
107. Hess ST, Girirajan TPK, Mason MD (2006) Ultra-high resolution imaging by fluorescence photoactivation localization microscopy. Biophys J 91:4258–4272
108. Klar TA, Jakobs S, Dyba M, Egner A, Hell SW (2000) Fluorescence microscopy with diffraction resolution barrier broken by stimulated emission. Proc Natl Acad Sci U S A 97:8206–8210
109. Takasaki Kevin T, Ding Jun B, Sabatini BL (2013) Live-cell superresolution imaging by pulsed STED two-photon excitation microscopy. Biophys J 104:770–777
110. Specht EA, Braselmann E, Palmer AE (2016) A critical and comparative review of fluorescent tools for live cell imaging. Annu Rev Physiol 79:93–117
111. Niehorster T, Loschberger A, Gregor I, Kramer B, Rahn H-J, Patting M et al (2016) Multi-target spectrally resolved fluorescence lifetime imaging microscopy. Nat Methods 13:257–262
112. Giordano L, Shvadchak VV, Fauerbach JA, Jares-Erijman EA, Jovin TM (2012) Highly Solvatochromic 7-Aryl-3-hydroxychromones. J Phys Chem Lett 3:1011–1016
113. Shcheslavskiy VI, Neubauer A, Bukowiecki R, Dinter F, Becker W (2016) Combined fluorescence and phosphorescence lifetime imaging. Appl Phys Lett 108:091111
114. Papkovsky DB, Dmitriev RI (2013) Biological detection by optical oxygen sensing. Chem Soc Rev 42:8700–8732
115. Hirvonen LM, Fisher-Levine M, Suhling K, Nomerotski A (2017) Photon counting phosphorescence lifetime imaging with TimepixCam. Rev Sci Instrum 88:013104
116. Becker W (2012) Fluorescence lifetime imaging--techniques and applications. J Microsc 247:119–136
117. Blacker TS, Mann ZF, Gale JE, Ziegler M, Bain AJ, Szabadkai G et al (2014) Separating NADH and NADPH fluorescence in live cells and tissues using FLIM. Nat Commun 5:3936
118. Chudakov DM, Lukyanov S, Lukyanov KA (2005) Fluorescent proteins as a toolkit for in vivo imaging. Trends Biotechnol 23:605–613
119. Mishin AS, Belousov VV, Solntsev KM, Lukyanov KA (2015) Novel uses of fluorescent proteins. Curr Opin Chem Biol 27:1–9
120. Nothdurft R, Sarder P, Bloch S, Culver J, Achilefu S (2012) Fluorescence lifetime imaging microscopy using near-infrared contrast agents. J Microsc 247:202–207
121. Wolfbeis OS (2015) An overview of nanoparticles commonly used in fluorescent bioimaging. Chem Soc Rev 44:4743–4768
122. Ma N, Digman MA, Malacrida L, Gratton E (2016) Measurements of absolute concentrations of NADH in cells using the phasor FLIM method. Biomed Opt Express 7:2441–2452
123. Blacker TS, Duchen MR (2016) Investigating mitochondrial redox state using NADH and NADPH autofluorescence. Free Radic Biol Med 100:53–65
124. Cannon TM, Shah AT, Skala MC (2017) Autofluorescence imaging captures heterogeneous drug response differences between 2D and 3D breast cancer cultures. Biomed Opt Express 8:1911–1925
125. Mongeon R, Venkatachalam V, Yellen G (2016) Cytosolic NADH-NAD(+) redox visualized in brain slices by two-photon fluorescence lifetime biosensor imaging. Antioxid Redox Signal 25:553–563
126. Wagener KC, Kolbrink B, Dietrich K, Kizina KM, Terwitte LS, Kempkes B et al (2016) Redox indicator mice stably expressing genetically encoded neuronal roGFP: versatile tools to decipher subcellular redox dynamics in neuropathophysiology. Antioxid Redox Signal 25:41–58
127. Dmitriev RI, Papkovsky DB (2015) Intracellular probes for imaging oxygen concentration: how good are they? Methods Appl Fluoresc 3:034001
128. Dmitriev RI, Kondrashina AV, Koren K, Klimant I, Zhdanov AV, Pakan JM et al (2014) Small molecule

phosphorescent probes for O2 imaging in 3D tissue models. Biomater Sci 2:853–866
129. Dmitriev RI, Okkelman IA, Foley T, Papkovsky DB (2017) Live cell microscopy of intestinal organoid oxygenation. FASEB J 31:590.1
130. Zhdanov AV, Okkelman IA, Golubeva AV, Doerr B, Hyland NP, Melgar S et al (2017) Quantitative analysis of mucosal oxygenation using ex vivo imaging of healthy and inflamed mammalian colon tissue. Cell Mol Life Sci 74:141–151
131. Zhdanov AV, Golubeva AV, Okkelman IA, Cryan JF, Papkovsky DB (2015) Imaging of oxygen gradients in giant umbrella cells: an ex vivo PLIM study. Am J Phys 309:C501–C5C9
132. Dmitriev RI, Papkovsky DB (2015) Multi-parametric O2 imaging in three-dimensional neural cell models with the phosphorescent probes. In: Lossi L, Merighi A (eds) Neuronal cell death: methods and protocols. Springer New York, New York, NY, pp 55–71
133. Zhdanov AV, Okkelman IA, Collins FWJ, Melgar S, Papkovsky DB (2015) A novel effect of DMOG on cell metabolism: direct inhibition of mitochondrial function precedes HIF target gene expression. Biochim Biophys Acta 1847:1254–1266
134. Roussakis E, Li Z, Nichols AJ, Evans CL (2015) Oxygen-sensing methods in biomedicine from the macroscale to the microscale. Angew Chem Int Ed 54:8340–8362
135. Yazgan G, Dmitriev RI, Tyagi V, Jenkins J, Rotaru G-M, Rottmar M et al (2017) Steering surface topographies of electrospun fibers: understanding the mechanisms. Sci Rep 7:158
136. Poëa-Guyon S, Pasquier H, Mérola F, Morel N, Erard M (2013) The enhanced cyan fluorescent protein: a sensitive pH sensor for fluorescence lifetime imaging. Anal Bioanal Chem 405:3983–3987
137. Tantama M, Hung YP, Yellen G (2011) Imaging intracellular pH in live cells with a genetically-encoded red fluorescent protein sensor. J Am Chem Soc 133:10034–10037
138. Aigner D, Dmitriev R, Borisov S, Papkovsky D, Klimant I (2014) pH-sensitive perylene bisimide probes for live cell fluorescence lifetime imaging. J Mater Chem B 2:6792–6801
139. Hille C, Berg M, Bressel L, Munzke D, Primus P, Löhmannsröben H-G et al (2008) Time-domain fluorescence lifetime imaging for intracellular pH sensing in living tissues. Anal Bioanal Chem 391:1871
140. Kuchibhotla KV, Lattarulo CR, Hyman BT, Bacskai BJ (2009) Synchronous hyperactivity and intercellular calcium waves in astrocytes in Alzheimer mice. Science 323:1211–1215
141. Wilms CD, Schmidt H, Eilers J (2006) Quantitative two-photon Ca2+ imaging via fluorescence lifetime analysis. Cell Calcium 40:73–79
142. Wilms CD, Eilers J (2007) Photo-physical properties of Ca2+−indicator dyes suitable for two-photon fluorescence-lifetime recordings. J Microsc 225:209–213
143. Rinnenthal JL, Börnchen C, Radbruch H, Andresen V, Mossakowski A, Siffrin V et al (2013) Parallelized TCSPC for dynamic intravital fluorescence lifetime imaging: quantifying neuronal dysfunction in neuroinflammation. PLoS One 8:e60100
144. Heim N, Garaschuk O, Friedrich MW, Mank M, Milos RI, Kovalchuk Y et al (2007) Improved calcium imaging in transgenic mice expressing a troponin C-based biosensor. Nat Methods 4:127–129
145. Sotelo-Hitschfeld T, Niemeyer MI, Mächler P, Ruminot I, Lerchundi R, Wyss MT et al (2015) Channel-mediated lactate release by K^+-stimulated astrocytes. J Neurosci 35:4168
146. San Martín A, Ceballo S, Ruminot I, Lerchundi R, Frommer WB, Barros LF (2013) A genetically encoded FRET lactate sensor and its use to detect the warburg effect in single cancer cells. PLoS One 8:e57712
147. Shimolina LE, Izquierdo MA, López-Duarte I, Bull JA, Shirmanova MV, Klapshina LG et al (2017) Imaging tumor microscopic viscosity in vivo using molecular rotors. Sci Rep 7:41097
148. Brand MD, Nicholls DG (2011) Assessing mitochondrial dysfunction in cells. Biochem J 435:297–312
149. Foster KA, Galeffi F, Gerich FJ, Turner DA, Müller M (2006) Optical and pharmacological tools to investigate the role of mitochondria during oxidative stress and neurodegeneration. Prog Neurobiol 79:136–171
150. Kalyanaraman B, Darley-Usmar V, Davies KJA, Dennery PA, Forman HJ, Grisham MB et al (2012) Measuring reactive oxygen and nitrogen species with fluorescent probes: challenges and limitations. Free Radic Biol Med 52:1–6
151. Jenkins J, Papkovsky DB, Dmitriev RI (2016) The Ca^{2+}/Mn^{2+}-transporting SPCA2 pump is regulated by oxygen and cell density in colon cancer cells. Biochem J 473:2507–2518
152. Dmitriev RI, Borisov SM, Jenkins J, Papkovsky DB (2015) Multi-parametric imaging of tumor spheroids with ultra-bright and tunable nanoparticle O2 probes. Proc SPIE 9328:932806–932808
153. Lowell BB, Spiegelman BM (2000) Towards a molecular understanding of adaptive thermogenesis. Nature 404:652–660
154. Bal NC, Maurya SK, Sopariwala DH, Sahoo SK, Gupta SC, Shaikh SA et al (2012) Sarcolipin is a newly identified regulator of muscle-based thermogenesis in mammals. Nat Med 18:1575–1579
155. Fedorenko A, Lishko PV, Kirichok Y (2012) Mechanism of fatty-acid-dependent UCP1 uncoupling in brown fat mitochondria. Cell 151:400–413
156. Zhou H, Sharma M, Berezin O, Zuckerman D, Berezin MY (2016) Nanothermometry: from microscopy to thermal treatments. ChemPhysChem 17:27–36
157. Repasky EA, Evans SS, Dewhirst MW (2013) Temperature matters! and why it should matter to tumor immunologists. Cancer Immunol Res 1:210–216
158. Lukinavičius G, Blaukopf C, Pershagen E, Schena A, Reymond L, Derivery E et al (2015) SiR-Hoechst

is a far-red DNA stain for live-cell nanoscopy. Nat Commun 6:8497
159. Laviv T, Kim BB, Chu J, Lam AJ, Lin MZ, Yasuda R (2016) Simultaneous dual-color fluorescence lifetime imaging with novel red-shifted fluorescent proteins. Nat Methods 13:989–992
160. Weber P, Schickinger S, Wagner M, Angres B, Bruns T, Schneckenburger H (2015) Monitoring of apoptosis in 3D cell cultures by FRET and light sheet fluorescence microscopy. Int J Mol Sci 16:5375
161. Nobis M, McGhee EJ, Morton JP, Schwarz JP, Karim SA, Quinn J et al (2013) Intravital FLIM-FRET imaging reveals dasatinib-induced spatial control of src in pancreatic cancer. Cancer Res 73:4674–4686
162. Matano M, Date S, Shimokawa M, Takano A, Fujii M, Ohta Y et al (2015) Modeling colorectal cancer using CRISPR-Cas9-mediated engineering of human intestinal organoids. Nat Med 21:256–262
163. Görlitz F, Kelly DJ, Warren SC, Alibhai D, West L, Kumar S et al (2017) Open source high content analysis utilizing automated fluorescence lifetime imaging microscopy. J Vis Exp 119:55119

Part II

Manufacturing

5 Fabrication and Handling of 3D Scaffolds Based on Polymers and Decellularized Tissues

Anastasia Shpichka, Anastasia Koroleva, Daria Kuznetsova, Ruslan I. Dmitriev, and Peter Timashev

Abstract

Polymeric, ceramic and hybrid material-based three-dimensional (3D) scaffold or matrix structures are important for successful tissue engineering. While the number of approaches utilizing the use of cell-based scaffold and matrix structures is constantly growing, it is essential to provide a framework of their typical preparation and evaluation for tissue engineering. This chapter describes the fabrication of 3D scaffolds using two-photon polymerization, decellularization and cell encapsulation methods and easy-to-use protocols allowing assessing the cell morphology, cytotoxicity and viability in these scaffolds.

Keywords

Decellularization • Fibrin gel • Microscopy • MTT-assay • Scaffolds • Two-photon polymerization

A. Shpichka (✉)
Institute for Regenerative Medicine, Sechenov First Moscow State Medical University, Moscow, Russia
e-mail: ana-shpichka@yandex.ru

A. Koroleva
Laser Zentrum Hannover e.V., Hannover, Germany

D. Kuznetsova
Institute of Biomedical Technologies, Nizhny Novgorod State Medical Academy, Nizhny Novgorod, Russia

R.I. Dmitriev
Metabolic Imaging Group, School of Biochemistry and Cell Biology, University College Cork, Cork, Ireland

P. Timashev (✉)
Institute for Regenerative Medicine, Sechenov First Moscow State Medical University, Moscow, Russia

Institute of Photonic Technologies, Research Center Crystallography and Photonics RAS, Moscow, Russia
e-mail: timashev.peter@gmail.com

R.I. Dmitriev (ed.), *Multi-Parametric Live Cell Microscopy of 3D Tissue Models*, Advances in Experimental Medicine and Biology 1035, DOI 10.1007/978-3-319-67358-5_5

5.1 Introduction

To date, the number of scaffold materials and fabrication methods proposed for tissue engineering has significantly increased [1–15]. To create an "ideal" scaffold, most scientists try to mimic the native extracellular matrix at the nanoscale level. Therefore, this scaffold should promote cell attachment, proliferation, and differentiation, deliver and retain cells and growth factors, ensure nutrient and oxygen delivery and optimum mechanical and biological environment for tissue regeneration [2, 3].

The most frequently used for tissue engineering are electrospinning, freeze drying, decellularization, and laser-based techniques (Table 5.1). However, this chapter mostly focuses on three methods of scaffold fabrication (two-photon polymerization, decellularization, and cell encapsulation) in order to show the main trends in this field and to present different approaches.

All these methods (two-photon polymerization, decellularization, and cell encapsulation) have their specific limitations. For instance, two-photon polymerization is relatively expensive and permits only the formation of microscale-sized scaffolds. Decellularized materials can cause serious infectious diseases, because the process of their production requires animal or human tissues and organs, which can be contaminated with prions, viruses, bacteria, or fungi. When the cells are encapsulated within a gel, it is hard to manipulate with gel structure and mechanical properties. Nevertheless, two-photon polymerization, decellularization, and cell encapsulation enable the fabrication of biocompatible and biodegradable structures, which can be used to achieve a particular goal in tissue

Table 5.1 Overview of methods for 3D scaffold fabrication in tissue engineering

Method	Material	Application	Commercially available *	References
Electrospinning	PLA	Skin	Yes	[1, 2]
	PLGA	Cartilage		
	PLA/PGA	Cartilage		
	Silk/HAP	Bone		
	Chitosan/PCL	Nerve		
Decellularization	Human and animal tissue and organs	Bone	Yes	[4, 5]
		Cartilage		
		Lung		
Stereolithography	MPLA	Bone	No	[3]
Two-photon polymerization	MPLA	Bone	No	[6–9]
	MPLA	Nerve		
	AC + MeHA	Nerve		
Selective laser sintering	PCL	Bone	No	[10]
3D inject printing	Collagen + CaP	Bone	Yes	[11]
Bioplotting	PCL	Bone	Yes	[12]
Phase-separation	PLA/HAP	Bone	Yes	[1]
Gas foaming	PLA	Bone	Yes	[2]
Particulate leaching	Silk fibroin	Cartilage	Yes	[13]
Freeze drying	Chitosan/PLA	Tendon	Yes	[1, 2]
	Gelatin-PHEMA	Skin		
Self-assembly	Peptide	Cartilage	No	[14]
Cell encapsulation	Alginate	Bone	Yes	[15]

Note. *approximate values
PLA polylactic acid, *PGA* polyglycolic acid, *PLGA* poly(lactic-co-glycolic acid), *MPLA* methacrylated branched polylactide, *PCL* polycaprolactone, *AC* allyl-chitosan, *MeHA* methacrylated hyaluronic acid, *HAP* hydroxyapatite; *CaP* calcium phosphate, *GAG* glycosaminoglycan, *PHEMA* poly([MAG]-2-hydroxyethl methacrylate)

engineering. Their role in modern tissue engineering cannot be overestimated.

This chapter aims to describe the 3D scaffold fabrication using three different methods and protocols of cell morphology and cytotoxicity assessment via SEM, Live/Dead staining, including confocal microscopy, and MTT-assay.

5.2 Materials

Prepare all solutions using deionized water and analytical grade reagents. Prepare and store all reagents at room temperature (unless indicated otherwise). Diligently follow all waste disposal regulations when disposing waste materials. We do not recommend adding sodium azide to the reagents. (*see* **Note 1**).

5.2.1 Reactive Photo-Curing System

Important: preparation and handling of photosensitive monomer composition as well as two-photon polymerized (2PP) scaffolds fabrication should be performed in a yellow light photochemical lab environment.

1. Resolving tetrafunctional polylactides with terminal methacrylic groups (PLA): Add 1.2 mL of dichloromethane to 600 mg of PLA. Weight 6 mg of photoinitiator powder and mix on a magnetic stirrer until PLA and photoinitiator are completely dissolved. Store at 4–8 °C in brown glass bottles wrapped with Parafilm, no longer than one month.
2. IRGACURE® 2959, IRGACURE® 369 (Ciba, Germany), Michler's ketone (Sigma-Aldrich, St. Louis, MO, USA) (*see* **Note 2**).
3. Glass coverslips.

5.2.2 Cell Cultures and Medium

All solutions, glassware, etc., should be sterile and all procedures should be carried out under aseptic conditions and in the sterile environment of a laminar flow cabinet.

1. L929 mouse fibroblast cell line (*see* **Note 3**).
2. Human adipose-derived stem cells (hASCs) (*see* **Notes 3, 4**).
3. Growth medium: DMEM/F12, 10% fetal bovine serum, 1% penicillin-streptomycin. Store at 4 °C for no longer than two weeks.
4. TrypLE Express Enzyme (1X) (Gibco BRL, Bethesda, MD, USA) (*see* **Note 5**).
5. Sterile phosphate buffered saline (PBS), without calcium and magnesium.
6. Trypan Blue: 0.4% solution in water.
7. 75 cm^2 cell culture flask.
8. Petri dishes or 24, 48-well plates.
9. Glass-bottom Petri dishes (*see* **Note 6**).

5.2.3 Fibrin Gel Components

All solutions and glassware, should be sterile and all procedures should be carried out under aseptic conditions and in the sterile environment of a laminar air flow HEPA-filter cabinet.

1. Fibrinogen solution: gradually dissolve 1 g of fibrinogen in 40 mL sterile PBS at 37 °C (*see* **Note 7**) under aseptic conditions to achieve the concentration 25 mg/mL. Aliquot into Eppendorf microtubes (0.5 and/or 1.0 mL). Store at −20 °C in tubes wrapped with Parafilm.
2. Thrombin stock solution: dissolve 1 KU thrombin in 10 mL sterile PBS under aseptic conditions to make stock concentration of 100 U/mL. Aliquot into Eppendorf tubes (300 μL or less). Store at −20 °C in tubes wrapped with Parafilm.
3. Thrombin solution: add 50 μL thrombin stock solution to 950 μL sterile PBS and mix (*see* **Note 8**).

5.2.4 Material and Agents for Decellularization

1. Bovine pericardium (*see* **Note 9**).
2. Sodium dodecyl sulfate (SDS): 0.25% solution in hypotonic buffer (*see* **Note 10**). Store at 4 °C, no longer than 1 year.
3. Distilled water.

4. Hypotonic buffered solution: 10 mM Tris-HCl, pH 7.5. Store at 4 °C, no longer than one year.
5. Phosphate buffered saline (PBS).
6. Hypertonic buffered solution: mix 120 mL of 5 M NaCl, 4 mL of 1 M $MgSO_4$, 2 mL of 0.5 M EDTA, 10 mL of 1 M HEPES, add distilled water to 900 mL. Adjust pH to 7.0 and add distilled water to 1000 mL. Store at 4 °C, no longer than one year (*see* **Note 11**).

5.2.5 MTT-Assay Components

1. 96-well plate.
2. MTT solution: dissolve MTT (3-(4,5-dimethyl thiazol-2-yl)-2,5-diphenyltetrazoliumbromide) in MEM without supplements and without phenol red at a concentration of 1 mg/mL. Sterilize it using a syringe filter with 0.22 μm pore size (*see* **Note 12**).
3. Eagle minimum essential medium (MEM), without phenol red, without glutamine and without $NaHCO_3$.
4. Isopropyl alcohol (analytical grade).

5.2.6 Live/Dead Staining Components

1. Live/Dead Double Staining Kit (Sigma-Aldrich, St. Louis, MO, USA). Store at −20 °C protected from light and moisture.
2. Assay solution: add 10 μL Calcein Green AM solution (Solution A) and 5 μL Propidium iodide solution (Solution B) to 5 mL PBS (*see* **Notes 13, 14**).
3. Phosphate buffered saline (PBS).

5.2.7 SEM Microscopy Components

1. Phosphate buffered saline (PBS).
2. Glutaraldehyde: 2.5% solution in PBS (*see* **Note 15**).
3. Osmium tetroxide: 4% solution in water (*see* **Note 16**).
4. Deionized water.
5. Ethanol: 30%, 40%, 70%, 90%, 95%, 100% in water.
6. Hexamethyldisilazane (HDMS).
7. Ethanol-HDMS solution: 1:1 solution.

5.3 Methods

Carry out all procedures at room temperature unless otherwise specified.

5.3.1 Fabrication via Two-Photon Polymerization

Preparation and handling of photosensitive monomer composition as well as 2PP scaffolds fabrication should be performed in a yellow light photochemical lab environment.

1. Place the volume of photosensitive material composition on a glass coverslip to achieve required sizes and thickness of monomer sample and let it to dry out.
2. Put the glass coverslip with material to the down side on the stage under the objective of the 2PP setup (Fig. 5.1).
3. Fabricate the structure in the volume of monomer using custom 3D design and applying defined optimum structuring speed and laser intensity.
4. Develop the produced structure in corresponding solvent until non-polymerized material is completely washed away. PLA structures should be developed in dichloromethane.
5. Rinse the structure in ethanol for several minutes to remove rest material debris.

5.3.2 Tissue Decellularization

1. Treat the bovine pericardium with hypotonic buffered solution for 14 h at 4 °C.
2. Remove buffer and then wash the pericardium with hypotonic buffered solution with 0.25% SDS for 24 h at room temperature.
3. Remove the previous buffer and wash with PBS for 30 min at 4 °C.

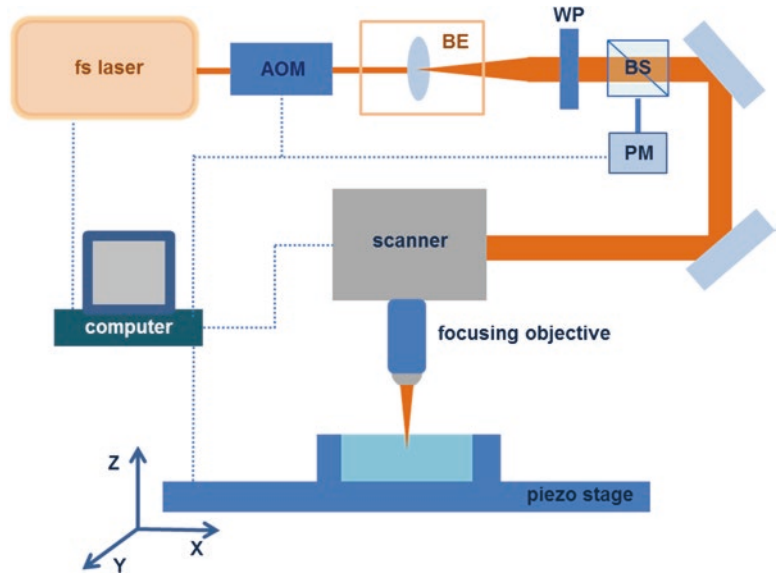

Fig. 5.1 The scheme of two-photon polymerization setup. *AOM* acousto-optical modulator, *BE* beam expander, *WP* half-wave plate, *BS* beam splitter, *PM* power meter

4. Wash the tissues with distilled water for 12 h at 4 °C.
5. Remove water and wash the pericardium with isotonic buffered solution (12 h at 4 °C).
6. Treat the pericardium with hypertonic buffered solution for 6 h at 4 °C.
7. Wash tissues with PBS for 3 h at 4 °C.

5.3.3 Scaffold Seeding

All solutions and glassware should be sterile and all procedures should be carried out under aseptic conditions and in the sterile environment of a laminar flow cabinet.

1. Sterilize the scaffolds (*see* **Note 17**).
2. Remove adipose-derived stem cells (ASC) from culture flasks by enzymatic digestion using TrypLE Express Enzyme and centrifuge them (200 g, 3 min).
3. Resuspend cells in culture medium and adjust cell suspension at a density of 5×10^6 cells/mL (*see* **Note 18**).
4. Put carefully one scaffold to each well in a 48-well plate.
5. Add 20 µL of a cell suspension of 5×10^6 cells/mL (1×10^5 cells/scaffold).
6. Incubate the scaffolds with cells for 15 min.
7. Add 200 µL culture medium and incubate at 37 °C.

5.3.4 Cell Encapsulation in Fibrin Hydrogel

All solutions and glassware should be sterile and all procedures should be carried out under aseptic conditions and in the sterile environment of a laminar flow cabinet.

1. Remove adipose-derived stem cells (ASCs) from culture flasks by enzymatic digestion using TrypLE Express Enzyme and collect them by centrifugation (200 g, 3 min).
2. Resuspend cells in culture medium and adjust cell suspension at a density of 5×10^6 cells/mL.
3. Add 100 µL of the fibrinogen solution to each well in a 24-well plate.
4. Add 60 µL of a cell suspension of 5×10^6 cells/mL ($=3 \times 10^5$ cells/well) and mix.
5. Add 100 µL of the thrombin solution to the cell and fibrinogen mixture (*see* **Note 19**) to observe the stable hydrogel.
6. Incubate at 37 °C for 3 min.
7. Add 100–200 µL culture medium and incubate at 37 °C.

Table 5.2 Extraction ratios for test materials of various thicknesses [16]

Thickness (mm)	Extraction ratio*
≤0.5	6 cm^2/mL
>0.5	3 cm^2/mL
≤1	3 cm^2/mL
>1	1.25 cm^2/mL
Irregular	0.1–0.2 g/ml, 6 cm^2/ml

*The values are expressed as the ratio of the surface area or mass of the test sample to the volume of extractant used

5.3.5 Extract Preparation for MTT-Assay

All solutions and glassware should be sterile and all procedures should be carried out under aseptic conditions and in the sterile environment of a laminar flow cabinet [16].

1. Sterilize the samples (*see* **Note 17**).
2. Put the scaffolds into a tube, add an appropriate MEM volume (Table 5.2), and tightly close the tube (*see* **Note 20**).
3. Incubate these samples at 37 °C for 24 h.
4. Take this medium (extract) and dilute it (*see* **Note 21**).

5.3.6 MTT-Assay

All solutions and glassware should be sterile and all procedures should be carried out under aseptic conditions and in the sterile environment of a laminar flow cabinet [17].

5.3.6.1 Day 1

1. Remove L929 cells from culture flasks by enzymatic digestion using TrypLE Express Enzyme and collect them by centrifugation (200 g, 3 min).
2. Resuspend cells in culture medium and adjust cell suspension at a density of 1×10^5 cells/mL (*see* **Note 18**).
3. Using a multichannel pipette, dispense 100 µL culture medium only (blank) into the peripheral wells of a 96-well plate.
4. In the remaining wells, dispense 100 µL of a cell suspension of 1×10^5 cells/mL ($=1 \times 10^4$ cells/well).
5. Incubate cells for 24 h (5% CO_2, 37 °C, >90% humidity) so that cells form a half-confluent monolayer.
6. Examine each plate under a phase contrast microscope to ensure that cells are evenly distributed across the wells of plate (*see* **Note 22**).

5.3.6.2 Day 2

1. After 24 h incubation, aspirate culture medium from the cells.
2. Per each well, add 100 µL of treatment medium containing either the appropriate concentration of sample extract, or the negative control, or the positive control, or nothing but blank (*see* **Note 23**).
3. Incubate cells for 24 h (5% CO_2, 37 °C, >90% humidity).

5.3.6.3 Day 3

1. After 24 h treatment, examine each plate under a phase contrast microscope to identify systematic cell seeding errors and growth characteristics of control and treated cells. Record changes in the morphology of the cells due to cytotoxic effects of the test sample extract, but do not use these records for any quantitative measure of cytotoxicity (*see* **Note 24**).
2. After the plate examination, carefully remove the culture medium (*see* **Note 25**).
3. Add 50 µL of MTT solution to each test well.
4. Incubate the plates for 2 h in the incubator at 37 °C.
5. Remove the MTT solution and add 100 µL isopropyl alcohol in each well.
6. Sway this plate and subsequently transfer it to a microplate reader equipped with a 570 nm filter to read the absorbance (reference wavelength 650 nm).
7. Record and save data (*see* **Note 26**).
8. Calculate the reduction of viability using the following equation (*see* **Note 27**) [17]:

Viab. % = $100 \times OD_{570e}/OD_{570b}$, where OD_{570e} is the mean value of the measured optical density of the 100% test sample extracts or its dilutions; OD_{570b} is the mean value of the measured optical density of the blanks.

5.3.7 Live/Dead staining

1. Remove the growth medium and wash cells in scaffolds with PBS three times to remove residual esterase activity.
2. Add 200 µL of assay solution per one scaffold with cells and incubate the mixture at 37 °C in CO_2-incubator for 20 min.
3. Measure fluorescence using a fluorescence microscope with 490 nm excitation for simultaneous monitoring of viable and dead cells. With 545 nm excitation, only dead cells can be observed.

5.3.8 Scanning Electron Microscopy (SEM)

1. Remove the growth medium and wash cells/scaffold with PBS twice for 2 min.
2. Rinse the samples with 2.5% glutaraldehyde for 15 min.
3. Wash scaffold with PBS three times for 10 min.
4. Fix the cell-seeded scaffolds with 4% osmium tetroxide for 30 min (*see* **Note 16**).
5. Wash with deionized water three times for 5 min (*see* **Note 28**).
6. Dehydrate the samples using ethanol (30%, 50%, 70%, 90%, 95%, 95%, 100%, 100%, 100% – 15 min for each solution) (*see* **Note 28**).
7. Treat the scaffolds with ethanol-HDMS (1:1) solution for 1 h.
8. Remove and add HDMS twice for 10 min.
9. Store the samples in dry environment.
10. Sputter 50-nm gold layer on the samples.
11. Observe with a scanning electron microscope using customer adjustments (Fig. 5.2).

5.3.9 Confocal Microscopy

1. Place a glass-bottom Petri dish with the stained cell-seeded scaffold on the object table in an inverted laser scanning confocal microscope. See the Table 5.3 for typical settings.

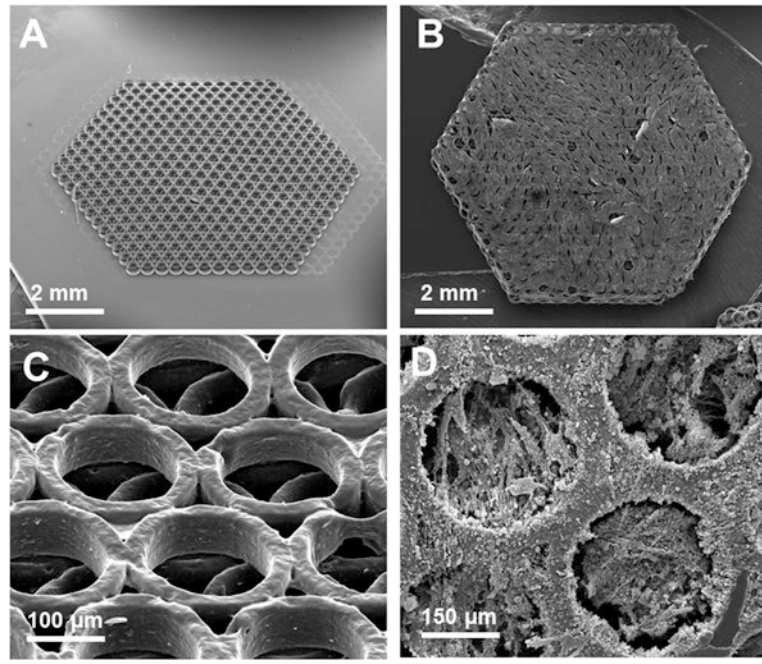

Fig. 5.2 Typical SEM of scaffolds with (**b**, **d**) and without (**a**, **c**) cells

Table 5.3 Example of confocal microscope settings used for analysis of cells growing within scaffolds

Setting	Value
Microscope model (manufacturer, country)	LSM 880 inverted laser scanning confocal microscope (Carl Zeiss, Germany)
Objective	C-Plan-Apochromat 40x/1.3 oil immersion
Image size, pixels	1024 × 1024
Area of fluorescence signal registration, μm	212.3 × 212.3
Pixel dwell time, μs	2.06
Data acquisition time for one image, s	10.13
Confocal diaphragm, Airy unit	1

2. On the central slice cell level, find the sample focal plane, which is characterized by maximum cell square with fluorescence signal.
3. Vary the power of excitation beam and the detector digital gain to find the value where fluorescence signal is little less than the maximum value at the given image bit depth. In our case, the excitation beam power was set 10 μW for 405 nm laser and 6 μW for 488 nm laser (*see* **Note 29**).

5.4 Notes

1. Before opening, bring all reagents, stored at 4 °C or below, to room temperature and incubate for at least 15 min. This prevents absorbing the excessive moisture from the air.
2. Type of photoinitiator for the preparation of reactive photo-curing system is determined by the wavelength of laser irradiation used for 2PP structuring. For example, Irgacure 2959 ptotoinitiator has the peak absorption at appr. 260 nm and should be applied for 2PP structuring at 515 nm. Photoreactive curing mixture for near infrared laser system (780 nm) should be prepared with Irgacure 369 (absorption peak at approx. 325 nm) and Michler' ketone (absorption peak at aprox. 390 nm) photoinitiators.
3. All cell cultures should be free of mycoplasma contamination and routinely checked.
4. hASCs were obtained from human adipose tissue collected from patients undergoing elective plastic surgery after obtaining informed consent. Isolation of the cells took place according to a protocol described elsewhere [18]. We used five to seven passages of hASCs.
5. Instead of TrypLE Express Enzyme, 0.25% Trypsin/1 mM EDTA solution can be used. However, TrypLE Express Enzyme has some important advantages compared to some trypsin preparations: it is animal-origin free and is more specific than crude trypsin preparations thus reducing the cell damage during preparations. TrypLE Express is stable at room-temperature (up to 2 years) and provided as ready to use solution. TrypLE Express can be directly substituted for trypsin in existing protocols. Simple dilution inactivates it, avoiding the need for use of trypsin inhibitors.
6. Glass-bottom Petri dishes are used for confocal microscopy and can be replaced by any other glass-bottom vessels or chambers, e.g. from Nunc, MatTek Corp. or Ibidi GmbH.
7. Fibrinogen solution is easy to foam. Avoid bubbles; do not shake! Dissolve fibrinogen by small portions. This can last for more than 3 h.
8. We find that it is best to prepare this fresh each time.
9. Biomaterial should pass veterinary control and be free of any infectious agents.
10. SDS precipitates at 4 °C. Therefore, it may need to be warmed prior to use.
11. Any hypertonic buffered solution can be used. We prefer this recipe described in [19].
12. MTT solution should be used the same day.
13. Since the buffer solution of Calcein-AM is gradually hydrolyzed to generate fluorescent Calcein, the working solution cannot be stored for more than few hours. Close the bottle cap tightly after using a portion of Calcein AM solution to avoid moisture.
14. Propidium iodide is suspected to be highly carcinogenic; careful handling is required.

15. Glutaraldehyde is a toxic hazardous substance. Avoid contact with skin and eyes. Avoid inhalation of vapors or mist. Wash hands before and immediately after handling the product. Glutaraldehyde is corrosive to the respiratory tract, highly inflammable, toxic (if swallowed or inhaled, in contact with skin), harmful if swallowed or inhaled, fatal if inhaled and causes severe skin burns and eye damage, serious skin and eye irritation, an allergic skin reaction, allergy or asthma symptoms or breathing difficulties if inhaled, respiratory irritation, damage to organs. Moreover, it is very toxic to aquatic life with long lasting effects. Store in cool place. Keep container tightly closed in a dry and well-ventilated place. Containers, which are opened, must be carefully resealed and kept upright to prevent leakage. Recommended storage temperature is −20 °C. Store under inert gas. A licensed disposal company should dispose glutaraldehyde and contaminated items.
16. Osmium tetroxide is a highly toxic hazardous substance. Avoid contact with skin, eyes, and clothing. Avoid inhalation of vapors or mist. Wash hands before and immediately after handling the product. Osmium tetroxide is extremely destructive to tissue of the mucous membranes and upper respiratory tract, eyes, and skin. It causes spasm, inflammation and edema of the larynx, spasm, inflammation and edema of the bronchi, pneumonitis, pulmonary edema, burning sensation, cough, wheezing, laryngitis, shortness of breath, headache. Store in cool place. Keep container tightly closed in a dry and well-ventilated place. Containers, which are opened, must be carefully resealed and kept upright to prevent leakage. Recommended storage temperature is 2–8 °C. A licensed disposal company should dispose osmium tetroxide and contaminated items.
17. We sterilize scaffolds with 70% ethanol (two washes for 30 min) and then expose them to UV for 3 h [7]. Alternatively, gamma-irradiation and ethylene oxide sterilization can be used.
18. The Neubauer hemocytometer (Sigma-Aldrich) or other cell counters can be used (e.g. from Bio-Rad, Beckman Coulter, or Roche). You need to stain cells with Trypan Blue (0.2% final conc.) to differ live and dead cells.
19. Add thrombin carefully to cells and fibrinogen because the mixture can start to form a gel. While adding, continuously mix it for homogenous cell distribution.
20. For most test materials, extractions are performed under static conditions. However, agitation may be deemed appropriate as an effort to more closely mimic an end use or to ensure that the extraction media come in contact with all relevant material surfaces. In any case, when agitation is considered appropriate, the method used should be marked.
21. At least four different concentrations of the test sample extract or the positive control extract should be tested. The highest concentration used should be 100% extract and the other concentrations will be adequately spaced within a single logarithmic range. For the negative control, only the 100% extract should be tested. Culture medium should be used as blank.
22. This incubation period ensures cell recovery, and adherence and progression to exponential growth phase. This check is performed to identify experimental errors.
23. Positive and negative controls should be included in every cytotoxicity test. Positive control material is material which, when tested in accordance with ISO 10993-5, provides a reproducible cytotoxic response. The purpose of the positive control is to demonstrate an appropriate test system response. For example, an organotin-stabilized polyurethane has been used as positive control for solid materials and extracts. Dilutions of phenol, for example, have been used as a positive control for extracts. In addition to a material, pure chemicals (SDS or Triton X100) can also be used to demonstrate the

performance of the test system. Negative control material is material which, when tested in accordance with ISO 10993-5, does not produce a cytotoxic response. The purpose of the negative control is to demonstrate background response of the cells. For example, high-density polyethylene for synthetic polymers, and aluminium oxide ceramic rods for dental material have been used as negative controls. 'Blank' is extraction vehicle not containing the test sample, retained in a vessel identical to that which holds the test sample and subjected to conditions identical to those to which the test sample is subjected during its extraction. The purpose of the blank is to evaluate the possible confounding effects due to the extraction vessel, vehicle and extraction process.

24. Undesirable growth characteristics of control cells can indicate experimental error and can be cause for rejection of the assay.
25. This is an important step, because reductive chemicals in the extract can also reduce MTT, causing false negative results.
26. The data generated will be recorded in the raw data file. The results will be presented in tabular form, including experimental groups with the test item, negative, blank and positive controls. A decrease in number of living cells results in a decrease in the metabolic activity in the sample. This decrease directly correlates to the amount of blue-violet formazan formed, as monitored by the optical density at 570 nm.
27. The lower the Viab.% value, the higher the cytotoxic potential of the test sample is. If viability is reduced to <70% of the blank, it has a cytotoxic potential. The 50% extract of the test sample should have at least the same or a higher viability than the 100% extract; otherwise, the test should be repeated.
28. All wastes should be carefully collected, because they can contain osmium traces.
29. For correct data processing, all images must be acquired under the same conditions. The parameters of excitation light (wavelengths, powers) and registration (diameter of confocal diaphragm, number of pixel, pixel dwell time, detection range, and detector digital gain) must remain the same between control and test groups.

Acknowledgments This work was supported by the Russian Science Foundation, grant 15-15-00132.

References

1. Lu T, Li Y, Chen T (2013) Techniques for fabrication and construction of three-dimensional scaffolds for tissue engineering. Int J Nanomedicine 8:337–350
2. Loh QL, Choong C (2013) Three-dimensional scaffolds for tissue engineering applications: role of porosity and pore size. Tissue Eng Part B Rev 19(6):485–502
3. Skoog SA, Goering PL, Narayan RJ (2012) Stereolithography in tissue engineering. J Mater Sci 25(3):845–856. https://doi.org/10.1007/s10856-013-5107-y
4. Cheng CW, Solorio LD, Alsberg E (2014) Decellularized tissue and cell-derived extracellular matrices as scaffolds for orthopaedic. Tissue Eng Biotechnol Adv 32(2):462–484
5. O'Neill JD, Anfang R, Anandappa A, Costa J, Javidfar JJ, Wobma HM et al (2013) Decellularization of human and porcine lung tissues for pulmonary. Tissue Eng Ann Thorac Surg 96(3):1046–1056
6. Koroleva A, Gittard S, Schlie S et al (2012) Fabrication of fibrin scaffolds with controlled microscale architecture by a two-photon polymerization–micromolding technique. Biofabrication 4:015001
7. Timashev P, Kuznetsova D, Koroleva A et al (2016) Novel biodegradable star-shaped polylactide scaffolds for bone regeneration fabricated by two-photon polymerization. Nanomedicine 11(9):1041–1053. https://doi.org/10.2217/nnm-2015-0022
8. Timashev PS, Bardakova KN, Minaev NV et al (2016) Compatibility of cells of the nervous system with structured biodegradable chitosan-based hydrogel matrices. Appl Biochem Microbiol 52(5):508–514
9. Timashev PS, Vedunova MV, Guseva D et al (2016) 3D in vitro platform produced by two-photon polymerization for the analysis of neural network formation and function. Biomed Phys Eng Express 2(3):1–8
10. Williams JM, Adewunmi A, Schek RM, Flanagan CL, Krebsbach PH, Feinberg SE et al (2005) Bone tissue engineering using polycaprolactone scaffolds fabricated via selective laser sintering. Biomaterials 26(23):4817–4827
11. Inzana JA, Olvera D, Fuller SM, Kelly JP, Graeve OA, Schwarz EM et al (2014) 3D printing of composite calcium phosphate and collagen scaffolds for bone regeneration. Biomaterials 35(13):4026–4034

12. Yilgor P, Sousa RA, Reis RL, Hasirci N, Hasirci V (2008) 3D plotted PCL scaffolds for stem cell based bone tissue engineering. Macromol Symp 269:92–99
13. Yan L-P, Oliveira JM, Oliveira AL, Caridade SG, Mano JF, Reis RL (2011) Macro/microporous silk fibroin scaffolds with potential for articular cartilage and meniscus tissue engineering applications. Acta Biomater 8(1):289–301
14. Cheng T-Y, Chen M-H, Chang W-H, Huang M-Y, Wang T-W (2013) Neural stem cells encapsulated in a functionalized self-assembling peptide hydrogel for brain tissue engineering. Biomaterials 34(8):2005–2016
15. Tang M, Chen W, Weir MD, Thein-Han W, Xu HHK (2012) Human embryonic stem cell-encapsulation in alginate microbeads in macroporous calcium phosphate cement for bone tissue engineering. Acta Biomater 8(9):3436–3445
16. ISO 10993-12 (2012) Biological evaluation of medical devices—part 12: sample preparation and reference materials. 28 p
17. ISO 10993-5 (2009) Biological evaluation of medical devices—Part 5: tests for in vitro cytotoxicity. 42 p
18. Gruene M, Pflaum M, Deiwick A, Koch L, Schlie S, Unger C et al (2011) Adipogenic differentiation of laser-printed 3D tissue grafts consisting of human adipose-derived stem cells. Biofabrication 3:015005
19. Waterman-Storer CM (2001) Microtubule/organelle motility assays. Curr Protoc Cell Biol 00:13.1:13.1.1–13.1.21

Part III

Application Methods and Protocols

6 Multi-Parametric Imaging of Hypoxia and Cell Cycle in Intestinal Organoid Culture

Irina A. Okkelman, Tara Foley, Dmitri B. Papkovsky, and Ruslan I. Dmitriev

Abstract

Dynamics of oxygenation of tissue and stem cell niches are important for understanding physiological function of the intestine in normal and diseased states. Only a few techniques allow live visualization of tissue hypoxia at cellular level and in three dimensions. We describe an optimized protocol, which uses cell-penetrating O_2-sensitive probe, Pt-Glc and phosphorescence lifetime imaging microscopy (PLIM), to analyze O_2 distribution in mouse intestinal organoids. Unlike the other indirect and end-point hypoxia stains, or point measurements with microelectrodes, this method provides high-resolution real-time visualization of O_2 in organoids. Multiplexing with conventional fluorescent live cell imaging probes such as the Hoechst 33342-based FLIM assay of cell proliferation, and immunofluorescence staining of endogenous proteins, allows analysis of key physiologic parameters under O_2 control in organoids. The protocol is useful for gastroenterology and physiology of intestinal tissue, hypoxia research, regenerative medicine, studying host-microbiota interactions and bioenergetics.

Keywords

Cell cycle • FLIM • Intestinal organoids • Live cell microscopy • Oxygen • Phosphorescence quenching • PLIM

I.A. Okkelman • D.B. Papkovsky
Laboratory of Biophysics and Bioanalysis, School of Biochemistry and Cell Biology, University College Cork, Cork, Ireland

T. Foley
Department of Anatomy and Neuroscience, University College Cork, Cork, Ireland

R.I. Dmitriev (✉)
Metabolic Imaging Group, School of Biochemistry and Cell Biology, University College Cork, Cork, Ireland
e-mail: r.dmitriev@ucc.ie

R.I. Dmitriev (ed.), *Multi-Parametric Live Cell Microscopy of 3D Tissue Models*, Advances in Experimental Medicine and Biology 1035, DOI 10.1007/978-3-319-67358-5_6

6.1 Introduction

The mechanisms of how O_2 contributes to pathophysiological states of intestinal tissue are controversial: both hypoxia and high O_2 were linked to tumorigenesis [1, 2]. The studies of gut dysbiosis in type-2 diabetes [3, 4] and inflammatory bowel disease patients [5] suggested that elevated O_2 contributes to the development and progression of these diseases. Since most pathogenic microorganisms are facultative anaerobes with flexible oxidative metabolism, hypoxia [6, 7] and heterogeneous O_2 environment can contribute to their virulence [8]. Therefore new experimental approaches for direct quantification and dynamic monitoring of tissue and luminal O_2 are needed.

A number of methods were recently suggested for analysis of hypoxia in the intestine [9], which can be structured based on their spatial and temporal resolution, ability to provide quantitative read-out and compatibility with specific experimental model: cultured cells, 3D culture, tissue explants and in vivo. Microelectrodes, "hypoxia stains" such as pimonidazole or HIF-α, CAIX, luciferase reporters, and phosphorescent probes [10–12] are commonly used. The most disadvantageous methods are the Clark electrode, which consumes oxygen, shows signal drift and provides point measurements, and "hypoxia stains", which are qualitative, indirect and end-point [10, 13].

In contrast, imaging with quenched-phosphorescence probes allows real-time analysis of tissue O_2 via non-invasive, non-chemical and reversible photophysical process [12]. This approach can be realized using several different detection modalities, with phosphorescence lifetime imaging microscopy (PLIM) considered as the most accurate and reliable [11, 14, 15]. Advanced cell-permeable phosphorescent O_2 imaging probes can efficiently stain cells and tissues, provide high brightness, stable calibration, minimal photobleaching and photodamage of the sample under one and two-photon excitation [10, 15–17]. This methodology has been successfully applied to analyze O_2 gradients in live intestine, oxygenation in neural stem cell and tumor spheroids, tissue explants and other models [18–26]. However, strong light absorption, scattering and autofluorescence of mammalian tissue limit the in vivo applicability of fluorescence imaging to relatively thin samples (up to 200 μm for one-photon and 500 μm for two-photon excitation) [27]. On the other hand, imaging of intestinal organoids (200-500 μm size) in vitro is free from these limitations. It provides sub-cellular spatial resolution, ability to track individual cells, multiplexing with other fluorescent markers, and extract important and physiologically relevant information about the intestinal tissue: at rest, under normal and diseased state or under pharmacological treatment [28, 29].

Intestinal organoids is a 3D model of intestinal tissue, grown in soft 3D matrices, such as Matrigel®. The organoids display the characteristic villi-crypt organization formed by heterogeneous epithelial cell monolayer with lumen. The epithelium has complex composition with stem and Paneth cell niches at the bottom of the crypts, amplification zones of actively proliferating non-differentiated cells and main lineages of differentiated cells: enterocytes, goblet cells and enteroendocrine cells [29, 30]. Published methods allow preparation of different organoid cultures: epithelial monolayer structures from isolated intestinal crypts or stem cells [31], neonatal spheroid-like organoids with myofibroblasts and epithelium [32] and co-cultures of isolated intestinal myofibroblasts and neuronal cells [33]. Organoids from gastric and colon tissue of human [34, 35] and mouse origin [36] are also known. The ease of production, flexibility and possibility of genetic manipulation (e.g. using CRISPR-Cas9 method) make organoid cultures attractive for studies of host - microbe interactions [37–39], development of infections [40, 41], cancer [42–44], intestinal fibrosis [45, 46], inflammatory bowel disease [47], stem cells research [48] and regenerative medicine [30, 49, 50]. However, control of organoid oxygenation and metabolic state in such experiments is not normally implemented, which often makes the experiments ambiguous and difficult to reproduce.

The presented protocol describes isolation of crypts from small intestine of adult mice, their

culturing in Matrigel to produce organoids, staining of the organoids with the probes and analysis of O_2, cell cycle and other markers and cell phenotypes in the organoid. The method can be easily adapted for different cultivation conditions, combining live and fixed cell imaging, and for time-lapse measurements.

6.2 Materials

Prepare all solutions using ultrapure water (Milli-Q grade, sterile-filtered 0.22 μm, 18 MΩ cm). Store all reagents at 4 °C, for no longer than 4 weeks (unless specified otherwise). To prevent contamination, perform all cell culture under laminar flow (class II Microbiological Safety Cabinet with HEPA filter) and aseptically. Wear gloves at all times and spray all used materials and surfaces with 70% ethanol. Unless provided sterile, autoclave all glass and plasticware (121 °C, 20 min) and filter-sterilize media prior to use.

6.2.1 Animals

Adult (8 weeks or older) mice of breed of choice. All the procedures with animals should be performed under animal license issued by the corresponding authority (e.g. Department of Health and Children, Ireland) and in accordance with relevant legislation (e.g. Directive 2010/63/EU adopted by the European Parliament and the Council of the European Union).

6.2.2 FLIM-PLIM Microscope

6.2.2.1 Requirements for PLIM Microscope

One-photon laser scanning microscope with excitation sources and detectors spectrally compatible with Pt-Glc probe [26]: 405 nm pulsed diode laser for excitation, red-sensitive (up to 700 nm) photodetector and 640-660 nm bandpass or longpass filters for emission collection. Additional lasers and filters for the other probes, such as Hoechst 33342 (emission 438–458 nm, excitation 405 nm), Alexa Fluor 488 (512–536 nm emission, excitation at 488 nm) and Rhodamine/TMRM (565–605 nm emission, 546 nm excitation), as required. PLIM hardware and software for measuring lifetimes in the range 10–100 μs, for example from Becker & Hickl GmbH (see Chaps. 2, 3, and 4 for details). Reliable temperature control and atmospheric control (O_2 and humidity) of sample compartment are necessary.

6.2.2.2 Example of Microscope Setup

Confocal FLIM-PLIM-TCSPC system (Becker & Hickl GmbH, Germany) based on an upright AxioExaminer Z1 microscope (Carl Zeiss) with 63x/1.0 W-Plan Apochromat dipping water immersion objective, heated stage (t = 37 °C) with motorized Z-axis control [51]. A DCS-120 confocal scanner (Becker & Hickl) with two excitation and two emission channels is connected to the microscope. On/off switchable 405 nm BDL-SMC picosecond diode laser (Becker & Hickl) and picosecond supercontinuum 400–650 nm laser SC400-4 (Fianium, UK) connected to the DCS-120 scanner with an optical fibre are used for the excitation of the O_2 probe and other fluorophores, respectively. Emission filters (Semrock) include: 635–675 nm (Pt-Glc probe), 438–458 nm (DAPI and Hoechst 33342), 512–536 nm (Alexa Fluor 488, EGFP) and 565–605 nm (rhodamine, Alexa Fluor 555). An R10467U-40 photon counting detector, with >30% quantum efficiency at 400–700 nm (Hamamatsu Photonics K.K.) connected to the scanner and TCSPC hardware for emission detection. MicroToolBox, version 2011 software (Carl Zeiss) controls the microscope, image acquisition and data processing are performed with SPCImage software (Becker & Hickl).

Typical settings for O_2 measurement in intestinal organoids are: excitation—405 nm laser; emission filter—635–675 nm; software parameters: PS FLIM, MCS FLIM, trigger marker 0, Offset −9%, 32 MT units (204.8 μs time range), routing channel X2. Tpxl 201.5 μs, T1 line 84 ms, T2 frame 244 s, shift fixed 20, single-exponential decay, offset manually selected from 0 to channel

22, tail-enhanced fit. Binning factor of 3–5, frame collection time 120 s, Stop T = ON. Multiplexing—PXL, steps.

6.2.3 Microscopy Imaging Supplies

Tissue culture minidish (35/10 mm) cell+ (Sarstedt, 83.1800.003). The growth area can be decreased by insertion of autoclaved silicon micro-well chamber (e.g. µ-chamber from Ibidi, 81201).

Options:

a. Glass bottom mini-dishes, 35 mm, No. 1.5 cover glass (MatTek Corporation P35G-1.5-14-C).
b. Glass bottom µ-dishes, 35 mm, low, Grid-500 (Ibidi 81168). Also compatible with inverted microscope.
c. µ-chambers, 12 well (Ibidi 81201). The silicon part is autoclavable and can be reused with any plastic or glass surface, when adhered.

6.2.4 Chemicals and Plasticware

1. Dulbecco's modified Eagle's medium, phenol red-, glucose-, pyruvate- and glutamine-free (Sigma, D5030).
2. 'Imaging medium': DMEM supplemented with sodium bicarbonate (1.2 g/l), HEPES-Na, pH 7.2 (10 mM), sodium pyruvate (1 mM), L-glutamine (2 mM) and glucose (5 mM), without phenol red.
3. D(+)-Glucose, powder (Sigma, G8270). Prepare 1 M stock solution in sterile MQ-water and store at 4 °C.
4. L-Glutamine, 200 mM solution, sterile (Sigma, G7513)
5. HEPES solution, 1 M, pH 7.2, sterile (Sigma, H0887)
6. Sodium pyruvate solution, 100 mM, sterile (Sigma, S8636)
7. Phosphate buffered saline (PBS), Ca^{2+} and Mg^{2+}-free (Sigma, P4417)
8. EDTA, disodium salt, dihydrate (Sigma, E5134). Prepare 2 mM solution of EDTA in PBS pH 7.2, sterilized by filtration ('Dissociation buffer'—DB).
9. Albumin, from bovine serum, BSA (Sigma, A4503). Prepare fresh before crypts isolation 0.5% (w/v) BSA/PBS solution, sterilize by filtration and store at +4 °C. Prepare BSA-coated tubes by incubating 50 ml and 15 ml tubes with sterile BSA/PBS solution overnight with gentle shaking, aspirate liquid under sterile conditions, keep closed prior use.
10. B-27 media Supplement, serum-free (50x concentrate) (Invitrogen, 17,504–044). Aliquot under sterile conditions and store at −20 °C before use. Use in 1:50 dilution.
11. N2Supplement, (100x concentrate) (Invitrogen, 17,502-048). Aliquot under sterile conditions and store at −20 °C before use. Use in 1:100 dilution.
12. N-Acetyl-L-cysteine (NAC) (Sigma, A9165). Prepare 500 mM (500x) stock solution in water, sterilize by filtration, aliquot and store at −20 °C. Use in 1:500 dilution.
13. Penicillin-streptomycin solution (P/S), 100x concentrate, sterile (Sigma, P0781)
14. Recombinant murine EGF (epidermal growth factor) (Peprotech, 315-09). Dilute lyophilized powder in sterile 0.1% (w/v) BSA/PBS to concentration 500 µg/ml (10,000x stock solution). Aliquot stock solutions and store at −20 °C. Defrosted aliquots can be kept for 1 week at 4 °C without noticed loss of activity.
15. Recombinant human R-spondin-1 (Peprotech, 120-38). Dilute lyophilized powder in sterile 0.1% (w/v) BSA/PBS to concentration 1 mg/ml (1000x stock solution). Aliquot stock solutions and store at −20 °C. Defrosted aliquots can be kept for 1 week at 4 °C without noticed loss of activity.
16. Recombinant murine Noggin (Peprotech, 250-38). Dilute lyophilized powder in sterile 0.1% (w/v) BSA/PBS to concentration 100 µg/ml (1000x stock solution). Aliquot stock solutions and store at −20°C. Defrosted aliquots can be kept for 1 week at 4 °C.
17. Prepare *Basal Culture Medium (BCM)*: supplement DMEM F12 [Ham] medium (Sigma,

D6421) with 1% penicillin/streptomycin, 1% N2, 2% B-27, 1% Gln and 1 mM NAC.
18. For *complete BCM (Growth Medium—GM)*, add EGF (50 ng/ml), R-spondin (1 μg/ml) and Noggin (100 ng/ml) prior to use and storage at 4 °C for one week.
19. Matrigel®, growth factor reduced (GFR), basement membrane matrix, phenol red-free, LDEV-free (Corning, 356231). Thaw Matrigel stock on ice overnight, aliquot and store at −20 °C until further use. Thaw aliquots only once, liquid Matrigel can be kept on ice (0 °C) up to 4 days. Avoid using diluted Matrigel for imaging, as this produces less stable gels which impact the quality of imaging. *Important:* Matrigel® matrix should have minimal amount of growth factors, to prevent uncontrolled growth and differentiation of organoids. Matrigel from alternative suppliers can have different gelling properties and adverse effects on organoid growth.
20. Sterile plastic tubes of 1.5 ml, 15 ml and 50 ml (Sarstedt, 72.690.001, 62.554.002, 62.559.001). For crypts isolation procedure prepare four 50 ml tubes and three 15 ml tubes, one of each should be coated with BSA overnight.
21. 24-well flat bottom plates, sterile, tissue culture grade (Corning, CLS3526-50EA).
22. Plastic syringes, 20 ml (Becton Dickinson PlastiPak Luer 300,613)
23. Cell scraper 16 cm (Sarstedt, 83.1832)
24. Cell strainer, 70 μm nylon (BD Falcon 352,350)
25. Stainless steel pins, 0.2 mm (Fine Science Tools, 26,002-20)
26. Surgical scissors, 12 cm (91402-12) and delicate forceps-smooth/angled 45/9 cm (11063-07) (Fine Science Tools)
27. Cover glass, No. 1.5, 22 × 50 mm (Corning 2940-225).
28. Hemocytometer Bright-line (Sigma, Z359629)
29. Sylgard® 184 silicon elastomer kit (Dow Corning). Use it to cover the bottom of one plastic Petri-dish with a thick silicon layer (used for tissue dissection).
30. Humidified CO_2/37 °C incubator, optional with O_2 control.
31. Dimethyl sulfoxide (DMSO), 'hybri-max' grade (Sigma, D2650)
32. FCCP (carbonyl cyanide 4-(trifluoromethoxy)phenyldydrazone) (Sigma, C2920)
33. Glucose oxidase, from Aspergillus niger, Type X-S, 100-250 U/g solid (Sigma G7141)
34. Nitrogen gas, 99.99% in cylinders (Irish Oxygen, Cork, Ireland)
35. Catalase from bovine liver, 2–5 U/mg protein (Sigma, C1345)
36. Potassium cyanide, KCN (Sigma, 601780). Caution, KCN is extremely toxic and volatile agent, inhibitor of electron transport chain. In contact with acids it liberates toxic gas. Use necessary precautions during work: eye, skin and respiration protection. Use in well-ventilated environment.

6.2.5 Live imaging probes and reagents for immunofluorescence

1. O_2-sensitive phosphorescent probe Pt-Glc synthesized as described in [26], 1 mM solution in DMSO.
2. Bis-Benzimide Hoechst 33342 (Sigma, B2261)
3. 5-bromo-2′-deoxyuridine (Sigma, B5002)
4. Cholera toxin, subunit B (CTX), recombinant, Alexa Fluor 488 conjugate (Invitrogen, C34775)
5. Other fluorescent probes for multiplexing (see Table 6.1).
6. Fetal bovine serum (FBS), sterile-filtered (Sigma, F7524)
7. Methanol, HPLC grade (Sigma, 34966)
8. Pro-long Gold Anti-Fade mounting medium (Invitrogen, P36930)
9. Sodium chloride (Sigma, S3014)
10. Trizma base (Sigma, T6066)
11. Tween 20 (Sigma, P1379)
12. Anti-mucin 2 antibody, rabbit polyclonal (H-300) Marker of goblet cells (Santa Cruz biotechnology, sc-15334). *See* **Note 11**.

Table 6.1 Live imaging probes and recommended conditions for intestinal organoids. NOTE: one wash with growth medium after staining is sufficient for the subsequent imaging

Fluorescent probe, excitation/emission, nm	Staining concentration, time	Remarks, localization
Cholera toxin, subunit B (CTX)-Alexa Fluor 488 conjugate, 488/510 nm	44 nM, 30 min	Binds to ganglioside GM1 located in lipid-rafts and endosomes
Transferrin-Alexa Fluor 488 conjugate, 488/510 nm	1.6 μM, 30 min	Marker of clathrin-mediated endocytosis and endosomes
Hoechst 33342, 405/430 nm	1–2 μM, 30 min	Nuclear stain for live cell imaging, can be used for FLIM of dividing cells
TMRM, 546/580 nm	20–100 nM, 15 min	Stains polarized mitochondria (20 nM, needs to be present in bathing solution continuously)
Calcein Green AM, 488/510 nm	1 μM, 30 min. Allow 15 min after wash for de-esterification	Cytosolic Ca^{2+} probe, stains cytoplasm. Also pH sensitive
MitoTracker Green, 488/510 nm	25–50 nM, 30 min	Mitochondrial stain
LysoTracker red, 590/620 nm	50–100 nM, 30 min	Lysosomal stain
CellTox Green, 488/510 nm	0.1%, 5–15 min	Membrane integrity probe, stains damaged and dead cells. Used to analyze cell viability, together with Hoechst 33342. Sytox Green (Molecular Probes) can be used instead

6.2.6 Reagents for Synthesis of Pt-Glc Probe

Protect from light your reaction mixture and components on all stages. Handle the chemicals in fume hood with safety precautions, accordingly to good laboratory practice. Wear gloves, lab coat, safety glasses and facemask, if necessary. Dispose the chemicals in designated "waste" disposal, accordingly to the regulations at your workplace. Make yourself familiar with decontamination and first-aid procedures for DMF, triethylamine, methanol, DMSO and TFA before you start the experiment.

1. Pt(II) meso-tetra(pentafluorophenyl)porphine (PtTFPP) (Frontier Scientific, PtT975)
2. β-D-thioglucose, sodium salt (Carbosynth UK, MT05991)
3. N,N-dimetlylformamide, anhydrous (DMF) (Sigma 227,056)
4. Triethylamine (Sigma T0886)
5. Trifluoroacetic acid (TFA), HPLC grade (Sigma 302,031)
6. Methanol, HPLC grade (Sigma 34,860)
7. Dimethyl sulfoxide (DMSO), Hybri-Max grade, sterile (Sigma D2650)
8. Phosphate buffered saline (PBS) (Sigma P4417)
9. Triton X-100 (Sigma T8787)
10. Water, HPLC grade, e.g. purified using Milli-Q system (Millipore)
11. Microcentrifuge 1.5 ml PP tubes "eppendorf" (Sarstedt)
12. HPLC glass vials, with caps
13. Analytical RP-HPLC column, e.g. Zorbax XDB-C18 4.6x150 mm, 5 μm (Agilent)
14. Solid-phase extraction C18 cartridges Discovery DSC-18, 5 g/20 ml volume (Supelco 52608-U)
15. Automatic pipettes, for 20, 200, 1000 μl volumes
16. Filter tips for automatic pipettes

17. Vacuum pump and manifold (Promega)
18. Thermostat for 40 °C
19. Microcentrifuge, table-top (Eppendorf, MiniSpin)
20. HPLC system with quaternary pump, autosampler and diode array absorbance detector (e.g. Agilent 1100 series)
21. Vacuum concentrator (Eppendorf 5301)
22. Spectrophotometer, to measure absorbance spectra 350-600 nm (Hewlett Packard 8453)

6.3 Methods

6.3.1 Synthesis of Phosphorescent O_2 Probe Pt-Glc

Five hundred nmoles reaction scale is described. The reaction can be scaled up to 2–3 μmoles accordingly, with the proportionally increased amounts of thioglucose and triethylamine.

1. Take the PtTFPP and β-D-thioglucose sodium salt from the fridge (store dry at 4 °C), equilibrate them at room temperature for 10–15 min.
2. Weigh 0.585 mg (500 nmoles) of PtTFPP in microcentrifuge tube and add 100 μl of DMF. Mix to dissolve.
3. Weigh 0.55 mg (5x excess, 2.5 μmoles) of β-D-thioglucose sodium salt in glass HPLC vial.
4. Transfer the PtTFPP solution to the glass HPLC vial containing β-D-thioglucose sodium salt, add 17 μl (~122 μmoles) of triethylamine (TEA), mix thoroughly by pipetting.
5. Close the HPLC vial, cover with foil (protection from light) and leave in incubator at 40 °C overnight (16 h). β-D-thio-glucose will gradually dissolve during the reaction.
6. Transfer the reaction mixture into 1.5 ml Eppendorf tubes and spin down insoluble matter (10 min at 12,000 g). Transfer the supernatant into fresh glass vial.
7. Analyze the reaction mixture using RP-HPLC using linear gradient of methanol in water/0.1% TFA. Column: Zorbax XDB-C18 (or equivalent) 4.6x150 mm, 5 μm; Flow rate—1 ml/min; gradient duration: 20 min (0–100% methanol); detection: absorbance at 395 nm (PtTFPP); injection volume—1–5 μl; product (Pt-Glc) retention time ~ 15–17 min.
8. NOTE: unconjugated PtTFPP can be dissolved at concentration 1 mM and injected (1–5 μl) for comparison. Single (80–90% purity) peak of Pt-Glc is expected upon analysis of reaction mixture.
9. For purification use new plastic columns (SPE C18 cartridges, Supelco, Sigma) on a vacuum manifold device and connect to the pump.
10. Equilibrate the SPE C18 column with 20 ml of H_2O/0.1% TFA solution.
11. Dilute reaction mixture with H_2O/TFA up to 500 μl volume and apply on the column evenly.
12. Wash the column with 5 ml of H_2O/TFA, then with 20 ml of 45% MeOH—55% H_2O/TFA with pump flow.
13. Elute the product with mixture of 70% MeOH—30% H_2O/TFA (~20 ml) using gravity flow. Collect the most hydrophilic red colored fraction, aliquot in 6–10 polypropylene tubes and dry (room temperature, vacuum concentrator, >3 h).
14. Reconstitute the aliquot of dry product in 100 μl of DMSO (or less, depending on expected concentration, to have it around 1 mM) and measure the concentration in PBS/0.25% Triton X100 solution using absorbance at 395 and Beer-Lambert law (extinction coefficient of PtTFPP (A_{395}) is 257,000 M^{-1} cm^{-1}). For experiments, dissolve in sufficient volume to have 1–2 mM concentration in DMSO.
15. Store dried conjugates at −18 °C. They are stable for at least 2 years.
16. Perform RP-HPLC (as described in point 7) to test the purity of the product. This must be of >75%.

6.3.2 Isolation of Crypts from Mouse Small Intestine and Culture of Organoids (Adapted from Mahe et al. [36] and Sato et al. [31])

6.3.2.1 One Day before Isolation of Crypts

1. Prepare one 50 ml and one 15 ml BSA-coated tubes.
2. Prepare 150 ml of PBS, sterilize it by autoclaving and dispense in four 25 ml aliquots into 50 ml tubes and one 40 ml aliquot into BSA-coated tube.
3. Prepare two 10 ml aliquots in 15 ml tubes of sterile dissociation buffer (DB).
4. Prepare 500 ml of sterile DMEM F12 [Ham] medium with 1% penicillin/streptomycin and 1% Gln, dispense in two 50 ml aliquots. Keep one aliquot on ice (for washing). Supplement the second aliquot with B27, N2 and NAC to obtain BCM, pre-warm it at room temperature before use. Fresh BCM can be prepared from DMEM F12 [Ham]/penicillin/streptomycin/Gln medium.
5. Place a 500 µl aliquot of Matrigel on ice and keep it for further use (sufficient for 9-10 seedings of organoids, *see* **Note 1**)

6.3.2.2 Crypt Isolation and Seeding

1. Place on ice: (a) a 500 µl aliquot of Matrigel; (b) vials with PBS [5], DMEM-F12 [HAM]/1% penicillin/streptomycin/1% Gln media [1]; (c) Sylgard pre-coated Petri dish.
2. Sacrifice an animal and excise proximal half of the small intestine.
3. Wash unopened intestine from feces using ice-cold PBS and syringe with cut 18 G1/2 needle.
4. Open up the intestine longitudinally with scissors. Stretch the tissue with mucosal side facing up on a pre-chilled Petri dish pre-coated with Sylgard using insect pins or small needles. Gently scrub the villi with cell scraper, rinse the tissue with ice-cold PBS and cut into 5 mm pieces. This procedure should be performed on ice with tissue soaked in cold PBS. Excessive tissue damage influences cell viability.
5. Transfer all pieces of the intestine into the first 50 ml tube with 25 ml of ice-cold PBS. Gently invert the tube 5–10 times, then let the tissue settle and remove supernatant. Transfer the residue to another tube with cold 25 ml PBS. Repeat the washing two more times.
6. Transfer tissue fragments into the first 15 ml tube with 10 ml DB. Gently rotate for 5 min at 4 °C.
7. Discard the supernatant, transfer the tissue to another 15 ml tube with 10 ml DB and rotate for further 40 min at 4 °C (in a cold room).
8. After incubation vigorously shake the tissue for 1 min while keeping it cooled. This should separate the crypts and make the solution cloudy.
9. Filter 10 ml of the suspension of crypts through a 70 µm cell strainer into a 50 ml BSA-coated tube with 40 ml of ice-cold PBS. The filtrate contains crypts and small amounts of villi.
10. Centrifuge at 600 g for 15 min at 4 °C.
11. Discard the supernatant, add aseptically 20 ml of ice-cold DMEM F12 [Ham]/1% penicillin/streptomycin/1% Gln medium and gently resuspend the pellet of crypts by pipetting. Centrifuge again at 600 g for 15 min at 4 °C.
12. From this stage onwards all the procedures should be performed under sterile conditions.
13. Discard the supernatant and re-suspend the pellet in 10 ml of ice-cold DMEM F12 [Ham]/1% penicillin/streptomycin/1% Gln medium. Take 10 µl aliquot of this suspension and count the total number of crypts in this volume and in the stock solution (multiply by 1000). With proper isolation the number of crypts should normally be around 60 per 10 µl.
14. Calculate the required seeding number of crypts for your experiment. Transfer the required aliquot into BSA-coated 15 ml tube and centrifuge as in step 10. Remove the supernatant and keep the tube on ice.
15. Add Matrigel to crypt pellet to produce approximately 200–500 crypts per 50 µl. Mix well without forming bubbles and keep the vial on ice.

16. Add 50 µl aliquots of Matrigel/crypts mixture to the wells of pre-warmed 24 well plate (*see* **Note 2**). Transfer the plate into CO_2 incubator 37 °C for 5 min to solidify the Matrigel.
17. Prepare the necessary volume of growth medium (GM) with growth factors and add 500 µl of it to each well to fully cover the solidified Matrigel. Fill the empty wells with sterile water.
18. Transfer the plate to an incubator and culture organoids at 5% CO_2, 37 °C (**Notes 3 and 4**).
19. Replace the media with fresh every 3–4 days and split organoids as required (i.e. weekly).

6.3.2.3 Passaging Organoid Cultures (1–2 Times a Week)

1. To split the organoids, remove growth medium from the well and disintegrate the Matrigel with sterile pipette tip (see **Note 5**).
2. Collect Matrigel pieces into 15 ml tube by rinsing the well with 10 ml of DMEM F12 [Ham]/1% penicillin/streptomycin/1% Gln medium. Gently rock the tube and centrifuge the tube at 600 g for 5 min.
3. Discard supernatant and repeat the washing of organoid pellet (*see* **Note 6**).
4. Resuspend the organoid pellet in freshly thawed Matrigel at desired concentration (>200 crypts/50 µl).
5. Seed 50 µl aliquots of the Matrigel in pre-warmed 24-well plate as above (steps 16–19). Add GM and continue the cultivation.

6.3.3 Live Imaging of Organoids

One day prior to imaging repeat Steps of Sect. 6.3.2.3. Seed 20 µl of the Matrigel with organoids in 35 mm tissue culture dish with micro-well or alternative imaging substrate (see Sect. 6.2.3). If imaging requires significant number of organoids in the field of view, seed them at higher density (*see* **Note 7**).

6.3.3.1 Staining of Intestinal Organoids with Live Imaging Probes

1. On the day of imaging dilute Pt-Glc probe in 200 µl of GM to produce 2 µM solution.
2. Replace medium in organoid culture with this solution and incubate for 1.5 h at regular cultivation conditions. Make sure that probe solution is sufficient to cover Matrigel layer in the micro-well of microscopy dish.
3. (Optional) Simultaneously stain organoids with other live imaging probes, e.g. Hoechst 33342 and TMRM (see Table 6.1).
4. Gently remove Pt-Glc-containing medium from the microscopy dish, rinse once with imaging medium without disturbing Matrigel layer and add 2–3 ml of imaging medium and immediately proceed to imaging.

6.3.3.2 Microscopy

1. Turn on the microscope, lasers, camera, incubator system, computer and other operating electronic blocks. Allow the system to warm up for 30 min. Prepare system control software. Select the appropriate filter cubes for the probe(s) used. Set up the incubator system (e.g. 37 °C, 19% O_2, 5% CO_2 in sample compartment).
2. Take a microscopy dish with stained organoids and place it on the microscope stage. Select the objective and bring it to working position. (*see* **Note 8**)
3. Preview the sample in transmission light mode. Select the organoids and regions of interest (ROI) for imaging, adjust focus.
4. Perform quick preview scan in fluorescence intensity mode (excitation at 405 nm, emission at 650 nm). Examine probe distribution in organoids and adjust image acquisition settings for PLIM. While optimizing the settings, parameters such as acquisition time, image quality, spatial resolution and sufficient signal intensities collected are taken into consideration (*see* **Note 9**).
5. (Optional for 3D scanning) Find the two extreme points (the top and bottom of the organoid) and select the range and increment for Z-stacks.
6. Collect sets of images (Z-stack frames in confocal PLIM for Pt-Glc probe), using the settings specified in Sect. 6.2.2.2.
7. When image acquisition is complete, save the data (raw intensity or PLIM images). Typical images of intestinal organoids stained with

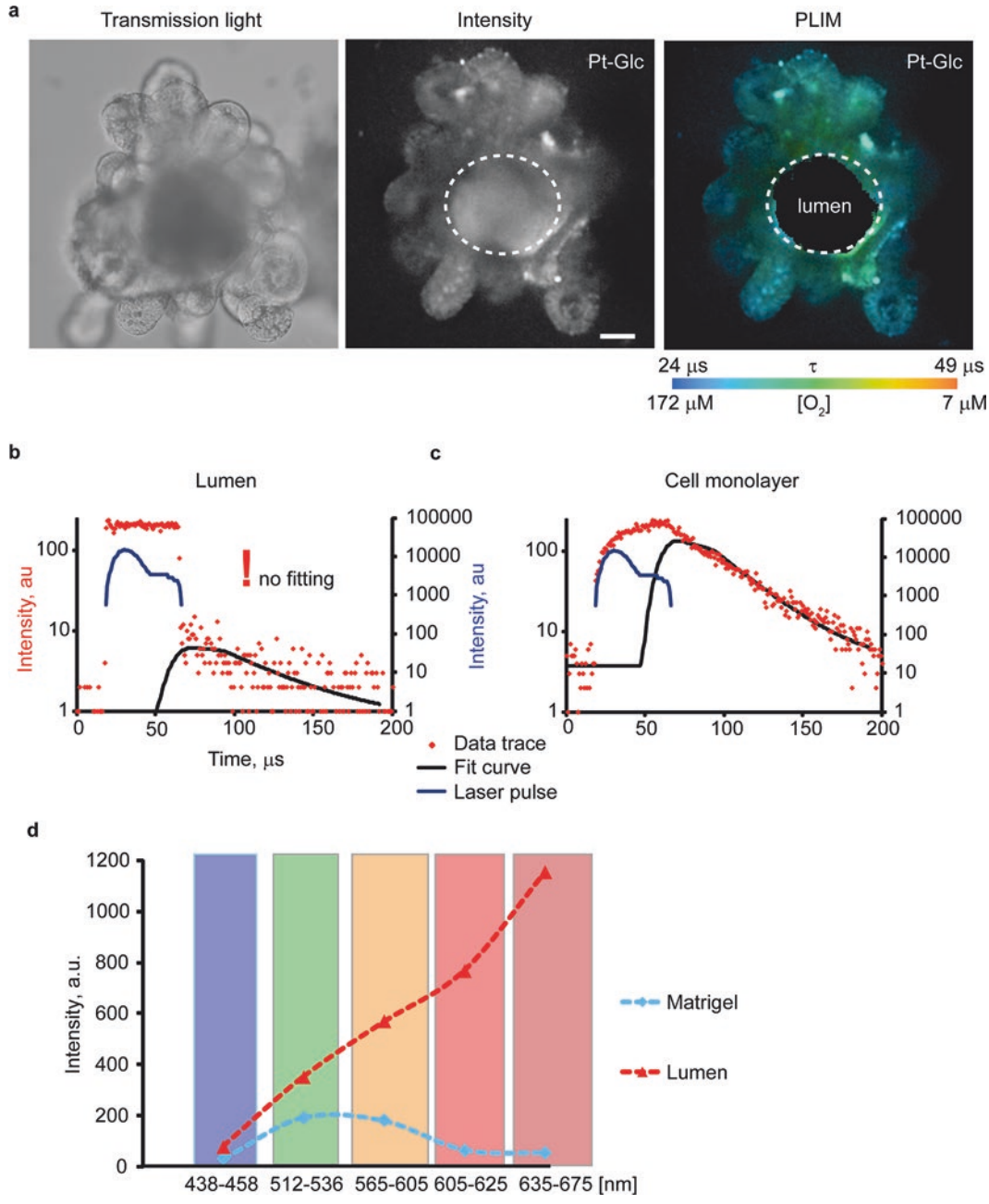

Fig. 6.1 (**a**) Appearance and staining of intestinal organoids with Pt-Glc probe. From left to right: transmission light image, phosphorescence intensity image and phosphorescence lifetime/O_2 distribution. Note that transmission light and PLIM images were taken separately. Intensity image shows strong autofluorescence in the lumen (*circled*), which is excluded (dark area of lumen) from the analysis using threshold function (SPCImage software). Scale bar is 50 μm. (**b**, **c**) Comparison of phosphorescence decays for pixels selected in lumen (**b**) and cells stained with Pt-Glc (**c**). *Green* line indicates laser "on" time, *blue* dots indicate distribution of photons in time, red curve fits the decay. (**d**) Average spectra of autofluorescence of Matrigel and organoids, collected with different bandpass emission filters (indicated on X-axis, nm) under excitation with 405 nm laser

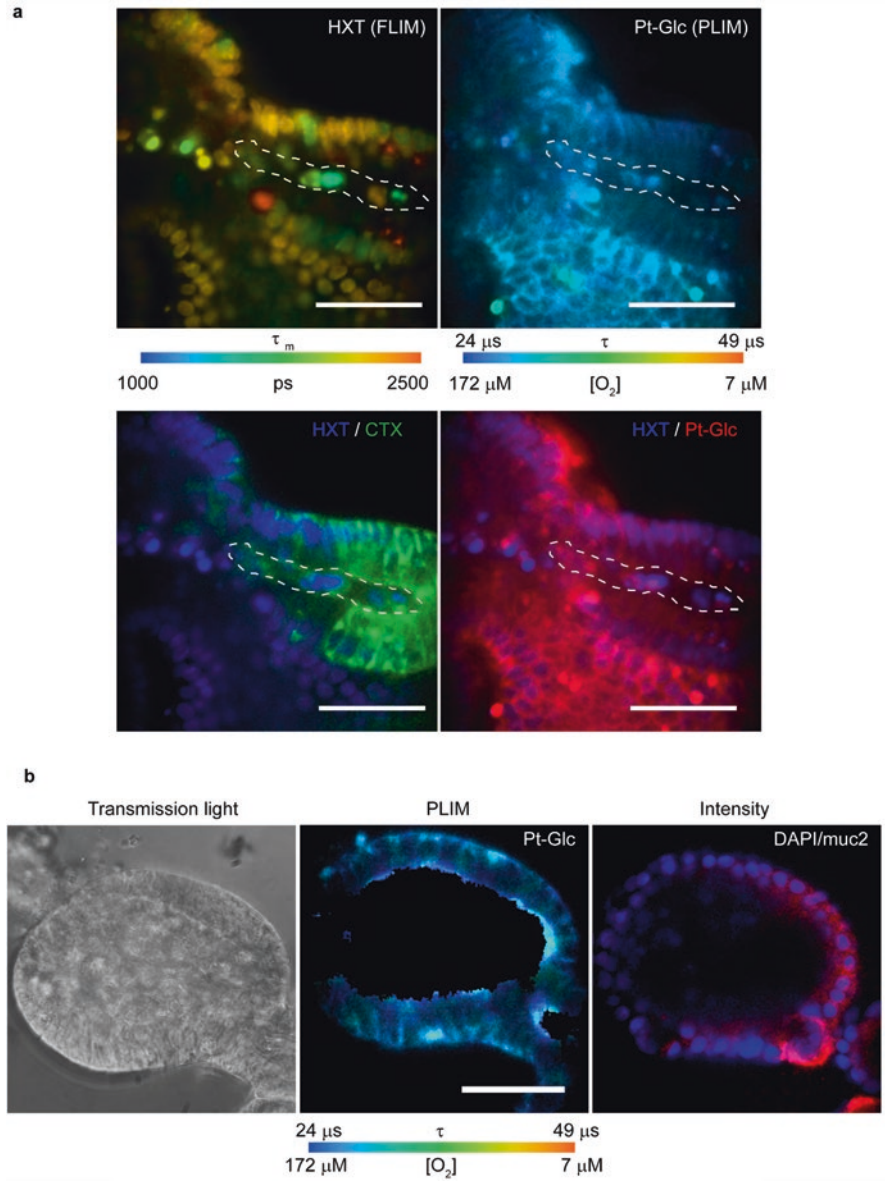

Fig. 6.2 Examples of multi-parametric imaging of intestinal organoids. (**a**) Live imaging of intestinal organoids, pre-stained with Hoechst 33342 + BrdU (HXT), Pt-Glc) and CTX-Alexa 488 (CTX): FLIM of HXT informs on cell proliferation (405 nm exc., 438–458 nm em.) (*top-left*); PLIM of Pt-Glc informs on oxygenation in intestinal organoids (405 nm exc., 635–675 nm em.) (*top-right*). *Bottom* panels display intensity images of HXT merged with CTX-Alexa 488 and Pt-Glc, informing on localization of the probes and structure of crypt. Intestinal organoids were incubated with 100 µM BrdU for 4 h and stained with HXT and CTX-Alexa 488 for 1 h prior to imaging procedure. (**b**) Multi-parametric analysis of O_2 distribution (false-color PLIM image, live organoid) combined with immunofluorescent staining against mucin-2 (shown in *red*, with nuclei labeled in *blue*, fixed organoid). Scale bar is 50 µm

Pt-Glc (transmission light, intensity and PLIM image) are shown in Fig. 6.1 (*see* **Note 10**).

8. (Optional) After or before each cycle of O_2 imaging, other fluorescent probes can be imaged in each cycle (see Table 6.1). This can be useful for easier pre-focusing on the sample/region of interest or for multi-parametric assays such as analysis of cell proliferation. The example of multi-parametric live imaging of intestinal organoids is shown on Fig. 6.2 (*see* **Note 11**).
9. Repeat measurements several times to ensure consistency and reproducibility of images (*see* **Note 12**).
10. (Optional) Apply stimuli/drugs to the sample, for example 2 μM FCCP to activate or 1 mM KCN to block cellular respiration, and monitor changes in oxygenation within the organoids by measuring sample every 1–5 min. Organoid resting state (i.e. without drug addition) must be imaged first. Make sure that 'autosave' option is on, to record subsequent replicates. Drug additions can be done between scans. The addition of 1/10th of volume of 10x concentrate of drug is recommended. Diffusion and action of drugs in 200-500 μm size organoids and Matrigel is slower than for cell monolayers and prolonged incubations (5–30 min) may be required for observe the complete effect. The effect of FCCP treatment on organoid oxygenation is shown in Fig. 6.3 (*see* **Note 13**).

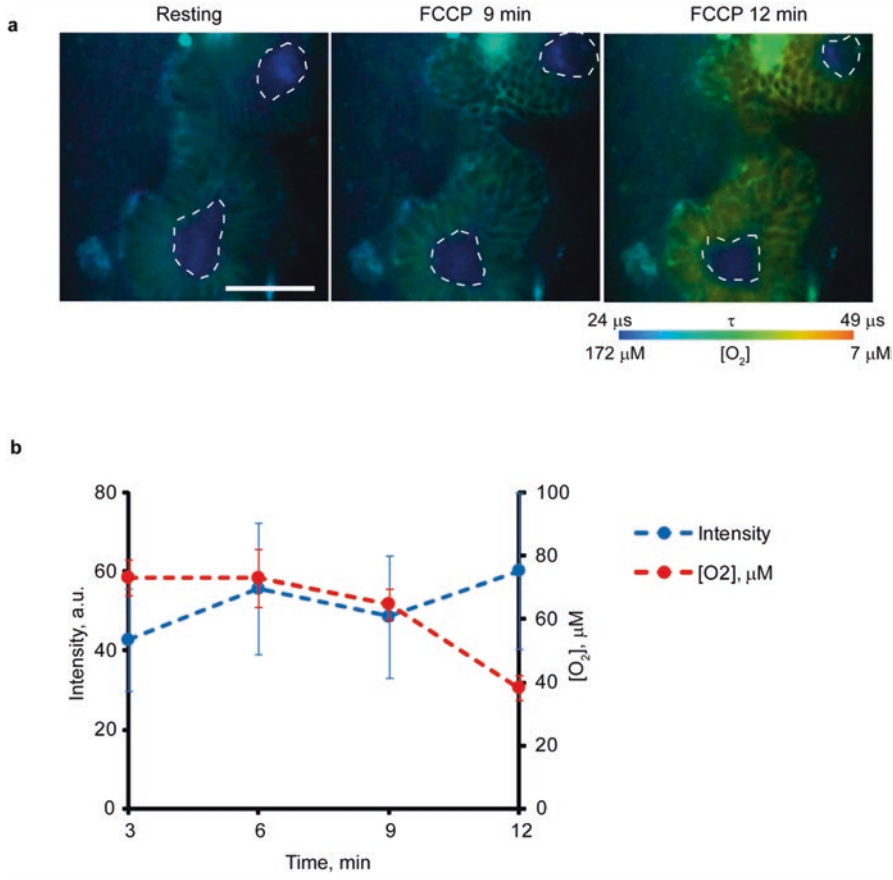

Fig. 6.3 Characteristic changes in organoid oxygenation upon treatment with mitochondrial uncoupler FCCP (2 μM). Organoids were grown and measured under 21% O_2/in growth medium, containing 17.5 mM glucose. (**a**) false-color O_2 distribution PLIM maps at different time points. Scale bar is 100 μm. (**b**) Average oxygenation (*red*) and phosphorescence intensity (*blue*) changes post FCCP treatment

11. After the live imaging organoids can be analyzed by immunofluorescence method according to Sect. 6.3.3.3.
12. Process imaging data according to Sect. 6.3.4.

6.3.3.3 Fixation and Immunofluorescent Staining of Organoids

1. Prepare organoids for imaging and (if required) image them live as described in Sects. 6.3.3.1 and 6.3.3.2.
2. Remove imaging medium from the microscopy dish with organoids, rinse the sample 3 times with warm PBS trying not to disturb the Matrigel layer.
3. Add pre-chilled (−20 °C) methanol on top of Matrigel layer and incubate at −20 °C for 15 min to fix the organoids. After fixation Matrigel becomes slightly white due to dehydration. It will become transparent again after washing with buffers. Methanol fixation retains rigid structure of Matrigel without changing localization of organoids. Use fresh, high quality methanol, residual water can reduce the quality of fixation.
4. Rinse the sample three times with 2 ml of TBST buffer to remove methanol and rehydrate the sample.
5. Add 2 ml blocking solution (5% FBS in TBST) to the sample and incubate 1 h at room temperature.
6. Remove blocking solution, add 2 ml primary antibody solution in blocking buffer at recommended dilution, and incubate overnight at 4 °C. Diffusion of antibodies in thick Matrigel layer is slow; therefore higher concentration of antibodies may be required (optimized in a separate experiment).
7. Wash the sample five times with TBST, add secondary antibodies labeled with Alexa Fluor 488 or 594 dyes at recommended dilution, and incubate for 1 h at room temperature. If required, co-stain nuclei with DAPI (5–10 μM, 30 min).
8. Wash the sample five times with TBST. Add water (for upright microscopy) or mount in anti-fading medium (for inverted microscopy) and perform fluorescence imaging under corresponding settings. Typical immunofluorescence images are presented in Fig. 6.2b. (*see* **Note 14**).
9. Process the imaging data. See details in Sect. 6.3.4.

6.3.3.4 Calibration of the phosphorescent O_2 probe

This procedure is optional and can be performed for any available O_2 probes. However, this procedure needs O_2 control module installed in the microscope incubator.

1. Prepare intestinal organoids for imaging and stain them with O_2 probe as described in Sects. 6.3.2, 6.3.2.1, 6.3.2.2, 6.3.2.3, 6.3.3, and 6.3.3.1.
2. Wash the sample once with imaging medium, add 2 ml of low glucose (2.5 mM) medium containing 1 mM KCN and incubate for 30 min. (*see* **Note 15**)
3. Bring the specimen to the microscope equipped with O_2 control, set them up for O_2 imaging, adjust brightness and focus in preview mode as described in Protocol Sect. 6.3.3.2.
4. Check the efficiency of inhibition of organoid respiration by KCN by PLIM under ambient air (21%). The phosphorescence lifetimes should achieve lowest levels (~20 μs, if Pt-Glc is used).
5. Set the incubator to another O_2 concentration (e.g. 15%), equilibrate the sample for 15–20 min and then collect PLIM image. Repeat image acquisition several times for statistics.
6. Repeat step 5 for several other O_2 concentrations (e.g. 12, 10, 5, 2, 1%).
7. For 0% O_2 point change the medium for fresh containing 20 mM glucose, 250 μg/ml glucose oxidase, 30 μg/ml catalase, and no KCN. After 20 min incubation record the PLIM images. (*see* **Note 16**).
8. Calculate mean lifetime values for each O_2 concentration. Plot these data points, fit them with two-site model function and determine parameters of calibration (**Note 17**). The example of calibration is presented in Fig. 6.4.

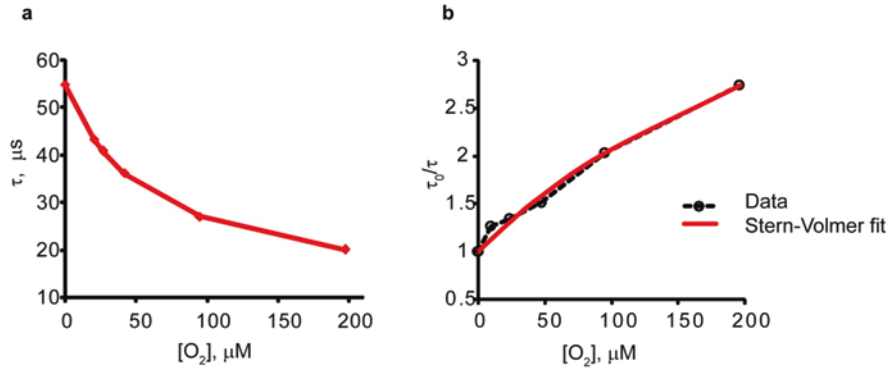

Fig. 6.4 Calibration of Pt-Glc probe in intestinal organoids: (**a**) relationship between phosphorescence lifetime (τ) and O_2 concentration. (**b**) Calibration in linearized form (Stern-Volmer plot), fitted with two-site model

6.3.4 Processing of imaging data

Example of data processing for PLIM microscope with dedicated SPCImage software (Becker & Hickl GmbH). For other PLIM platforms data processing protocol should be modified accordingly.

1. Open SPCImage software and import selected data file.
2. Calculate emission lifetime values ('Decay Matrix') for the image (ROI or whole frame).
3. Export the phosphorescence intensity and lifetime images as TIFF or ASCII files. (*see* **Note 18**).
4. Using Microsoft Excel or other relevant software and probe calibration function (see Sect. 6.3.3.4), apply arithmetic transformation to ASCII lifetime image. Save the O_2 concentration matrix as a new ASCII file.
5. Apply batch processing to other images from the same experiment, 2D stacks or time points.
6. Reconstruct 3D intensity, lifetime and/or O_2 concentration images using Fiji software (VolumeViewer Plugin) and save them. (*see* **Note 19**).

6.4 Notes

1. All reagents used during isolation of crypts (including Matrigel) should be ice-cold. Sterile solutions should be maintained throughout the procedure to avoid contamination.
2. Place drops of Matrigel to the center of the well without spreading it across the surface. We advise seeding crypts in Matrigel to centers of wells and fill surrounding areas and wells with sterile water. This will reduce media evaporation in sample wells in CO_2-incubator. 24-well plate should be pre-incubated at 37 °C for at least 30 min. At lower solidifying temperature crypts/organoids will precipitate from Matrigel to the bottom forming a 2D layer. Diluted Matrigel (less viscous) will have the same negative effect.
3. It is expected that 2 h after seeding the crypts already start forming closed round aggregate structures, elongating and dividing on the next day. All non-crypt-based cellular structures normally die within several days after seeding and do not affect organoid growth. Seeding crypts at very high concentration can inhibit growth of organoids. During their growth and cell renewal organoids accumulate dead cells in their lumen. Overgrowing leads to organoid death.
4. Organoids can also be grown in other media or under low O_2 using a hypoxia chamber or incubator with O_2 control in which all the cultivation and splitting have to be carried out. We recommend culturing organoids for 1–2 weeks under standard conditions prior to physiological experiments.
5. Organoids in Matrigel are not easy to disintegrate. For better efficiency of the process, control it using transmission light microscope. Several suppliers provide

dissociation reagents for intestinal organoids dissociation (e.g. Gentle cell Dissociation Reagent by IntestiCult, 07174). These have better efficiency but should be used with care to preserve viability of crypts. After splitting it is difficult to produce organoids of standard size, fresh primary crypts produce more homogeneous organoid structures.

6. Remains of old Matrigel can affect stability, clarity and imaging of the sample, so try to remove them completely during re-seeding avoiding the loss of organoids.
7. Splitting of organoids usually leads to increase of size heterogeneity in organoid culture. When more homogeneous cultures are needed, we recommend to seed freshly isolated crypts directly on imaging dish and grow them for desired time,.
8. Control of temperature, O_2, pH, and humidity is essential, large fluctuations should be avoided. Minimize the time the sample spends outside the incubator. The imaging medium must contain 5–20 mM HEPES-Na, pH 7.2 to maintain physiological pH (no CO_2 control). In long-term experiments (>1 h) evaporation of the medium can be significant. Monitor this daily and refill evaporated medium/water as needed.
9. Initial optimization is essential and should be carried out quickly enough, avoiding sample degradation, photodamage or photobleaching. Many microscopes possess 'preview' function for quick optimization of image acquisition settings.
10. Tissue autofluorescence can interfere with fluorescence and phosphorescence microscopy imaging [27, 28]. Intestinal organoids display strong autofluorescence in the lumen, with emission maximum at around 635–675 nm (excited at 405 nm) (Fig. 6.1) and relatively long lifetime of ~4 ns. This red emission has to be considered when analyzing the luminal part of organoids. In our experiments, it did not interfere with phosphorescence lifetime and O_2 determination in organoid tissue, nor with the other fluorescent cell and tissue stains. Matrigel® matrix produced low autofluorescence in spectral range of 438–675 nm ensuring minimal interference with imaging of organoids.
11. PLIM with Pt-Glc probe allows multiplexing with other live cell imaging probes, and subsequent fixation of the organoid tissue and immunofluorescent analysis [22, 26]. Furthermore, combined PLIM-FLIM set-up (also provided by some vendors) [24, 28, 52] enables multiplexing in spectral and time domains (i.e. ns and μs probes). It can be illustrated by multiplexing of Hoechst 33342 (FLIM) and Pt-Glc (PLIM) lifetime imaging (Fig. 6.2). Fluorescence lifetime of Hoechst 33342 is affected by BrdU incorporation into nuclear DNA during S-phase allowing simple detection of dividing cells in organoids culture (amplification zone) [28]. Many live cell imaging probes for important physiological parameters, including Ca^{2+} (Fluo-4, Oregon Green BAPTA-1), pH (BCECF, fluorescent proteins), endogenous NAD(P)H and FAD, organelle-specific tracers, toxicity, membrane integrity, apoptosis, proliferation or cell type markers (see Table 6.1 and also Chap. 4), are compatible with Pt-Glc (λ_{exc} = 405 nm, λ_{em} = 650 nm) [26]. Intestinal organoids expressing specific fluorescent protein tags and biosensor constructs can also be produced and analyzed [53]. An example of multiplexed imaging of live intestinal organoids co-stained with Pt-Glc (red), marker of cell nuclei (Hoechst 33342, blue) and lipid raft-specific probe Cholera Toxin (CTX-Alexa Fluor 488, green) is presented on Fig. 6.2.
12. Image acquisition time, laser power and total number of scans can have an impact on cell viability. This should be optimised to ensure fast image acquisition time, sufficient signal to noise ratio and minimal sample photodamage.
13. Uncoupler FCCP increases cellular and tissue respiration leading to tissue deoxygenation (affects O_2-sensitive probe signal intensity and phosphorescence lifetime, see Fig. 6.3). FCCP treatment together with TMRM staining (mitochondrial membrane potential) is a good positive control for estimating of functional status

of mitochondria. Similarly to FCCP treatment, any other drugs can be tested to analyze the mitochondrial function.

14. O_2 imaging can be coupled with subsequent sample fixation, immunofluorescence staining and correlative analysis [22, 54]. Using gridded dishes (Sect. 6.2.3), the organoids that were imaged alive can be identified and analyzed by immunofluorescence. It is important to find the same focus, however the perfect match between live and fixed organoid images is not possible, since fixation affects organoid shape. As an example we performed live O_2 imaging and then immunostaining of organoids with antibodies against goblet cell marker mucin-2 (Fig. 6.2b). We found that organoid staining with antibodies and live cell imaging probes was not compromised by Matrigel (20 µl volume). Conversely, rigid structure of the latter protects organoids from vibration during the microscopy and helps producing high-quality images. Importantly, we performed fixation of organoids with cold methanol (−18 °C), whereas conventional 4% paraformaldehyde "melts" the Matrigel and does not allow identification of organoids. However, when only the immunofluorescence analysis of organoids is needed we recommend using paraformaldehyde fixation as it usually ensures better quality images. In addition, fixation with methanol is not compatible with all antibodies.
15. We found that high glucose content in the medium slows down the effect of KCN. KCN is also unstable in aqueous media and calibration procedure should be completed in 3–5 h.
16. Zero O_2 point is normally not achievable on standard O_2 incubators; therefore enzymatic or chemical deoxygenation of the sample is recommended. Repeat lifetime measurements to ensure that they reached maximal values (τ_0 ~ 55 µs, for Pt-Glc in organoids on our microscope). To prevent effect of photobleaching of the sample, we recommend using different regions of interest for different calibration points and replicates.
17. O_2 PLIM relies on the detection of changes in phosphorescence signal from an O_2 -sensitive probe or sensor [15, 18, 55]. Paramagnetic O_2 molecules interact with long-lived excited triplet states of the luminophore and quench its phosphorescence lifetime (τ) and intensity (I) signals (Fig. 6.4). The process is direct, reversible and non-chemical. In an ideal case, τ and I relationship with O_2 concentration obeys Stern-Volmer equation [56] (Eq. (6.1)). However, for a common cases of heterogeneous probe distribution or its microenvironment, more complex models are used, such as the two-site model [57], which is shown in simplified form [58] as Eq. (6.2):

$$I_0 / I = \tau_0 / \tau = 1 + K_{sv} \times [O_2]; \quad (6.1)$$

$$\text{Two - site model} : \tau 0 / \tau = \frac{1}{\frac{f}{1 + Ksv1 \times [O2]} + 1 - f}; \quad (6.2)$$

I_0 and τ_0 are unquenched intensity and lifetime values (at zero O_2). K_{sv} is the Stern-Volmer quenching constant, f is the fraction of the total emission of the first component [16, 58].

Unlike the phosphorescence intensity, the lifetime signal is largely independent on probe concentration/distribution in the sample, photobleaching, measurement geometry and instabilities of the detection system, and therefore it provides more stable calibration and O_2 measurements [15]. The calibration parameters τ_0, f and K_{sv} are a feature of particular phosphorescent material. O_2 calibrations produced on different instruments, tissue samples or probe batches may differ slightly. Therefore, we recommend calibration of each microscope, biological model and measurement setup, when possible. Once this is done with organoid culture, lifetime calibration of the probe can then be used for many months or years.

For calibration, an incubator with O_2 control mounted on microscope stage is required.

To eliminate O_2 gradients in the sample which can skew O_2 calibration, respiration of organoids pre-stained with the probe must be fully inhibited [59]. We found that potassium cyanide (KCN) and sodium azide (NaN_3) ensured this effect, while drugs Antimycin A, piericidine A and myxothiazole did not block respiration of intestinal organoids. After the inhibition of respiration, organoids are exposed to various O_2 in the medium and phosphorescence lifetime images are recorded. Average lifetime values are determined for each O_2 concentration and then fitted in a suitable software (e.g. Origin, OriginLab). For mouse intestinal organoids and Pt-Glc (loading concentration 2 μM, loading time 1.5 h, 37 °C), the parameters of the calibration were: τ_0 = 54.8711 μs, f = 0.82587 and K_{sv} = 0.01683 μM^{-1}. Therefore, the following equation can be used for calculation of O_2 concentration in organoids:

$$\left[O_2,\ \mu M\right] = (0.82587 / (-0.7413 + \tau / 54.8711) - 1) / 0.01683; \quad (6.3)$$

where τ is in μs.

18. Different vendors of imaging equipment use different file formats and data processing algorithms. Transmission and luminescence intensity images are easy to handle in TIFF format. Lifetime images can be handled as color TIFF files, or converted into O_2 concentration images via ASCII files.
19. Pt-Glc showed efficient in-depth staining of the organoids in as little as 0.5–1.5 h and bright phosphorescent signals, which fitted well with mono-exponential decay (Fig. 6.1). Several other nanoparticle phosphorescent probes were also tested, but they provided much slower and weaker staining of intestinal epithelia (not shown). Pt-Glc did not show any significant non-specific staining of Matrigel matrix with little accumulation in the lumen (Fig. 6.1). We also noticed large structures of unknown origin outside of the organoids with bright phosphorescent staining and high lifetime values (not shown). These structures, which look like aggregates of dead cells and also observed with other fluorescent probes, did not affect the O_2 measurements in the organoids. Typical intensity signals and phosphorescence decays of Pt-Glc probe in organoids are presented in Fig. 6.1 (blue dots). The SPCImage software (or other relevant [60]) is used to fit the decays (red line) and calculate phosphorescence lifetimes. This is normally done by adjusting the initial fitting parameters T1 and T2 in SPCImage software and binning factor, for randomly selected pixels. Then, the fitting is applied for the whole field or selected region of interest. Application of O_2 calibration function on a pixel-by-pixel basis converts calculated phosphorescence lifetime values into O_2 concentrations giving the 2D O_2 maps. Regions with low probe signal, such as lumen, are excluded from the fitting and will be shown in black (Fig. 6.1). Confocal scanning at different depths produces a stack of 2D sections, which can be then assembled into 3D image of O_2 distribution.

Acknowledgments This work was supported by Science Foundation Ireland (SFI) grants 13/SIRG/2144 (RID) and 12/RC/2276 (IAO and DBP).

References

1. Lopez-Lazaro M (2009) Role of oxygen in cancer: looking beyond hypoxia. Anti Cancer Agents Med Chem 9(5):517–525
2. Sung HJ, Ma W, Starost MF, Lago CU, Lim PK, Sack MN et al (2011) Ambient oxygen promotes tumorigenesis. PLoS One 6(5):e19785
3. Qin J, Li Y, Cai Z, Li S, Zhu J, Zhang F et al (2012) A metagenome-wide association study of gut microbiota in type 2 diabetes. Nature 490(7418):55–60
4. Karlsson FH, Tremaroli V, Nookaew I, Bergström G, Behre CJ, Fagerberg B et al (2013) Gut metagenome in European women with normal, impaired and diabetic glucose control. Nature 498(7452):99–103
5. Rigottier-Gois L (2013) Dysbiosis in inflammatory bowel diseases: the oxygen hypothesis. ISME J 7(7):1256–1261
6. Schaffer K, Taylor CT (2015) The impact of hypoxia on bacterial infection. FEBS J 282(12):2260–2266

7. Jennewein J, Matuszak J, Walter S, Felmy B, Gendera K, Schatz V et al (2015) Low-oxygen tensions found in Salmonella-infected gut tissue boost Salmonella replication in macrophages by impairing antimicrobial activity and augmenting Salmonella virulence. Cell Microbiol 17(12):1833–1847
8. Marteyn B, West NP, Browning DF, Cole JA, Shaw JG, Palm F et al (2010) Modulation of Shigella virulence in response to available oxygen in vivo. Nature 465(7296):355–358
9. Zheng L, Kelly CJ, Colgan SP (2015) Physiologic hypoxia and oxygen homeostasis in the healthy intestine. Am J Phys Cell Phys 309(6):C350–C360
10. Wolfbeis OS (2015) Luminescent sensing and imaging of oxygen: fierce competition to the Clark electrode. BioEssays 37(8):921–928
11. Roussakis E, Li Z, Nichols AJ, Evans CL (2015) Oxygen-sensing methods in biomedicine from the macroscale to the microscale. Angew Chem Int Ed 54(29):8340–8362
12. Papkovsky DB, Dmitriev RI (2013) Biological detection by optical oxygen sensing. Chem Soc Rev 42(22):8700–8732
13. Krohn KA, Link JM, Mason RP (2008) Molecular imaging of hypoxia. J Nucl Med 49(Suppl 2):129S–148S
14. Devor A, Sakadzic S, Srinivasan VJ, Yaseen MA, Nizar K, Saisan PA et al (2012) Frontiers in optical imaging of cerebral blood flow and metabolism. J Cereb Blood Flow Metab 32(7):1259–1276
15. Dmitriev RI, Papkovsky DB (2012) Optical probes and techniques for O2 measurement in live cells and tissue. Cell Mol Life Sci 69(12):2025–2039
16. Quaranta M, Borisov SM, Klimant I (2012) Indicators for optical oxygen sensors. Bioanal Rev 4(2-4):115–157
17. Dmitriev RI, Papkovsky DB (2015) Intracellular probes for imaging oxygen concentration: how good are they? Methods Appl Fluoresc 3(3):034001
18. Kelly CJ, Zheng L, Campbell EL, Saeedi B, Scholz CC, Bayless AJ et al (2015) Crosstalk between microbiota-derived short-chain fatty acids and intestinal epithelial HIF augments tissue barrier function. Cell Host Microbe 17(5):662–671
19. Albenberg L, Esipova TV, Judge CP, Bittinger K, Chen J, Laughlin A et al (2014) Correlation between intraluminal oxygen gradient and radial partitioning of intestinal microbiota in humans and mice. Gastroenterology 147(5):1055–63.e8
20. Dmitriev R, Borisov S, Kondrashina A, Pakan JP, Anilkumar U, Prehn JM et al (2015) Imaging oxygen in neural cell and tissue models by means of anionic cell-permeable phosphorescent nanoparticles. Cell Mol Life Sci 72(2):367–381
21. Dmitriev RI, Borisov SM, Jenkins J, Papkovsky DB (2015) Multi-parametric imaging of tumor spheroids with ultra-bright and tunable nanoparticle O2 probes. In: Proceedings SPIE
22. Dmitriev RI, Zhdanov AV, Nolan YM, Papkovsky DB (2013) Imaging of neurosphere oxygenation with phosphorescent probes. Biomaterials 34(37):9307–9317
23. Zhdanov AV, Golubeva AV, Okkelman IA, Cryan JF, Papkovsky D (2015) Imaging of oxygen gradients in giant umbrella cells: an ex vivo PLIM study. Am J Phys Cell Phys 309(7):C501–C5C9
24. Jenkins J, Borisov SM, Papkovsky DB, Dmitriev RI (2016) Sulforhodamine nanothermometer for multiparametric fluorescence lifetime imaging microscopy. Anal Chem 88(21):10566–10572
25. Zhdanov AV, Okkelman IA, Golubeva AV, Doerr B, Hyland NP, Melgar S et al (2017) Quantitative analysis of mucosal oxygenation using ex vivo imaging of healthy and inflamed mammalian colon tissue. Cell Mol Life Sci 74(1):141–151
26. Dmitriev RI, Kondrashina AV, Koren K, Klimant I, Zhdanov AV, Pakan JMP et al (2014) Small molecule phosphorescent probes for O2 imaging in 3D tissue models. Biomater Sci 2(6):853–866
27. James ML, Gambhir SS (2012) A molecular imaging primer: modalities, imaging agents, and applications. Physiol Rev 92(2):897–965
28. Okkelman IA, Dmitriev RI, Foley T, Papkovsky DB (2016) Use of fluorescence lifetime imaging microscopy (FLIM) as a timer of cell cycle S phase. PLoS One 11(12):e0167385
29. Ponsioen B, Snippert HJ (2017) Cancer systems biology: live imaging of intestinal tissue in health and disease. Curr Opin Syst Biol 2:19–28
30. Leushacke M, Barker N (2014) Ex vivo culture of the intestinal epithelium: strategies and applications. Gut 63(8):1345–1354
31. Sato T, Vries RG, Snippert HJ, van de Wetering M, Barker N, Stange DE et al (2009) Single Lgr5 stem cells build crypt–villus structures in vitro without a mesenchymal niche. Nature 459(7244):262–265
32. Ootani A, Li X, Sangiorgi E, Ho QT, Ueno H, Toda S et al (2009) Sustained in vitro intestinal epithelial culture within a Wnt-dependent stem cell niche. Nat Med 15(6):701–706
33. Pastuła A, Middelhoff M, Brandtner A, Tobiasch M, Höhl B, Nuber AH et al (2015) Three-dimensional gastrointestinal organoid culture in combination with nerves or fibroblasts: a method to characterize the gastrointestinal stem cell niche. Stem Cells Int 2015:3710836
34. McCracken KW, Catá EM, Crawford CM, Sinagoga KL, Schumacher M, Rockich BE et al (2014) Modelling human development and disease in pluripotent stem-cell-derived gastric organoids. Nature 516:400–404
35. Sato T, Stange DE, Ferrante M, Vries RG, Van Es JH, Van den Brink S et al (2011) Long-term expansion of epithelial organoids from human colon, adenoma, adenocarcinoma, and Barrett's epithelium. Gastroenterology 141(5):1762–1772
36. Mahe MM, Aihara E, Schumacher MA, Zavros Y, Montrose MH, Helmrath MA et al (2013) Establishment of gastrointestinal epithelial organoids. Curr Protoc Mouse Biol 3:217–240

37. Zhang YG, Wu S, Xia Y, Sun J (2014) Salmonella-infected crypt-derived intestinal organoid culture system for host–bacterial interactions. Phys Rep 2(9):e12147
38. Bermudez-Brito M, Plaza-Díaz J, Fontana L, Muñoz-Quezada S, Gil A (2013) In vitro cell and tissue models for studying host–microbe interactions: a review. Br J Nutr 109(S2):S27–S34
39. Lukovac S, Belzer C, Pellis L, Keijser BJ, de Vos WM, Montijn RC et al (2014) Differential modulation by Akkermansia muciniphila and Faecalibacterium prausnitzii of host peripheral lipid metabolism and histone acetylation in mouse gut organoids. MBio 5(4):e01438–e01414
40. Yin Y, Bijvelds M, Dang W, Xu L, van der Eijk AA, Knipping K et al (2015) Modeling rotavirus infection and antiviral therapy using primary intestinal organoids. Antivir Res 123:120–131
41. Forbester JL, Goulding D, Vallier L, Hannan N, Hale C, Pickard D et al (2015) The interaction of Salmonella enterica Serovar Typhimurium with intestinal organoids derived from human induced pluripotent stem cells. Infect Immun 83(7):2926–2934
42. Onuma K, Ochiai M, Orihashi K, Takahashi M, Imai T, Nakagama H et al (2013) Genetic reconstitution of tumorigenesis in primary intestinal cells. Proc Natl Acad Sci 110(27):11127–11132
43. Matano M, Date S, Shimokawa M, Takano A, Fujii M, Ohta Y et al (2015) Modeling colorectal cancer using CRISPR-Cas9-mediated engineering of human intestinal organoids. Nat Med 21:256–262
44. Mahnke A, Meier RJ, Schatz V, Hofmann J, Castiglione K, Schleicher U et al (2014) Hypoxia in leishmania major-skin lesions impairs the NO-dependent leishmanicidal activity of macrophages. J Invest Dermatol 134(9):2339–2346
45. Rodansky ES, Johnson LA, Huang S, Spence JR, Higgins PD (2015) Intestinal organoids: a model of intestinal fibrosis for evaluating anti-fibrotic drugs. Exp Mol Pathol 98(3):346–351
46. Liu J, Walker NM, Ootani A, Strubberg AM, Clarke LL (2015) Defective goblet cell exocytosis contributes to murine cystic fibrosis–associated intestinal disease. J Clin Invest 125(3):1056–1068
47. Wen Y-A, Li X, Goretsky T, Weiss HL, Barrett TA, Gao T (2015) Loss of PHLPP protects against colitis by inhibiting intestinal epithelial cell apoptosis. Biochim Biophys Acta 1852(10):2013–2023
48. Yan KS, Chia LA, Li X, Ootani A, Su J, Lee JY et al (2012) The intestinal stem cell markers Bmi1 and Lgr5 identify two functionally distinct populations. Proc Natl Acad Sci 109(2):466–471
49. Okamoto R, Watanabe M (2015) Role of epithelial cells in the pathogenesis and treatment of inflammatory bowel disease. J Gastroenterol 51(1):1–11
50. Grant CN, Mojica SG, Sala FG, Hill JR, Levin DE, Speer AL et al (2015) Human and mouse tissue-engineered small intestine both demonstrate digestive and absorptive function. Am J Phys 308(8):G664–GG77
51. Dmitriev RI, Borisov SM, Düssmann H, Sun S, Müller BJ, Prehn J et al (2015) Versatile conjugated polymer nanoparticles for high-resolution O2 imaging in cells and 3D tissue models. ACS Nano 9(5):5275–5288
52. Jahn K, Buschmann V, Hille C (2015) Simultaneous fluorescence and phosphorescence lifetime imaging microscopy in living cells. Sci Rep 5:14334
53. Fujii M, Matano M, Nanki K, Sato T (2015) Efficient genetic engineering of human intestinal organoids using electroporation. Nat Protoc 10(10):1474–1485
54. Dmitriev R, Papkovsky D (2015) Multi-parametric O2 imaging in three-dimensional neural cell models with the phosphorescent probes. Methods Mol Biol 1254:55–71
55. Jenkins J, Dmitriev RI, Morten K, McDermott KW, Papkovsky DB (2015) Oxygen-sensing scaffolds for 3-dimensional cell and tissue culture. Acta Biomater 16(0):126–135
56. Stern O, Volmer M (1919) Über die abklingzeit der fluoreszenz. Phys Z 20:183–188
57. Carraway E, Demas J, DeGraff B, Bacon J (1991) Photophysics and photochemistry of oxygen sensors based on luminescent transition-metal complexes. Anal Chem 63(4):337–342
58. Borisov SM, Klimant I (2007) Ultrabright oxygen optodes based on cyclometalated iridium (III) coumarin complexes. Anal Chem 79(19):7501–7509
59. Foster KA, Galeffi F, Gerich FJ, Turner DA, Müller M (2006) Optical and pharmacological tools to investigate the role of mitochondria during oxidative stress and neurodegeneration. Prog Neurobiol 79(3):136–171
60. Arena ET, Rueden CT, Hiner MC, Wang S, Yuan M, Eliceiri KW (2016) Quantitating the cell: turning images into numbers with ImageJ. Wiley Interdiscip Rev Dev Biol 6(2). https://doi.org/10.1002/wdev.260

7

Imaging of Intracellular pH in Tumor Spheroids Using Genetically Encoded Sensor SypHer2

Elena V. Zagaynova, Irina N. Druzhkova, Natalia M. Mishina, Nadezhda I. Ignatova, Varvara V. Dudenkova, and Marina V. Shirmanova

Abstract

Intracellular pH (pHi) is one of the most important parameters that regulate the physiological state of cells and tissues. pHi homeostasis is crucial for normal cell functioning. Cancer cells are characterized by having a higher (neutral to slightly alkaline) pHi and lower (acidic) extracellular pH (pHe) compared to normal cells. This is referred to as a "reversed" pH gradient, and is essential in supporting their accelerated growth rate, invasion and migration, and in suppressing anti-tumor immunity, the promotion of metabolic coupling with fibroblasts and in preventing apoptosis. Moreover, abnormal pH, both pHi and pHe, contribute to drug resistance in cancers. Therefore, the development of methods for measuring pH in living tumor cells is likely to lead to better understanding of tumor biology and to open new ways for cancer treatment. Genetically encoded, fluorescent, pH-sensitive probes represent promising instruments enabling the subcellular measurement of pHi with unrivaled specificity and high accuracy. Here, we describe a protocol for pHi imaging at a microscopic level in HeLa tumor spheroids, using the genetically encoded ratiometric (dual-excitation) pHi indicator, SypHer2.

Keywords

Intracellular pH • Genetically encoded sensor • SypHer2 • Cancer cell • Spheroids • Ratiometric imaging • Fluorescence

E.V. Zagaynova (✉) • I.N. Druzhkova • N.I. Ignatova
V.V. Dudenkova • M.V. Shirmanova (✉)
Institute of Biomedical Technologies, Nizhny Novgorod State Medical Academy,
Minin and Pozharsky Square, 10/1,
Nizhny Novgorod 603005, Russia
e-mail: ezagaynova@gmail.com; shirmanovam@mail.ru

N.M. Mishina
Shemyakin–Ovchinnikov Institute of Bioorganic Chemistry RAS, Miklukho-Maklaya St., 16/10,
Moscow 117997, Russia

R.I. Dmitriev (ed.), *Multi-Parametric Live Cell Microscopy of 3D Tissue Models*,
Advances in Experimental Medicine and Biology 1035, DOI 10.1007/978-3-319-67358-5_7

7.1 Introduction

Intracellular pH is an important regulator of many of the functions taking place inside cells [1]. In normal cells, intracellular pH (pHi) is lower than extracellular pH (pHe), with the pHi and pHe values lying mostly in the range 7.0–7.2 and 7.3–7.4, respectively. Cancer cells generally have a reversed intra-extracellular pH gradient, with higher values of pHi (7.12–7.65) and lower pHe (6.2–6.9). Extracellular acidosis in solid tumors is a consequence of enhanced glycolysis, which occurs in cancer cells even if oxygen availability is not limited (the "Warburg effect"). To extrude the glycolytic byproducts, lactate and H^+, and to maintain their pHi in a narrow physiological range, cancer cells upregulate multiple membrane H^+ transporters [2, 3].

The reversed pH gradient is considered a hallmark of neoplastic tissue, enabling cancer progression [3–5]. An elevated pHi in cancer cells promotes high proliferative activity and the evasion of apoptosis, drives a metabolic switch from oxidative phosphorylation to aerobic glycolysis, promotes genetic instability, and contributes to the multidrug resistance of cancer cells. An increased pHi and a decreased pHe coordinately enhance invasion and metastasis. Therefore, accurate measurement of pHi in living cancer cells is likely to be of great importance for better understanding cellular functions as well as for monitoring tumor growth and the responses of cancer cells to a range of treatments.

Given the significant role of pHi in tumor development, it is crucially important to be able to measure it with both high accuracy and spatiotemporal resolution. Fluorescence imaging based on pH-sensitive fluorescent probes offers excellent opportunities as a highly sensitive, low cost technique for real-time, non-invasive pH determination in cells and tissues. Despite the variety of synthetic pH sensitive fluorescent dyes available, measuring pHi remains problematic, especially in living cells and tissues. These shortcomings include problems with intracellular delivery; with self-redistribution of the dyes and their leakage from the cells; their interactions with other molecules in the cell, and their own cytotoxicity [6, 7]. As a result, the current applications for such synthetic probes are limited to the assessment of pHi in cell cultures, in dissociated spheroids and in tissues ex vivo.

In this context, pH indicators based on green fluorescent protein (GFP) represent promising instruments for overcoming the limitations of the synthetic dyes [8–10]. Being genetically encoded, they can be directed to any particular compartment within a cell or allowed to distribute themselves by diffusion within the cytosol, consequently, enabling the subcellular measurement of pH with unrivaled specificity.

Various genetically encoded pH indicators for measuring cytosolic pH have been developed so far, including GFP [11], EGFP [12], EYFP [12], ECFP [12], pHluorins [13–16], deGFP [17], E^2GFP [18], E^1GFP [19], GFpH [20], YFpH [20], SypHer [21] and SypHer2 [22]. A number of GFP mutants, such as pHluorin [16], EYFP-mito [12], MitoSypHer [21], mtAlpHi [23] and GFP-pH [24] have also been engineered to monitor the pH of the mitochondrial matrix. There are additional examples of pH-sensitive fluorescent proteins targeted toward the Golgi apparatus in cancer cell lines [25, 26]. Serresi et al. have described an application where E1GFP fused to the HIV-Tat protein is used in the measurement of pH changes along the endo-lysosomal pathway [19].

However, it should be mentioned that in cancer studies the use of genetically encoded pH sensors has previously been recorded mostly for monolayer cell cultures. Since animal tissues have poor permeability to light, pHi sensing with genetically encoded indicators in the more complicated models of cancer, such as tumor spheroids and animal tumors in vivo remains challenging. For these purposes, the new types of optimized ratiometric or fluorescence lifetime based pH indicators are required, as they show absorption and fluorescence in the optical window, and have enhanced brightness and broad dynamic ranges.

Recently, we have developed a new genetically encoded pH sensitive ratiometric indicator,

SypHer2, based on the cpYFP fluorophore, and have shown its applicability for pHi analysis in cultured cancer cells and tumor xenografts [22, 27]. SypHer2 has two excitation peaks, one at 420 nm and the other at 500 nm, and a single emission peak at 516 nm [22]. The stable expression of SypHer2 in tumor cells opens up possibilities for continuous pH monitoring in living cells and tissues.

Tumor spheroids are three-dimensional multicellular aggregates of a spherical shape. It has been shown that membrane receptors involved in regulating cell adhesion and metabolism are expressed in spheroids and that extracellular matrix is synthesized. This is important for cell aggregation and cell-to-cell interaction [28]. Typically, large tumor spheroids have three main zones: the necrotic nucleus, an inner zone of resting cells and an external, actively proliferating layer [29, 30]. The heterogeneous microenvironment within a spheroid, which is largely due to the presence of distinct gradients of nutrients and oxygen [31–33], results in morphological, metabolic and pH heterogeneity. In general, in many of their physiological characteristics and kinetics of growth, spheroids are similar to solid tumors before neoangiogenesis and represent realistic and easily handled models of tumor growth in vitro.

We believe that the use of tumor spheroids and genetically encoded pH-indicators will increase our knowledge of pH fluctuations during tumor formation, so we describe here a method for intracellular pH sensing in HeLa tumor spheroids, using the ratiometric cpYFP-based sensor SypHer2 in association with confocal fluorescence microscopy.

7.2 Materials

7.2.1 Reagents

Reagents for transfection

1. Vector plasmid pLCMV-puro-SypHer2
2. Envelope plasmid pMD.G (Didier Trono Lab)
3. Packaging plasmid pΔR8.91 (Didier Trono Lab)
4. Dulbecco's modified Eagle medium (DMEM) (Invitrogen, cat. no. 41965–039)
5. Fetal calf serum, FCS (Invitrogen, cat. no. 16000–044)
6. Penicillin/streptomycin (Invitrogen, cat. no. 15070–063)
7. L-Glutamine (Invitrogen, cat. no. 25030–024)
8. Trypsin/EDTA solution (Invitrogen, cat. no. R-001-100)
9. Calcium Phosphate Transfection Kit (Invitrogen, cat.no. K2780–01)
10. Polybrene (hexadimethrine bromide) (Sigma-Aldrich, cat. no. 107689)
11. Puromycin dihydrochloride (Sigma-Aldrich, cat. no P9620)
12. HEK293T cell line (HEK293T/17) (ATCC, cat. no. CRL-11268)
13. Mammalian cells

Reagents for cells and spheroids culturing

1. DMEM medium (PanEco)
2. DMEM medium without phenol red (Life Technologies)
3. Glutamine (PanEco)
4. Penicillin/streptomycin sulfate 100x (PanEco)
5. Fetal bovine serum (FBS) (Hyclone)
6. Trypsin-Versene (EDTA) 0.25% (PanEco)
7. Versene solution (PanEco)
8. Phosphate buffered saline, PBS (PanEco)

Reagents for pH calibration

1. Low-sodium buffer:
   Potassium gluconate −130 mM
   Sodium gluconate—20 mM
   Magnesium sulfate—0.5 mM
2. MOPS—30 mM
3. Tris (hydroxymethyl) aminomethane—30 mM
4. MES—30 mM
5. HCl—1 mM
6. KOH—1 mM
7. Ionophores: Nigericin—5 μM, Monensin—5 μM
8. Distilled water

7.2.2 Equipment

1. Laminar flow biosafety cabinet (Thermo Scientific, USA)
2. Humidified CO_2-incubator (Sanyo, Japan)
3. Centrifuge 5702 R (Eppendorf, Germany)
4. Inverted light microscope (Leica, Germany)
5. Inverted fluorescence microscope: DM IL LED (Leica, Germany)
6. Inverted laser scanning confocal microscope: LSM 880 (Carl Zeiss, Germany) equipped with a 405 nm diode laser and an Argon laser with a 488 nm wavelength, and Plan-Apochromat 20x/0.8 and C-Plan Apochromat 40x/1.3, with oil immersion, objectives)
7. Hemocytometer or BioRad TC10 automated cell counter (Bio Rad, USA)
8. pH meter (Hanna Instruments, Russia)
9. 300 µL multichannel pipette
10. 1000 µL automatic pipette
11. 5 mL serological pipette
12. T25 flasks
13. Tissue culture dish with cover glass-bottom (Fluorodish, China)
14. Ultra-low attachment 96-well round-bottom plates (ULA, Corning® 7007)
15. 60 mm tissue culture dishes
16. 15- or 50 mL conical centrifuge tubes, sterile
17. 0.45 µm pore size syringe filter unit: Millex-HP (Millipore, cat. no. SLHP033RS)
18. 5 or 10 mL syringes, sterile

7.3 Methods

7.3.1 Transfection

7.3.1.1 Production of Lentiviral Particles

Day 1—preparation HEK293T cells for transfection

1. Plate HEK293T cells on 60-mm dishes at a density of 1.5×10^6 cells per dish using 3 mL complete growth medium.
2. Incubate for the next 24 h at 37 °C and 5% CO_2. Ideally the cells should be ~80% confluent on the day of transfection.

Day 2—transfection with plasmid mix using Calcium phosphate precipitation

3. Two hours before transfection, replace the medium on the dishes with fresh growth medium preheated to 37 °C.
4. Prepare the plasmid mix (for one 60 mm dish):
   5 µg vector plasmid (pLCMV-puro-SypHer2)
   1.2 µg envelope plasmid (pMD.G)
   4 µg packaging plasmid (pΔR8.91)
5. Follow manufacturer's protocol for the Calcium Phosphate Transfection Kit (Invitrogen, cat. no. K2780–01 https://tools.thermofisher.com/content/sfs/manuals/capo4_man.pdf) with a total 10 µg DNA. Briefly, add to the plasmid mix 18 µl of 2 M $CaCl_2$ (Invitrogen), then top up the DNA-$CaCl_2$ mix with sterile H_2O (Invitrogen) to 150 µl. While vortexing the DNA-$CaCl_2$ solution, add 150 µl 2 × HBS (Invitrogen) dropwise. Incubate at room temperature for 30 min, and then add the precipitate dropwise to the medium containing the cells. Incubate the cells overnight (for 15–17 h) at 37 °C and 5% CO_2 (*see* **Note 1**).

Day 3—Observation of the cells and changing of medium

6. Change the medium to fresh 3 mL complete growth medium preheated to 37 °C. Incubate cells at 37 °C, 5% CO_2 for 24 hours (*see* **Note 2**).

Day 4—Collecting first harvest of supernatant

Caution! From this point on, supernatants contain infectious lentiviral particles.

7. Harvest the culture medium from each plate to a 15- or 50-mL centrifuge tube. Store the supernatant at 4 °C.

8. Add fresh complete growth medium to the cell monolayer and incubate at 37 °C, and 5% CO_2 for 24 hours.

Day 5—Collecting second harvest of supernatant

9. Harvest the medium from the cells and pool with the supernatant from the first harvest (Day 4).
10. Centrifuge the supernatant for 5 min at 1500 rpm to remove cell debris and filter through a 0.45 μm filter. Filtered supernatants can be stored at 4 °C for up to 3 days (*see* **Note 3**).

7.3.1.2 Lentiviral infection and selection

Day 1—Preparation HeLa Kyoto cells for transduction

11. Plate HeLa Kyoto cells on 60 mm dishes at a density of 1.0×10^6 cells per dish, using 3 mL complete growth medium. Incubate for the next 24 h at 37 °C and 5% CO_2. Ideally cells should be ~70% confluent on the day of transduction (*see* **Note 4**).

Day 2—Transduction

12. Change the medium to fresh 1.5 mL complete growth medium containing 8 μg/mL polybrene. Polybrene increases the efficiency of viral infection.
13. Add 1.5 mL of the lentiviral particle solution and incubate the HeLa Kyoto cells at 37 °C and 5% CO_2 overnight.

Day 3

14. Remove the virus-containing medium, replace with 3 mL of fresh complete growth medium, and incubate the HeLa Kyoto cells at 37 °C and 5% CO2 overnight.

Day 4

15. Observe the HeLa Kyoto cells with fluorescence microscope. Transduction efficiency may be assessed visually by the presence of fluorescence of SypHer2.
16. Change the medium in the infected and control dishes to fresh 3 mL complete growth medium containing 1 μg/mL puromycin (*see* **Note 5**).

Day 5+

17. Observe cells over a week, change to fresh puromycin-containing medium as needed every few days. Grow the infected HeLa Kyoto cells in the presence of puromycin for a few days after the control cells are dead. Once the cells are recovering from puromycin selection they can be transferred to a culture flask for further propagation.

7.3.2 Passaging HeLa-SypHer2 Cell Culture

All solutions and equipment that come into contact with the cells must be sterile. Always use proper sterile technique and work in a laminar flow hood.

1. Grow HeLa-SypHer2 cells in T25 cell culture flasks in DMEM supplemented with 10% FBS, 2 mM glutamine, 10 μ/mL penicillin and 10 mg/mL streptomycin (complete medium). Warm all reagents to 37 °C prior to use.
2. Remove a freshly confluent (~80–90%) T25 flask of HeLa-SypHer2 cells from the cell culture incubator and place in a sterile cell culture hood (*see* **Note 6**).
3. Remove medium using a 5 mL serological pipette.
4. Add 2 mL Versene solution and gently wash the cells twice using a 5 mL serological pipette.
5. Remove the Versene solution using a 5 mL serological pipette.
6. Add 1 mL 0.25% Trypsin/EDTA using an automatic pipette and incubate at 37 °C for 3–5 min until the cells detach. Observe the cells under a microscope to confirm their

detachment. If the cells are less than 90% detached, increase the incubation time by a few minutes, checking for dissociation every 30 s.
7. Add 1 mL of complete medium to stop trypsinization and gently resuspend the cells using a 5 mL serological pipette to obtain a suspension of single cells.
8. Remove 1.5 mL of the cell suspension from the flask.
9. Add 4.5 mL of complete fresh medium to the flask.
10. Put the flask into a cell culture incubator (37 °C and 5% CO_2).
11. Subculture cells three times a week.

7.3.3 Spheroid Generation

1. Prepare a suspension of single cells as described above.
2. Transfer 1–2 mL of the cell suspension to a 15 mL conical tube.
3. Centrifuge at 1.0 rpm for 5 min.
4. Discard the supernatant and wash the pellet with 1 mL complete medium.
5. Resuspend the cells in 1 mL of complete culture medium to obtain a suspension of single cells.
6. Count the cells using a hemocytometer or automated cell counter and adjust the concentration to 0.5×10^3 cells/mL.
7. Seed 200 μL of the cell suspension per well (100 cells per well) into 96-well ultra-low attachment round bottom plates using a multichannel pipette. During manual seeding, ensure that the pipette tips do not scratch the bottom or the sides of the wells to avoid damaging the Corning Ultra-Low Attachment surface coating.
8. Place the microplate in a cell culture incubator (37 °C and 5% CO_2).
9. Gently remove 100 μL of the culture medium and add 100 μL of fresh culture medium into each well every three days of cultivation. Try to replace the medium without losing any spheroids (*see* **Note 7**).
10. Three days after seeding, visually confirm tumor spheroid formation by microscopic examination in transmitted light (*see* **Notes 8 and 9**).

7.3.4 Fluorescence Microscopy

7.3.4.1 Preparation of Spheroids for Fluorescence Microscopy

1. Remove the 96-well ultra-low attachment plates from the cell culture incubator and place within a sterile cell culture hood.
2. Using a 1000 μL automatic pipette, gently harvest the required number spheroids from the wells and transfer them into a microtube. Wait for 1–5 min until the spheroids sink to the bottom of the microtube (*see* **Note 10**).
3. Gently remove the supernatant using a 1000 μL automatic pipette.
4. Add 1 mL DMEM life medium without phenol red to the spheroids and transfer the spheroids onto a glass bottom dish using a 1000 μL automatic pipette.
5. Place the dish with the spheroids in a humidified incubator (37 °C and 5% CO_2) for 30–60 min to allow for spheroid attachment.
6. Ensure that the spheroids have attached, either visually or by using an inverted light microscope (*see* **Notes 11, 12**).
7. Image the spheroids using confocal fluorescence microscopy (*see* **Note 13**).

7.3.4.2 Confocal Fluorescence Microscopy

An inverted confocal microscope should be used for microscopic imaging of the SypHer2-expressing tumor spheroids (we use an LSM 880, Carl Zeiss, Germany).

1. Select the objective depending on your task. If an image of a whole spheroid is required, it is best to use a 20x objective. For more precise analysis of individual cells from different zones of a spheroid, use a 40x/1.3 oil immersion objective. Place a drop of immersion oil on the objective lens, if required.

2. Set up the microscope to view the SypHer2 emission. For ratiometric imaging, the fluorescence of SypHer2 can be excited at two wavelengths, corresponding closely to its two excitation peaks (420 nm and 500 nm [27]. In the LSM 880 a diode laser with a wavelength 405 nm, and an Argon laser line of 488 nm are used to excite SypHer2 fluorescence. Emission is detected in the range of 500–551 nm. Enter the correct parameters for image acquisition (e.g., image size—1024 × 1024 pixels, image depth—16 bit, pixel dwell time—2.06 µs, confocal diaphragm—1 a.u., with an excitation beam power—10 µW for both lasers, the detector digital gain—550. Image acquisition time is 10.13 s) (*see* **Note 14**).

   For spheroids:

3. Place the glass-bottom dish with attached spheroids on the microscope stage so that the spheroid is as close to the center of the objective as possible.
4. Find a spheroid in the field of view and adjust it to the center.
5. By varying the focus plane, first find the position where the spheroid's cells adhere to the dish (the bottom edge of the spheroid), then adjust the focus to the required depth in the spheroid (*see* **Note 15**).
6. Sequentially record two fluorescence images, one for each of the two excitation wavelengths (*see* **Note 16**).

   For cell monolayer:

3. Place the glass-bottom dish with the HeLa-SypHer2 cells in a calibration buffer on the microscope stage.
4. Find the focal plane of the sample on the central slice level of the cells where a square is maximally occupied by cells.
5. Sequentially record two fluorescence images, one for each of the two excitation wavelengths (*see* **Note 16**).
6. Repeat n. 3–5 for each pH point.
7. Save all acquired images in TIFF format.

7.3.5 Calibration of the SypHer2 Sensor

Calibration is required to convert the I_{488}/I_{405} ratio to pH units. It is important to perform calibration of the sensor with the same microscope settings and in identical conditions to those used in the imaging of the tumor spheroids. In the case of any changes in the settings/conditions, a new calibration should be undertaken.

1. Monolayers of HeLa-SypHer2 cell culture on glass-bottom dishes are used for the calibration of SypHer2. Seed the cells at a concentration of 3–5 × 10^4 cells/mL, total volume 2 mL, on glass-bottom dishes in DMEM medium with 10% FBS. Use one dish for each calibration point.
2. 24 hours after seeding the cells on the glass-bottom dish, remove the culture medium from the dish using a 5 mL pipette and add 2 mL of fresh DMEM medium without phenol red 2 h before fluorescence microscope investigation.
3. Add 5 µM nigericin and 5 µM monensin to a low-sodium buffer (*see* **Notes 17, 18, 19**).
4. Adjust the pH of the low-sodium buffer containing the ionophores to the required pH values using 1 mM HCl or 1 mM KOH (*see* **Notes 3–5**). 30 mM MOPS can be used for the pH range 6.9–8.0; 30 mM Tris—for pH 8.1–9.0; and 30 mM MES – for pH 6.0–6.8.5. Rinse the pH electrode with distilled water between measurements (*see* **Notes 20, 21**).
5. Remove the DMEM medium from the dish using a 5 mL serological pipette.
6. Wash the cells once with 1 mL of buffer solution with the specified pH value and add 2 mL of the buffer solution to the cells.
7. Incubate the cells in the ionophore-containing buffer solution with the specified pH value over a period of 5 min to balance the extracellular and intracellular pH (*see* **Note 22**).
8. Image the cells using fluorescence confocal microscopy and calculate the I_{488}/I_{405} fluorescence ratio as indicated in Sect. 3.6.
9. Plot the I_{488}/I_{405} ratios against the corresponding pH values. Carry out statistical (regression)

analysis on the data to obtain the calibration function. Evaluate the results of the regression analysis (*see* **Note 23**). The R-squared value should be close to 1.

10. Use the calibration function to convert the I_{488}/I_{405} values to pH units for the test samples (monolayer cells or spheroids).

7.3.6 Data Processing

1. The fluorescence images are analyzed using ImageJ software (NIH). Open the two images corresponding to the two excitation wavelengths, I_{405} and I_{488} (*File* → *Import* → …).
2. For each image calculate the background signal in an area without cells (select the region of interest using the selection tool on the program panel, then go to *Analyze* → *Measure,* see *Mean* in the table).
3. Subtract the background signal from the corresponding image (go to *Process* → *Math* → *Subtract,* enter the calculated mean value).
4. Convert both images to 32-bit. Go to *Image* → *Type* → *32-bit*. At this step, you may save the images (optional): go to *File* → *Save as*, choose TIFF format.
5. Threshold the I_{405} image to remove pixel values from the background. Go to *Image* → *Adjust* → *Threshold*, adjust the maximum threshold to its maximum value, and then adjust the minimum threshold value to remove the pixel values representing areas without cells.
6. Go to *Process* → *Image Calculator* and perform pixel by pixel division of the fluorescence intensities I_{488}/I_{405}.
7. Save the resulting I_{488}/I_{405} image in TIFF format (*see* **Note 24**).
8. Calculate the I_{488}/I_{405} ratio in the cells of interest (select a cell on the TIFF image using a selection tool from the program panel, then go to *Analyze* → *Measure,* see *Mean* in the table). Export these measurements to a spreadsheet.
9. Based on these measurements, construct a calibration curve (in the case of calibration) or convert the I_{488}/I_{405} values to pH units using the calibration curve (in the case of spheroids).

7.4 Anticipated Results

7.4.1 Calibration of SypHer2 in Cell Monolayer

Using lentiviral transduction, a HeLa Kyoto cell line stably expressing the cytoplasmic pH-sensor SypHer2 was established. The transduction efficiency was assessed by fluorescence microscopy by the presence of emission from the SypHer2. ~80–90% of cells exhibited SypHer2 fluorescence.

To calibrate the SypHer2 signal, its fluorescence resulting from excitation at two wavelengths, 488 nm and 405 nm, and the corresponding I_{488}/I_{405} ratios were registered in monolayered HeLa cells in buffer solutions with pH values 6.9, 7.1, 7.3, 7.5, 7.7 in the presence of the ionophores nigericin/monensin.

As can be seen from Fig. 7.1a, with increasing pH, the fluorescence excited at 405 nm slightly decreased while that at 488 nm increased, resulting in an increase of the I_{488}/I_{405} ratio of intensities. The I_{488}/I_{405} ratio was calculated from 50–70 randomly selected individual cells for each pH point (Fig. 7.1b). The relationship between the I_{488}/I_{405} ratio and the pH was well-approximated by an exponential fit ($R^2 = 0.99$, the solid line, Fig. 7.1c). The equation of the fit is

$$y = 0.38013 + 2.44706 \times 10^{-15} \times e^{4.3724x},$$

where y is the I_{488}/I_{405} ratio and x is the pH.

7.4.2 Characterization and Growth of HeLa-SypHer2 Spheroids

The spheroids were generated from HeLa cells stably expressing SypHer2, and their morphology was analyzed on days 3, 5, 7 and 10 of their growth (Fig. 7.2).

A plating density of 100 cells/well resulted in spheroid sizes ~200 μm, 300 μm, 500 μm and 800 μm on days 3, 5, 7 and 10, respectively, as measured on the images in transmitted light. On the 3rd day the cells formed multicellular agglomerates, which became tighter by day 5. On the 7th day one could distinguish an inner spheroid

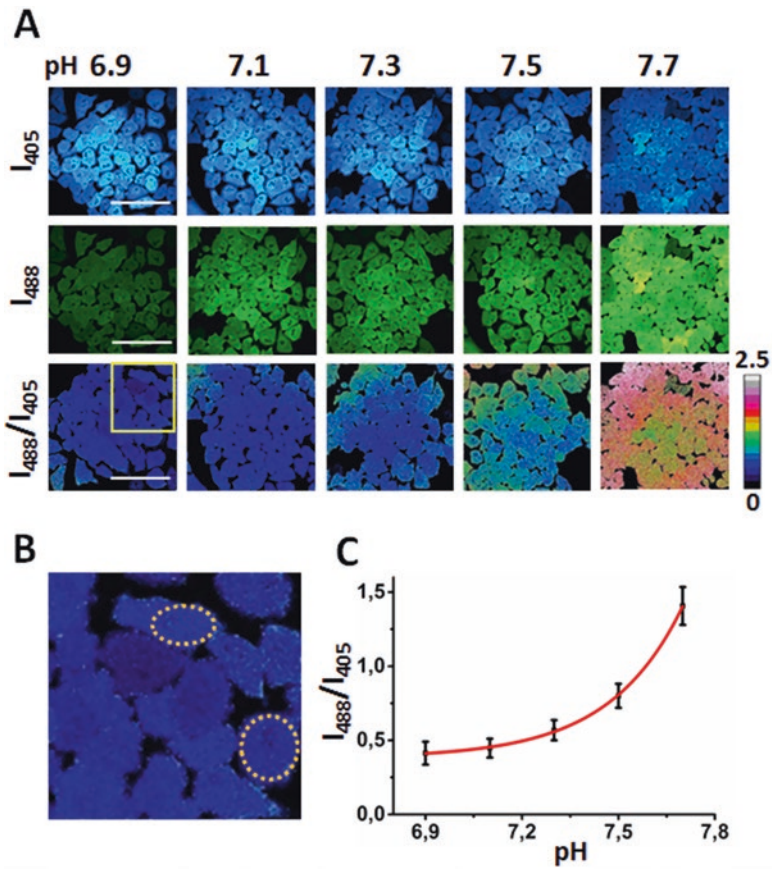

Fig. 7.1 Calibration of the SypHer2 sensor on a HeLa cell monolayer. (**a**) Fluorescence images using excitation at 405 nm and 488 nm (detection in the range 500–551 nm) and I_{488}/I_{405} ratio images at different pH values. Image size is 213 × 213 μm. Bar is 100 μm (applicable to all images in the row). (**b**) Examples of the cell selection for calculation of the I_{488}/I_{405} ratio. Enlarged area shown in the yellow square on the I_{488}/I_{405} ratio image in (**a**). Two representative cells are indicated by dashed circles. (**c**) I_{488}/I_{405} ratio values plotted versus pH. The red curve shows the exponential fit, $R^2 = 0.99$, mean ± SD, n = 30

core of tightly packed cells and a thin outer shell of loosely packed cells. By day 10 of cultivation, the spheroids began to disintegrate due to their considerable size.

To assess the viability of the cells constituent in the tumor spheroids, double live/dead fluorescent staining was conducted using Calcein and Propidium iodide (Sigma live/dead double staining kit). Live/dead assay was performed on whole spheroids at all indicated time-points. The fluorescence signal was visualized using an inverted DM IL LED fluorescence microscope (Leica, Germany) equipped with a YFP ET filter (Ex: BP 500/20, Em: BP 535/30) for calcein (live cells) and a TX2 green filter (Ex: BP 560/40, Em: BP 645/75) for Propidium iodide (PI, dead cells). The live/dead assays revealed the appearance of single dead cells in the spheroid core starting from the 5th day of cultivation and the formation of a massive necrotic core on the 10th day of cultivation. The development of a necrotic core in the central region is a specific feature of spheroids of more than 500 μm diameter [29, 30].

To analyze the internal structure and arrangements of the spheroids at different stages of growth, 5 μm thick cryosections were prepared and stained with hematoxylin and eosin (H&E). For cryosectioning, the spheroids (minimum 30 pieces) were taken from the plate, placed in OCT compound and cut using a cryostat Leica CM1900UV (Leica, Germany).

Correlating with the spheroid growth data, histological examination revealed a uniform spherical shape and a compact structure of the spheroids with a defined outer perimeter and lim-

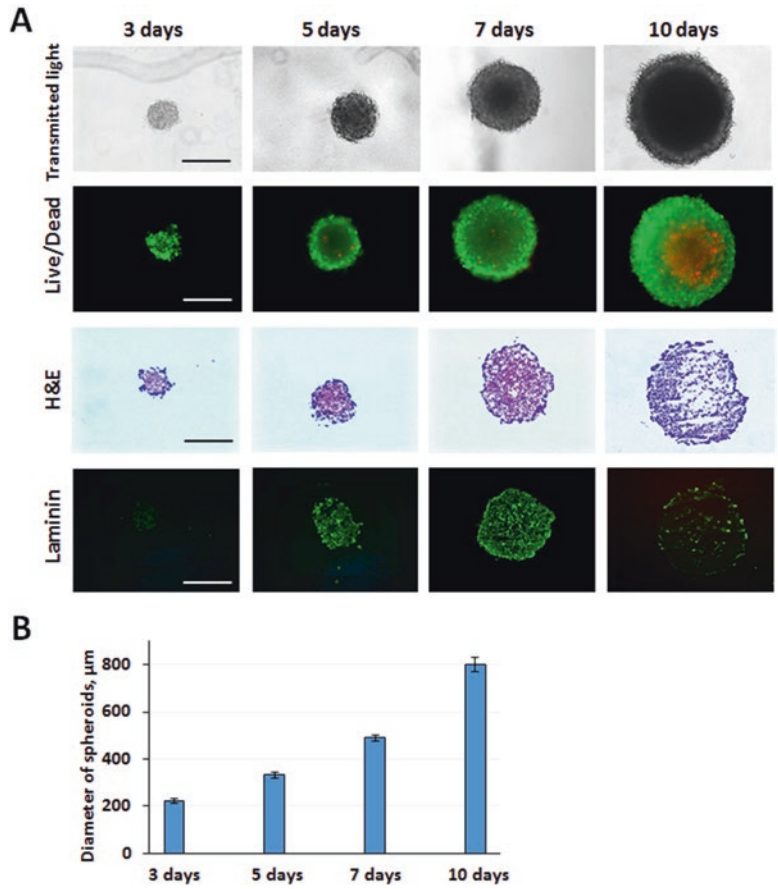

Fig.7.2 Characterization of HeLa-SypHer2 tumor spheroids during their growth. (**a**) Images of the spheroids in transmitted light, live (calcein, *green*) and dead (PI, *red*) staining, histological images (frozen sections, H&E) and immunofluorescent staining for laminin (frozen sections, FITC-conjugated antibodies to laminin) at days 3, 5, 7 and 10 of spheroid cultivation. Bar is 500 µm (applicable to all images in the row). (**b**) Growth rate of the spheroids. The diameter of spheroids was measured on the images in transmitted light. Mean ± SD, n = 7

ited degrees of necrosis in the center on the 5th and 7th days. A higher level of necrosis and loss of structural integrity were seen on the 10th day.

Additionally, the deposition of laminin, the key glycoprotein of the extracellular matrix (ECM), was examined in the spheroids during their growth. For this, separate cryosections were incubated with the primary antibodies to laminin (ab11575, Abcam, USA) overnight, and then with secondary antibodies conjugated to FITC (ab6825, Abcam, USA). The fluorescence signal was visualized using the YFP ET filter (Ex: BP 500/20, Em: BP 535/30) on the inverted DM IL LED fluorescence microscope (Leica, Germany). The results showed weak immunofluorescence on the 3rd day of culturing and increasing laminin expression from days 5 to 7 that indicated ECM formation. At day 10, degradation of the ECM was detected as indicated by reduced immunofluorescence.

7.4.3 pHi in Tumor Spheroids

Measurements of pHi in HeLa spheroids on days 3, 5, 7 and 10 of their growth were implemented using the protocol described. Fig. 7.3a shows the fluorescence intensities of SypHer2, I_{405} and I_{488}, and the resulting I_{488}/I_{405} ratio in a complete 7-day tumor spheroid. The non-uniform distribution of the I_{488}/I_{405} ratios, with higher values detected in the peripheral region of the spheroid, indicates a more alkaline pHi in the outer layers of cells and a more acidic pHi in the core. It can be seen that the confocal images acquired with the X20 objective allow visualization of the whole spheroid, but individual cells cannot be distinguished at this magnification due to the homogenous distribution of the fluorescent sensor within each cell and the high density of the cells within the spheroid.

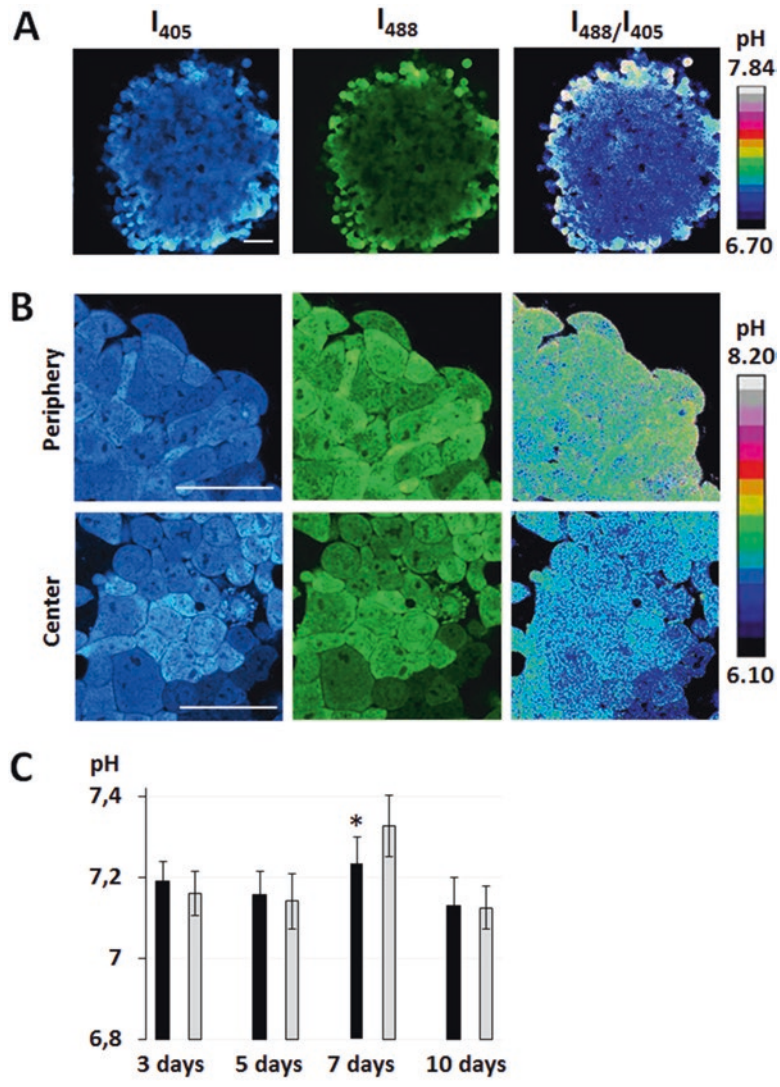

Fig. 7.3 pHi mapping in living HeLa tumor spheroids using genetically encoded pH-sensor SypHer2. Fluorescence images of a spheroid at day 7 of its growth, using excitation at 405 nm and 488 nm (detection in the range 500–551 nm) and the I_{488}/I_{405} ratio image obtained with a X20 objective (**a**) or with a X40 objective (**b**). In (**b**) representative regions from the spheroid core and periphery are shown. (**c**) Dynamics of pHi in the central (*black columns*) and peripheral parts (*gray columns*) of tumor spheroids during their growth, mean ± SD, n = 7 spheroids. Bar is 50 μm (applicable to all images in the row). *– statistically significant difference between the pHi values in the core and peripheral parts of spheroid at the same time point, $p < 0.05$. Note, on day 7, the cells in the outer layers of the spheroid have a more alkaline pHi than those in the spheroid core

For more accurate measurement of the pHi in individual cells of the living tumor spheroids a X40 objective was used (Fig. 7.3b). pHi values were calculated using a calibration curve obtained on monolayer HeLa-SypHer2 cells in identical conditions and with identical microscope settings. Analysis of pHi separately in the core and on the periphery of the spheroids during their growth showed a statistically significant difference between the central and peripheral parts on the 7th day, 7.23 ± 0.06 *vs* 7.32 ± 0.07 respectively ($p = 0.00000$, n = 7 spheroids, for each spheroid the pH was calculated from 10–15 cells). On other days of observation the pHi across the spheroid was fairly homogenous, although it fluctuated slightly around 7.15 units (Fig. 7.3c). It should be mentioned that the pHi value measured previously in monolayer HeLa cells under standard cultivation conditions was 7.34 ± 0.11 [27], which is close to the pHi in actively proliferating cells in the peripheral rim of the HeLa spheroid.

In general, the methods for measuring pH in multicellular spheroids are limited. Previously, radial pH gradients have been demonstrated on 3D tumor spheroids of different origin. For

example, early studies by Acker's group had shown a continuous decrease of pH towards the center in seven different types of spheroids [34, 35]. Those first measurements of pH in spheroids were performed using pH-sensitive microelectrodes that did not allow discrimination between the intra- and extracellular pH values.

In several studies, analysis of the cytoplasmic pH in tumor spheroids has been carried out using synthetic fluorescent pH-sensitive dyes and fluorescence microscopy. Using the membrane-permeant form of carboxy-SNARF-1, Hulikova et al. showed 0.1–0.2 units of difference in pHi between the center and the periphery for both HT29 and HCT116 spheroids, with the more acidic pHi in their cores [36]. Using carboxy-SNARF-1, Swietach et al. found that spheroids of RT112 bladder carcinoma cells had an acidic core with a pHi 0.25 units lower than that at their surface [37]. Human colon carcinoma HCT116 spheroids developed radial gradients of pHi, with the lowest level reached at their cores, as measured with carboxy-SNARF-1 [38]. pHi imaging in 3D models of metastatic ovarian cancer OvCa, using SNARF-4 F, detected a pH gradient along their radii, with more acidic cores being observed consistently for both small and large spheroids [39]. The possibility of measuring pHi with the use of the pH-sensitive fluorescence dye BCECF was also shown on human duodenum-derived spheroids [40]. Thus, our data showing non-uniform pHi with more alkaline values in cells of the rapidly proliferating crust correlate with the results obtained using exogenous pH-sensitive dyes.

It is generally accepted that the development of pHi gradients in spheroids correlates to the gradients in nutrient concentration, including glucose, ATP and oxygen, resulting in the reorganization of metabolic pathways and changes in the growth probability of cells [31–33]. Insufficient penetration of oxygen, nutrients and ATP in combination with a lack of a transport system to remove waste from the center of the spheroid leads to a hypoxia-induced accumulation of metabolic by-products, mostly lactate, in the cell cytoplasm [31, 36, 39, 41]. However, the exact mechanisms responsible for the regulation of pHi in such a heterogeneous microenvironment are yet to be established.

Therefore, multicellular tumor spheroids, in combination with fluorescent genetically encoded pH-indicators, offer a promising approach for dynamic imaging of the cytoplasmic pH in cancer cells in providing both high accuracy and spatiotemporal resolution.

7.5 Notes

1. *Caution!* You must follow safety procedures and work in an environment suitable for handling lentiviruses. Please follow all safety guidelines from your institution and from the CDC and NIH for work in a Biosafety Level 2 (BL2) facility.
2. HEK293T cells can detach easily from the plate. Add the fresh medium carefully onto the side of the plate.
3. The cleared supernatant can be used directly, stored at −80 °C as aliquots, or concentrated if needed. Avoid repeated freeze-thaw cycles.
4. Plate and maintain one uninfected dish of cells in parallel as a positive control for the puromycin selection.
5. The appropriate concentration of puromycin for each cell type is different. If the concentration for the desired cell type is unknown, a titration experiment must be performed.
6. Use an inverted light microscope (Leica, Germany) to make sure that the adherent cell culture reaches 80–90% confluence. If it does not, change the culture medium for fresh and return the flask to the incubator for 24–48 h. Re-check the confluence of cells in the flask. Adherent cultures should be passaged when they are in the log phase, before they reach confluence. Normally, cells stop growing when they reach confluence (contact inhibition), and it takes them longer to recover when reseeded.
7. Avoid removal of the spheroids from the wells during changes of medium. In order to avoid damaging the spheroids do not

immerse the tip of the pipette as far as the bottom of well.

8. The rate of spheroid growth and their initial size depend on the seeding density of the cells. Typically, in 2 days after seeding, HeLa cells seeded at 100 cells per well form loose multicellular aggregates and, by day 3, the cells form more compact spheroids of 200 μm in diameter. By day 10, the spheroids usually began to lose their tight structure and to disintegrate after reaching a large size (800 μm). In our experience the best spheroid age for pH studies is 5–7 days.
9. If the cells do not form spheroids after 3 days, this can be a consequence of bacterial contamination, of using a high-passage cell culture (more than 10 passages) or other problems with the cells (e.g. prolonged tripsinization or non-compliance with the cell culturing protocol).
10. While harvesting 10-day spheroids, be careful to avoid damaging them with the pipette. To harvest large 10-days spheroids we recommend first cutting the pipette tip using scissors.
11. If the spheroids have not attached to the bottom, place the dish back into the incubator and wait for another 30–40 min, or decrease the volume of medium in the dish by removing 500–700 μL.
12. Multiple single cells close to the cellular agglomerates indicate damage to the spheroid. Such spheroids are not appropriate for investigation. Choose undamaged spheroids for any study.
13. Perform additional staining to characterize the spheroids, depending on the task; e.g. staining using calcein and Propidium iodide to assess the viability of cells, hematoxylin and eosin staining to examine the histopathology of the spheroids, immunofluorescent staining with antibodies to laminin staining to assess the extracellular matrix (ECM), etc.
14. We recommend selecting and approbating the settings for image acquisition on the cells in the buffer with the highest pH value selected for calibration, as it provides the highest SypHer2 fluorescence intensity excited at 488 nm. Be careful to use a laser power that does not damage the cells and does not photobleach the sensor. You should vary the power of the excitation beam and the detector digital gain to find values that allow a fluorescence signal to be obtained within the dynamic range of the detection, but close to the maximum, as other pH values will give a lower fluorescence intensity.
15. Alternatively, a Z-series can be used for recording the data in all focal planes. We usually use 3.5 μm steps along the z-axis to obtain 0.7–0.8 μm sections. In our experience the confocal scanning of the spheroids and, consequently, the measurement of pH, is limited to a depth of 50 μm owing to the poor permeability of spheroids to the probing light. Scanning at greater depths may distort the I_{488}/I_{405} ratio.
16. For correct data processing all fluorescence images must be acquired in identical conditions. The parameters of the excitation light (wavelengths, powers) and registration of the signal (diameter of the confocal diaphragm, number of pixel, pixel dwell time, detection range, detector digital gain) must be the same for both the calibration and pH measurements in the tumor spheroids.
17. If monensin is not available, it is possible to use 10 μM nigericin solution.
18. Only freshly prepared ionophore-containing buffer solution should be used. Low-sodium buffer without ionophores should be kept at 4 °C.
19. Alternatively, the ionophores (nigericin and monensin) can be added to the cells before incubation in the buffer solutions. In this case, incubate the cells with the ionophores for 5 min, wash the cells once with 1 mL of buffer solution with the specified pH value, then add buffer solution with the specific pH required and incubate for 5 min as per the protocol. Incubation should be at room temperature (20 ºC).

20. After each single measurement, the pH electrode is rinsed with distilled or deionized water by stirring in a glass, manually or by using a magnetic stirrer (the latter is preferable). If you use ionophore-containing buffers, rinse the pH electrode for ~2 min. If you are using buffer solutions without ionophores, 30 s is sufficient.
21. The more pH points you use the more accurate the calibration will be. We recommend using a minimum of five pH values in the physiological pH range (e.g. 6.9, 7.1, 7.3, 7.5, 7.7).
22. All adjustments of the pH of buffer solutions, incubation of cells with buffer solutions and further pH measurements in cells and spheroids should be performed at the same temperature to avoid pH shifts. We carry out all these manipulations at room temperature (20 °C).
23. Within the pH range 6.0–8.0 the calibration curve is typically best approximated by an exponential fit.
24. To produce colored images we use ImageJ 1.39p software. Go to Plugins → *LUT* → *Ratio*. However, keep in mind that the colored image is not appropriate for calculating the I_{488}/I_{405} ratio.

Acknowledgements Transfection of HeLa cells with SypHer2 gene was performed as part of project #17-14-01086, the Russian Science Foundation. The study pHi in tumor spheroids was supported by the Russian Science Foundation (project # 14-25-00129-П). The authors are grateful to Dr. Vsevolod V. Belousov (IBC RAS), Maria Lukina (NNSMA) and Fedor Kulagin (NNSMA).

References

1. Lee AH, Tannock IF (1998) Heterogeneity of intracellular pH and of mechanisms that regulate intracellular pH in populations of cultured cells. Cancer Res 58(9):1901–1908
2. Damaghi M, Wojtkowiak JW, Gillies RJ (2013) pH sensing and regulation in cancer. Front Physiol 4:370
3. Webb BA, Chimenti M, Jacobson MP et al (2011) Dysregulated pH: a perfect storm for cancer progression. Nat Rev Cancer 11:671–677
4. Rauch C, Blanchard A, Wood E et al (2009) Cell membranes, cytosolic pH and drug transport in cancer and MDR: physics, biochemistry and molecular biology. In: Multiple drug resistance. Nova Science Publishers, Inc., Hauppauge, NY, pp 1–24
5. Robey IF, Baggett BK, Kirkpatrick ND et al (2009) Bicarbonate increases tumor pH and inhibits spontaneous metastases. Cancer Res 69:2260–2268
6. Han J, Burgess K (2010) Fluorescent indicators for intracellular pH. Chem Rev 110:2709–2728
7. pH Indicators (2010) The molecular probes handbook: a guide to fluorescent probes and labeling technologies, 11th edn, ch. 20, pp 883–902
8. Bizzarri R, Serresi M, Luin S et al (2009) Green fluorescent protein based pH indicators for in vivo use: a review. Anal Bioanal Chem 393:1107–1122
9. Bencina M (2013) Illumination of the spatial order of intracellular pH by genetically encoded pH-sensitive sensors. Sensors 13:16736–16758
10. Germond A, Fujita H, Ichimura T et al (2016) Design and development of genetically encoded fluorescent sensors to monitor intracellular chemical and physical parameters. Biophys Rev 8:121–138
11. Kneen M, Farinas J, Li Y, Verkman AS (1998) Green fluorescent protein as a noninvasive intracellular pH indicator. Biophys J 74:1591–1599
12. Llopis J, McCaffery JM, Miyawaki A et al (1998) Measurement of cytosolic, mitochondrial, and Golgi pH in single living cells with green fluorescent proteins. Proc Natl Acad Sci U S A 95:6803–6808
13. Nehrke K (2006) Intracellular pH measurements in vivo using green fluorescent protein variants. Methods Mol Biol 351:223–239
14. Mahon MJ (2011) pHluorin2: an enhanced, ratiometric, pH-sensitive green fluorescent protein. Adv Biosci Biotechnol 2:132–137
15. Miesenbock G, Angelis De DA, Rothman JE (1998) Visualizing secretion and synaptic transmission with pH-sensitive green fluorescent proteins. Nature 394:192–195
16. Orij R, Postmus J, Ter Beek A et al (2009) In vivo measurement of cytosolic and mitochondrial pH using a pH-sensitive GFP derivative in Saccharomyces cerevisiae reveals a relation between intracellular pH and growth. Microbiology 155:268–278
17. Hanson GT, McAnaney TB, Park ES et al (2002) Green fluorescent protein variants as ratiometric dual emission pH sensors. Structural characterization and preliminary application. Biochemistry 41:15477–15488
18. Bizzarri R, Arcangeli C, Arosio D et al (2006) Development of a novel GFP-based ratiometric excitation and emission pH indicator for intracellular studies. Biophys J 90:3300–3314
19. Serresi M, Bizzarri R, Cardarelli F, Beltram F (2009) Real-time measurement of endosomal acidification by a novel genetically encoded biosensor. Anal Bioanal Chem 393:1123–1133

20. Awaji T, Hirasawa A, Shirakawa H et al (2001) Novel green fluorescent protein-based ratiometric indicators for monitoring pH in defined intracellular microdomains. Biochem Biophys Res Commun 289:457–462
21. Poburko D, Santo-Domingo J, Demaurex N (2011) Dynamic regulation of the mitochondrial proton gradient during cytosolic calcium elevations. J Biol Chem 286:11672–11684
22. Matlashov ME, Bogdanova YA, Ermakova GV et al (2015) Fluorescent ratiometric pH indicator SypHer2: applications in neuroscience and regenerative biology. Biochim Biophys Acta 1850(11):2318–2328. https://doi.org/10.1016/j.bbagen.2015.08.002
23. Abad MFC, Di Benedetto G, Magalhães PJ et al (2004) Mitochondrial pH monitored by a new engineered green fluorescent protein mutant. J Biol Chem 279:11521–11529
24. Rossignol R, Gilkerson R, Aggeler R et al (2004) Energy substrate modulates mitochondrial structure and oxidative capacity in cancer cells. Cancer Res 64:985–993
25. Rivinoja A, Kokkonen N, Kellokumpu I et al (2006) Elevated Golgi pH in breast and colorectal cancer cells correlates with the expression of oncofetal carbohydrate T-antigen. J Cell Physiol 208:167–174
26. Lar˙zaro-Dier˙guez F, Jimer˙nez N, Barth H et al (2006) Actin filaments are involved in the maintenance of Golgi cisternae morphology and intra-Golgi pH. Cell Motil Cytoskeleton 63:778–791
27. Shirmanova MV, Druzhkova IN, Lukina MM et al (2015) Intracellular pH imaging in cancer cells in vitro and tumors in vivo using the new genetically encoded sensor SypHer2. Biochim Biophys Acta 1850:1905–1911
28. Hofschröer V, Koch KA, Ludwig FT et al (2017) Extracellular protonation modulates cell-cell interaction mechanics and tissue invasion inhuman melanoma cells. Sci Rep 7:42369. https://doi.org/10.1038/srep42369
29. Hirschhaeuser F, Menne H, Dittfeld C et al (2010) Multicellular tumor spheroids: an underestimated tool is catching up again. J Biotechnol 148:3–15
30. Sirenko O, Mitlo T, Hesley J et al (2015) High-content assays for characterizing the viability and morphology of 3D cancer spheroid cultures. Assay Drug Develop Technol 13:402–414
31. Jamieson LE, Harrison DJ, Campbell CJ (2015) Chemical analysis of multicellular tumour spheroids. Analyst 140:3910–3920
32. Langan LM, Dodd NJF, Owen SF et al (2016) Direct measurements of oxygen gradients in spheroid culture system using electron paramagnetic resonance oximetry. PLoS One 11:e0149492
33. Zanoni M, Piccinini F, Arienti C et al (2016) 3D tumor spheroid models for in vitro therapeutic screening: a systematic approach to enhance the biological relevance of data obtained. Sci Rep 6:19103. https://doi.org/10.1038/srep19103
34. Acker H, Carlsson J, Holtermann G et al (1987) Influence of glucose and buffer capacity in the culture medium on growth and pH in spheroids of human thyroid carcinoma and human glioma origin. Cancer Res 47:3504–3508
35. Carlsson J, Acker H (1988) Relations between pH, oxygen partial pressure and growth in cultured cell spheroids. Int J Cancer 42:715–720
36. Hulikova A, Vaughan-Jones RD, Swietach P (2011) Dual role of CO2/HCO3(−) buffer in the regulation of intracellular pH of three-dimensional tumor growths. J Biol Chem 286:13815–13826
37. Swietach P, Wigfield S, Cobden P et al (2008) Tumor-associated carbonic anhydrase 9 spatially coordinates intracellular pH in three-dimensional multicellular growths. J Biol Chem 283:20473–20483
38. Swietach P, Patiar S, Supuran CT et al (2009) The role of carbonic anhydrase 9 in regulating extracellular and intracellular pH in three-dimensional tumor cell growths. J Biol Chem 284:20299–20310
39. Evans CL, Abu-Yousif AO, Park YJ et al (2011) Killing hypoxic cell populations in a 3D tumor model with EtNBS-PDT. PLoS One 6:e23434
40. Weinlich M, Baumstark C, Usta E et al (2002) Human duadenal spheroids for noninvasive intracellular pH measurement and quantification of regulation mechanism under physiological conditions in vitro cell. Dev Biol Anim 38:7–13
41. Cshitcholtan K, Sykes PH, Evans JJ (2012) The resistance of intracellular mediators to doxorubicin and cisplatin are distinct in 3D and 2D endometrial cancer. J Transl Med 10:38

8 Application of Fluorescence Lifetime Imaging (FLIM) to Measure Intracellular Environments in a Single Cell

Takakazu Nakabayashi, Kamlesh Awasthi, and Nobuhiro Ohta

Abstract

Fluorescence lifetime imaging (FLIM) has now been used in many bioscience fields, which comes from the quantification of fluorescence lifetime. The procedure for obtaining lifetime images is very similar to that used in fluorescence microscopy. However, obtaining reliable lifetime images requires an understanding of the theory of fluorescence lifetime, principle of FLIM systems, and evaluation procedure of intracellular environments. In this chapter, the materials, methods, and notes on FLIM measurements have been described, in conjunction with a brief explanation of the background of FLIM.

Keywords

Fluorescence lifetime imaging • TCSPC • Femtosecond laser • Intracellular pH • Intracellular environment • Ratiometric method

8.1 Introduction

Fluorescence spectroscopy is now an indispensable tool in life sciences as it demonstrates a superior advantage in terms of very high sensitivity, versatility of sample condition, and ease of combination with other spectroscopic methods. Fluorescence has several parameters that are useful for obtaining information on molecules: intensity (yield), spectral position (wavelength) and shape (bandwidth), lifetime, and polarization. Intensity is the most well known parameter for analyzing biological and chemical samples using fluorescence; however, other fluorescence parameters also have a wealth of information that can be used to identify and clarify environment in a living cell. Fluorescence lifetime, which is an inherent physical parameter of a molecule, is determined only by structure and environment of fluorophores and is defined as the average time of a molecule remaining in the fluorescent excited

T. Nakabayashi (✉)
Graduate School of Pharmaceutical Sciences, Tohoku University, Aoba-ku, Sendai 980-8578, Japan
e-mail: takan@m.tohoku.ac.jp

K. Awasthi • N. Ohta (✉)
Department of Applied Chemistry and Institute of Molecular Science, National Chiao Tung University, 1001, Ta-Hsueh Road, Hsinchu 30010, Taiwan
e-mail: nohta@nctu.edu.tw

R.I. Dmitriev (ed.), *Multi-Parametric Live Cell Microscopy of 3D Tissue Models*,
Advances in Experimental Medicine and Biology 1035, DOI 10.1007/978-3-319-67358-5_8

state. Fluorescence lifetime is expected to provide more quantitative information on intracellular environments than fluorescence intensity, which is largely changed by several experimental factors, such as photobleaching of fluorescent molecules, optical alignment, and fluctuation of excitation light intensity. Changes in the fluorescence lifetime can be quantitatively analyzed even when the magnitude of the change is small. The measurement of fluorescence lifetime is also applicable even in samples showing considerable light scattering, such as skin.

Fluorescence lifetime imaging (FLIM) microscopy enables us to map the distribution of fluorescence lifetime of a sample in two or three spatial dimensions. FLIM is very powerful for obtaining quantitative values of physiological parameters and rate constants of photo-induced processes with spatial resolution. Intracellular ion concentrations, such as pH or Ca^{2+}, and occurrence of Förster resonance energy transfer (FRET) can be evaluated by FLIM. Both exogenous and endogenous fluorophores used for fluorescence intensity measurements can also be applied to FLIM. FLIM has now been applied in a variety of biological systems, as introduced in review articles [1–8]. In this chapter, we briefly describe the theory of fluorescence lifetime, experimental procedures including materials and methods for obtaining fluorescence lifetime images, and some of our experimental results using FLIM. The notes for measurements of FLIM are then described in detail.

8.2 Theory

8.2.1 Basic Equations

A Jablonski diagram illustrating electronic and vibrational states of a molecule is used to understand fluorescence and related photophysical processes (Fig. 8.1).

Molecules in excited singlet states formed by absorption of excitation light transfer to the ground singlet state (S_0) via the emission of a photon, which is defined as fluorescence. In large molecules in condensed phases, the observed fluorescence arises from vibrationally relaxed state belonging to the lowest excited singlet state (S_1) irrespective of excited states initially populated, which is called as Kasha's rule. This means that even when a molecule is excited to higher electronic states such as S_2 or S_3, fluorescence is usually observed only from the vibrationally relaxed S_1 state. Therefore, the peak position (wavelength) and the bandwidth of the fluorescence spectrum in condensed phases remain unchanged even with different excitation wavelengths. Only fluorescence intensity depends on excitation wavelength; the intensity is proportional to absorbance at the excitation wavelength.

The time dependence of the population in the S_1 state (N_1) following excitation by a pulsed light is given by:

$$\frac{dN_1}{dt} = -kN_1 \tag{8.1}$$

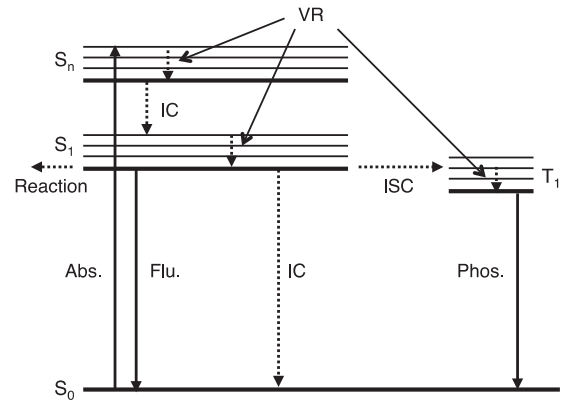

Fig. 8.1 Jablonski diagram. Thick- and thin-solid lines represent electronic states and vibrational states, respectively. VR Vibrational relaxation; IC Internal conversion; ISC Intersystem crossing; Abs. Absorption; Flu. Fluorescence; Phos. Phosphorescence

where k is the rate constant of the transition from the S_1 state, and the duration of the excitation pulse is assumed to be much shorter than the fluorescence lifetime (τ_f). The fluorescence decay profile ($I_f(t)$) after the excitation of a pulsed light is therefore given by the following form because the fluorescence intensity is proportional to N_1:

$$I_f(t) = I_0 \exp\left(-\frac{t}{\tau_f}\right) \tag{8.2}$$

where I_0 is the fluorescence intensity just after photoexcitation ($t = 0$). τ_f is given as the reciprocal of k. When the fluorescence signals of several different fluorescent species are simultaneously detected, the observed $I_f(t)$ is given as follows:

$$I_f(t) = \sum C_i \exp\left(-\frac{t}{\tau_i}\right) \tag{8.3}$$

where τ_i and C_i are the fluorescence lifetime and the preexponential factor of the ith component, respectively. Note that C_i corresponds to the magnitude of the contribution of the ith component to the observed decay profile. Thus the average fluorescence lifetime (τ_{ave}) can be evaluated by the following equation.

$$\tau_{ave} = \frac{\sum C_i \tau_i}{\sum C_i} or \frac{C_i \tau_i^2}{\sum C_i \tau_i} \tag{8.4}$$

The rate constant k is given by the sum of the radiative rate constant (k_r), which represents the transition rate from the S_1 to S_0 states with emitting a fluorescence photon, and the non-radiative rate constant (k_{nr}), which includes all the transitions from the S_1 state to other electronic states without emitting a photon (Fig. 8.1). Therefore, fluorescence lifetime is given by reciprocal of the sum of the radiative and non-radiative rate constants:

$$\tau_f = \frac{1}{k_r + k_{nr}} \tag{8.5}$$

In Eq. (8.5), the rate constants of chemical reactions from the S_1 state are included in k_{nr}. Then, the fluorescence quantum yield (Φ_f) is proportional to τ_f as follows.

$$\Phi_f = \frac{k_r}{k_r + k_{nr}} = k_r \tau_f \tag{8.6}$$

Kasha's rule mentioned above comes from the fact that τ_f in the S_n states ($n \geqq 2$) is usually much shorter (femtosecond range) than that in the S_1 state (subnanosecond to nanosecond range), and therefore Φ_f for the fluorescence from the S_n state is much lower than that from the S_1 state. Vibrational relaxation from highly excited vibrational states to the ground vibrational state is also in the range of femto- to picoseconds [9], and so the fluorescence comes from the vibrationally relaxed S_1 state.

8.2.2 Non-Radiative Transitions

The change in the physiological parameter affecting k_r or k_{nr} results in the change in fluorescence lifetime, whose observation can be used for evaluating the physiological parameters. The origin of the rate constants and the parameters influencing k_{nr} or k_r should well be known for the application of the fluorescence lifetime to measure intracellular environments.

One of the most important non-radiative processes from the S_1 state is the relaxation to the S_0 state with dissipation of the excited energy into intramolecular vibrations and/or into surrounding medium as heat, which is called as internal conversion (Fig. 8.1). Roughly speaking, the rate constant of internal conversion (k_{ic}) exhibits an inverse exponential dependence on the square of the energy difference between the initial and final electronic states. The very short fluorescence lifetime of the S_n states ($n \geqq 2$) is ascribed to the very large value of k_{ic} in these states, which arises from the small energy difference between S_n states ($n \geqq 1$) (Fig. 8.1). The k_{ic} value also depends on environments around the fluorophores, which is used to measure bulk parameters such as viscosity and polarity using the fluorescence lifetime of suitable fluorophores.

Interactions with protein also induce the remarkable change in k_{ic} of the fluorophore, which is applied to distinguish between protein-bound and free states of the fluorophore. For example, the fluorescence lifetime of coenzyme NADH becomes longer after the change from the free state (around 300 ps in water) to the protein-bound state (1–2 ns) [1, 2, 5], which is thought to arise both from the steric hindrance for the rotation between the pyridine and amide in the protein-bound state and from the increase in k_{ic} in polar environments such as water [10]. On the other hand, fluorescence lifetime of coenzyme FAD becomes shorter after the change from the free state (2–3 ns in water) to the protein-bound state (femto- to picoseconds) [1, 2, 5], which arises from the electron transfer from the S_1 state of FAD to amino acids surrounding FAD in the protein. Fluorescent dyes developed for sensing of specific ions such as Ca^{2+} also exhibit a remarkable change in the fluorescence lifetime with binding of these dyes to a target ion, which can be used to make the quantitative evaluation of the concentration of the target ion with the fluorescence lifetime.

FRET that describes the non-radiative energy transfer from a photoexcited donor fluorophore to an acceptor molecule also increases k_{nr} of the donor fluorophore, resulting in the decrease in the fluorescence lifetime of the donor. The rate of FRET can directly be evaluated by comparing the fluorescence lifetime of the donor in the presence and absence of the acceptor molecule [3]. Intersystem crossing is another non-radiative process, which is the transition from the S_1 state to the triplet state (Fig. 8.1). The acceleration of intersystem crossing is observed by substitution of a heavy atom such as iodine in a molecule, which is called as heavy-atom effect.

Dynamic quenching is also an important non-radiative process to be concerned. Dynamic quenching is the non-radiative process induced by the collision of target ions or molecules with the fluorescent molecule in the S_1 state. The relation of the observed τ_f with the concentration of quencher (ion or molecule), [Q], is given by the following equation called as Stern–Volmer expression:

$$\frac{\tau_0}{\tau_f} = 1 + k_Q \tau_0 [Q] \tag{8.7}$$

where τ_0 is the fluorescence lifetime in the absence of the quencher and k_Q is the rate constant of dynamic quenching. The quencher concentration can therefore be evaluated by the proportionality relation between the inverse of the fluorescence lifetime and the quencher concentration. Dynamic quenching becomes significant when the fluorescence lifetime of the fluorophore is sufficiently long such as ten nanoseconds in water, which is due to the occurrence of the collision with the quencher within the fluorescence lifetime.

8.2.3 Radiative Transitions

The radiative rate constant (k_r) is proportional to the molar extinction coefficient of the $S_1 \leftarrow S_0$ absorption, and it becomes larger with increasing the extinction coefficient. The k_r value is nearly independent of most physiological parameters. However, the refractive index of the medium was shown to be evaluated by the fluorescence lifetime of the fluorophore, based on the proportionality relation between k_r and the square of the refractive index [11]. The difference in the fluorescence lifetime of the fluorophore between cell interior and membrane was discussed in terms of the difference of the refractive index between the two media [12].

8.2.4 Evaluation of Physiological Parameters

As discussed in Ref. [6], the procedures for evaluating intracellular environments with fluorescence lifetime are roughly classified into three categories, that is, dynamic quenching method, method based on the detection of the rate constant affected by bulk parameters, and ratiometric method. In the dynamic quenching method, the standard curve which gives a relation between the fluorescence lifetime of the fluorophore and the quencher concentration is first pre-

pared using Eq. (8.7), and then the quencher concentration in the sample is determined by the measured fluorescence lifetime.

If the fluorescence lifetime is correlated with a bulk parameter such as viscosity or temperature, the preparation of the standard curve between the fluorescence lifetime and the bulk parameter also enables us to evaluate the bulk parameter in a cell.

The ratiometric method is used for evaluating the concentration of target ion or molecule when the fluorescence lifetime of the fluorophore changes with the binding to the target. When the free and target-bound fluorophores coexist and the fluorescence signals of both the species are simultaneously detected, the observed fluorescence decay curve exhibits a multi-exponential function as given in Eq. (8.3), and the average fluorescence lifetime can be evaluated using Eq. (8.4). The pre-exponential factor represents the ratio of the concentration of the free and target-bound fluorophores, and τ_{ave} is changed with the target concentration. Therefore, the target concentration can be determined by the standard curve between τ_{ave} and the target concentration when the free and bound fluorophores exist with the equilibrium constant in the ground state. The details of the application of the ratiometric method with the fluorescence lifetime are shown in Ref. [6].

8.3 Examples and Materials

8.3.1 Example of Lifetime Measurements

The applications of FLIM in the evaluation of intracellular environments and occurrence of FRET have been introduced by many excellent reviews [1–8]. Here we briefly describe our FLIM results of the endogenous nicotinamide adenine dinucleotide (NADH) and the exogenous fluorophore talaporfin that is a dye used for photodynamic therapy (PDT).

Even in the absence of exogenous fluorescent dyes, cells exhibit fluorescence called autofluorescence, which results from endogenous fluorophores present within cells. NADH, a key cofactor involved in various physiological processes, is a representative autofluorescent fluorophore exhibiting blue fluorescence. The fluorescence lifetime of NADH depends on the environment, which can be used to monitor intracellular environment using the autofluorescence lifetime of NADH. The autofluorescence lifetime of NADH was recently shown to be capable of evaluating intracellular pH without using exogenous probes [13]. The autofluorescence intensity and corresponding lifetime images of NADH in HeLa cells are shown in Fig. 8.2 [13].

The magnitude of the intensity reflects the concentration of NADH in the organelle, and the intracellular dull round and bright regions on the intensity image are assigned to a nucleus and mitochondria, respectively. The autofluorescence lifetime of NADH became shorter with increasing intracellular pH, and the plots of τ_{ave} against intracellular pH become the standard curve for evaluating intracellular pH using the autofluorescence lifetime of NADH without exogenous probes. The observed change in the autofluorescence lifetime of NADH with intracellular pH can be explained in terms of the change in the interaction between NADH and proteins. It was also shown in Fig. 8.2 that the autofluorescence lifetime depends on organelle and that the fluorescence lifetime in nuclei is shorter than that in other regions. This result is attributed to the dependence of the autofluorescence lifetime of NADH on the enzyme to which it is bound.

We have also shown the cellular distribution of τ_{ave} of talaporfin sodium, one of the representative organic fluorophores used for PDT, in normal and cancer cells (Fig. 8.3) [14]. The histograms of τ_{ave} were obtained from the analysis of the fluorescence lifetime image. The peak of τ_{ave} is different between normal and cancer cells, which reflects the different intracellular environment around dye molecules from each other. This result suggests that FLIM of talaporfin sodium is applicable to the *in vivo* detection of cancer cells.

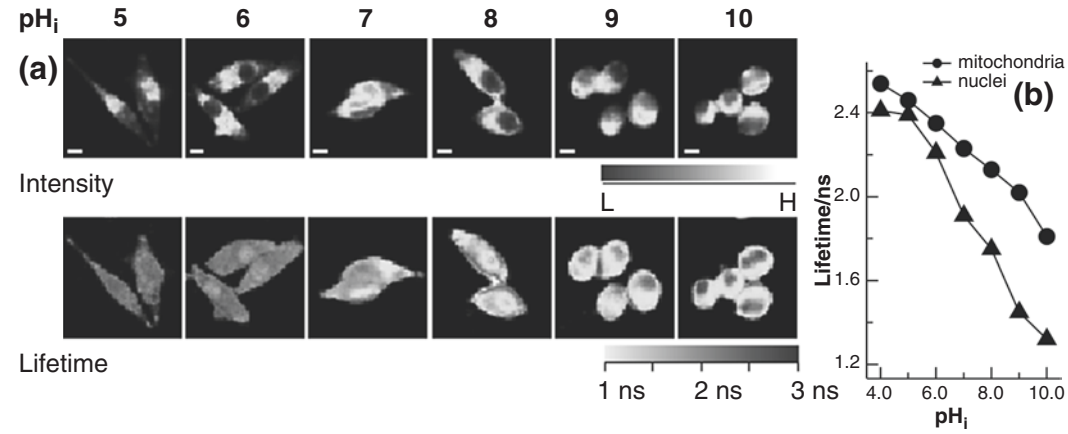

Fig. 8.2 (**a**) Fluorescence intensity (*upper*) and lifetime images (*lower*) of NADH in HeLa cells with changing intracellular pH (pH$_i$). Scale bar is 10 μm. (**b**) Plots of the fluorescence lifetime as a function of intracellular pH using the values obtained at mitochondria (*circles*) and at nuclei (*triangles*). Excitation and detection wavelengths were 370 nm and 417–477 nm, respectively. Reprinted with permission from Ogikubo et al. 2011 [13]. Copyright 2011 American Chemical Society

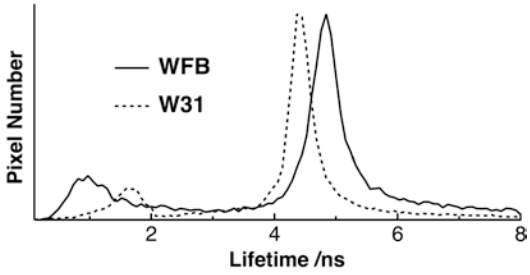

Fig. 8.3 Histograms of the average fluorescence lifetime of talaporfin sodium in normal (*solid line*) and cancer (*dotted line*) cells. Wistar-king A rat fetus fibroblast (WFB) cells and W31 cells that are the malignant transformed cells from WFB were used as normal and cancer cells, respectively. Excitation wavelength was 405 nm and the fluorescence in the wavelength region longer than 590 nm was detected [14]

8.3.2 Materials

The sample preparation for FLIM is very similar to that for standard fluorescence microscopy. The sample preparation for FLIM of endogenous NADH in HeLa cells with changing intracellular pH is as follows (*see* **Note 1**).

1. Cell medium for HeLa cells is first prepared by adding 50 ml fetal bovine serum (FBS) and 5 ml penicillin–streptomycin to 450 ml of Dullbecco's modified Eagle's medium (DMEM). The prepared medium is called DMEM (+/+) and is stored at 4 °C for long-term use.
2. FBS must be heat-inactivated at a temperature of 56 °C for 30 min before mixing it with the medium.
3. Stocked HeLa cells are thawed to room temperature and mixed with 4 ml of DMEM (+/+). The solution is centrifuged at 1500 rpm for 2 min and the supernatant solution is then aspirated. After aspiration, the resultant pellet is suspended in 5–10 ml of DMEM (+/+).
4. HeLa cells are plated in a 10-cm dish with 8 ml of DMEM (+/+) and are grown in a 5% CO_2 humidified atmosphere at 37 °C for 1–2 days.
5. Cells are washed with phosphate buffered saline (PBS) buffer, and after aspiration of PBS from the dish, 1–2 ml of trypsin/EDTA is added to the dish. Cells are incubated with trypsin for 2 min. Preparation of PBS: 10× PBS is prepared by mixing 80 g of NaCl, 2 g of KCl, 29 g of Na_2HPO_4•$12H_2O$, and 2 g of KH_2PO_4 in 1000 ml of milli-Q water (a sensitivity of 18 MΩ cm at 25 °C) with pH 7.2–7.4; 1× PBS solution is prepared by mixing 100 ml of 10× stock solution in 900 ml of milli-Q water.

6. DMEM (+/+) is then added to the dish to inactivate trypsin, and cells are collected in a conical tube. Cells are washed by centrifugation and suspended in DMEM (+/+) and then plated in an eight-well chambered coverglass and incubated for a day. The cell suspension volume in each well is 0.4 ml (*see* **Note 2**).
7. In the experiment of sensing of intracellular pH, calibration of intracellular pH is performed by the so-called nigericin/high K^+ method [15], in which cells are incubated in KCl-rich medium including nigericin that makes an equilibrium between intracellular and extracellular pH. Nigericin is an H^+/K^+ ionophore and equilibrates intracellular and extracellular pH by exchange of H^+ across the plasma membrane in the presence of a depolarizing concentration of K^+ in extracellular medium.
8. In the nigericin/high K^+ method, HeLa cells are rinsed once with KCl-rich medium (125 mM KCl, 20 mM NaCl, 10 mM HEPES, 10 mM MES, 0.5 mM $CaCl_2$, 0.5 mM $MgCl_2$, and 13.4 μM nigericin) and then incubated with the same KCl-rich medium at different pH for 15 min in a humidified atmosphere at 37 °C. After incubation with the KCl-rich medium, measurement of the fluorescence lifetime with different intracellular pH is started. The nigericin/high K^+ method enables us to evaluate intracellular pH by measuring extracellular (medium) pH. The medium pH is adjusted using HCl and NaOH solutions.

Sample preparation of exogenous dyes for FLIM is very similar to that of the above-mentioned endogenous dyes. In case of small molecules such as organic fluorophores, intracellular dye loading is usually performed just prior to the measurement. For example, talaporfin sodium is loaded as follows (*see* **Note 3**).

1. Commercially available talaporfin sodium is dissolved in FBS-free DMEM at concentrations of 1–100 μM.
2. The dye solution is added to the cultured cells in an eight-well chambered coverglass. Cells are incubated for 30 min in a 5% CO_2 humidified atmosphere at 37 °C and are washed twice with calcium- and magnesium-free PBS. During this procedure, great care should be taken to avoid light irradiation to the sample because PDT can occur in cells during light irradiation, thus resulting in cellular damage.
3. Confirm dye loading and very weak background signals by a fluorescence microscope. When the fluorescence is only observed within a cell, FLIM measurements are initiated.

8.4 Methods

8.4.1 Time-Domain Method

Fluorescence lifetime can be measured using two methods: time-domain and frequency-domain methods. The time-domain method is a time-resolved measurement of a fluorescence decay curve using a pulsed excitation light such as a femtosecond pulse laser and a detection system having enough time resolution. All of the fluorescence lifetimes of the fluorophores responsible for the observed fluorescence can be quantitatively evaluated by analyzing the fluorescence decay curve with a multi-exponential function (see Eq. (8.3)). The time resolution is determined by the duration of the excitation pulse and the time resolution of the detection system. Time-correlated single photon counting (TCSPC) system, streak camera, and time-gated systems such as intensified CCD (ICCD) are used as the detection system in the time-domain method. An example of a FLIM system based on the time-domain method is shown in Fig. 8.4.

The FLIM system consists of a pulse laser and a microscope system; the latter is the same as the standard laser fluorescence microscope system used for intensity image measurements, except for the detector. As mentioned above, the detection system should have enough time resolution to evaluate the fluorescence lifetime of the fluorophore.

TCSPC is based on the detection of the arrival time of a single fluorescence photon following photoirradiation with a pulsed excitation light.

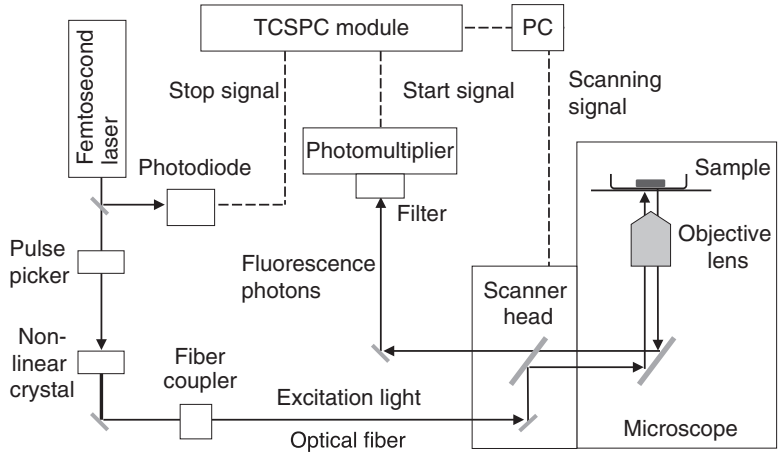

Fig. 8.4 Schematic diagram of FLIM system composed of a femtosecond mode-locked Ti:sapphire laser as an excitation source, scanning inverted confocal microscope, and TCSPC module

The measurement of the arrival time is repeated many times with periodical excitation light pulses, and plots of the number of fluorescence photons against arrival time result in the shape of fluorescence decay profile. TCSPC is typically used for FLIM because of its high time resolution and high sensitivity. For example, the combination of a microchannel-plate photomultiplier tube (MCP-PMT) with a TCSPC system gives a time-resolution less than 30 ps. Laser scanning microscope is used for obtaining the image with TCSPC, and fluorescence decay at each pixel of the image is measured by synchronizing the scanning of the spot of the excitation beam with the start–stop triggers for the decay measurement. Any type of laser scanning microscopes (such as a confocal or two-photon microscope) can be combined with TCSPC.

In the time-gated method, the fluorescence signal is detected only when the gate having a definite time width is open, and the time-resolved image is obtained by sequentially changing the time (delay time) between the excitation pulse and the opening of the gate. The gate width ranges from subnano to nanoseconds, indicating that the time resolution of the time-gated method is usually lower than TCSPC. A fluorescence lifetime image is obtained from the analysis of the delay time dependence of fluorescence intensity in the image. A two-dimensional image is obtained at once using a two-dimensional camera having a time-gated detection such as ICCD, which shortens the measurement time compared with TCSPC.

8.4.2 Frequency-Domain Method

In the frequency-domain method, a sinusoidal-modulated light is used to excite fluorophores, and fluorescence lifetime is evaluated by measuring both the phase delay of the observed fluorescence and the reduction of the amplitude. The modulation of the excitation light can be made by an acousto-optic modulator, and an inexpensive continuous wave (cw) laser is adequate as the excitation light source in the frequency-domain method. If the fluorescence of fluorophores shows a single-exponential decay, the relation between fluorescence lifetime and phase delay (ϕ) of the fluorescence is given by

$$\tau_{\mathrm{f}} = \frac{\tan\phi}{\omega} \tag{8.8}$$

where ω is the angular frequency of the sinusoidal excitation light. The time resolution is determined by the angular frequency and the frequency response of the detection system. Both laser scanning and ICCD are used for obtaining the image with the frequency-domain method. The measurement time in the frequency-domain method is typically much shorter than that in the time-domain method; this difference is very important for FLIM, as

the time-domain method generally takes time to obtain lifetime images with sufficient signal to noise (S/N) ratio.

8.4.3 Comparison between Time-Domain and Frequency-Domain Methods

The time-domain method has the advantage of being capable of detailed analyses of the fluorescence decay profile, resulting in quantitative evaluation of the fluorescence lifetime of each decaying component using Eq. (8.3) when fluorescence shows a multi-exponential decay. However, it takes time to obtain a lifetime image with the time-domain method, and the prolonged laser irradiation occasionally causes damage to biological samples. Compared with the TCSPC method, the time-gated method reduces the measurement time; however, the time resolution of the time-gated method usually becomes lower, as mentioned above. The necessity of an expensive pulse laser is also a disadvantage of the time-domain method. On the other hand, lifetime images can be obtained in a short time using the frequency-domain method, which enables live cell imaging by frequency-domain FLIM. However, the quantitative analysis is somewhat difficult when the fluorescence shows a multi-exponential decay, which is generally observed in biological samples.

8.4.4 Procedure for FLIM Measurements

The procedure for FLIM experiment is almost identical to typical measuremenets of intensity images with a microscope. The example of the procedure and notes for FLIM using TCSPC is as follows, which is based on the diagram of the FLIM system in Fig. 8.4 and a femtosecond mode-locked Ti:sapphire laser is used as an excitation source (*see* **Notes 4, 5**).

1. Turn on the pulse laser, confocal microscope, and fluorescence detection systems, and several accessories such as a photodiode to detect excitation laser pulses. Systems need a warm-up period. The warm-up time to yield a stable experimental condition depends on the type of system.
2. Tune the output power of the green diode laser used for exciting the Ti:sapphire laser to 5–10 W. Open the shutter of the diode laser to excite the Ti:sapphire laser. The fundamental output of the Ti:sapphire laser is typically more than 1 W at 800 nm. Set the output wavelength of the Ti:sapphire laser at the value required in the experiment (*see* **Note 6**).
3. Measure the shape of the output beam against the wavelength and confirm the mode-locking of the output of the Ti:sapphire laser. If the pulse shape is not appropriate and/or the output power is insufficient, adjust the Ti:sapphire laser by tuning the mirrors (*see* **Note 7**).
4. The second harmonic generation (SHG) (visible light) or the third harmonic generation (THG) (UV light) of the Ti:sapphire laser, which is used as the excitation light source, is obtained using non-linear crystals such as beta barium borate (BBO). Adjust the angle of the crystal with respect to the laser beam to fulfill phase matching conditions. The maximum power of SHG (THG) is obtained at phase matching conditions (*see* **Note 8**).
5. The excitation light is coupled to an optical fiber using a fiber coupler and is introduced into the scanner head of a confocal microscope (*see* **Note 9**).
6. A portion of the fundamental output from the Ti:sapphire laser is taken out and is introduced into a high-speed photodiode to obtain the electrical signal of the pulse trains. This electrical signal is used as the trigger signal to start or stop the fluorescence decay measurement (Fig. 8.4).
7. Set the standard sample such as a standard slide on the stage of the microscope and the excitation light beam is focused onto the standard sample with an objective lens.
8. The fluorescence from the standard sample is collected with the same objective lens and is

introduced into the scanner head, followed by an appropriate dichroic mirror and/or an interference filter to extract the fluorescence of interest. The fluorescence is then detected by the detector having enough time resolution (*see* **Note 10**).

9. Start the measurement of the fluorescence decay of the standard sample.
10. Adjust the focus of the intensity image and the timing between the start (or stop) trigger pulse coming from the photodiode and the arrival of a fluorescence photon at the detector by measuring the fluorescence decay of the standard sample (*see* **Note 11**).
11. Replace the standard sample with the eight-well chambered coverglass having cultured cells on the stage of the microscope and start the FLIM measurement of the one well that is used as an experimental calibration well.
12. Adjust experimental parameters including time range in the decay, gain and offset of the detector, laser power, accumulation time, and pixel dwell time while doing repeated measurements of the fluorescence image (or fluorescence decay profile) of the cells in the calibration well. The pixel dwell time is the irradiation time at each pixel of the image. The measurement of FLIM should be finished as soon as possible while keeping the intensity of the excitation light as low as possible because biological samples are easily damaged by irradiation of laser light (*see* **Note 12**).
13. Change the well and start the FLIM measurement of the sample. The measurement of the fluorescence decay profile is synchronized with the scanner of the microscope and the fluorescence decay at each pixel of the image is sequentially obtained (*see* **Note 13**).
14. The instrumental response function (IRF), which represents the time response of the system, is necessary to fit the observed decay profile (see Fig. 8.5). IRF is obtained by measuring the time profile of the scattered excitation light or the fluorescence decay of the fluorophore whose lifetime is much shorter than the time resolution of the system (*see* **Notes 14, 15**).

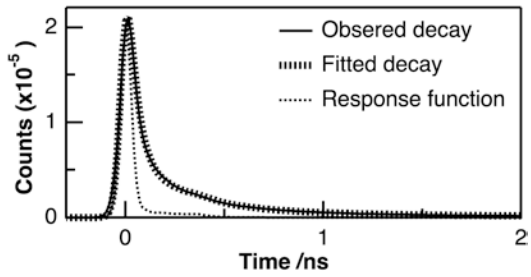

Fig. 8.5 Fluorescence decay (*solid line*) of the model compound of GFP chromophore (4-hydroxybenzylidene-1,2-dimethylimidazolinone) in a PMMA film. The fitted curve obtained by the convolution of IRF (*dotted line*) with a multi-exponential function is shown by a thick-dotted line. Excitation and detected wavelengths were 379 and 450 nm, respectively. Reprinted with permission from Nakabayashi et al. 2011 [16]. Copyright 2011 American Chemical Society

15. Fluorescence decay profile at each pixel is simulated by the convolution of IRF with a single- or multi-exponential decay using the least square method. Fluorescence lifetime and pre-exponential factor of each decaying component are evaluated, and the results are then converted into a fluorescence lifetime image. The size of the image is typically 256 × 256 or 512 × 512 pixels (*see* **Notes 16, 17**).

8.5 Notes

1. Compared with intensity measurements, FLIM measurements are very useful for endogenous fluorophores because more quantitative analysis is possible even for weak fluorescence such as autofluorescence. The fluorescence lifetime of endogenous fluorophores has been shown to provide valuable information on intracellular conditions, which results from the fact that endogenous fluorophores are related to cellular physiological processes and metabolic activities. There are several typical endogenous fluorophores in a single cell. As shown in the review [5], each endogenous fluorophore has characteristic absorption and fluorescence spectra, and it is possible to select the auto-

fluorescence of the target endogenous fluorophore using appropriate excitation and detection fluorescence wavelengths.

2. Cell tissue culture media generally exhibit background fluorescence, which lowers S/N ratio of the fluorescence image. Opti-MEM without phenol red may be used as a background-free medium for visible light excitation, whereas cell media including organic molecules exhibit non-negligible fluorescence for UV light excitation. Therefore, it is better to investigate in advance the fluorescence of the medium with the excitation wavelength used.
3. Exogenous fluorophores developed for fluorescence intensity measurements can also be used for FLIM. Exogenous fluorophores developed to be sensitive to a specific ion usually show the equilibrium between the free and ion-bound states in the ground electronic state, and the ion concentration can be evaluated using the standard curve of the fluorescence intensity only from one of the equilibrated species against ion concentration. In FLIM, on the other hand, fluorescence of both free and ion-bound species should be simultaneously detected as far as the ratiometric method is used. This is a major difference between fluorescence intensity and lifetime measurements.
4. The duration of the excitation pulse determines the time resolution of the experiment, and so that a shorter pulse width is better for FLIM. In many laboratories, the femtosecond mode-locked Ti:sapphire laser is used as the excitation light source for FLIM because of its sufficiently short pulse width (less than one hundred femtosecond), high stability of the output intensity, and ease of use. The repetition of the mode-locked Ti:sapphire laser is typically in MHz, which is also very convenient for accumulating fluorescence signals and reducing the measurement time because of the high repetition rate. Some Ti:sapphire lasers have tunability of the output wavelength in the range of approximately 740–990 nm; therefore, the second and third harmonic outputs of 370–450 nm and 270–330 nm, respectively, can be used as the excitation wavelength.
5. The low cost picosecond diode lasers are also used for FLIM. The wavelength of the diode laser is fixed, so that some diode lasers should be prepared to use several fluorescent dyes in FLIM. The output power of the diode laser is much lower than that of the Ti:sapphire laser; however, in the case of TCSPC, the sample is usually excited by laser pulses with very low excitation intensity because of the detection limit of the single-photoelectron event, that is, less than one fluorescence photon must be generated per each excitation pulse in TCSPC. A high-power pulse laser is not always necessary for TCSPC, and many types of low cost picosecond diode lasers are now available for TCSPC.
6. In the ratiometric method, excitation and detection wavelengths must be carefully selected. The magnitude of C_i in Eq. (8.4) usually depends on both the excitation and detection wavelengths; thus, τ_{ave} depends on both of these wavelengths. It is strongly recommended to select the wavelengths showing a large change in τ_{ave} with changing concentration of the target ion or molecule.
7. In the case of mode-locked lasers, confirmation of mode-locking, which is the most significant technique to generate femtosecond pulses, is very important because only cw beam appears without mode-locking. Attainment of mode-locking can be confirmed by monitoring the shape of the output intensity against wavelength because the spectral shape becomes broad due to the uncertainty principle when femtosecond pulses are generated by mode-locking. A very sharp peak showing a single oscillation wavelength is observed when the output is cw. The shape can be easily monitored using a simple spectrometer such as a fiber module spectrometer.
8. The repetition rate of the laser pulses must be reduced by a pulse picker when the measured fluorescence lifetime is as long as the time interval between consecutive excitation

pulses. This is because the decay profile should be measured until the fluorescence decay is completely finished to obtain the quantitative value of the fluorescence lifetime. It is recommended that the time interval between consecutive pulses is longer than the quadruple of the fluorescence lifetime.

9. The pulse width of femtosecond light becomes longer (more than twice in some cases) due to the group velocity dispersion (GVD) after passing through a medium such as an optical fiber. In almost all of FLIM experiments, however, the increase in the pulse width due to GVD is negligible because remarkable effect of GVD only appears for femtosecond pulses to be a few picoseconds and the time-resolution of FLIM is usually more than 10 picoseconds.
10. MCP-PMT is very sensitive and easily breakable with strong light. The scattered excitation light should completely be removed using a suitable filter, and the mounting of the filter must be checked before turning on the high voltage of MCP-PMT. Strong fluorescence intensity should also not be allowed to enter the detection system, as it can damage detectors.
11. Spatial resolution of FLIM is determined by objective lens, which is the same as that of a conventional microscope.
12. Photobleaching becomes severe in TCSPC because accumulation of a certain amount of photon numbers is necessary to obtain the fluorescence decay profile with sufficient S/N ratio. Therefore, attention must be paid to photobleaching for determining laser power, accumulation time, and pixel dwell time for FLIM. To reduce the amount of photobleaching, it is better to decrease the dwell time and the laser power, while the accumulation time may have to be increased.
13. Fluorescence lifetime images can be automatically generated in many FLIM software programs; however, the fitting result of the fluorescence decay and the residue in the fitting should be confirmed after the measurement. If the fitting is insufficient, fitting parameters such as the number of exponential decays and initial values for fitting must be changed.
14. Figure 8.5 shows the example of IRF obtained by TCSPC with an MCP-PMT [16]. IRF of PMT is usually asymmetric, e.g., a small shoulder may be observed in the region of 0–0.5 ns, as shown in Fig. 8.5. Since the observed decay reflects such a shoulder, the acquisition of the exact shape of IRF is essential for entirely reproducing the obtained decay profiles.
15. IRF can be obtained by measuring the time profile of the excitation light reflected from the coverglass. IRF with a full width at half maximum (FWHM) of ~60 ps (Fig. 8.5) makes it possible to estimate a fluorescence lifetime as short as 30 ps using a convolution method.
16. The entering of scattered excitation light into the detector also becomes the artifact of the observed fluorescence decay, which appears as a component with a fluorescence lifetime much shorter than the time resolution of the system.
17. The quantitative estimation of the background signal is sometimes necessary to analyze the observed fluorescence decay profile. The background can be evaluated by measuring the signals at the area where fluorescent cells are non-existent, and the obtained value is subtracted from the decay at all pixels.

References

1. Chorvat D Jr, Chorvatova A (2009) Multi-wavelength fluorescence lifetime spectroscopy: a new approach to the study of endogenous fluorescence in living cells and tissues. Laser Phys Lett 6:175–193
2. Berezin MY, Achilefu S (2010) Fluorescence lifetime measurements and biological imaging. Chem Rev 110:2641–2684
3. Becker W (2012) Fluorescence lifetime imaging-techniques and applications. J Microsc 247:119–136
4. Marcu L (2012) Fluorescence lifetime techniques in medical applications. Ann Biomed Eng 40:304–331
5. Ohta N, Nakabayashi T (2014) Intracellular autofluorescent species: structure, spectroscopy, and photophysics. In: Ghukasyan VV, Heikal AA (eds) Natural biomarkers for cellular metabolism, biology,

techniques, and applications. CRC Press, Boca Raton, pp 41–64
6. Nakabayashi T, Ohta N (2015) Sensing of intracellular environments by fluorescence lifetime imaging of exogenous fluorophores. Anal Chem 31:275–285
7. Sarder P, Maji D, Achilefu S (2015) Molecular probes for fluorescence lifetime imaging. Bioconjug Chem 26:963–974
8. Hirvonen LM, Suhling K (2017) Wide-field TCSPC: methods and applications. Meas Sci Technol 28:012003
9. Nakabayashi T, Okamoto H, Tasumi M (1998) Vibrational relaxation dynamics of trans-stilbene in the lowest excited singlet state. Pump and probe wavelength dependencies of the picosecond time-resolved anti-Stokes Raman spectrum. J Phys Chem A 102:9686–9695
10. Nakabayashi T, Islam MS, Li L et al (2014) Studies on external electric field effects on absorption and fluorescence spectra of NADH. Chem Phys Lett 595-596:25–30
11. Suhling K, Siegel J, Phillips D et al (2002) Imaging the environment of green fluorescent protein. Biophys J 83:3589–3595
12. van Manen HJ, Verkuijlen P, Wittendorp P et al (2008) Refractive index sensing of green fluorescent proteins in living cells using fluorescence lifetime imaging microscopy. Biophys J 94:L67–L69
13. Ogikubo S, Nakabayashi T, Adachi T et al (2011) Intracellular pH sensing using autofluorescence lifetime microscopy. J Phys Chem B 115:10385–10390
14. Awasthi K, Yamamoto K, Furuya K et al (2015) Fluorescence characteristics and lifetime images of photosensitizers of talaporfin sodium and sodium pheophorbide a in normal and cancer cells. Sensors 15:11417–11430
15. Thomas JA, Buchsbaum RN, Zimniak A et al (1979) Intracellular pH measurements in Ehrlich ascites tumor cells utilizing spectroscopic probes generated in situ. Biochemistry 18:2210–2218
16. Nakabayashi T, Hino K, Ohta Y et al (2011) Electric-field-induced changes in absorption and fluorescence of the green fluorescent protein chromophore in a PMMA film. J Phys Chem B 115: 8622–8626

Quantitative Imaging of Ca^{2+} by 3D–FLIM in Live Tissues

9

Asylkhan Rakymzhan, Helena Radbruch, and Raluca A. Niesner

Abstract

The calcium concentration within living cells is highly dynamic and, for many cell types, a reliable indicator of the functional state of the cells—both of isolated cells, but even, more important, of cells in tissue. In order to dynamically quantify intracellular calcium levels, various genetically encoded calcium sensors have been developed—the best of which are those based on Förster resonant energy transfer (FRET). Here we present a fluorescence lifetime imaging (FLIM) method to measure FRET in such a calcium sensor (TN L15) in neurons of hippocampal slices and of the brain stem of anesthetized mice. The method gives the unique opportunity to determine absolute neuronal calcium concentrations in the living organism.

Keywords

Förster resonant energy transfer (FRET) • Fluorescence lifetime imaging (FLIM) • Genetically encoded calcium indicators (GECI) • *CerTN L15* mouse strain • Parallelized time-correlated single photon counting (TCSPC)

A. Rakymzhan
Deutsches Rheuma-Forschungszentrum, a Leibniz Institute, Charitéplatz 1, 10117 Berlin, Germany

H. Radbruch
Neuropathology, Charité–Universitätsmedizin, Charitéplatz 1, 10117 Berlin, Germany

R.A. Niesner (✉)
Deutsches Rheuma-Forschungszentrum, a Leibniz Institute, Charitéplatz 1, 10117 Berlin, Germany

German Rheumatism Research Center, Charitéplatz 1, 10117 Berlin, Germany
e-mail: niesner@drfz.de

9.1 Introduction

Intracellular calcium is a general signaling molecule for cellular activation or even overactivation. Referring to neurons, the typical time-averaged calcium concentration amounts to 100 nM, excluding the very short calcium oscillations connected to the transmission of information from dendrites through the axon to other neurons, i.e. physiologic state. If neurons are affected over longer periods of time, their

R.I. Dmitriev (ed.), *Multi-Parametric Live Cell Microscopy of 3D Tissue Models*, Advances in Experimental Medicine and Biology 1035, DOI 10.1007/978-3-319-67358-5_9

time-averaged calcium concentration increases drastically towards 1 μM and beyond [1, 2]. This state defines neuronal dysfunction ultimately leading to neuronal damage and neuronal death.

The best adequate genetically encoded indicators of calcium to be used to quantify intracellular calcium in live 3D tissues or even in living organisms are those based on Förster resonant energy transfer (FRET) [1, 3]. FRET relies on the resonant transfer of energy from a donor molecule that has been previously excited by a laser, to an acceptor molecule, that consequently emits a fluorescence photon. FRET may take place only if the donor and acceptor molecules are within few tens of nm. The FRET efficiency decreases with the 6th power of the distance between the two molecules [4–7]. There are protein constructs based on calcium sensitive molecules such as Troponin C, which use adequate fluorescent protein FRET pairs to monitor intracellular calcium: several generations of GECIs have been reported such as TN L15, TN XXL, among others [3].

To avoid effects of photobleaching and signal-to-noise-ratio differences between donor and acceptor molecules in typically highly scattering tissue, the best way to quantify FRET is by FLIM of the donor [8, 9].

Here we describe a method to acquire and evaluate data in brain slices and the brain stem of CerTN L15 mice to measure neuronal calcium in vivo. We demonstrated the advantages of this approach on the example of neuronal dysfunction quantification both in hippocampal slices and in a murine model of chronic neuroinflammation [2, 10–14].

9.2 Materials

1. CerTN L15 mice expressing under the Thy1 promotor (mainly in neurons) the TN L15 Ca^{2+} sensor. The TN L15 sensor is a FRET-based sensor containing Troponin C with Cerulean (FRET-donor) and Citrine (FRET-acceptor)
2. Artificial cerebro-spinal fluid (ACSF) containing 124 mM NaCl, 1.25 mM NaH_2PO_4, 26 mM $NaHCO_3$, 3 mM KCl, 1.6 mM $CaCl_2$, 1.8 mM $MgSO_4$ and 10 mM glucose, adjusted to pH 7.35
3. Vibratome (VT 1200 S, Leica)
4. 16x parallelized time-correlated single-photon counting (TCSPC) system
   Note: It may be any TCSPC device.
5. TrimScope II two-photon microscope
   Note: It may be any two-photon microscope that can be equipped with a TCSPC device.

9.3 Methods

Carry out all procedures at 37 °C in order to insure perfect metabolic state of the brain tissue both in the case of hippocampus slices and in anaesthetized mice.

9.3.1 Preparation of Hippocampus Slices from Adult *CerTN L15* Mice

1. Kill a *CerTN L15* mouse by cervical dislocation.
2. Remove the mouse brain immediately and place it into 4 °C cold aerated (carbogen, 95% O_2 and 5% CO_2) artificial cerebrospinal fluid (ACSF).
3. Cut 400 μm-thick brain slices the vibratome and isolate hippocampal slices.
4. Allow the slices to recover for at least 45 min at room temperature before transferring them to a heated slice chamber. Continuously perfuse the slice with previously warmed carbogen-aerated ACSF.

9.3.2 Preparing the Brain Stem of *CerTN L15* Mice for Imaging

1. Anesthetize a *CerTN L15* mouse with Isoflurane using a mask.
2. Expose the brain stem by carefully removing the musculature above the dorsal neck area and the dura mater between the first cervical vertebra and the occipital skull bone.

3. Access the deeper brain stem areas by inclining the head and superfuse the brain with isotonic Ringer solution.
4. Control anaesthesia depth by continuous CO2 measurements of exhaled gas recorded with a CI-240 Microcapnograph (Columbus Instruments, USA) and by an Einthoven three-lead electrocardiogram (ECG).
   Note: In order to avoid breathing artefacts during brain stem imaging, the ECG signal was used as an external trigger for the galvanometric scanner of the microscope, which controls image acquisition. In this way, each fluorescence z-stack was recorded at exactly the same tissue region within the organ, at the same point in the respiratory cycle.

9.3.3 Acquiring Time-Resolved Fluorescence Images of Cerulean

5. Focus the excitation laser beam into the sample by an objective lens for deep-tissue imaging (e.g. 20x dipping lens, NA 0.95, WD 2 mm – Olympus, Hamburg, Germany) and scanned it over the sample.
6. Record the fluorescence signal in a time-resolved manner with the p-TCSPC detector. *Note*: The p-TCSPC device is based on parallel photon detection with multi-anode (16 channels) photomultiplier tubes (PMT) and on evaluation relying on time-to-digital converter (TDC) electronics. Thus, the electronic dead time of the device is reduced to 5.5 ns while the FLIM repetition rate is limited only by the laser, i.e. 80 MHz, and no longer by the TCSPC electronics. The width of the instrument response function (IRF) as measured by SHG amounts to 280 ps. Further, the IRF is highly symmetric (no after pulsing) and can be well approximated by a Gaussian distribution. The jitter of the instrument lays at <10 ps. The mean dark counts/channel amount to 5000 cps and do not exceed 10,000 cps. The cross talk between TDC channels is 3%.
7. Acquire three-dimensional (e.g. 300 × 300 ×50 μm^3, 512 × 512 × 26 voxel) time-resolved fluorescence images of either the hippocampus slices or of the brain stem of anesthetized mice with the p-TCSPC setup at λ_{exc} 850 nm and $\lambda_{detection} = 460 \pm 30$ nm. Use a peak photon flux ϕ of approx. 10^{30} photons/s·cm^2 to avoid photo-damage and time bins of 1–100 ps for appropriate time resolution.

9.3.4 Evaluating the FRET-Ratio from Cerulean FLIM Data

8. Acquire from the 3D time-resolved fluorescence data of Cerulean the fluorescence decay curve in a region.
9. Determine using a bi-exponential fitting algorithm the fluorescence lifetimes of unquenched and FRET-quenched Cerulean (Fig. 9.1).
   Note: For instance, Matlab provides such fitting routines.
   Note: In the case of TN L15 the fluorescence lifetime of unquenched Cerulean $\tau 2$ amounts ~2300 ps and $\tau 1$ of FRET-quenched Cerulean ~600 ps.
10. Perform a bilinear approximation in each pixel of the 3D time-resolved fluorescence image stack using the equation:

$$I(t) = a_1 \cdot e^{-t/\tau_1} + a_2 \cdot e^{-t/\tau_2}$$

with $I(t)$ the time-resolved fluorescence signal with subtracted background, τ_1 and τ_2 the fluorescence lifetimes of quenched and unquenched Cerulean and the prefactors a_1 and a_2 the corresponding concentrations (Fig. 9.2).
11. From the prefactors a1 and a2 calculate:

$$FRET\ ratio = \frac{a_1}{a_1 + a_2} \cdot 100$$

in each pixel of the 3D image. Using a corresponding calibration curve—such as the one described in [12], this value indicates

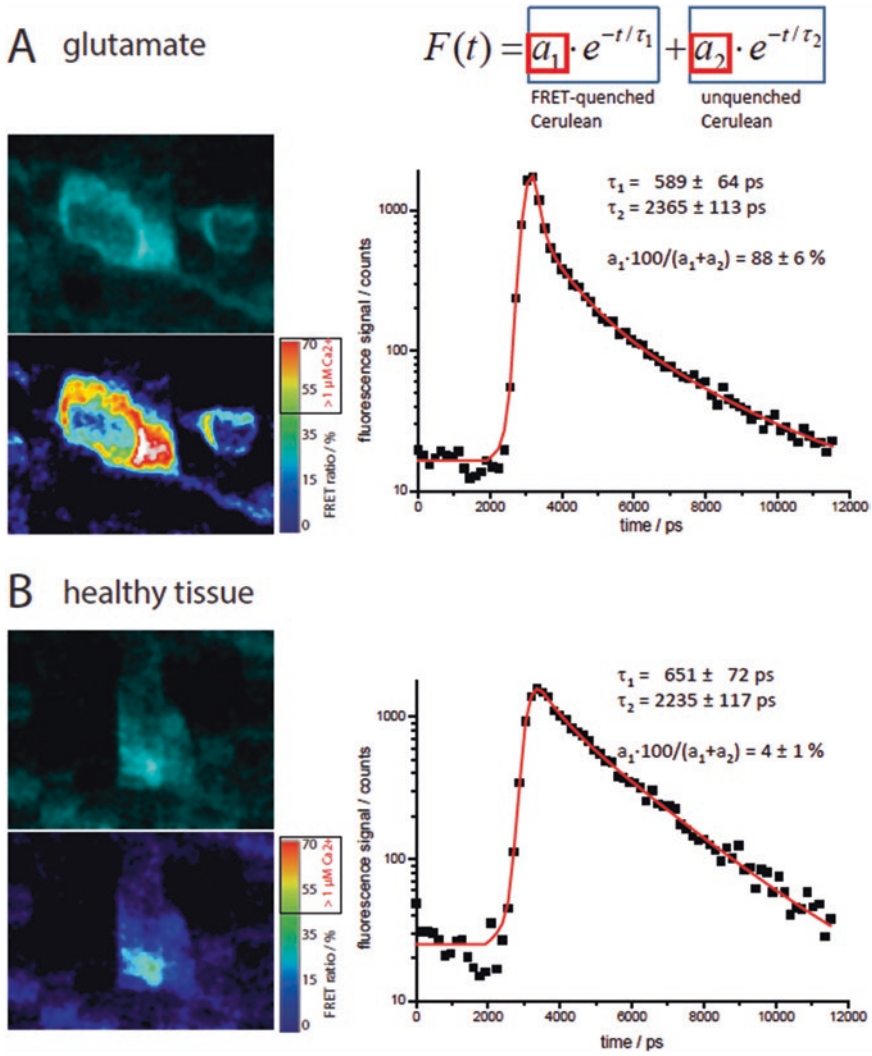

Fig. 9.1 Validation of calcium response in hippocampus slices of *CerTN L15* mice by FRET-FLIM. The series of fluorescence images of Cerulean in hippocampus slices of *CerTN L15* mice is well described by a bi-exponential function. The first part corresponds to FRET-quenched Cerulean, the second to unquenched Cerulean. The fluorescence lifetime of unquenched Cerulean was validated by bi-exponentially evaluating FLIM data acquired in 70–100 µm depth in healthy brain slices. Following the calibration curve for the TN L15 construct, the calcium concentration in healthy neurons is 100 nM (**b**). After treatment with either KCl, glutamate or ionomycin the contribution of a shorter fluorescence lifetime (of FRET-quenched Cerulean) dramatically increases, resulting in a calcium concentration of 3.8 µM (**a**). λ_{exc} = 850 nm, $\lambda_{detection}$ = 460 ± 30 nm

the absolute intracellular calcium concentration.*Note*: Using the described approach in 3D we measured the neuronal dysfunction (FRET ratio > 47%) in acute hippocampal slices of *CerTN L15* mice, within the glial scar formed at their surface, as depicted in Fig. 9.3. Intravital 3D FLIM in the brain stem of *CerTN L15* mice affected by experimental autoimmune encephalomyelitis (EAE) revealed absolute neuronal calcium concentrations and the level of tissue dysfunction during and after inflammation of the central nervous system [10, 11].

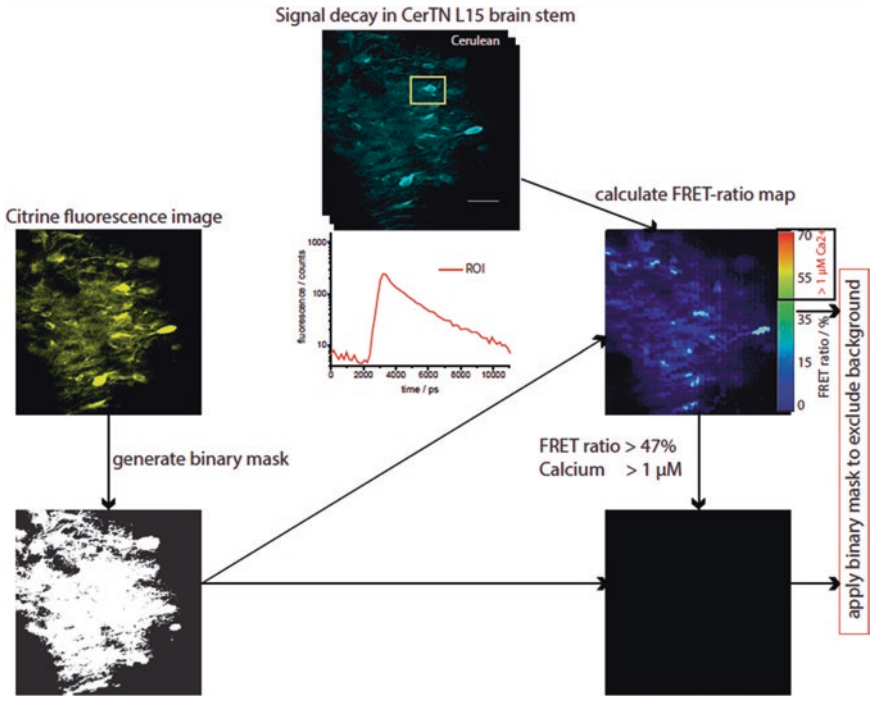

Fig. 9.2 Quantifying neuronal dysfunction by intracellular calcium in vivo: 3D FRET-FLIM in brain tissue of *CerTN L15* mice. Work flow for acquiring and evaluating FRET-FLIM data in the brain tissue of *CerTN L15* mice. First a series of fluorescence intensity images of Cerulean (the donor in the Ca-sensitive FRET construct TN L15) are rapidly acquired with a parallelized time-correlated single-photon counting device. The fluorescence image of Citrine (the acceptor of the FRET pair) is used to create a digital mask [1–0] resolving signal from background. The mask is applied to all images of the time-resolved series. Each pixel of the image series contains the Cerulean fluorescence decay curve, which can be well approximated by a bi-exponential function. The short term corresponds to Cerulean quenched by FRET, whereas the other term describes the decay of unquenched Cerulean. After bilinear evaluation in each pixel, the pre-factors of the two terms, i.e. the relative concentrations of unquenched and FRET-quenched Cerulean, are calculated. The percentage of FRET quenched Cerulean in the total Cerulean concentration describes the FRET ratio. A FRET ratio of over 47% corresponds to 1 µM free calcium known to cause neuronal death. λ_{exc} = 850 nm, $\lambda_{detection}$ = 460 ± 30 nm, scale bar = 50 µm

9.4 Notes

Carry out all procedures at 37 °C in order to insure perfect metabolic state of the tissue.

1. *Note*: Experimental autoimmune encephalomyelitis (EAE)

   We crossed the *CerTN L15* transgenic C57BL/6 mice (kindly provided by O. Griesbeck) with *LysM tdRFP* mice (myeloid cells and neutrophil granulocytes express tdRFP) to generate *CerTN L15 x LysM tdRFP* mice. Active EAE was performed by immunizing these mice subcutaneously with 150 µg of $MOG_{35–55}$ (Pepceuticals, UK) emulsified in CFA (BD Difco, Germany). The mice additionally received 200 ng Pertussis toxin (PTx, List Biological Laboratories, Inc.) intraperitoneally at the time of immunization and 48 h later. Intravital FLIM was performed on day 15 after immunization, i.e. at the peak of disease.

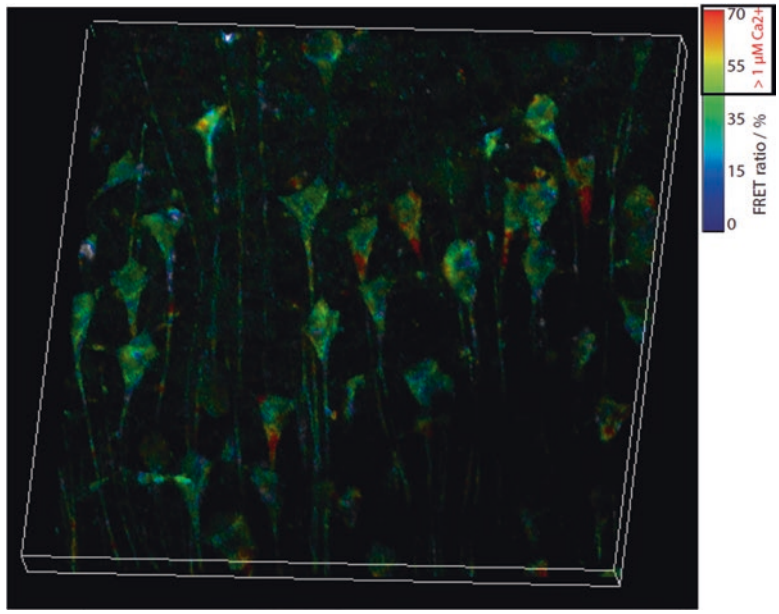

Fig. 9.3 Calcium response in hippocampal slices of *CerTN L15* mice reveals neuronal dysfunction in the superficial glial scar. FRET-ratio 3D image (300 × 300 µm², 512 × 512 pixel) at the surface of a hippocampal slice of a *CerTN L15* mouse (between surface, 10 µm and 40 µm tissue depth). In this area, a glial scar is built as a reaction to the cutting procedure. In this glial scar, most neurons are either dysfunctional, displaying high calcium levels or dead. λ_{exc} = 850 nm, $\lambda_{detection}$ = 460 ± 30 nm, z-step = 5 µm

Acknowledgments We thank Robert Günther and Peggy Mex for excellent technical assistance. This work was supported by DFG FOR 2165 (NI1167/4-1 to R.A.N.) and TRR130, TPC01 and TP17 (to R.A.N. and H.R., respectively).

References

1. Heim N, Garaschuk O, Friedrich MW, Mank M, Milos RI, Kovalchuk Y, Konnerth A, Griesbeck O (2007) Improved calcium imaging in transgenic mice expressing a troponin C-based biosensor. Nat Methods 4(2):127–129
2. Herz J, Siffrin V, Hauser AE, Brandt AU, Leuenberger T, Radbruch H, Zipp F, Niesner RA (2010) Expanding two-photon intravital microscopy to the infrared by means of optical parametric oscillator. Biophys J 98(4):715–723
3. Rose T, Goltstein PM, Portugues R, Griesbeck O (2014) Putting a finishing touch on GECIs. Front Mol Neurosci 7:88
4. Jares-Erijman EA, Jovin TM (2003) FRET imaging. Nat Biotechnol 21:1387–1395
5. Elangovan M, Wallrabe H, Chen Y, Day RN, Barroso M, Periasamy A (2003) Characterization of one- and two-photon excitation fluorescence resonance energy transfer microscopy. Methods 29(1):58–73
6. Tao W, Rubart M, Ryan J, Xiao X, Qiao C, Hato T, Davidson MW, Dunn KW, Day RN (2015) A practical method for monitoring FRET-based biosensors in living animals using two-photon microscopy. Am J Phys Cell Physiol 309(11):C724–C735
7. Day RN, Tao W, Dunn KW (2016) A simple approach for measuring FRET in fluorescent biosensors using two-photon microscopy. Nat Protoc 11(11):2066–2080
8. Radbruch H, Bremer D, Mothes R, Günther R, Rinnenthal JL, Pohlan J, Ulbricht C, Hauser AE, Niesner R (2015) Intravital FRET: probing cellular and tissue function in vivo. Int J Mol Sci 16(5):11713–11727
9. McGinty J, Soloviev VY, Tahir KB, Laine R, Stuckey DW, Hajnal JV, Sardini A, French PM, Arridge SR (2009) Three-dimensional imaging of Förster resonance energy transfer in heterogeneous turbid media by tomographic fluorescent lifetime imaging. Opt Lett 34(18):2772–2774
10. Mossakowski AA, Pohlan J, Bremer D, Lindquist R, Millward JM, Bock M, Pollok K, Mothes R, Viohl L, Radbruch M, Gerhard J, Bellmann-Strobl J, Behrens J, Infante-Duarte C, Mähler A, Boschmann M, Rinnenthal JL, Füchtemeier M, Herz J, Pache FC, Bardua M, Priller J, Hauser AE, Paul F, Niesner R, Radbruch H (2015) Tracking CNS and systemic sources of oxidative stress during the course of chronic neuroinflammation. Acta Neuropathol 130(6):799–814

11. Radbruch H, Bremer D, Guenther R, Cseresnyes Z, Lindquist R, Hauser AE, Niesner R (2016) Ongoing oxidative stress causes subclinical neuronal dysfunction in the recovery phase of EAE. Front Immunol 7:92
12. Rinnenthal JL, Börnchen C, Radbruch H, Andresen V, Mossakowski A, Siffrin V, Seelemann T, Spiecker H, Moll I, Herz J, Hauser AE, Zipp F, Behne MJ, Niesner R (2013) Parallelized TCSPC for dynamic intravital fluorescence lifetime imaging: quantifying neuronal dysfunction in neuroinflammation. PLoS One 8(4):e60100
13. Bremer D, Pache F, Günther R, Hornow J, Andresen V, Leben R, Mothes R, Zimmermann H, Brandt AU, Paul F, Hauser AE, Radbruch H, Niesner R (2016) Longitudinal intravital imaging of the retina reveals long-term dynamics of immune infiltration and its effects on the glial network in experimental autoimmune uveoretinitis, without evident signs of neuronal dysfunction in the ganglion cell layer. Front Immunol 7:642
14. Siffrin V, Radbruch H, Glumm R, Niesner R, Paterka M, Herz J, Leuenberger T, Lehmann SM, Luenstedt S, Rinnenthal JL, Laube G, Luche H, Lehnardt S, Fehling HJ, Griesbeck O, Zipp F (2010) In vivo imaging of partially reversible th17 cell-induced neuronal dysfunction in the course of encephalomyelitis. Immunity 33(3):424–436

Live Cell Imaging of Viscosity in 3D Tumour Cell Models

10

Marina V. Shirmanova, Lubov' E. Shimolina, Maria M. Lukina, Elena V. Zagaynova, and Marina K. Kuimova

Abstract

Abnormal levels of viscosity in tissues and cells are known to be associated with disease and malfunction. While methods to measure bulk macroscopic viscosity of bio-tissues are well developed, imaging viscosity at the microscopic scale remains a challenge, especially in vivo. Molecular rotors are small synthetic viscosity-sensitive fluorophores in which fluorescence parameters are strongly correlated to the microviscosity of their immediate environment. Hence, molecular rotors represent a promising instrument for mapping of viscosity in living cells and tissues at the microscopic level. Quantitative measurements of viscosity can be achieved by recording time-resolved fluorescence decays of molecular rotor using fluorescence lifetime imaging microscopy (FLIM), which is also suitable for dynamic viscosity mapping, both in cellulo and in vivo. Among tools of experimental oncology, 3D tumour cultures, or spheroids, are considered a more adequate in vitro model compared to a cellular monolayer, and represent a less labour-intensive and more unified approach compared

M.V. Shirmanova (✉) • E.V. Zagaynova
Institute of Biomedical Technologies, Nizhny Novgorod State Medical Academy, Minin and Pozharsky Square, 10/1, Nizhny Novgorod 603005, Russia
e-mail: shirmanovam@mail.ru

L.E. Shimolina • M.M. Lukina
Institute of Biology and Biomedicine, Nizhny Novgorod State University, Gagarin Avenue, 23, Nizhny Novgorod 603950, Russia

Institute of Biomedical Technologies, Nizhny Novgorod State Medical Academy, Minin and Pozharsky Square, 10/1, Nizhny Novgorod 603005, Russia

M.K. Kuimova (✉)
Department of Chemistry, Imperial College London, South Kensington, London SW7 2AZ, UK
e-mail: m.kuimova@imperial.ac.uk

R.I. Dmitriev (ed.), *Multi-Parametric Live Cell Microscopy of 3D Tissue Models*, Advances in Experimental Medicine and Biology 1035, DOI 10.1007/978-3-319-67358-5_10

to animal tumour models. This chapter describes a methodology for microviscosity imaging in tumour spheroids using BODIPY-based molecular rotors and two photon-excited FLIM.

Keywords
Microviscosity • Molecular rotors • Fluorescence lifetime imaging microscopy (FLIM) • Cancer cell • Tumour spheroid

10.1 Introduction

The microscopic viscosity of the plasma membrane is one of the key parameters that controls a range of vital cellular processes associated with membrane permeability, intracellular transport, enzymatic activity, diffusion controlled functions, biosynthetic processes and molecular interactions [1]. It is known that abnormal levels of viscosity are associated with malignant transformation, but the published data on viscosity in cancer are limited and provide contradictory viscosity values. The first attempts to estimate the viscosity in cancer were made by Guyer et al. using the ultracentrifugation of cells suspensions. This study established that the relative viscosity of whole tumour cells is higher compared to that of normal cells, and associated this phenomenon with accumulation of lactic acid in tumour [2, 3]. Doblas et al. used magnetic resonance elastography on cancer patients and demonstrated that the viscosity of malignant hepatic tumours was higher than that of benign lesions and significantly varied among the different tumour types [4]. Importantly, these studies were performed on 'bulk' cells and did not provide organelle-specific viscosity quantification. Therefore, the resulting values might not be physiologically meaningful and cannot be easily compared between different methods.

At the same time, the microscopic viscosity of individual domains of live cells in vitro was determined using various spectroscopic or microscopic methods. Aqueous cytoplasm domain of cancer cells was reported to be less viscous compared with normal cells using radiofrequency electron paramagnetic resonance [5]. Rebelo et al. determined with atomic force microscopy that cancerous cells in culture are less viscous than non-tumorigenic cells [6]. In a model for progressive ovarian cancer, Ketene et al. utilised atomic force microscopy to demonstrate that mouse ovarian cells are more viscous when they are benign [7]. Using FRAP (fluorescence recovery after photobleaching), Sigley et al. showed the decreased diffusion of a free form of enhanced green fluorescence protein (EGFP) in the cytoplasm of tumorigenic (immortalised) cells as compared with noncancerous cells, which was associated with increased cytoplasmic viscosity, while in the nucleus increasingly severe neoplastic transformation was associated with increased mobility of EGFP (decreased viscosity) [8].

The relationship between viscosity and chemoresistance of cancer cells was also investigated. It was revealed by Huang et al. with the use of fluorescence probe TMA-DPH in cellulo that the plasma membrane microviscosity is higher in cells resistant to cisplatin [9]. Increased microviscosity was detected in plasma membranes isolated from cancer cells resistant to doxorubicine by staining with fluorescent probe pyrene [10]. It was also found by diffusion time distribution analysis that microviscosity of plasma membrane of multidrug-resistant cancer cells is more heterogeneous in comparison with non-resistant ones [11]. The rapid increase in membrane fluidity following cisplatin treatment was detected in cancer cells ongoing apoptosis by a spin-labeling method using electron paramagnetic resonance [12].

Fluorescent molecular rotors are viscosity-sensitive fluorophores that allow viscosity quantification in the microscopic environment of live cells [13, 14]. Radiative relaxation of the rotor's exited state competes with intramolecular

rotation, with relative radiative/non-radiative rates strongly dependent on the environment, most dominantly, on the local viscosity. Fluorescence ratiometric or fluorescence lifetime-based detection from molecular rotors allows to overcome difficulties associated with an unknown fluorophore concentration and, thus, enables quantitative viscosity mapping to be performed [13]. Thus, ratiometric or lifetime-based rotors were previously used to quantitatively measure viscosity of individual organelles of live cells, under normal physiological conditions and chemical and photochemical perturbations [15–28]. Although the relationship between abnormal viscosity and cancer has not been specifically investigated using molecular rotors, we have recently reported the feasibility study of the use of fluorescent molecular rotors BODIPY-C10 and BODIPY++, Scheme 10.1, in combination with Fluorescence Lifetime Imaging Microscopy (FLIM) to image microscopic viscosity in vivo in mouse tumours, both in single cells and in connective tissues [29]. We found that viscosities recorded from single tumour cells in vivo correlated well with the in cellulo values from the same cancer cell line. Importantly, our new method allowed both the imaging and the dynamic monitoring of viscosity changes in real time, in cellulo and in live animals. For example, the changes of cellular microviscosity during a light-induced cancer treatment termed Photodynamic Therapy (PDT) were reported in cellulo. We have demonstrated using two independent molecular rotors that PDT of cultured cells causes a large viscosity increase [24, 25] and investigated the mechanism of this process in model lipid bilayers constructed as giant unilamellar vesicles (GUVs) [28].

Thus, the literature data indicate that viscosity has the potential to be a biomarker for human malignancy and, furthermore, can serve as a predictor of a tumour response to therapeutic intervention. Molecular rotors combined with FLIM offer an excellent opportunity for quantitatively measuring and imaging microscopic viscosity in different cancer models- from monolayer cultured cells to animal tumours.

Among the available molecular rotors, BODIPY-based structures are widely used as FLIM-based viscosity probes owing to the ease of synthetic modification, a high sensitivity in a wide range of viscosities (10–5000 cP), good dynamic range of fluorescence lifetimes corresponding to this viscosity range, temperature independence, and monoexponential fluorescence decays that allow straightforward data interpretation [16–18, 27, 30, 31]. To date BODIPY-based FLIM measurements provided the wealth of biologically relevant information on model lipid membranes [32–34], bacterial [15, 19] and eukaryotic cells and cellular organelles [20–29], and allowed viscosity monitoring during lipid (photo)oxidation [28], cell death [25], bacterial sporulation and deactivation [15], bacterial membrane viscosity changes in response to variations in temperature [19], as well as viscosity mapping in animal tumours in vivo [29].

Tumour spheroid cultures have been recognized as the physiologically relevant model for basic cancer research and anticancer drug develop-

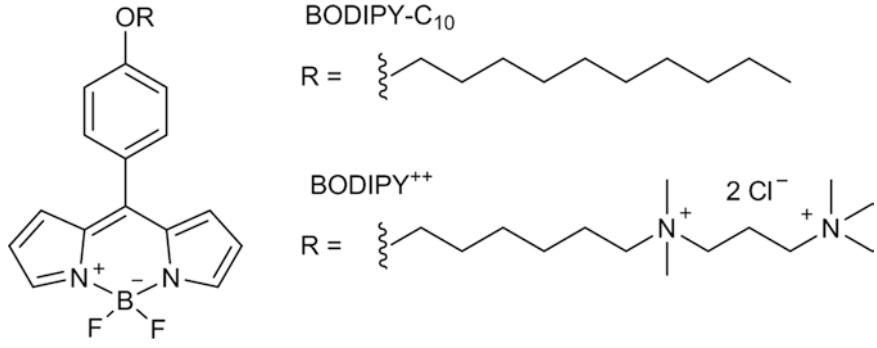

Scheme 10.1 The molecular structure of molecular rotors BODIPY-C10 and BODIPY++

ment [35, 36]. These 3D cellular systems possess cell-to-cell interaction and chemical gradients (oxygen, nutrients or metabolites), reflecting in vivo features of tumours and therefore recreate the complexity of human tissues, while retaining the ability for high-throughput screening and cellular level imaging. To the best of our knowledge, viscosity imaging has yet to be realized in tumour spheroids. In this chapter we present a protocol for quantitative microviscosity imaging in tumour spheroids using BODIPY-based molecular rotors and two photon-excited FLIM.

10.2 Materials

HeLa Kyoto (human cervical carcinoma) cell line
DMEM cell culture media (Life Technologies) supplemented with 100 μg/ml penicillin, 100 μg/ml streptomycin sulfate and 10% fetal bovine serum (FBS)
DMEM media without phenol red
Hank's solution without Ca^{2+}/Mg^{2+}
Molecular rotors based on BODIPY structure: hydrophobic BODIPY-C10 and amphiphilic BODIPY++ (Scheme 10.1), synthesised as previously reported [17, 25] and dissolved in DMSO (1 mM)
Versen buffer
Trypsin- EDTA 0.25%
96-well round bottom ultra low attachment microplates
Glass-bottom FluoroDishes for microscopy
Ice
Fluorescein solution containing 1 M KI
Sugar
Clean cover slips
2 μM Calcein AM and 4 μM Propidium Iodide (Live/Dead Cell Double Staining Kit, Sigma)

10.2.1 Equipment

Cell culture incubator (37°C, 5% CO_2, humidified atmosphere)
Laminar flow hood
Automatic pipettes, cell culture dishes
Microcentrifuge
Multiphoton tomograph MPTflex (JenLab GmbH, Germany) equipped with a tuneable 80 MHz, 200 fs Ti:Sa laser MaiTai (Spectra Physics, USA).
TCSPC-based FLIM module with SPC-150 detector (Becker & Hickl GmbH, Germany) integrated into the MPTflex system.
SPCImage™ version 4.8 (Becker & Hickl GmbH) for FLIM analysis.
Inverted Laboratory Microscope Leica DMIL Led

10.3 Methods

10.3.1 Cell Culturing

Grow HeLa Kyoto cells in 25 cm^2 flask in DMEM containing 10% FBS, 100 μg/ml penicillin, and 100 μg/ml streptomycin. Maintain cells by splitting them every 2–3 days with Trypsin-EDTA 0.25%. HeLa cells should be split when they are 70–80%-confluent, after they formed a tightly packed layer of cells (*see* **Note 1**).

10.3.2 Generation of Tumour Spheroids

1. Remove a freshly confluent (~80%) flask of HeLa cells from the cell culture incubator and place within a sterile cell culture hood.
2. Wash cell monolayer twice with Vercen buffer (2.5 ml for a 25 cm^2 flask), add Trypsin-EDTA 0.25% (1 ml for a 25 cm^2 flask) to detach cells and incubate cells at 37°C for 2–5 min.
3. Check cell detachment under a microscope and neutralize Trypsin- EDTA with complete growth medium DMEM (5 ml for a 25 cm^2 flask).
4. Centrifuge cell suspension at 1.000 rpm for 5 min at room temperature.
5. Remove supernatant, tap the tube and resuspend cell pellet in 1 ml of complete growth medium using a pipette. This should yield a single cell suspension without cell clusters.

6. Count cells using a Goryaev's chamber and dilute the cell suspension to obtain 0.5×10^3 cells/ml).
7. Transfer the cell suspension to a sterile dish and, using a multichannel pipette, dispense 200 µl/well (100 cells) into ultra-low attachment 96-well round bottom plates.
8. Transfer the plates to an incubator (37 °C, 5% CO_2, 80% humidity). Three days later, visually confirm tumour spheroid formation using light microscope (*see* **Note 2**).
9. Exchange media every 3 days. Remove plate from the incubator, carefully remove 100 µL of media per well and replace with 100 µL fresh culture media. Return plate to the incubator.

10.3.3 Preparation of Spheroids for Live Cell Viscosity Imaging

1. Carefully transfer the required number of spheroids (usually 8–10) from the plate to Eppendorf using an automatic 1-ml pipette, wash with 1 ml DMEM media without phenol red (*see* **Notes 3 and 4**).
2. Gently replace the media with fresh DMEM media without phenol red and transfer the spheroids in 1 ml media on the glass-bottom FluoroDishes using a 5 ml-pipette (*see* **Note 5**).
3. Transfer the dishes to an incubator (37°C, 5% CO_2, 80% humidity) for 2 h for attachment and confirm tumour spheroid attachment visually or using light microscope (*see* **Note 6**).
4. Carefully replace the culture media with ice-cold Hank's solution without Ca^{2+}/Mg^{2+} (drop by drop) and incubate spheroids at +4°C (on ice) for 10–12 min. Ice-cold solution and incubation on ice are used to prevent endocytosis.
5. Prepare Hank's medium or PBS solution containing 4.5 µM in BODIPY, by diluting BODIPY DMSO stock. The final incubation solution should contain less than, 0.5% DMSO by volume and should be kept ice-cold.
6. Replace Hank's solution in the cell dish with ice-cold BODIPY solution.
7. Image spheroids kept in BODIPY solution using two-photon FLIM microscopy (room temperature is 20°C) (*see* **Note 7**).
8. It is desirable to perform imaging within 30 min of adding BODIPY to spheroids. At longer incubation times an intracellular uptake of BODIPY and its aggregation within cells may occur (*see* **Note 8**).

10.3.4 Two-Photon Excited Microscopy and FLIM of Tumour Spheroids

1. Set up the scan head of the MPTflex system in the inverted position for in vitro imaging (*see* **Note 9**).
2. Place the glass-bottom dish with attached spheroids on the adapter ring connected with a microscope objective so that the spheroid is maximally close to the centre of the objective.
3. Enter the correct FLIM parameters (e.g. pixel dwell time—44 µs, acquisition time—11.7 s).
4. Select an excitation wavelength of 850 nm to excite BODIPY fluorescence and laser power < 12 mW (typically 5–7 mW); fluorescence detection is at 500–600 nm. Start scanning and, using the XY and Z positioning by an integrated motorized stage, bring a spheroid in the field of view and adjust the focus to the middle cross-section of the spheroid (*see* **Notes 10 and 11**).
5. Adjust magnification, if necessary.
6. Record FLIM image using 127 × 127 pixels resolution and check in the SPCImage software that the pixel intensities are appropriate (≥5000 photons per decay per pixel or >100 photons in the maximum of the decay in the case of monoexponential decay are required for adequate fitting) (*see* **Note 12**). The acquisition time for one optical section is typically 12 s.
7. Increase the laser power and/or acquisition time if required. Adjust the excitation power for each image depth, if required.

8. Record FLIM images for each tumour spheroid at intervals starting from t = 0 up to 30 min. At longer incubation times an intracellular uptake of BODIPY and its aggregation within the cells may occur.
9. At the end of the acquisition, record an instrument response function, IRF, using exactly the same excitation parameters as for the data acquisition. An IRF is required for the accurate data fitting. The IRF could be recorded by using an SHG signal from dried sugar or urea film on the coverslip (425 nm detection for 850 nm excitation) or by using fluorescein solution containing 1 M KI as a quencher, resulting in a very short fluorescence decay (500–600 nm detection for 850 nm excitation).
10. Save each individual image and the IRF acquired.
11. Perform live/dead cell staining using dual channel confocal imaging with 2 μM Calcein AM and 4 μM Propidium Iodide, to ensure that viscosity imaging was performed on live cells.

10.3.5 Data Analysis

1. Import FLIM image and IRF into SPCImage software
2. Fix the "offset" and "scatter" parameters by checking corresponding boxes on the SPCImage software interface.
3. Use "Incomplete Multiexponential" fitting model (go to *Options* and select *Model*)
4. Adjust the binning to achieve pixel intensities of ≥5000 photons per decay per pixel or >100 photons in the maximum of the decay in the case of monoexponential decay.
5. Fit time-resolved fluorescence decays in the region of interest using a monoexponential model. The $\chi^2 \leq 1.20$ value indicates that the model used provides a reasonable fit. Discard the data that does not display monoexponential fit, as this may be indicative of aggregation and self-quenching of the dye, rendering the lifetime/viscosity calibration unusable (*see* **Note 12**).
6. Calculate the histogram of fluorescent lifetime τ in each image.
7. In the case of mixed mono- and bi-exponential decays in the field of view, analyse individual pixels with monoexponential decays only and export these measurements to a spreadsheet. Record on the spreadsheet the relevant image information (e.g., well or spheroid number, relative time point).
8. Convert experimentally measured lifetimes (in ns) to viscosity values (in cP) using calibration plot for your viscosity probe. Calculate the viscosity using the following equations:

$$x = y^2 / 0.0206 \text{, for BODIPY++}$$

$$x = y^{2.1887} / 0.0221 \text{, for BODIPY-C10, where}$$

x—viscosity (in cP), *y*—fluorescence lifetime τ (in ns).

10.4 Notes

All manipulations with cell culture and spheroids should be performed in sterile conditions.

1. For spheroids preparation HeLa cell culture within 4–10 passage numbers are used.
2. The absence of formed spheroids after three days can be a consequence of cell culture contamination.
3. The spheroids can be cultured in the DMEM media without phenol red over the whole time. Then the replacement of media is not required.
4. For transferring the spheroids of big size (5 days and later) we recommend to cut the tip of the 1 ml-pipette using sterile scissors or scalpel.
5. We recommend to transfer small 3-day spheroids on the glass-bottom FluoroDishes in 0.5 ml DMEM media without phenol red for faster and more effective attachment.
6. If the spheroids did not attached after 2 h, remove 0.3–0.5 ml of the medium from the dish, and transfer the plates to an incubator

(37°C, 5% CO_2, 80% humidity) for 30 min to 1 h. Then confirm the attachment.

7. The medium containing BODIPY++ cannot be removed during FLIM imaging, otherwise the dye will diffuse from the membrane, at least in the outside region of a spheroid. BODIPY-C10 accumulates inside cells via endocytosis and the medium containing BODIPY-C10 can be washed once the desired level of staining has been achieved. In our experience good cell staining can be achieved after 10 min incubation.
8. If imaging of viscosity is required for period of time longer than 30 min (for example when monitoring dynamic processes with characteristic times of 30 min to 1 h), there is an option to keep the spheroids in the cold (<10°C), using a temperature-controlled stage. Cold temperature will stop the endocytosis of the dye and the exclusive membrane staining will be maintained for longer periods of time. However, cold temperature will affect the base viscosity of the membrane (the viscosity will increase) and it may also affect the dynamics of metabolism and the nature of the process under observation.
9. Any inverted confocal or multiphoton FLIM systems will be suitable for the data acquisition.
10. Depending on the laser, other wavelengths in the range 780–900 nm can be used to excite BODIPY fluorescence using multiphoton excitation. Select a wavelength that results in the brightest fluorescence signal. One-photon excitation (450–500 nm) results in an excessive amount of scattering from spheroid samples, and poor depth penetration, but can be used successfully in a monolayer cell culture.
11. It is recommended to image spheroids without BODIPY as a control, to estimate the levels of autofluorescence of the sample and to make sure that autofluorescence does not contaminate the signal for the BODIPY rotor. For example, the high level of autofluorescence can result in biexponential fluorescence decay, even in the absence of aggregation. To locate a spheroid, first select an excitation wavelength of 740 nm to excite autofluorescence from cells (NAD(P)H is predominantly excited at this wavelength) and move it to the centre of the field of view; then select an excitation wavelength of 850 nm to acquire a control image in the absence of BODIPY.
12. Biexponential decays may be indicative of aggregation. We are unable to check for aggregation due to the fixed filters in MPTflex system (and therefore we discarded biexponential data as quenching), however, on a FLIM system with variable filters, this can be done by testing monomer and aggregate-specific emission wavelength ranges, as described in ref. [34]

10.5 Anticipated Results

Using the protocol described here, we have generated tumour spheroids from human cervical cancer cells HeLa and visualized microscopic viscosity using BODIPY-based fluorescent molecular rotors and FLIM.

Figure 10.1 shows representative confocal z-stack of living tumour spheroid stained with BODIPY++ rotor on the day 5 after cell seeding. By this time spheroids normally reach the size of 500–550 μm. FLIM images were recorded using 850 nm pulsed excitation and a fixed pre-fitted emission filter for 409–660 nm fluorescence detection. After 10 min incubation with the solution of the rotor, bright fluorescence, typical of BODIPY++ was observed from 3D cell culture. BODIPY++ rotor penetrated to a full depth of the spheroids, showing an efficient staining of the plasma membranes of cells at all depths. The decays recorded from the plasma membranes of cells following incubation with BODIPY++ were monoexponential, as could be seen from the goodness of fit (χ^2) values close to 1. Fluorescence lifetimes of BODIPY++ were narrowly (and symmetrically) distributed around 2.58 ± 0.04 ns, with no differences between cells from the core and the periphery of the spheroids. We converted FLIM maps to viscosity maps, using previously reported calibrations [33]. According to the

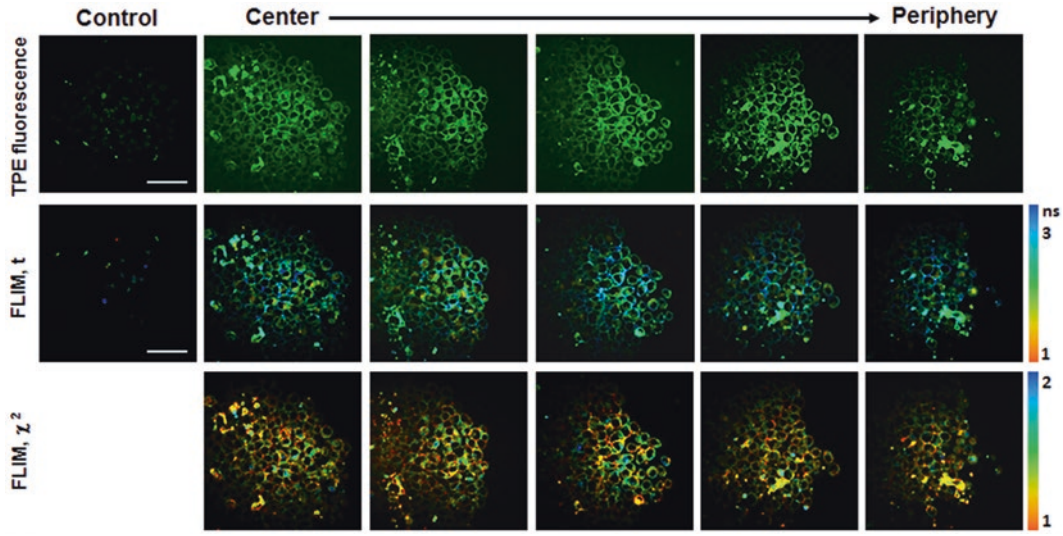

Fig. 10.1 Two-photon excited (TPE) fluorescence and FLIM images of living tumour spheroid incubated with 4.5 μM solution of BODIPY++. Z-stack of the spheroid was obtained at day 5 of the growth. Excitation was 850 nm, detection −409–660 nm. Control spheroid imaged at identical conditions that was not incubated with BODIPY++ is also shown in the first column. The χ^2 maps confirm good monoexponential fitting in the areas where $\chi^2 \approx 1$ (indicated by the *orange colour*). Scale bar is 150 μm and is applicable to all images

calibration curves, the membrane viscosity in HeLa cells in the spheroids at this stage of growth was 359 ± 11 cP.

The plasma membrane staining upon incubation with BODIPY++ was reported previously for monolayers of cells [18, 29]. It is important to note that membrane microviscosity values obtained for HeLa cells in spheroids were the same as for HeLa monolayer culture (349 ± 15 cP, unpublished data), and rather close to the values measured in mouse colon carcinoma cells CT26 in monolayer culture and in animal tumours (377 ± 27 cP and 386 ± 19 cP, respectively [29]) using BODIPY++.

In some cells within a spheroid, BODIPY++ was internalized into the cells. The areas of internalised rotor produced biexponential fluorescence decays (the areas with χ^2 values of >1.5 in Fig. 10.1), presumably, due to BODIPY++ aggregation. In the case of biexponential decays, viscosity measurements were impossible.

Since a tumour spheroid represents a heterogeneous formation and is composed of cells with different proliferative and metabolic activities, as well as other phenotypic characteristics, we examined weather membrane microviscosity differs for spheroids of different sizes (i.e. during spheroid growth). Monitoring of the viscosity was performed from day 3 to day 10 of the spheroid growth using BODIPY++ (Fig. 10.2).

Prior to spheroid transfer to the glass-bottom dishes for imaging, their morphology was assessed by conventional transmission microscopy. HeLa cells typically formed multicellular spheroids within 3 days after seeding. At this stage of growth, spheroids represented non-compact agglomerates of large cancer cells. By day 5 the spheroids became rounder and had a compact structure, in which a more dense, homogenous core and an outer layer of actively proliferating cells can be distinguished. By day 10 the spheroids begin to disintegrate due to their large size. As the spheroids grew, their diameter increased from ~400 μm (day 3) to ~800 μm (day 10).

Fluorescence lifetime of BODIPY++ was analysed at the centre and at the periphery of all spheroids, at all time-points. Fluorescence lifetime measurements and subsequent calculation of viscosity showed no significant differences between viscosity values recoded for spheroids of different sizes, nor between central and

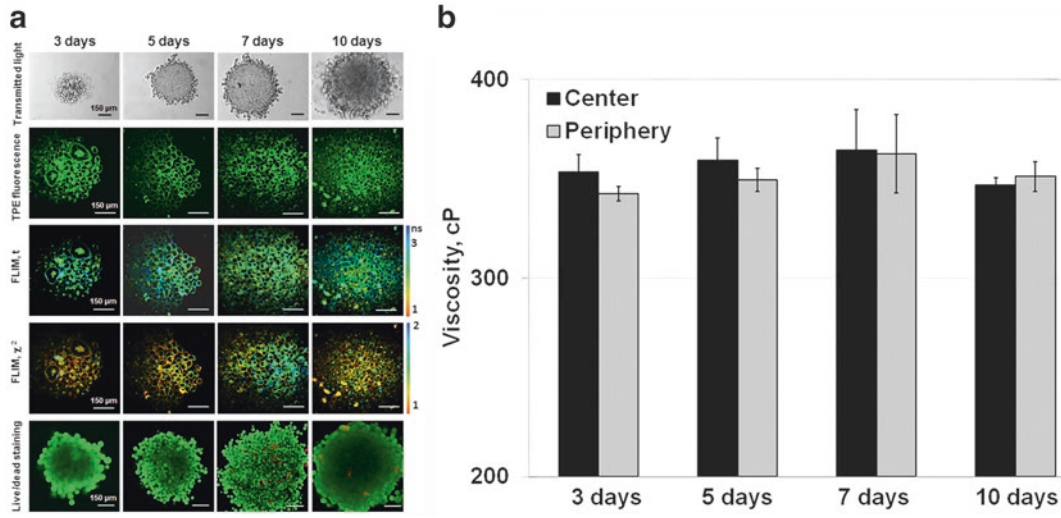

Fig. 10.2 Measuring microviscosity during spheroid growth. (**a**) Transmission, two-photon excited (TPE) fluorescence and FLIM images of living tumour spheroid incubated with 4.5 μM solution of BODIPY++ and live/dead cell staining using calcein-AM (viable cells, *green*) and propidium iodide (PI, dead cells, *red*). (**b**) Quantification of viscosity in central and peripheral areas of the tumour spheroids incubated with BODIPY++. M ± SD, n = 4 spheroids for each time-point (10 measurements from each spheroid). For BODIPY++ excitation wavelength was 850 nm, detection was 409–660 nm. The χ^2 maps confirm good monoexponential fitting in the areas where $\chi^2 \approx 1$ (indicated by the *orange colour*). Images of the middle cross sections of the spheroids are shown. Scale bars are 150 μm

peripheral zones (Fig. 10.2). Fluorescence lifetime of the rotor was ~2.5 ns that corresponded to a viscosity value of ~350 cP.

To ensure that neither the spheroid growth over several days, nor the addition of BODIPY affected cellular viability, the live/dead staining of spheroids was performed immediately after FLIM imaging. For this 2 μM Calcein AM and 4 μM Propidium Iodide (Live/Dead Cell Double Staining Kit, Sigma) were added to the dishes, and fluorescence of the dyes was imaged using LSM 880 microscope (Carl Zeiss, Germany). For Calcein AM the excitation wavelength was 488 nm, registration range was 550–570 nm, for Propidium Iodide, 543 nm for excitation and 600–700 nm for detection was used. Analysis of cell viability using live/dead staining showed that during the whole period of growth spheroids consisted of viable cells; and an insignificant number of dead cells within spheroids appeared on days 7 and 10. Therefore, we did not detect any changes of microscopic viscosity of plasma membranes in HeLa cells during tumour spheroid growth, as well as in living cells across individual spheroids, which indicates that microviscosity of membrane is a relatively stable parameter, not affected by the metabolic and proliferative activity of cells and by the heterogeneity of the cellular microenvironment. BODIPY++ was demonstrated to be a non-toxic and highly spheroid-permeable dye, suitable for viscosity imaging.

Finally, we tested another molecular rotor BODIPY-C10 for mapping microviscosity in living tumour spheroids. BODIPY-C10 is a hydrophobic molecule that displays extremely poor water solubility. Previous studies with BODIPY-C10 in monolayer cell cultures showed the intracellular uptake of this molecular rotor with punctate cellular distribution, probably located in the endocytotic vesicles [27]. Incubation of HeLa spheroids with BODIPY-C10 resulted in fast penetration of the rotor into the cells at all depths of the spheroid and punctate staining of the cell cytoplasm (Fig. 10.3). Monoexponential fitting of time resolved fluorescence decays showed fluorescence lifetimes 2.02 ± 0.05 ns, corresponding to the viscosity of

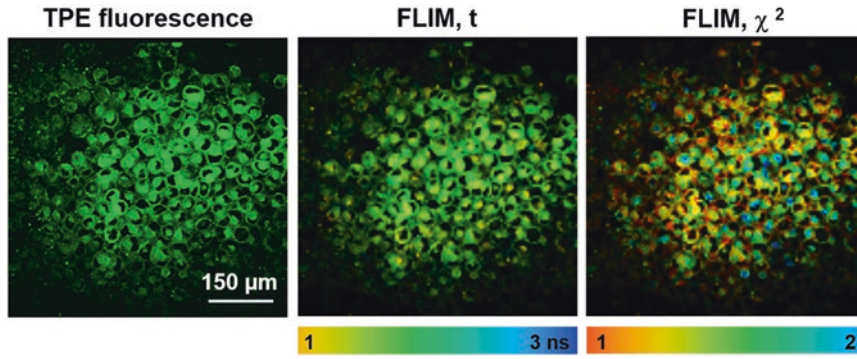

Fig. 10.3 Two-photon excited (TPE) fluorescence and FLIM images of living tumour spheroid incubated with 4.5 μM solution of BODIPY-C10. Excitation was 850 nm, detection was 409–660 nm. The χ^2 maps confirm good monoexponential fitting in the areas where $\chi^2 \approx 1$ (indicated by the *orange colour*). Images of the middle cross sections of the spheroid on the 7th day of growth are shown. Scale bar is 150 μm

210 ± 11 cP. Again, no differences in the viscosity were found between cells from the centre and the periphery of spheroids. This viscosity value is consistent with those measured in the internal cellular organelles previously using the same rotor [18].

Therefore, we demonstrate the possibility of non-invasive mapping of microviscosity of living tumour spheroids using non-toxic BODIPY-based fluorescent molecular rotors and FLIM. As expected, water-soluble BODIPY++ rotor displayed localisation in the plasma membrane of cells, while BODIPY-C10 with poor aqueous solubility showed distribution into the hydrophobic regions of the cellular cytoplasm. The viscosity value recorded for the plasma membrane of cells in 3D culture are higher than that for the internal staining, and both values are consistent with measurements performed for monolayer cell cultures. Measuring viscosity of plasma membrane upon the spheroids growth showed that viscosity value is constant for multicellular nodules of different sizes.

Acknowledgements This work has been financially supported by the Russian Foundation for Basic Research (#15-02-05189). MKK is thankful to the Engineering and Physical Sciences Research Council (UK) for the Career Acceleration Fellowship (EP/I003983/1). The authors are thankful to Varvara Dudenkova (NNSMA) for technical assistance with confocal microscopy and FLIM and to Dr. Nadezhda Ignatova (NNSMA) for her help with spheroid preparation.

References

1. Shinitzky M (1984) Membrane fluidity and cellular functions. In: Shinitzky M (ed) Physiology of membrane Fluidity, vol 1. CRC Press, Boca Raton, pp 1–51
2. Guyer MV (1942) Increased viscosity of cells of induced tumors. Cancer Res 2:16–18
3. Guyer MV (1947) Relative viscosities of tumor cells as determined by the ultracentrifuge. Anat Rec 73:17–27
4. Doblas S (2011) Magnetic resonance elastography measurements of viscosity: a novel biomarker for human hepatic tumor malignancy. Proc Intl Soc Mag Reson Med 19:389
5. Halpern HJ et al (1999) Diminished aqueous microviscosity of tumors in murine models measured with in vivo radiofrequency electron paramagnetic resonance. Cancer Res 59:5836–5841
6. Rebelo LM et al (2013) Comparison of the viscoelastic properties of cells from different kidney cancer phenotypes measured with atomic force microscopy. Nanotechnology 24:055102
7. Ketene AN et al (2012) The effects of cancer progression on the viscoelasticity of ovarian cell cytoskeleton structures. Nanomedicine 8:93–102
8. Sigley J et al (2017) Diffusion and binding of mismatch repair protein, MSH2, in breast cancer cells at different stages of neoplastic transformation. PLoS One 12:e0170414
9. Huang Z (2003) NMR studies of the relationship between the changes of membrane lipids and the cisplatin-resistance of A549/DDP cells. Cancer Cell Int 3:5
10. Chekhun VF et al (2002) Structural alterations of plasma membranes of Guerin's carcinoma cells upon the development of resistance to doxorubicine. Exp Oncol 24:279–283
11. Boutin C et al (2009) High heterogeneity of plasma membrane microfluidity in multidrug-resistant cancer cells. J Biomed Opt 14:034030

12. Rebillard A et al (2007) Cisplatin-induced apoptosis involves membrane fluidification via inhibition of NHE1 in human colon cancer cells. Cancer Res 67:7865–7874
13. Kuimova MK (2012) Molecular rotors image intracellular viscosity. Chimia (Aarau) 66:159–165
14. Haidekker MA, Theodorakis EA (2010) Environment-sensitive behavior of fluorescent molecular rotors. J Biol Eng 4:1–11
15. Loison P et al (2016) Effect of ethanol perturbation on viscosity and permeability of an inner membrane in Bacillus subtilis spores. Biochim Biophys Acta Biomembr 1858:2060–2069
16. Peng XJ et al (2011) Fluorescence ratiometry and fluorescence lifetime (FLIM) imaging: dual mode imaging cellular viscosity by a single molecular rotor. J Am Chem Soc 133:6626–6635
17. Yang Z et al (2013) A self-calibrating bipartite viscosity sensor for mitochondria. J Am Chem Soc 135:9181–9185
18. Lopez-Duarte I et al (2014) A molecular rotor for measuring viscosity in plasma membranes of live cells. Chem Commun 50:5282–5284
19. Mika JT et al (2016) Measuring the viscosity of the Escherichia coli plasma membrane using molecular rotors. Biophys J 111:1528–1540
20. Gatzogiannis E et al (2012) Mapping protein-specific micro-environments in live cells by fluorescence lifetime imaging of a hybrid genetic-chemical molecular rotor tag. Chem Commun 48:8694–8696
21. Wang L, Xiao Y, Deng L (2013) Activatable rotor for quantifying lysosomal viscosity in living cells. J Am Chem Soc 135:2903–2906
22. Jiang N et al (2014) Dual mode monitoring probe for mitochondrial viscosity in single cell. Sensors Actuators B Chem 190:685–693
23. Chen S et al (2015) Mapping live cell viscosity with an aggregation-induced emission fluorogen by means of two-photon fluorescence lifetime imaging. Chem Eur J 21:4315–4320
24. Izquierdo MA et al (2015) Dual use of porphyrazines as sensitizers and viscosity markers in photodynamic therapy. J Mater Chem B 3:1089–1096
25. Kuimova MK, Botchway SW, Parker AW (2009) Imaging intracellular viscosity of a single cell during photoinduced cell death. Nat Chem 1:69–73
26. Levitt JA, Kuimova MK, Yahioglu G (2009) Membrane-bound molecular rotors measure viscosity in live cells via fluorescence lifetime imaging. C J Phys Chem 113:11634–11642
27. Kuimova MK, Yahioglu G, Levitt JA (2008) Molecular rotor measures viscosity of live cells via fluorescence lifetime imaging. J Am Chem Soc 130:6672–6673
28. Vyšniauskas A, Qurashi M, Kuimova MK (2016) Molecular rotor measures dynamic changes of lipid bilayer viscosity caused by oxidative stress. Chem Eur J 22:13210–13217
29. Shimolina LE et al (2017) Imaging tumor microscopic viscosity in vivo using molecular rotors. Sci Rep 7:41097. https://doi.org/10.1038/srep41097
30. Vyšniauskas A et al (2015) Unraveling the effect of temperature on viscosity-sensitive fluorescent molecular rotors. Chem Sci 6:5773–5778
31. Sherin PS et al (2017) Visualising the membrane viscosity of porcine eye lens cells using molecular rotors. Chem Sci 8:3523–3528. https://doi.org/10.1039/C6SC05369F
32. Nipper ME et al (2011) Detection of liposome membrane viscosity perturbations with ratiometric molecular rotors. Biochimie 93:988–994
33. Dent MR et al (2015) Imaging phase separation in model lipid membranes through the use of BODIPY based molecular rotors. Phys Chem Chem Phys 17:18393–18402
34. Wu Y et al (2013) Molecular rheometry: direct determination of viscosity in Lo and Ld lipid phases via fluorescence lifetime imaging. Phys Chem Chem Phys 15:14986–14993
35. Dubessy C et al (2000) Spheroids in radiobiology and photodynamic therapy. Crit Rev Oncol Hematol 36:179–192
36. Zanoni M et al (2016) 3D tumor spheroid models for in vitro therapeutic screening: a systematic approach to enhance the biologicalrelevance of data obtained. Sci Rep 6:19103. https://doi.org/10.1038/srep19103

Live Imaging of Cell Invasion Using a Multicellular Spheroid Model and Light-Sheet Microscopy

11

Marco Marcello, Rosalie Richards, David Mason, and Violaine Sée

Abstract

Three-dimensional cellular assays are becoming increasingly popular as a fundamental tool to bridge the gap between tissue culture systems and in vivo tissue. In particular, spheroids are recognised today as a necessary intermediate model between testing in monolayer cultures and testing in animals. This chapter describes a straightforward protocol, from sample preparation to image acquisition and initial post-processing, based on one of most widely used commercial light-sheet fluorescence microscopy platform, the Zeiss Lightsheet Z.1.

Keywords

Multicellular spheroid • Light-sheet fluorescence microscopy • Cell invasion • FEP tubes • Matrigel • Hanging drop • Glioblastoma • Multiview reconstruction

11.1 Introduction

The invasion of tumour cells into neighbouring tissue is a hallmark of cancer and constitutes the initial step of metastasis—the spread of tumour cells to distant tissues or organs [1]. Metastasis contributes to over 90% of cancer deaths [2]; however, the development of anti-metastatic therapies has been largely unsuccessful to date [3, 4], in part because of the absence of good predictive in vitro models for drug screening. 2D in vitro cell culture is currently the standard model used for initial preclinical drug testing. Yet, this model fails to replicate essential features of the tumour microenvironment such as oxygen and drug diffusion gradients, and cell-extracellular matrix (ECM) signalling. 3D multicellular tumour spheroids more closely represent tissue organisation in vivo and offer a powerful alternative to classical 2D models.

To elucidate the mechanisms of cell invasion and evaluate the effects of drugs on cell migration, spheroids need to be imaged in their entirety, live, over several hours. This brings new challenges in terms of sample preparation, microscopy, data analysis and interpretation. We here describe the use of a multicellular tumour spheroid model to investigate cellular migration

M. Marcello • R. Richards • D. Mason • V. Sée (✉)
Department of Biochemistry and Centre for Cell Imaging, Institute of Integrative Biology, University of Liverpool, Liverpool L69 7ZB, UK
e-mail: violaine@liverpool.ac.uk

R.I. Dmitriev (ed.), *Multi-Parametric Live Cell Microscopy of 3D Tissue Models*,
Advances in Experimental Medicine and Biology 1035, DOI 10.1007/978-3-319-67358-5_11

and invasion in 3D using light-sheet fluorescence microscopy (LSFM). In a typical spheroid invasion assay, spheroids are plated on, or embedded in, ECM in a 96-well plate. The plates are imaged using an inverted microscope and invasion is quantified by measuring the distance that cells have migrated away from the spheroid [5, 6]. While this technique has the advantage of being high-throughput, it only provides information about the movement of cells in the x–y plane and does not provide any information about the migration of cells within spheroids. A further disadvantage of this technique is the inability to track individual cells.

We here describe an experimental protocol to track the invasion of individual cells in the x, y and z planes using LSFM. Both the migration of cells within spheroids, as well as their invasion in to the surrounding matrix, can be studied. Such an approach provides important information about the effects of the 3D architecture of cells on cell migration. While it is possible to acquire 3D images using a confocal microscope, the depth penetration is poor. The development of LSFM, also known as single-plane illumination microscopy (SPIM), has led to a revolution in the imaging of large (>0.2 mm) living biological samples in 3D. LSFM was developed by Huisken et al. in 2004 and uses a plane of light, provided by dual illumination objectives, to provide optical sectioning [7]. The sheet of light illuminates only the focal plane of the detection objective, resulting in reduced photobleaching and phototoxicity compared to confocal microscopy [7, 8]. LSFM proved very soon to be an ideal tool to rapidly observe large living multicellular specimens obtained in a three-dimensional cell culture [9].

Spheroids are embedded in a solution of Matrigel and media and mounted in an FEP tube, which is suspended in a liquid-filled chamber where it can be moved through the light sheet to produce a z-stack. Light is detected by a CCD or CMOS camera, which allows for very fast image acquisition compared with traditional point-scanning confocal microscopy, which samples pixel by pixel. This makes LSFM an ideal technique for imaging cell movement in a large, tightly packed spheroid when z-stacks need to be acquired in rapid succession to facilitate the tracking of cells. To make analysis more amenable, the data can be down-sampled in space and bit-depth to allow further analysis on a range of computer hardware. From the raw or processed data it is possible to quantify the movements of cells within the spheroids, as well as those invading into ECM.

11.2 Materials

11.2.1 Cell Culture

1. U87 glioblastoma cells (HTB-14; ATCC, UK)
2. T-75 flasks
3. Minimum Essential Medium (MEM) supplemented with 10% v/v Foetal Bovine Serum and 1% v/v Sodium-Pyruvate
4. We used U87 cells stably expressing Histone 2B fused to Red Fluorescent protein (H2B-mRFP) using lentiviral transduction. The plasmid used for transduction was pHIV-H2BmRFP (Addgene, plasmid #18982)

11.2.2 Materials

1. 96-well Perfecta3D® Hanging Drop plates (3D Biomatrix, USA; ordered from Sigma) for spheroid formation
2. 0.22 μm PES filters (Biofil®, Guangzhou, China)
3. Teflon plunger (Brand GMBH, Wertheim, Germany)
4. Glass capillaries with green tag, size 3, inner diameter 1 mm (Brand GMBH, Wertheim, Germany)
5. Fluorinated Ethylene Propylene (FEP) tubing, 1/16”ID × 1/8”OD (S 1815–04, BOLA, Germany)
6. Parafilm

11.2.3 Chemicals

Corning® Matrigel® Basement Membrane Matrix, phenol red free (Corning, ordered from VWR, UK)

11.2.4 Equipment

1. Light-sheet microscope Z.1 (Zeiss, Germany)
2. Cell incubator set at 37 °C, 5% CO_2 (Sanyo, Japan)
3. TC20 automated cell counter (Bio-Rad, UK)
4. HP Z640 computer workstation (Hewlett-Packard, US) equipped with six central processing units (CPUs; Intel Xeon E5-2620v3 2.4 GHz) and 128 GB of DDR4 RAM (*see* **Note 1**).

11.3 Methods

11.3.1 Cell Staining for Imaging and Tracking

A nuclear marker is used to facilitate the automated identification of cells. We previously found that nuclear stains show poor penetration in spheroids; therefore, it was necessary to create a cell line stably expressing a fluorescent nuclear reporter protein. We expressed histone H2B by transducing U87 cells with the pHIV-H2BmRFP construct generated by Welm et al. [10] (*see* **Note 2**).

11.3.2 Formation of Multicellular Tumour Spheroids

1. Make a cell suspension using a pellet of 2.4×10^4 U87 cells in 1 mL of filtered growth media. Media needs to be filtered through a 0.22 μm PES filter as unfiltered media contains small particulates that spheroids adhere to.
2. Pipet the cell suspension (50 μl per well) into a 96-well Perfecta3D Hanging Drop plate where it will form a hanging droplet (Fig. 11.1). After three days, the cells will have compacted from a loose aggregate and formed a compact spheroid.
3. On day 3, transfer the spheroids to a 35 mm non-treated culture dish using a P1000 pipette. Depending on size/compactness of the spheroids, it is usually beneficial to cut the final segment of the blue P1000 tip to widen the diameter of the tip and avoid spheroid disruption during the transfer and change media every 2–3 days (2 mL media/dish). As spheroids settle at the bottom of the dish, the old media is simply aspirated with a pipette and replaced with fresh media.

11.3.3 Sample Mounting

1. Prepare all the materials needed for spheroid mounting: FEP tubes, Teflon plunger and glass capillary (Fig. 11.2a).
2. Collect individual spheroids from the tissue culture dish using a Pasteur pipette, and transfer in a droplet of media to an empty dish (Fig. 11.2b).
3. Aspirate the surrounding media using a pipette and replace with 50% ice-cold Matrigel and 50% growth media supplemented with 25 mM HEPES. *See* **Note 3** about the choice of Matrigel for embedding and **Note 4** for drug treatment, if required.
4. Insert a Teflon plunger into an FEP tube (several cm in length) and use it to draw the spheroid into the opposite end of the tube (Fig. 11.2c). Before drawing up the spheroid, a small amount of air needs to be drawn up to create an air gap where the tube can be cut using scissors to release it from the plunger (*see* **Note 5**).
5. Insert the FEP tube into a glass capillary, which is marginally wider in diameter than the FEP tube (Fig. 11.2d). If a close fit is achieved, there is no need for any additional fixative to hold the tube within the capillary.
6. Wrap the end of the FEP tube, which is not inside the glass capillary, in parafilm (Fig. 11.2e), insert the complete set-up (Fig. 11.2f) in the sample holder (Fig. 11.2g)

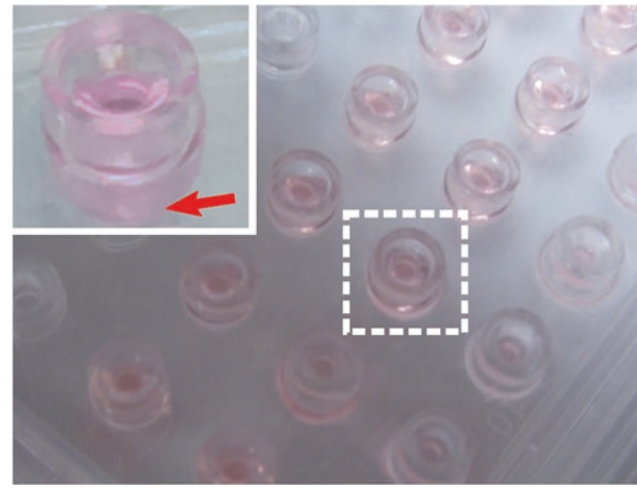

Fig. 11.1 Hanging Drop plate. The cell suspension is pipetted into the wells to form a hanging droplet (*red arrow*). Spheroids form within 3 days in the droplets. The spheroids are harvested by tapping the plate onto a large Petri dish, so that they can be pipetted and transferred into a 35 mm dish filled with cell culture medium

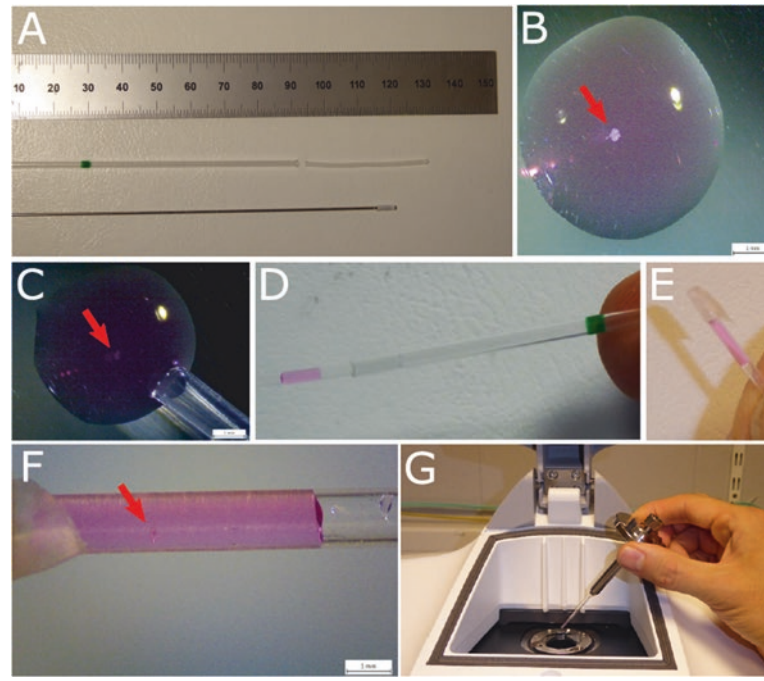

Fig. 11.2 Spheroid mounting. (**a**) From the top: ruler shown for scale, glass capillary (*left*) and FEP tube (*right*), Teflon plunger (**b**) single spheroid (*red arrow*) in a droplet containing the Matrigel-medium mix. (**c**) Drawing of the spheroid (*red arrow*) into the FEP tube. (**d**) Detail of FEP tube held within the glass capillary. (**e**) Sealing one end of the FEP tube with parafilm. (**f**) Detail view of the spheroid (*red arrow*) in the FEP tube. (**g**) Photograph of the whole capillary holder ready to be inserted into the LSFM microscope

and immerse in the sample chamber, which is filled with RO water and maintained at 37 °C for the duration of the experiment.

11.3.4 Image Acquisition

1. Excite the samples with the appropriate wavelength for the fluorophore used using a 10x illumination objective. Collect emitted light through the appropriate filter for the fluorophore using a 20x W Plan-Apochromat objective.
2. Acquire images every 3 min with a z-step of 1.66 µm, starting approximately 50 µm in front of the spheroid. Use the Lightsheet Z.1 Zen software (Zeiss) for image acquisition (Fig. 11.3). Acquisition can be performed from three angles if necessary for further 3D reconstruction, depending upon sample size

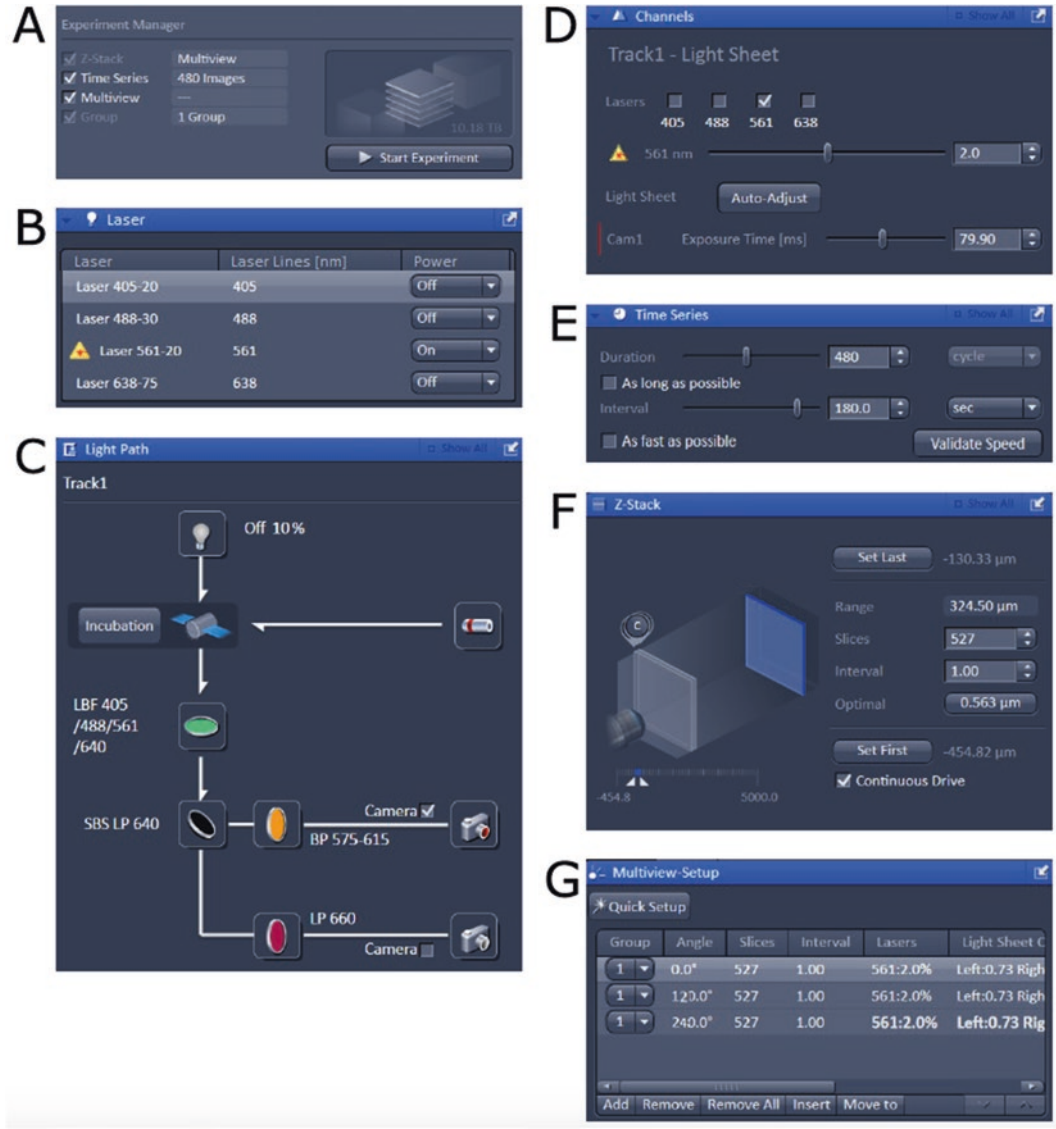

Fig. 11.3 Image acquisition. Select the preferred Z stack, Time Series and Multiview options in Experiment Design (**a**). Switch on the laser (**b**). Set up the appropriate light-path (**c**) laser intensity and exposure times (**d**) for the fluorescent labels in use. Decide the duration of the experiment and the time interval between the acquisitions (**e**). Set the z spacing (**f**): 1.66 micron in the example. Select the desired number of views (**g**), three evenly spaced (e.g. 0, 120, 240 degrees) being a suggested minimum

(*see* **Note 6**). Images are acquired using a pco. edge scientific complementary metal–oxide–semiconductor (sCMOS) camera.

11.3.5 Image Processing

We suggest using the following workflow to prepare the data for analysis (Fig. 11.4). Pre-processing the data is essential if you do not have access to a computer cluster, due to the large file sizes produced (up to 0.75 TB for one experiment). Down-sampling is acceptable in our case, as the loss in resolution has minimal effect upon the precision of feature detection.

1. Use the macro written in Fiji by D. Mason (available at https://bitbucket.org/davemason/

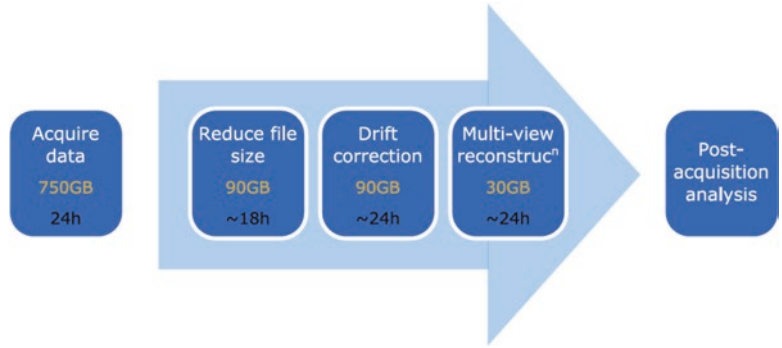

Fig. 11.4 Summary of steps to reduce file size and make data sets ready for image analysis. After acquisition, Fiji is used to first reduce file size by down-sampling and binning, and then to correct sample drift and register the multiple views. Approximate file sizes after each step and time to process are shown for a large spheroid imaged from three angles, although these are highly sample-dependent

lsfm_scripts). The macro loads one time point at a time and down-samples the data by decreasing bit depth from 16 bit to 8 bit and performing 2x spatial binning in X and Y. Options for cropping are also available. More down-sampling means a smaller file size and faster manipulation but less precise spot detection.

2. If you have used multiple acquisition angles (**Note 6**), you can register and fuse them using the Multiview Reconstruction Application plugin [11], following the tutorials on the ImageJ website (http://imagej.net/Multiview-Reconstruction also archived at: https://web.archive.org/web/20170222212102/http://imagej.net/Multiview-Reconstruction). If there is a problem with sample drift (*see* **Note 7**), the same plugin can also be used for drift correction.

11.3.6 Image Analysis

After processing, the data are amenable to feature detection and tracking using the open source software Fiji (for example via the Trackmate plugin) or using other software such as Imaris. Simple statistics such as instantaneous spot speed are provided in the output, however bespoke analysis can be used to query the data in a multitude of ways.

11.4 Notes

1. The computational requirements are offered as a guideline only and will be highly dependent upon your sample and acquisition settings. The down-sampling script referenced in 3.5.1 requires a single time point be loaded into memory at once therefore this should inform hardware requirements.
2. The use of longer excitation/emission wavelength red fluorescent proteins (RFPs) results in reduced autofluorescence, light scattering and excitation phototoxicity, making RFP (and variants) the most suitable fluorescent protein variant for long-time-lapse live-cell imaging in thick samples [12].
3. The most typical approach for preparing small samples for imaging using LSFM is to embed them in a hydrogel, such as agarose, which has a refraction index close to that of water. We initially attempted to embed spheroids in 1% (w/v) low-melt agarose diluted in cell culture medium. However, agarose is not an ideal embedding medium for long-term culture because it is not a physiological substrate; it also precluded cell invasion. We also tried embedding spheroids in collagen IV and MaxGel ECM (Sigma); however, we again found that the cells did not invade.

4. If drug treatment is required, the drug can be added to the growth media at the desired concentration.
5. FEP tubes: Spheroids were mounted in a Matrigel-medium mix in FEP tubes, thereby creating conditions suitable for stable long-term imaging. As the spheroid is contained in a discrete compartment the sample chamber can be filled with distilled water instead of media. This means that there is no need to dismantle and sterilise the chamber after each use as contamination is not an issue. Furthermore, much smaller volumes of expensive reagents (e.g. Matrigel, drugs) are required because the volume of the FEP tube is much smaller than the volume of the sample chamber.
6. Multi-view acquisition and reconstruction: Many small samples (below ~150 μm) can be imaged from a single angle. Some small and many larger samples such as spheroids will benefit greatly from acquiring multiple acquisition angles and reconstructing them post acquisition.

   While it is possible to carry out online dual side fusion using the Zen software, this does not include a registration step so can complicate multiview registration if the system is not perfectly aligned. We suggest that users who are doing more than one angle do not enable dual side fusion, and instead use the Multiview Registration Application to register both dual side data and multiple acquisition angles at the same time.
7. Drift: We found that an initial sample drift, typically upward, tended to occur in the first three hours of the experiment, before cells had begun to invade. Therefore, we chose to mount spheroids on the light-sheet microscope immediately after embedding but to delay imaging for 3 h after sample mounting, to allow the sample to stabilise.

References

1. Valastyan S, Weinberg RA (2011) Tumor metastasis: molecular insights and evolving paradigms. Cell 147:275–292
2. Mehlen P, Puisieux A (2006) Metastasis: a question of life or death. Nat Rev Cancer 6:449–458
3. Paez-Ribes M, Allen E, Hudock J, Takeda T, Okuyama H, Vinals F, Inoue M, Bergers G, Hanahan D, Casanovas O (2009) Antiangiogenic therapy elicits malignant progression of tumors to increased local invasion and distant metastasis. Cancer Cell 15:220–231
4. Coussens LM, Fingleton B, Matrisian LM (2002) Matrix metalloproteinase inhibitors and cancer: trials and tribulations. Science 295:2387–2392
5. Vinci M, Gowan S, Boxall F, Patterson L, Zimmermann M, Court W, Lomas C, Mendiola M, Hardisson D, Eccles SA (2012) Advances in establishment and analysis of three-dimensional tumor spheroid-based functional assays for target validation and drug evaluation. BMC Biol 10:29
6. Blacher S, Erpicum C, Lenoir B, Paupert J, Moraes G, Ormenese S, Bullinger E, Noel A (2014) Cell invasion in the spheroid sprouting assay: a spatial organisation analysis adaptable to cell behaviour. PLoS One 9(5):e97019
7. Huisken J, Swoger J, Del Bene F, Wittbrodt J, Stelzer EH (2004) Optical sectioning deep inside live embryos by selective plane illumination microscopy. Science 305:1007–1009
8. Stelzer EH (2015) Light-sheet fluorescence microscopy for quantitative biology. Nat Methods 12:23–26
9. Verveer PJ, Swoger J, Pampaloni F, Greger K, Marcello M, Stelzer EH (2007) High-resolution three-dimensional imaging of large specimens with light sheet-based microscopy. Nat Methods 4:311–313
10. Welm BE, Dijkgraaf GJ, Bledau AS, Welm AL, Werb Z (2008) Lentiviral transduction of mammary stem cells for analysis of gene function during development and cancer. Cell Stem Cell 2:90–102
11. Preibisch S, Saalfeld S, Schindelin J, Tomancak P (2010) Software for bead-based registration of selective plane illumination microscopy data. Nat Methods 7:418–419
12. Shcherbakova DM, Subach OM, Verkhusha VV (2012) Red fluorescent proteins: advanced imaging applications and future design. Angew Chem Int Ed Eng 51:10724–10738

Raman Imaging Microscopy for Quantitative Analysis of Biological Samples

12

Shinji Kajimoto, Mizuki Takeuchi, and Takakazu Nakabayashi

Abstract

Raman imaging microscopy is a powerful tool for label-free imaging of biological samples. It has the advantage of measuring the spatial distribution of endogenous proteins and lipids in cells, as well as obtaining chemical information on these endogenous molecules, such as hydrogen bonding and electrostatic interactions. However, because Raman intensity is very weak compared with fluorescence intensity, obtaining a reliable Raman image requires fast acquisition of a Raman image and rejection of background fluorescence. In this chapter, we describe the procedure for obtaining images of the Raman band of interest using a multipoint technique, which is the fast acquisition method for obtaining an image.

Keywords

Raman imaging microscopy • Raman spectrum • Molecular vibrations • Label-free imaging • Multipoint microscopy • Cell medium

12.1 Introduction

Over the last few decades, Raman imaging microscopy has attracted great attention by biologists as a nondestructive and label-free technique to study molecular distribution in living systems. All living systems consist of molecules, and the contents and distribution of molecules in or between cells determine structure and function of a living system. Therefore, it is essential to study molecular distribution within living cells, tissues, and organs in order to understand their functions.

"Raman scattering" is a phenomenon that was discovered in 1921 by Sir C. V. Raman. He was fascinated by the scattered blue light of sunlight from the Mediterranean Sea and started to investigate scattered light components with wavelengths different from incident light. He found that the energy difference between the incident and scattered light (frequency shifts) depends on the molecule observed. After publishing his first paper on Raman scattering in 1928 [1], he was

S. Kajimoto • M. Takeuchi • T. Nakabayashi (✉)
Graduate School of Pharmaceutical Sciences, Tohoku University, Aoba-ku, Sendai 980-8578, Japan
e-mail: takan@m.tohoku.ac.jp

R.I. Dmitriev (ed.), *Multi-Parametric Live Cell Microscopy of 3D Tissue Models*,
Advances in Experimental Medicine and Biology 1035, DOI 10.1007/978-3-319-67358-5_12

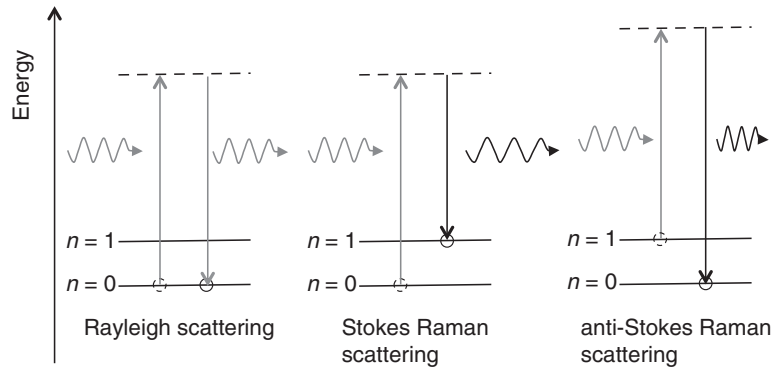

Fig. 12.1 Energy diagrams of Rayleigh scattering, Stokes Raman scattering, and anti-Stokes Raman scattering

given the Nobel Prize in Physics just two years later, in 1930, for the discovery of Raman scattering.

Raman scattering is the inelastic scattering process of a photon by a molecule (see Fig. 12.1). When photons are incident on molecules, almost all the photons scatter elastically and maintain the frequency of the incident light. This phenomenon is called Rayleigh scattering. A small fraction of the incident photons are scattered inelastically, either loosing or gaining some energy from a molecule. The inelastically scattered photons with lower photon energy appear at longer wavelengths (red-shifted) and are called Stokes Raman scattering, while those with higher photon energy appear at shorter wavelengths (blue-shifted) and are called anti-Stokes Raman scattering. The energy difference between an incident photon and an inelastic scattered photon, which is called Raman shift, corresponds to the energy of a molecular vibration causing the inelastic scattering of the incident photon. As shown in Fig. 12.1, Stokes Raman scattering corresponds to the transition with the energy of the final state higher than that of the initial state, and anti-Stokes Raman scattering corresponds to the energy of the final state lower than that of the initial state. Therefore, anti-Stokes Raman scattering arises only from molecules that are populated on excited vibrational states, resulting in very weak intensity compared with Stokes Raman scattering. The intrinsic vibrational energy levels in a molecule are determined by chemical structure and environment of the molecule. We can, therefore, obtain information on the chemical structure and intra- and inter-molecular interactions of the target molecule by measuring its Raman spectrum, which is a plot of the magnitude of Raman scattering (Raman intensity) against Raman shift. The energy of a vibration inducing Raman scattering is measured as the peak position of the Raman band.

Raman imaging microscopy, which maps the spatial distribution of the Raman band of interest in a sample, has great advantages compared with other imaging techniques. Since each molecule has its own Raman spectrum, the spatial distribution of endogenous chemical substances can be obtained by Raman imaging microscopy without labeling of probes [2, 3]. Namely, Raman imaging usually does not require chemical pretreatment and provides direct and quantitative information on molecular distributions in living systems. Infrared (IR) absorption spectroscopy also gives information on vibrations of a molecule and IR imaging microscopy is used to observe the spatial distribution of molecules in solids, such as tablets used in pharmaceutical science. However, IR spectroscopy is difficult to be applied to living systems because the very strong IR absorption of water greatly interferes with the observation of the IR absorption bands of other molecules. Furthermore, Raman spectroscopy has higher spatial resolution than IR spectroscopy, which comes from the fact that the visible light is generally used as the excitation source for Raman spectroscopy and the spatial resolution is higher at shorter wavelengths.

The disadvantage of Raman spectroscopy is that Raman intensity is very weak compared with

fluorescence. The cross-section for Raman scattering is estimated to be 10^{-30} ~ 10^{-25} cm^{-2}, which is much smaller than the absorption cross-section of fluorescent probes (10^{-16} cm^{-2} for typical dye molecules having a molar extinction coefficient, ε, of ~10^4 M^{-1} cm^{-1}). This means that the intensity of Raman scattering is ten orders of magnitude weaker than that of fluorescence and it takes time to measure a Raman spectrum or a Raman image with high signal-to-noise (S/N) ratio. Therefore, Raman imaging microscopy requires both a high-sensitive detection system and a fast acquisition technique.

In Raman imaging microscopy, the Raman spectrum at each spatial location is collected and the integrated intensity of the Raman band of interest is mapped to convert to an image of the Raman band. In this chapter, we first briefly introduce the classical theory of Raman scattering, examples of Raman spectra and Raman images of cells. We then describe materials, methods, and notes for Raman imaging microscopy with a multipoint technique that is one of the fast acquisition methods for obtaining an image.

12.2 Theory

There are two ways to interpret the physics of Raman scattering: classical and quantum interpretation. In classical interpretation, light is considered as an electromagnetic wave and Raman scattering results from the interaction between the oscillating electric field of light and the electron cloud of a molecule via its polarizability. On the other hand, in quantum interpretation, light is considered as a particle, and Raman scattering is thought to be the inelastic collision between a photon and a molecule. Classical interpretation is intuitive and is easy to understand the selection rule of Raman transition, namely that a molecular vibration does not always exhibit Raman scattering. Here we briefly introduce classical interpretation of Raman scattering and derive the selection rule. It is noted that introduction of quantum mechanical theory is necessary to understand some optical phenomena related to Raman scattering, such as the resonance effect.

The electric field of incident light with frequency ν_i is described as

$$E_i = E_0 e_1 \cos\left(2\pi \nu_i t\right) \tag{12.1}$$

where E_0 and $\boldsymbol{e_1}$ are the amplitude and the unit vector of the electric field, respectively. When incident light interacts with a molecule, the oscillating electric field causes a change in the electron density distribution of the molecule and then induces a dipole moment (induced dipole moment, μ_{ind}) in the molecule. When the amplitude of the electric field is sufficiently low, the induced dipole moment is the product of the electric field and the molecular polarizability, $\boldsymbol{\alpha}$, of the molecule.

$$\mu_{ind} = \alpha E_i = E_0 \alpha e_1 \cos\left(2\pi \nu_i t\right) \tag{12.2}$$

The molecular polarizability corresponds to the magnitude of the change in electron density in a molecule with an external electric field. This value is changed slightly in synchronization with molecular vibrations because the molecular structure is synchronously changed with vibrations. When the frequency of a molecular motion is ν_R, the molecular polarizability changes synchronously with ν_R:

$$\alpha = \alpha_0 + \Delta\alpha \cos\left(2\pi \nu_R t\right) \tag{12.3}$$

where $\boldsymbol{\alpha_0}$ is the mean polarizability and $\boldsymbol{\Delta\alpha}$ is the amplitude of the variation of the polarizability with the vibration. Eq. (12.2) is therefore expanded to:

$$\begin{aligned}\mu_{ind} = \alpha E_i &= \left(\alpha_0 + \Delta\alpha \cos\left(2\pi \nu_R t\right)\right) E_0 e \cos\left(2\pi \nu_i t\right) \\ &= E_0 \alpha_0 e_1 \cos\left(2\pi \nu_i t\right) \\ &\quad + \frac{1}{2} E_0 \Delta\alpha e_1 \cos\left(2\pi \left(\nu_i - \nu_R\right) t\right) \\ &\quad + \frac{1}{2} E_0 \Delta\alpha e_1 \cos\left(2\pi \left(\nu_i + \nu_R\right) t\right)\end{aligned} \tag{12.4}$$

Equation (12.4) shows that the induced dipole moment has three oscillating components with different frequencies. One component has a frequency of the incident light and the other two components have frequencies shifted by the frequency of the molecular vibration causing the change in molecular polarizability. A dipole oscillation with a certain frequency emits electromagnetic radiation (i.e., light) of the same frequency. Therefore, the first component causes light emission with the same frequency as the incident light, that is, Rayleigh scattering. The second and third components generate light emission shifted to lower frequency ($\nu_i - \nu_R$) and higher frequency ($\nu_i + \nu_R$), respectively. These lower- and higher-shifted light are Stokes Raman scattering and anti-Stokes Raman scattering, respectively.

As shown in Eq. (12.4), Raman scattering does not appear when the molecular polarizability remains unchanged with a molecular vibration ($\Delta\boldsymbol{\alpha} = 0$). It is therefore said that Raman scattering is observed only for molecular vibrations inducing the change in molecular polarizability ($\Delta\boldsymbol{\alpha} \neq 0$). The vibrations showing Raman scattering are called Raman active vibrations. Skeletal vibrations such as C = C stretching and C = O stretching modes are known to show strong Raman intensity.

12.3 Examples and Materials

12.3.1 Example of Raman spectra

Molecular vibrations of chemical substances existing in a cell or constructing plasma membranes can be probed using Raman spectroscopy. Fig. 12.2a shows a Raman spectrum of human cervical carcinoma (HeLa) cells, which is a representative immortal cell line cultured in scientific research. The excitation wavelength is 532 nm. The assignments of the observed bands are also shown in the same figure. The Raman band due to C–H bonds of fatty acids and proteins are observed at around 1450 cm^{-1}, and the Raman band at around 1650 cm^{-1} is ascribed to the amide band of proteins in a cell.

It should be noted that the Raman bands of proteins or fatty acids in Fig. 12.2 are ascribed to the summation of a variety of proteins or fatty acids in cells; it is difficult to distinguish a protein or fatty acid of interest from others by conventional Raman spectroscopic techniques. In Fig. 12.2a, however, some Raman bands assignable to protein cytochrome c (cyt c) are clearly observed, which is due to the so-called resonance Raman effect, a phenomenon of the

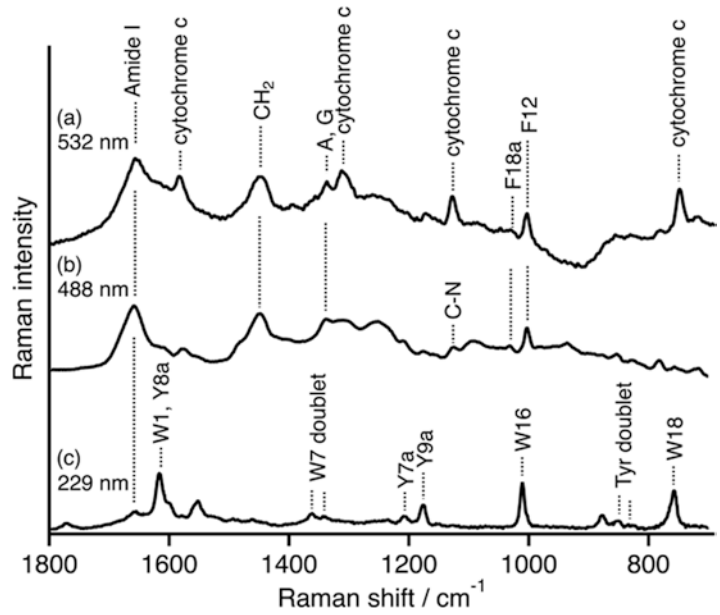

Fig. 12.2 Raman spectra of HeLa cells with the excitation wavelength of 532 nm (**a**), 488 nm (**b**), and 229 nm (**c**). *A, G* adenine and guanine, *F* phenylalanine, *W* tryptophan, *Y* tyrosine

remarkable enhancement of the Raman intensity that occurs when the wavelength of the excitation light is in the region of the electronic absorption of the observed molecule. An excitation wavelength of 532 nm is in resonance with the absorption of cyt c in the region of 500–570 nm, resulting in the strong enhancement of their Raman bands [4]. Actually, the Raman bands of cyt c disappear when the Raman spectrum of HeLa cells is observed at an excitation wavelength of 488 nm, which is not efficiently resonant with the absorption of cyt c.

Amino acids with an aromatic ring, such as tryptophan and phenylalanine, have an absorption band in the ultraviolet (UV) region of 220–300 nm. Therefore, the Raman bands of aromatic amino acids are remarkably enhanced with UV excitation. The Raman spectrum of HeLa cells with the excitation wavelength of 229 nm is shown in Fig. 12.2c. The obtained spectrum is markedly different from that obtained at the visible excitation (Fig. 12.2a, b), and the Raman bands due to tryptophan (W) and tyrosine (Y) in HeLa cells are clearly observed with 229 nm excitation wavelength. In conclusion, it is important to remember that the Raman spectrum of living cells and tissues changes with excitation wavelength.

12.3.2 Example of Raman imaging

Imaging of the spatial distribution of the Raman band of interest is obtained using a microscopic technique. Fig. 12.3 shows the example of an image of the C–H stretching Raman band in a single HeLa cell, together with a bright field image. All the images shown in this chapter were obtained using a multipoint confocal Raman imaging microscope (Phalanx-R, Tokyo Instruments, inc.), whose details are shown later.

The intensity between 2847 and 2918 cm^{-1} is integrated at each pixel, which is converted to an image of the C–H stretching Raman band. The intensity reflects the concentration of C–H bonds in each cellular compartment and the dull round region corresponds to the nucleus which has fewer C–H bonds than the cytosol. The Raman images at different depths are also obtained using a confocal microscopic technique, which is shown in Fig. 12.4.

12.3.3 Materials

The preparation of living cells for Raman microscopy is very similar to that for standard fluorescence microscopy. Endogenous proteins and

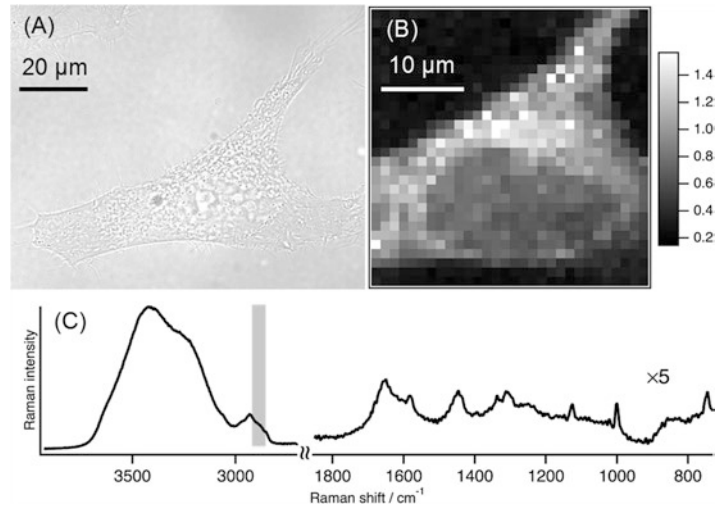

Fig. 12.3 Bright field (**a**) and confocal Raman (**b**) images of a single HeLa cell. The Raman image was obtained by the integration of the intensity in the area of the C–H stretching band, which is shown in a gray bar in the Raman spectrum of a single HeLa cell (**c**). The excitation wavelength was 532 nm

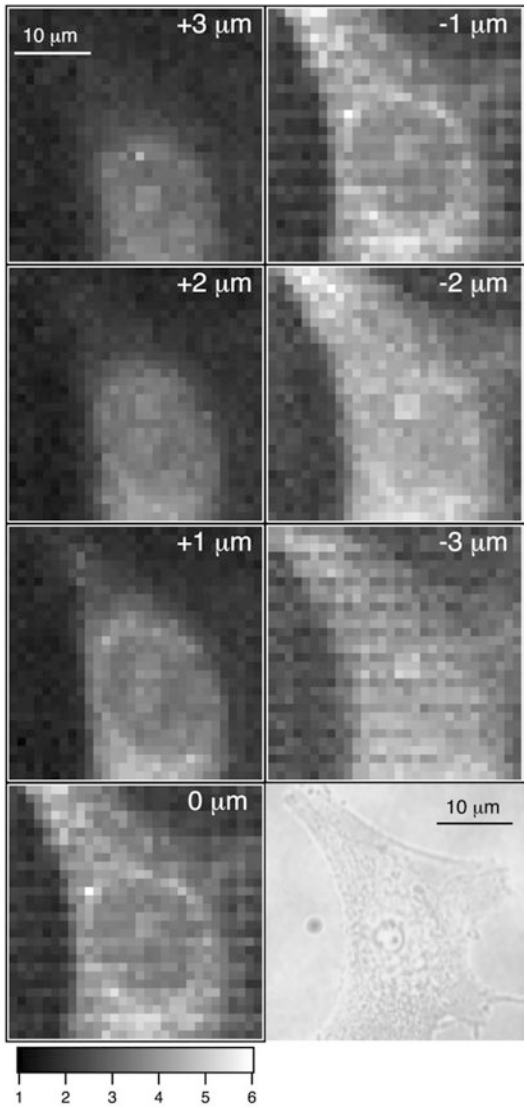

Fig. 12.4 Confocal Raman images of a single HeLa cell with changing position in the Z direction, together with a bright field image of the same cell. The excitation wavelength was 532 nm

lipids are usually probed in Raman measurements of cells and tissues without loading dye. The preparation of HeLa cells for Raman microscopy is shown as follows.

1. Culture medium for HeLa cells is prepared using DMEM, as shown in Chap. 8.
2. Stocked HeLa cells are thawed at room temperature and mixed with 4 ml of the culture medium. The cell suspension is centrifuged at 100 × *g* for 3 min then the supernatant is aspirated. The resultant pellet is suspended with 4 ml of the culture medium. Then HeLa cells are plated in 10 cm dishes with 8 ml of the culture medium and are incubated in a 5% CO_2 humidified atmosphere at 37 °C until semi-confluent.
3. Cells are washed with phosphate buffered saline (PBS) buffer, the PBS is aspirated, and then cells are incubated for 2 min with 1–2 ml of trypsin/EDTA. The culture medium is added to the dish, cells are centrifuged, then resuspended using the culture medium.
4. Cells are plated in a 5 cm glass-bottomed dish with 3 ml of the cultured medium and are incubated for one day.
5. Cells are washed at least twice using Hanks' Balanced Salt Solution (HBSS). After the HBSS is aspirated, 3 ml of HBSS is added into the glass-bottomed dish, and then the Raman measurement is initiated (*see* **Notes 1, 2**).

12.4 Methods

12.4.1 Measurement System

Any one-photon laser microscopes can be combined with Raman imaging microscopy. Confocal laser-scanning microscopes are mostly used for Raman imaging because tightly focusing of excitation laser-beam is necessary to obtain efficient Raman signals. Therefore, wide-field microscopy is usually considered not be suitable for Raman imaging microscopy. The construction of a confocal Raman imaging microscope is similar to that of a standard confocal fluorescence microscope except for the detection system. A highly sensitive detection system must be prepared for Raman imaging microscopy because Raman intensity is much weaker than fluorescence intensity and a spectrograph is usually equipped with the microscope to obtain Raman signals as a spectrum, resulting in the reduction of Raman intensity.

Highly sensitive charge-coupled device (CCD) cameras are mostly used in Raman imaging

microscopy. The quantum efficiency, which represents the conversion efficiency from incident photon to electron, is the most important term considered to select CCD for Raman imaging microscopy. The quantum efficiency should be as high as possible in the wavelength region where Raman signals appear. Noises such as dark current, reading noise, and shot noise should also be considered when obtaining a Raman image with high S/N ratio. CCD for Raman microscopy is usually cooled by thermoelectric (TE) cooling system to −50 ~ −100 °C to reduce dark current. A liquid-nitrogen cooled CCD is also used to measure very weak Raman spectra [5].

Because Raman intensity is very weak compared with fluorescence intensity as mentioned above, one of the serious problems in Raman imaging microscopy is that it takes a long time to obtain a Raman image. Prolonged laser irradiation is often necessary to obtain a Raman image, resulting in significant damage to biological samples. Development of a fast acquisition system for Raman images, as well as a high-efficient detection system is very important to apply Raman imaging microscopy to a variety of biological systems. The line scanning technique is one of the methods for fast acquisition of an image [6, 7].

Multipoint (multifocus) imaging microscopy is a fast acquisition method [8–10] commercially available from a few companies. In multipoint microscopy, an excitation laser is split into X by X using a spatial light modulator, then X^2 beamlets are focused with an objective lens onto a sample with keeping the array shape. The Raman signal from each spot is collected and transferred to a fiber bundle to rearrange two-dimensional Raman signals into a one-dimensional single line. Then the single line of the Raman signals is introduced into a spectrograph to be dispersed, and therefore X^2 Raman spectra are detected at once by the CCD detector. The obtained X^2 spectra are converted to a two-dimensional Raman image with the integration of the Raman band of interest at each point. Multipoint imaging microscopy ideally enables us to obtain a Raman image at once without the scan of the excitation laser beam.

12.4.2 Procedure for Raman imaging

The procedure for conventional Raman imaging microscopy is very similar to that for standard fluorescence microscopy except for the measurement time. In this chapter, we have shown the protocols to obtain Raman images using a multipoint confocal Raman imaging microscope with a TE-cooled CCD detector. There is some technical knowledge for multipoint confocal microscopy to be understood for obtaining a reliable image. The procedure for obtaining images of HeLa cells in the C–H stretching band region is as follows. An inverted microscope is used in this experiment and a simple bright field CCD camera is equipped to monitor bright field images of samples and beam spots.

1. Turn on the visible diode laser, CCD camera, confocal microscope, XYZ-piezo stage, and PC. Tune the laser power to ~0.5 W. CCD is cooled to ~ −50 °C (*see* **Notes 3–5**).
2. Select the 60X oil immersion objective lens and place it in the center of the sample stage. After stabilization of the CCD temperature, place one drop of immersion oil directly on the top of the objective lens (*see* **Note 6**).
3. Set a glass-bottomed dish on the stage of the microscope. This dish is empty and is only used for obtaining background signals (*see* **Note 7**).
4. The room is darkened (*see* **Note 8**).
5. Close the shutter of the laser and measure the dark noise of the system with 10 s accumulation time. The obtained background spectrum is automatically subtracted from the Raman spectrum at each pixel using a software program.
6. The excitation light is split into X by X with a spatial light modulator, and a total of X^2 beamlets of square matrix array are focused onto the glass-bottomed dish by the immersion objective lens. Signals at all the spots are collected by the same objective lens and are transferred to a fiber bundle. The Raman signals are rearranged to form a one-dimensional line by this fiber bundle and then are introduced into the spectrograph to

obtain the line of the Raman spectra (*see* **Note 9**).

7. Confirm using a bright field camera that the excitation beamlets keep a square matrix array (*see* **Note 10**).
8. The beamlets are focused onto the glass of the dish. Then measure the spectra at 100 points with 10 s accumulation time (*see* **Note 11**).
9. Set the glass-bottomed dish containing HeLa cells on the stage of the microscope and adjust the position of the objective lens to focus on HeLa cells by observing the bright field image (*see* **Note 12**).
10. Start the measurement of the Raman spectra at 100 spatial points with 10 s accumulation time. If necessary, scan the sample stage using the XY-piezo stage and aquire more points to interpolate the gaps between the beamlets and/or enlarge the observation area (*see* **Note 13**).
11. Measure Raman spectra step-by-step with changing z-axis every ~1 μm
12. Change the position of the sample stage to the area where cells are not observed and measure the Raman spectra with the same experimental conditions as in step 10.
13. Integrate the intensity across the C–H stretching band in wavenumber at each spatial point obtained by steps 10 to convert to the Raman image. At each height position, the Raman image is obtained by the same procedure. The image obtained here is called the Image 13.
14. Make the image of signals from the dish glass in step 8 with the same integration region as that of Image 13. The resultant image is called Image 14.
15. Make the image of signals obtained by step 12 with the integration of the intensity across the O–H stretching band in wavenumber to convert to the image of the O–H stretching band of the medium. The resultant image is called Image 15.
16. Image 14 sometimes has weak C–H stretching Raman bands due to the immersion oil. In this case, Image 14 is subtracted from Image 13 until the C–H stretching band completely disappears in the area where cells are not observed in the image. This is because the cell medium used in Raman measurements, such as HBSS, does not show any C–H stretching band. The image of the C–H stretching Raman band without the contribution from the immersion oil is obtained (*see* **Note 14**).
17. The image obtained by step 16 is divided by Image 15 to compensate the irregularity among the intensities of the beamlets (*see* **Note 15**).
18. Singular value decomposition (SVD) analysis is performed to reduce background noise in some cases (*see* **Note 16**).

12.5 Notes

1. Culture media including several nutrients often exhibit background fluorescence, which lowers the S/N ratio of a Raman image. Opti-MEM without phenol red, which is usually used as a background-free medium for fluorescence microscopy, also shows background fluorescence. On the other hand, inorganic media such as PBS do not show any disturbing fluorescence when there is no organic impurity in the buffer. It is recommended to measure the fluorescence spectrum of the medium in advance with the excitation wavelength to be used. It is also necessary to be aware that Raman signals due to substances constituting the culture medium also appear as background signals.
2. PBS is a buffered solution and is widely used as a medium for cells to maintain a neutral pH and osmotic pressure on cells. PBS is ease to preparation and a recipe to prepare PBS depends on researcher or laboratory. However, cells cannot live long in PBS, and therefore PBS is not suitable for Raman imaging microscopy because it takes a long time to obtain a Raman image. HBSS is a balanced salt solution maintaining physiological pH and osmotic pressure on cells.

HBSS is used as a medium for living cells and can keep cells alive for longer than PBS. HBSS is, therefore, adequate for Raman imaging microscopy as a cell medium exhibiting no fluorescence. However, preparation of HBSS is a little difficult and it may be better to buy HBSS than make it. It is also noted that HBSS cannot be used in a CO_2 incubator.

3. Autofluorescence from biological samples interferes with the measurement of a Raman spectrum. Cells and tissues have endogenous fluorophores and exhibit fluorescence without dye staining, which is called autofluorescence. An excitation wavelength exhibiting weak or no autofluorescence should be used in the Raman measurements of biological samples.
4. The magnitude of autofluorescence depends on the excitation wavelength because autofluorescence intensity is proportional to the absorption intensity of endogenous fluorophores. Representative autofluorescent fluorophores are tryptophan, nicotinamide adenine dinucleotide (NADH), and flavin adenine dinucleotide (FAD), whose absorption wavelengths are 250–300 nm, 300–400 nm, and 300–500 nm, respectively. The fluorescence wavelengths of these fluorophores are 300–450 nm (tryptophan), 400–600 nm (NADH), and 500–650 nm. The wavelength longer than 500 nm is therefore suitable as the excitation wavelength for measuring Raman spectra of biological samples.
5. A longer excitation wavelength is also appropriate for biological samples because damage of samples due to irradiation of excitation laser light becomes smaller using longer wavelengths.
6. Spatial resolution of Raman imaging microscopy, including z-axis resolution, is determined by objective lens, which is the same as that of other microscopes.
7. When placing the glass-bottomed dish on the stage, care must be taken not to introduce bubbles into the immersion oil.
8. The room (surroundings around the microscope) should be darkened to eliminate any stray light and the monitor of PC should be also turned off, if possible.
9. Scattered excitation light should not be allowed to enter the CCD detector that is easily broken by strong light. Care should also be taken not to damage the bright field camera with the introduction of strong light.
10. When the array of the beamlets is distorted, adjust the mirrors introducing the laser beam to the spatial light modulator.
11. The interval of the spots of the beamlets on the sample depends on the objective lens and the excitation wavelength. It is therefore recommended in advance to measure the interval of spots using the objective lens and the wavelength to be used.
12. Because of very weak Raman intensity, it takes more than several seconds to obtain a Raman image. Therefore, damage to samples due to prolonged photo-irradiation must be considered to determine experimental parameters, such as laser power, accumulation time, and pixel dwell time. Pixel dwell time is the irradiation time at each pixel of the image in a point-scanning confocal microscopy.
13. All imaging measurements should be performed with the same number of points because arithmetical operations between the images are necessary to obtain the final image.
14. The most serious problem in multipoint microscopy is that the confocal condition is often broken and the Raman band of the immersion oil is overlapped in the spectra of a cell. Therefore, very careful optical alignment is necessary, and if the band of immersion oil appears, this band must completely be removed using the procedures shown in the previous section.
15. The Raman image of the O–H stretching band of the medium ideally has no irregularity because the concentration of water must be the same in a dish. Therefore, the

appearance of irregularity in the image results from the irregularity among the intensities of the beamlets or inappropriate optical conditions such as slight inclination of the stage. The irregularity of beamlets can be compensated by the division of the image of the O–H stretching band of the medium. This procedure is only necessary for multipoint microscopy.

16. SVD is a mathematical technique, in which a raw matrix is decomposed into two sets of vectors and corresponding singular values. In the analysis of an image using SVD, a raw 4D data matrix (spatial × spatial × spatial × spectral) is converted into a 2D matrix A (spatial × spectral), and then the obtained 2D matrix is decomposed into three matrices as

$$A = U \times W \times V^{T} \qquad (12.5)$$

where U and V are matrices containing singular vectors, and W is a diagonal matrix where the diagonal elements represent the singular values in decreasing order. The components with large singular values correspond to the Raman spectra of samples and those with small singular values are just noise components in the spectrum [2, 11]. Therefore, the contribution of noise to the Raman spectra can be reduced using only the first several values of W (i.e. by replacing the rest values of W with zero) for the reconstruction of the spectra.

References

1. Raman CV, Krishnan KS (1928) A new type of secondary radiation. Nature 121:501–502
2. Uzunbajakava N, Lenferink A, Kraan Y et al (2003) Nonresonant confocal Raman imaging of DNA and protein distribution in apoptotic cells. Biophys J 84:3968–3981
3. van Manen H-J, Kraan YM, Roos D et al (2004) Intracellular chemical imaging of heme-containing enzymes involved in innate immunity using resonance Raman microscopy. J Phys Chem B 108:18762–18771
4. Spiro TG, Strekas TC (1972) Resonance Raman spectra of hemoglobin and cytochrome c: inverse polarization and vibronic scattering. Proc Natl Acad Sci U S A 69:2622–2626
5. Yamaguchi K, Niwa Y, Nakabayashi T et al (2016) Generation of self-clusters of galectin-1 in the farnesyl-bound form. Sci Rep 6:32999. (9 pages)
6. Okada M, Smith NI, Palonpon AF et al (2012) Label-free Raman observation of cytochrome c dynamics during apoptosis. Proc Natl Acad Sci U S A 109:28–32
7. Schie IW, Alber L, Gryshuk AL et al (2014) Investigating drug induced changes in single, living lymphocytes based on Raman micro-spectroscopy. Analyst 139:2726–2733
8. Okuno M, Hamaguchi H (2010) Multifocus confocal Raman microspectroscopy for fast multimode vibrational imaging of living cells. Opt Lett 35:4096–4098
9. Kong L, Zhang P, Yu J et al (2011) Rapid confocal Raman imaging using a synchro multifoci-scan scheme for dynamic monitoring of single living cells. Appl Phys Lett 98:213703
10. Samuel AZ, Yabumoto S, Kawamura K et al (2015) Rapid microstructure characterization of polymer thin films with 2D-array multifocus Raman microspectroscopy. Analyst 140:1847–1851
11. Tanaka S, Kato C, Horie K et al (2003) Time-resolved infrared spectra and structures of the excited singlet and triplet states of fluorenone. Chem Phys Lett 381:385–391